Kinetic Studies of the Atmospherically Implicated Halogen Oxide Radical and Peroxy Radical Cross-Reactions

A thesis submitted for the degree of Doctor of Philosophy
by

Michael Keith MacLeish Ward

Department of Chemistry
University College London
2014

I, Michael Keith MacLeish Ward, confirm that the work presented in this thesis is my own. Where information has been derived from other sources, I confirm that this has been indicated in the thesis.

Signed,

Acknowledgements

I want to thank my supervisor, David, foremost, for giving me the opportunity to work in his group at UCL over the last five years. It has allowed me to become not only a research scientist but also develop an appreciation of the value of engaging the public on the role of science in society. Thank you for your encouragement and input into my work and also for your friendship. It has been an adventure.

Many thanks go to Michael Parkes who taught me much about mass spectrometry during the time we spent on developing the PTR-MS setup. While that work did not make it into my thesis, the experience has readied me for my post-doctorate position in Université Lille 1. I would also like to thank the EPSRC for my funding.

My gratitude goes to the people who have worked in the Rowley Group during the time I spent in laboratory 245, in particular, Valerio, whom I miss working alongside, all the Master's project students (in particular Kaori, Alice & Luke and Ellie) and the Summer students (Abi, Jutta and Rashmi).

Thanks go to the number of great friends that I have been fortunate to have met over the years at UCL who I hope will remain so (in particular Mike, James, Kevin, Jess, Josie, Ana, Henry and Henry, Harry, Fawzi, Rich, Eddie, Stonesy, Helen, Emma, Belle, Briggsie and many others), and the CPSers.

My thanks and love go to my family (Mum, Dad, Jon, Shona, Jude, Dan and the boys: Elliot, Ethan and Willem) for their continued and unwavering support. Thank you Mum and Dad for allowing me to colonise the study and keeping me fed and watered during the write up, it really made a difference.

Last but certainly not least I would like to thank Jessica for seeing through my craziness over the last few months, you have been wonderful (and to her family, who excused my unsociable behaviour in Devon during the holidays).

List of Publications as a Result of the Studies Reported in this Thesis

In preparation:

Ward, M. K. M., Rowley, D. M., “Kinetics of the ClO + HO_2 reaction over the temperature range T = 210 – 298 K”

Ward, M. K. M., Rowley, D. M., “Temperature Dependence Studies on the Kinetics of the ClO + CH_3O_2 → Products Reaction, T = 250 – 298 K”

Ward, M. K. M., Rowley, D. M., “Kinetic Studies of the BrO + HO_2 Reaction Using Laser Flash Photolysis with UV Spectroscopy Over the Temperature Range T = 246 – 315 K”

Abstract

Throughout the 20th and early 21st centuries, the anthropogenic effects of global industrialisation on the composition of Earth's atmosphere have been observed. In particular, the effects of significant emissions of halogen containing species, which have been overwhelmingly manmade in origin, have greatly perturbed the ozone budget of the atmosphere. The occurrence of halogen oxide radicals, XO (where X = Cl, Br, I), which are formed by the reaction of photolytically released halogen atoms with ozone, has a profound impact on atmospheric chemistry. These XO radicals not only react with themselves but they are also believed to react in the atmosphere with other key radical species. In particular, XO react with naturally occurring peroxy radicals, RO_2, which are key members of the so called "odd hydrogen" radical family, HO_x, and determine global ozone budgets and the oxidative capacity of the atmosphere *i.e.* its ability to remove pollutants. Therefore, detailed laboratory studies of the kinetics of reactions of the type $XO + RO_2 \rightarrow$ Products are important in assessing their atmospheric importance and understanding the implications of such chemistry occurring throughout Earth's atmosphere.

This thesis discusses in detail some of the key processes that occur in the gas phase in Earth's atmosphere which determine its composition. This is then related to the fundamental principles of gas phase reaction kinetics which in turn are used to discuss experimental strategies for studying such processes. The results of the kinetic studies of three reactions of the form $XO + RO_2$: $ClO + HO_2$; $ClO + CH_3O_2$; and $BrO + HO_2$ are presented. These reactions were studied using the laser flash photolysis technique coupled with UV absorption spectroscopy employing a charge coupled device (CCD) detection system for radical monitoring. The application of CCD detection facilitated the real time monitoring of the XO radical species concentration in each reaction studied. This was afforded by the rapid acquisition of broadband sequential spectra by the CCD in which transmitted light intensities were converted to absorbances by Beer's law. Exploiting the vibronic structure characteristic to XO radicals *via* 'differential' spectroscopy, unequivocal monitoring of XO was afforded by converting the resultant differential absorbances into concentrations using the Beer-Lambert law. The obtained temporal XO concentration profiles were then analysed

using detailed numerical models. Through strict control of successive experimental conditions and constraints in each fitting model used, the initial concentrations of RO_2 were able to be inferred and their following temporal behaviour simulated alongside the measured temporal XO profiles in order to obtain kinetic information on each reaction investigated.

Specifically, the ambient temperature (T = 298 K) rate constants obtained for each reaction are found to be large: $k_{(\mathrm{ClO + HO_2})} = (8.47 \pm 2.31) \times 10^{-12}$ $\mathrm{cm^3\ molecule^{-1}\ s^{-1}}$; $k_{(\mathrm{ClO + CH_3O_2})} = (2.7 \pm 0.5) \times 10^{-12}$ $\mathrm{cm^3\ molecule^{-1}\ s^{-1}}$; and $k_{(\mathrm{BrO + HO_2})} = (2.89 \pm 0.31) \times 10^{-11}$ $\mathrm{cm^3\ molecule^{-1}\ s^{-1}}$. All ambient temperature results are in general agreement with previous studies which, for each reaction, is discussed in detail below in the appropriate discussion sections. The temperature dependence of each rate constant studied, which is significant for each reaction, was found to be suitably described by the following Arrhenius expressions:

$$k_{(\mathrm{ClO + HO_2})}\left(T/\mathrm{K}\right) = (4.07 \pm 3.55) \times 10^{-13}\, e^{\left(\frac{(949 \pm 197)}{T}\right)} \mathrm{cm^3\ molecule^{-1}\ s^{-1}}$$

$$k_{(\mathrm{ClO + CH_3O_2})}\left(T/\mathrm{K}\right) = 2.20^{+3.40}_{-1.30} \times 10^{-11}\, e^{\left(\frac{-(642 \pm 253)}{T}\right)} \mathrm{cm^3\ molecule^{-1}\ s^{-1}}$$

$$k_{(\mathrm{BrO + HO_2})}\left(T/\mathrm{K}\right) = 9.28^{+7.17}_{-4.04} \times 10^{-12} e^{\left(\frac{(316 \pm 157)}{T}\right)} \mathrm{cm^3\ molecule^{-1}\ s^{-1}}$$

This work reports the most significant negative temperature dependence of the ClO + HO_2 reaction to date. The temperature dependences found in this work for the ClO + CH_3O_2 and BrO + HO_2 reactions are in good agreement with the most recent results reported in the literature. The results for each reaction presented in this thesis are directly compared with one another and their potential atmospheric implications are discussed.

Table of Contents

Chapter 1: The Earth's Atmosphere: History, Composition and Physical Structure

Chapter 6: The Kinetics of the BrO + HO_2 Reaction 209

Table of Figures

Chapter 1

Chapter 2

Chapter 3

Chapter 4

Chapter 5

Chapter 6

Appendix I

Appendix II

Table of Tables

Chapter 4

Chapter 5

Chapter 6

Chapter 1: The Earth's Atmosphere: History, Composition and Physical Structure

1.1 Introduction

Science continues to develop, branch-out and cross over into an increasing number of fields and disciplines. It is a quest that delves into the curiosities we have concerning our world and solving the questions that follow them. One such field that has developed throughout the latter half of the 20th century is *atmospheric science*, a multi-disciplined field that encompasses chemistry, physics and meteorology controlled by fluid dynamics. As is discussed below, the importance of Earth's atmosphere to life is absolute and its complexity is arguably on a par with the workings of that of living organisms. Consequently, it is far from trivial to unravel the many labyrinthine interactions of gases that only constitute trace amounts of the atmosphere, yet determine its composition and the habitability and climate of Earth.

Unique to all other planets in the solar system, Earth possesses an atmosphere which resides in a state of reduced entropy – its composition of gases lies far from chemical equilibrium. It is apparent that the atmosphere is part of an Earth system in which ocean, atmosphere, land and life are all interlinked and interdependent on each other. The extent of the relationship between these entities is so close that some have even viewed the Earth system, whose principal components are discussed below, as a living macro-organism in its own right in the form of Gaia.[1] Whether we *are* parts of some super planetary macro-organism can never be definitely proved. As James Lovelock, the originator of this concept, points out, the Earth is "alive as a gene is selfish." However, what is gradually becoming more understood are the elaborate cycles involving elements ubiquitous throughout the planet, such as carbon, oxygen, nitrogen, sulphur and phosphorous and these are key features of the Earth system. In particular, these cycles have allowed the atmosphere to evolve to its present state which until recently has remained in a relatively constant composition and climate for at least the last tens of thousands of years.[2]

1.1.1 The Earth System

As touched upon above, the Earth behaves as a system – "*a set or assemblage of things connected, associated, or interdependent, so as to form a complex unity*" as defined in the Oxford English Dictionary. This "assemblage of things" comprises chiefly of the *atmosphere, hydrosphere, biosphere* and the *lithosphere* (Figure 1.1). As a system it is powered by the Sun *via* solar radiation – principally UV/visible rays, a product from nuclear fission deep within the Sun, that constantly bombard our planet. The heat from Earth's interior provides a secondary source of energy in the form of thermal energy derived initially from the planet's initial formation, the decay of radioactive elements, and the freezing of the inner core.[3] Together as a system, they all play a part in the resulting climate in which the atmosphere plays a dominant role.

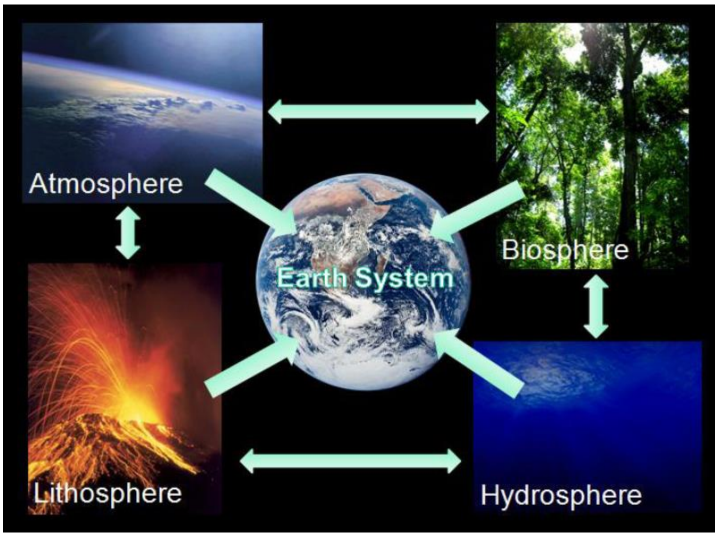

Figure 1.1 *An illustration of The Earth System in which each sphere is interconnected and in turn directly affect each other and ultimately Earth's climate.*

The Lithosphere consists of the Earth's strong crust and uppermost mantle and is broken into a number of tectonic plates. These plates float on the mantle – the much thicker and denser layer below the crust. Slow convection within the mantle causes tectonic motion which results in the characteristic position of land observed today.[4] At these plate boundaries, in which separate plates collide, seismic and volcanic activity results in which gases and aerosols are ejected from within the Earth into the atmosphere. At the same time the thickest parts of the Earth's crust provide a base and source of minerals upon which terrestrial life depends.

The Hydrosphere consists of the oceans, rivers and frozen water locked in primarily the poles and glaciers (the cryosphere). It is essential to all aspects of the biosphere, providing a medium for life in the form of the hydrologic cycle and it shapes the lithosphere through several erosional processes. The oceans are central to climate in which ocean circulation driven by wind (the topmost few hundred meters of ocean) and the thermohaline (slower, deep-ocean) components transport thermal energy and chemicals throughout the Earth system.[3] The cryosphere also plays a significant climatic role in reflecting solar radiation[4] back into space thus affecting the Earth reflecting (albedo) and therefore the global temperature. The significance of the hydrosphere is particularly evident when considering the hydrological cycle below.

The Biosphere is normally split into the marine (oceans) and terrestrial (land) systems but as a whole it may be considered as the narrow band at the Earth's surface where life evidently flourishes. The two biospheres are both inexorably dependent on sunlight yet it is the different needs of each sphere for life to flourish that explain the geographical distribution of this life. Terrestrial life typically needs ambient temperature and a relative balance of precipitation/evaporation levels and therefore these factors determine which ecosystems are found and where. This is fundamentally determined by *insolation* (*i.e.* the incident solar radiation) at the top of the atmosphere but also by other climatic variables.[3] In contrast, the marine biosphere is dependent on levels of nutrients as opposed to precipitation. The *euphotic zone* of the ocean is where there is enough solar radiation for photosynthesis to occur which is primarily undertaken by phytoplankton (to a depth of the first few 100 m). As a result, water in this region is oxygenated and the phytoplankton therein form the basis of the oceanic food chain. However photosynthesis also lowers the carbon content of the water and as a result life typically thrives in coastal areas or other regions where oceanic upwelling is significant in which water from the deep ocean replenishes nutrient levels.[1] Another important sub-sphere concerns human civilisation (the *anthrosphere*) whose environmental impact throughout the world is almost ubiquitous, in particular, on the effects on the atmosphere and climate which are becoming ever more apparent.

The Atmosphere, the principal player in Earth's climate is the gaseous layer that blankets Earth's surface whose composition is critical for supporting life. Key features include the natural "greenhouse effect" which provides a stable climate whereas the band of relatively elevated ozone (O_3) concentration in the stratosphere, the so called "ozone layer" acts as a filter for harmful solar ultraviolet (UV) radiation O_3 absorbs wavelengths of radiation strongly in the UV B region of the spectrum which is particularly damaging to biological systems. The role of ozone in the atmosphere is discussed in greater detail below.

The degree of interplay between the four main spheres of the Earth system is accentuated when considering the major fluxes of some of the critical components for life between "reservoirs." These include the carbon cycle, the hydrologic cycle and the occurrence of oxygen in its various allotropes. The global cycles of carbon and water in particular both characterise the modern day atmosphere and in turn the Earth's climate. These are discussed below.

1.1.2 The Water and Carbon Cycles

1.1.2.1 The Water Cycle

Water is essential to all life on Earth. It is a solvent whose interactions with hydrocarbons, amino acids and proteins eventually result in the formation of cells and thereafter provides a medium in which resulting organisms can import and export the chemicals that give life. On a global scale water is transported throughout the Earth system *via* physical fluxes powered by heat transfer from one component to the other. Evaporation and precipitation; the forward and reverse transportation of water into the atmosphere from the hydrosphere, play a key role in climate.[2] Atmospheric water vapour, the composition of which is highly variable in the lower atmosphere, is also a potent greenhouse gas in itself but also plays significant roles in a negative feedback loop in the climate system by the lowering of surface temperatures *via* evaporation/transpiration and condensing onto cloud condensation nuclei (CCN), forming clouds that can reflect incoming solar energy back into space.[5] Water is also key to the oxidative capacity of the atmosphere as it is one of the precursors to the hydroxyl radical, OH, the radical that is responsible for the removal of many pollutants such as volatile organic compounds (VOCs) that are potentially much more powerful on a molecular basis as greenhouse gases than CO_2. The precipitation of water out of the atmosphere onto land is also, evidently, critical to the terrestrial biosphere and is one of many processes that staunchly links the hydrosphere (*ergo* the hydrologic cycle) to the carbon cycle. It is also now evident that the atmospheric system and climate affect this hydrological cycle and *vice versa*.

The hydrologic cycle is a convenient means to describe the ways in which the hydrosphere interacts with the other components of the Earth system providing an inventory for where masses of water lie, which depend on their relative turnover times. Excluding the water estimated to reside in the lithosphere, mantle and core, the mass of the modern day terrestrial hydrosphere is approximately 94.3 % (of a total of 1.69×10^{24} g of water) ocean water; 1.9 % ice and 3.4 % groundwater (up to a depth of 5 km).[6] The surface water on land (lakes, wetlands, rivers, *etc*) accounts for only 0.014 % of the total water inventory and living organisms contribute 0.001 %.[6] However, the residence times for this water are many times shorter in these latter reservoirs than the larger reservoirs of water thus making them many times more important for the cycling of materials throughout the hydrosphere. Evidently, timescale as well as total amount are key to the role of water on Earth.

1.1.2.2 The Carbon Cycle

In all parts of the hydrosphere, carbon species occur in free and bound forms (analogously to water), simultaneously appearing in different aggregate and dispersed states which chemically and physically transform from one another under the influence of physical, biologic and geologic factors. Consequently, describing the masses of carbon within these two principal reservoirs of the hydrosphere in terms of importance, the oceanic and continental, has proven difficult since the parameters of the water cycle are sharply different from those of carbon turnover, although both are governed by general biogeochemical processes.[7] The organic and carbonate carbon content of living organisms of the biosphere are the most mobile part of the carbon cycle and together, represent a significant reservoir of atmospheric carbon, principally

CO_2. It is estimated that terrestrial ecosystems alone have been absorbing up to 30 % of additional anthropogenic CO_2 emitted over the past five decades.[8] Therefore, the biosphere, which shares the same space and materials as the hydrosphere, is also an important sink in atmospheric CO_2 and may therefore be significant in mitigating man-made climate change. The ocean holds the vast majority of inorganic and organic carbon in the hydrosphere, with the inorganic components (chiefly CO_2, HCO_3^- and CO_3^{2-}) dominating (total mass $\approx 3.81 \times 10^{15}$ g).[6] The organic component, which consists primarily of biota (4×10^{15} g), particulate organic matter (50×10^{15} g) and dissolved organic matter (1000×10^{15} g), is central to the uptake of CO_2 in which the ocean absorbs an estimated 1.61×10^{15} g C/yr. Biota, principally phytoplankton, are the main primary source of organic matter in the oceans reducing CO_2 *via* photosynthesis forming around 60×10^{15} g $C_{organic}$/yr net production and 1×10^{15} g $C_{inorganic}$/yr in the form of carbonate *via* biosynthesis. The organic matter produced from the death of biota must be metabolised by bacteria, forming pellets which in turn sink to the ocean bottom along with the inorganic carbonate. The burial of organic matter is only a fraction of its net production but still amounts to around 0.25×10^{15} g C/yr, essentially locking in it from the oxidising conditions above and providing an indirect flux of atmospheric CO_2 to the lithosphere.

The abundance of carbon in the global river system with the destruction and formation of organic matter are extremely important biogeochemical characteristics of the terrestrial hydrosphere/biosphere. Climatic zonation is the main factor in determining the distribution of the nature of organic matter and salts with regional humidity affecting the salinity of river systems which can in turn be highly seasonal. Consequently, distribution in such a dynamic system is complex. The terrestrial biosphere plays a significant role in driving abundances of organic matter, which is by in large supplied by humic matter from the soil, which it itself is controlled by climate. The increasingly perturbed global climate, with its increasingly erratic swings both in temporal length and severity is therefore a concern as this directly affects the health and productivity of ecosystems. An extreme event is defined as "an episode or occurrence" in which a statistically rare or unusual climatic period alters ecosystem structure and/or functions well outside the bounds of what is typical or normal variability.[9] This is general enough to include episodes such as combined heat-wave and drought followed by extreme precipitation and it is exactly these sorts of episodes that trigger time delayed responses in ecosystems. The damage of ecosystems by such events can turn them from net atmospheric carbon sinks to sources.[10] Therefore, the future of terrestrial ecosystems and the potential of CO_2 mitigation in the Northern hemisphere in particular, are in a state of mutual feedback with climate. Here, the atmosphere plays a critical role as it is the medium in which climate is expressed, thus the chemistry and physics that characterise the atmosphere thereby characterise Earth's climate system. Accordingly, it follows that the next section provides a description of the key features of Earth's atmosphere.

1.2 The Earth's Atmosphere: History, Composition and Physical Structure

1.2.1 A Brief History of Earth's Atmosphere

The Earth's atmosphere is the gaseous layer that blankets Earth's surface. Held close by Earth's gravitational pull, its mixture of constituent molecules and atoms known as air are prevented from escaping into the vacuum of space, barring the lightest molecules and atoms, namely hydrogen and helium. As discussed above, the atmosphere is a component of the Earth system contributing to the Earth's workings as a whole. The main spheres, differentiated by their differing states and phases of matter are identified as being the atmosphere, hydrosphere, biosphere and lithosphere which all interface one another, exchanging matter at vastly divergent rates. The energy required for these exchange processes is principally provided by the Sun under solar irradiation resulting from the relentless nuclear fusion deep within the star and from the heat of the Earth's interior, an artefact from its initial formation and nuclear fission within Earth's interior. As was discussed above, the dynamical exchange of material throughout the Earth System results in a complex interdependency between each component, ultimately determining their composition and structure.

Unique to our solar system, Earth's atmosphere is in a state of reduced entropy compared to the atmospheres of the other planets and those of their moons.[1,11] The strongest evidence for this being the lack of the observed atmospheric trace species, such as methane, on these bodies compared to the rich variety that reside on Earth.[12,13]

Trace species are either reactive compounds typically including volatile organic compounds (VOCs) or intermediates such as free radicals. Such species typically arise from the biosphere and the observation of this has led to the realisation that life has been vital in keeping the atmosphere and therefore the entire Earth system in a state far removed from chemical equilibrium. The existence of life on Earth and its relationship with the present day atmosphere is evidently complex. It is widely believed that the atmosphere has coevolved with life as evidenced by its emergence, aeons ago, through complex feedback loops involving chemical composition and the corresponding shifts in Earth's radiative balance.[14,15] The composition of the Earth's present day atmosphere is vastly different to the young Earth atmosphere formed by the outgassing of CO_2, N_2, H_2O, CO and H_2 as the planet initially cooled. The most dramatic change in Earth's composition with the emergence of life was the rise in O_2 levels which is directly associated with the evolution of photosynthetic apparatus – photon harvesting membranes found in some bacteria and more complex organelles found in plants and algae.[16] Photosynthesis is essentially the photo-reduction of CO_2 to carbohydrate performed by chlorophyll synthesising life forms as a source of carbohydrate:

$$2n\mathrm{CO_2} + 2n\mathrm{H_2O} + h\nu \rightarrow 2n(\mathrm{CH_2O}) + 2n\mathrm{O_2} \tag{1.1}$$

Photosynthesis is in essence the reverse of respiration – a form of low temperature 'combustion' which many life forms use to derive the energy needed to live. This reduction of carbon releases O_2 as a by product which is released into the atmosphere. There also exist inorganic processes in which O_2 can be formed from H_2O and CO_2 photochemically initiated by short wavelength UV radiation with the subsequent escape of hydrogen into space the net effects of which are summarised below:

$$2\mathrm{H_2O} + h\nu \rightarrow 2\mathrm{H_2} + \mathrm{O_2} \tag{1.2}$$

$$4\mathrm{CO_2} + h\nu \rightarrow 4\mathrm{CO} + 2\mathrm{O_2} \tag{1.3}$$

However, before the arrival of photosynthetic life, limiting factors such as *shadowing* existed – a result of the build up of O_2 which strongly absorbs solar radiation in the region below $\lambda = 280$ nm thus decreasing photolysis rates and hence reversing the expulsion of H_2. This is proposed to have limited atmospheric O_2 levels much below those levels inferred from geological mineral deposits younger than 2.2 Gyr (the notional emergence of photosynthetic life) and observed today in the atmosphere. With photosynthesis in place such shadowing was far less effective since photosynthetic apparatus requires light of wavelengths in the visible spectrum, except green light ($\lambda \sim 700$ nm, hence the colour of vegetation). However, crucially, O_2 levels have eventually risen to such levels (currently 20.95 % in dry air) principally because of the burial of the formed biogenic carbohydrate (discussed above), preventing its oxidation.

1.2.2 The Allotropes of Oxygen: the Provenance of Atmospheric Structure

Oxygen is vital to the Earth's atmosphere as we know it due to its ability to simultaneously exist in a number of allotropes under atmospheric conditions. While O_2 is the most stable, it strongly absorbs short wavelength (UV) solar radiation ($\lambda \leq$ 245 nm) where it undergoes photolysis forming atomic oxygen:

$$O_2 + h\upsilon\ (\lambda \leq 245\ \text{nm}) \rightarrow O + O \tag{1.4}$$

Due to the high atmospheric abundance of O_2, O atoms subsequently and principally react with molecular oxygen in a termolecular process to give the atmospherically important trace species, ozone:

$$O + O_2 + M \rightarrow O_3 + M \tag{1.5}$$

where M is a buffer species that stabilises the initially formed, thermally excited, O_3 *via* molecular collision. O_3 plays a number of key roles throughout the atmosphere, strongly absorbing photons in the near UV and at visible wavelengths causing dissociation:

$$O_3 + h\upsilon\ (\lambda < 800\ \text{nm}) \rightarrow O + O_2 \tag{1.6}$$

Due to the low pressures of the upper atmosphere this photoabsorption followed by reaction (1.5) produces temperature increases whose origin lies in the recombination of O with O_2 and is thereafter the source of the temperature structure that differentiates the lower and upper atmosphere.

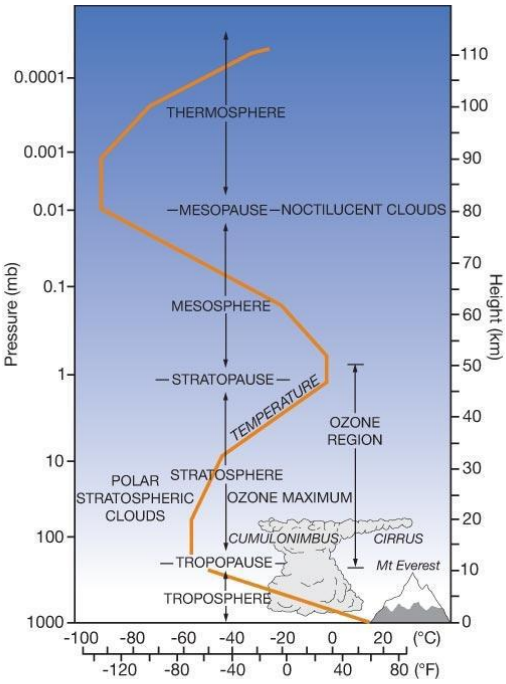

Figure 1.2 *The physical structure of Earth's atmosphere as a function of temperature.*[16]

The characteristic feature of increasing temperature with increasing height within the atmosphere begins at around 15 km (it varies with latitude) and reaches a maximum at *circa* 50 km (Figure 1.2). This region of temperature inversion is known as the stratosphere and, while there are subsequent layers above the temperature maximum marking its end (the *stratopause*), their chemistry and properties are beyond the scope of this work. The region beneath the stratosphere is coined the troposphere and begins at sea level and is essentially capped by the *tropopause* (the point at which the temperature ceases to decrease as a function of increasing altitude) marking the beginning of the stratosphere. Owing to the continuous decrease of atmospheric pressure with increasing altitude the troposphere is the densest region of the atmosphere containing around 80 % of the mass of the atmosphere.[16]

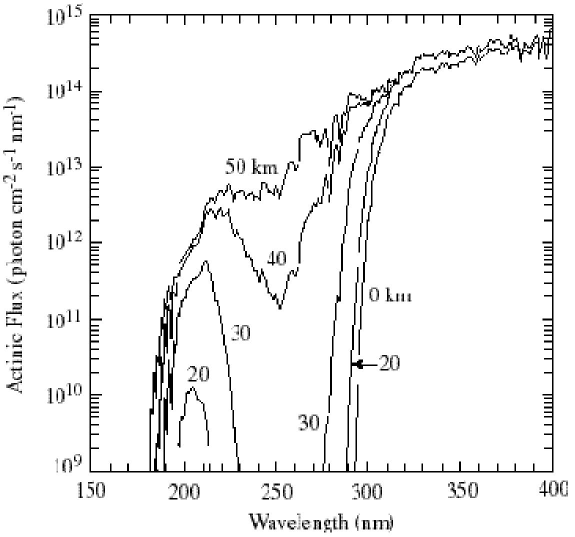

Figure 1.3 *The solar actinic flux as a function of wavelength at different altitudes in the atmosphere.*[15]

The temperature maximum of the stratosphere does not coincide with the maximum ozone level (which is at around 22 km) due to elevated ozone destruction at higher altitudes through both direct photodissociation and reaction of O_3 with oxygen atoms whose concentrations are increased as a consequence of the greater photolysis rates due to the levels of intense radiation imposed on this region:

$$O + O_3 \rightarrow 2O_2 \qquad (1.7)$$

Reactions (1.4) to (1.7) are known together as the odd oxygen cycle (O_x cycle) since there is rapid interchange between atomic oxygen and O_3 (reactions (1.5) and (1.6) are very fast). This cycle plays a vital role in shielding life from the most energetic parts of the Sun’s radiation which photolyses organic compounds including DNA giving rise to genetic implications. This filtering of light is demonstrated in Figure 1.3, above, which shows how the actinic (solar) flux varies with altitude.[15] The actinic flux is the quantity of light available to molecules at a particular point in the atmosphere and which, on absorption, drives the photochemical processes of the atmosphere. It should be noted that, at sea level, practically no solar light below 300 nm is detectable and this is the reason why light of shorter wavelengths than UV is predominantly absent from the troposphere. This, however, is important to the photochemistry of the lower atmosphere as is discussed below.

1.2.3 Mixing Processes within the Atmosphere

Due to the changes in temperature gradient, as discussed above, mixing between the stratospheric and tropospheric layers is strongly inhibited. As a consequence, only the longest lived trace species and pollutants are able to cross into the stratosphere from their source, typically, in the troposphere. In addition, the troposphere is much wetter and better mixed (thus, except for the shortest lived trace species, the composition is almost constant) than its overlying layer and there is a relative absence of short-wave radiation due to its absorption by stratospheric ozone. Consequently, the ensuing photochemistry of the troposphere is markedly different to that of the stratosphere and the implications of this are discussed below. Prior to this however is an explanation of the physical basis of why the troposphere is well mixed compared to the stratosphere.

The relatively sharp decrease in temperature with increasing altitude in the lowermost atmosphere, shown in Figure 1.2, originates from the proximity to the Earth's surface but also the compressibility of gases, as demonstrated by the decrease in atmospheric pressure from low to high altitudes. As air is principally a gas, therefore compressible, it becomes less dense with increasing height. This phenomenon permits adiabatic processes to occur *i.e.* changes in physical state which may happen without heat being added or withdrawn from the system. As a result, a hypothetical 'parcel' of dry air that is thermally isolated from its surrounding environment expands to maintain its ambient pressure when rising. The work done by this adiabatic expansion thus causes the air parcel to decrease in temperature according to the first law of thermodynamics. The rate of change in temperature with altitude is defined as the *adiabatic lapse rate*:

$$\Gamma = dT / dz \qquad (1.2\ \text{i})$$

If the adiabatic lapse of an air parcel, Γ_{parcel}, and that of the surrounding environment, Γ_{env}, differ, then it follows that vertical displacement of an air parcel may cause a disparity in the temperature between the air parcel and its surroundings which if positive, may initiate convection and vertical mixing:

$$\Delta T = (\Gamma_{\text{parcel}} - \Gamma_{\text{env}})\, dz \qquad (1.2\ \text{ii})$$

The concept of different parcels of air in the troposphere is also a suitable description as the water vapour content is highly variable thus providing a convenient parameter in differentiating between different pockets of air. This is because as water vapour cools it condenses, releasing latent heat and so counters the cooling effect of adiabatic expansion. As a consequence, pockets of air which have different amounts of water vapour (humidity) have different lapse rates and so, are potentially different in temperature. Therefore, if a parcel of air is displaced upwards and has a positive temperature difference between it and its surroundings (*i.e.* the air parcel is warmer) it will continue to rise following an initial displacement. This is because the air parcel is less dense than its surroundings and therefore more buoyant. The opposite is true for a parcel of air that has a negative temperature difference between it and its surroundings. The ramifications of this effect mean that vertical transport within the troposphere is typically facile, in general, and so vertical mixing is a key feature within this region. In addition to this, atmospheric turbulence caused by surface friction, eddy formation and convectional currents (the troposphere is largely heated by surface-to-air turbulent heat transfer rather than absorption of direct radiation), means tropospheric air is well mixed.[14]

Within the troposphere there exist two sub-layers: the planetary *boundary layer* which is typically the lowest 1 – 2 km above sea level and is the region of the atmosphere that actually interfaces with the surface. Globally, there are many different surfaces ranging from ocean, desert, tundra and foliaged. Consequently different regional boundary layers have different chemical characteristics as the shortest lived trace species are typically emitted from the surface and so boundary layers often have higher local concentrations of these surface emitted trace species. The boundary layer arises as a consequence of turbulence near the surface being capped by a layer of (relative) high stability. This higher layer is the so-called *free troposphere* and is responsible for trapping pollutants close to the ground, thus preventing their dilution throughout the whole troposphere and resulting in, for example, photochemical smog that may occur in polluted urban areas. However, the effectiveness of the free troposphere in capping the boundary layer is also highly time dependent (daily and seasonally). Thus, once trace species escape the boundary layer, they may be transported and mixed throughout a greater distance within the troposphere.

1.2.4 Changes in Atmospheric (Stratospheric and Tropospheric) Composition

1.2.4.1 Changes in Stratospheric Ozone

While the odd oxygen cycle provides a good qualitative description of stratospheric ozone behaviour, the relative rates of reactions (1.5) and (1.7) are such that this model actually predicts an overestimate of the measured average odd-oxygen ($[O] + [O_3]$) equilibrium concentration. This imbalance can only be attributed to additional O_3 loss mechanisms that give an overall reaction equivalent to that of reaction (1.7) however with a larger overall effective rate constant. Naturally occurring trace species found in the stratosphere such as NO and OH destroy O_3 in which their reaction products scavenge oxygen atoms and thus limit O_3 production:

$$\mathbf{X} + O_3 \rightarrow XO + O_2 \qquad (1.8)$$

$$XO + O \rightarrow O_2 + \mathbf{X} \qquad (1.9)$$

$$\textit{net: } O_3 + O \rightarrow 2O_2$$

where X = OH or NO.

However, much larger amounts of OH and NO than those found in the stratosphere would be needed to account for the discrepancy in O_3 levels from the O_x only cycle if it were not for their regeneration in the event of reaction (1.9). This renewal process results in a catalytic chain reaction in which only relatively small amounts of X are required to destroy large amounts of O_3 and gives an overall reaction equivalent to reaction (1.7). The effect of X on stratospheric ozone levels is often dependent on reaction (1.8), which is the rate determining step of this cycle. For both OH and NO, reaction with O_3 is slow, especially at stratospheric temperatures. Consequently, the levels of O_3 destruction by this process, while significant, are to an extent limited.

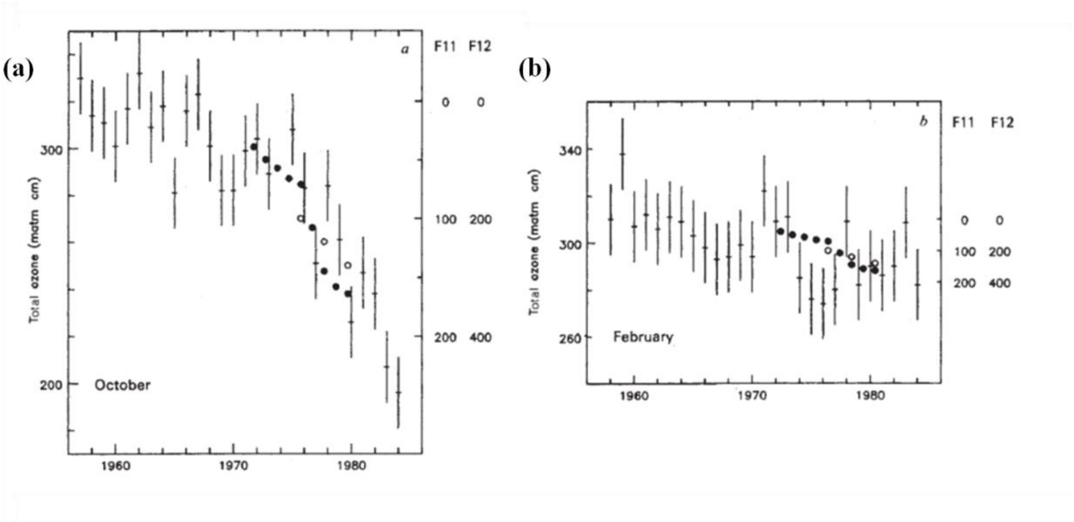

Figure 1.4 *Monthly means of total column* O_3 *at Halley Bay, Antarctica and Southern Hemisphere measurements of CFCs F-11 (solid circles) and F-12 (circles) in pptv from 1957 – 1984 for the Southern Hemisphere: (a) Spring; and (b) Summer. Adapted from Farman et al.*[17]

During the second half of the 20th century observations made in Southern Polar latitudes were reported to show large scale depletion events of stratospheric ozone.[16] These events occur in the early Antarctic spring when the Sun returns (Figure 1.4 (a)), implying a photo initiated process causing a severe decline in total O_3 concentrations compared to those later in the summer (Figure 1.4 (b)). While early measurements from the late 1950s showed no significant seasonal perturbations in O_3, later observations demonstrated annual O_3 destruction which since increased yearly. In time this perturbation has become known as the annual ozone "hole" due to the massive extent of O_3 lost. The cause of this additional ozone depletion was not actually a complete mystery as it had been previously predicted that emissions of a certain class of anthropogenic pollutant, namely chlorofluorocarbons (CFCs), could lead to a build up of chlorine containing compounds within the stratosphere.[18] CFCs are a solely man made, fully halogenated class of compound and were largely manufactured in significant quantities as "safe" refrigerants, solvents and aerosol propellants from the mid-twentieth century.[19] Their perceived safety was primarily from their chemical inertness under ambient conditions arising from the absence of hydrogen on the halocarbon frame. This makes degradation of CFCs in the troposphere difficult as the destruction of the majority of organic pollutants is initiated through reaction with the OH radical *via* hydrogen abstraction (discussed below).

However this, along with their insolubility in water, means CFCs have an estimated atmospheric lifetime in the range of 40 to 150 years allowing them to build up in the stratosphere and reach Polar stratospheric regions *via* the relatively slow 'Brewer-Dobson' circulation (in which air is transported upwards at the equator and downwards at the poles). This accumulation is shown in Figures 1.4 (a) and (b) with the concentrations of the most widely manufactured CFCs at the time, F-11 ($CFCl_3$) and F-12 (CF_2Cl_2) shown in Spring and late Summer. What is particularly interesting about this plot is the clear anti-correlation between CFCs and O_3 and how it changes over the Summer under conditions of continuous solar irradiation. The short-wave radiation that bombards the stratosphere determines the eventual fate of the CFCs and reveals the negative environmental impacts of such apparently inert compounds.

CFCs undergo photolytic dissociation at altitudes between 20 – 40 km, absorbing radiation in the far ultraviolet (λ ~ 200 nm) and liberating atomic chlorine in the process. For example, the compounds F–11 and F–12 degrade in the following manner respectively:

$$CFCl_3 + h\nu \rightarrow CFCl_2 + Cl \qquad (1.10)$$

$$CF_2Cl_2 + h\nu \rightarrow CF_2Cl + Cl \qquad (1.11)$$

These Cl free radicals then enter an ozone destroying catalytic cycle analogous to reactions (1.8) and (1.9):

$$Cl + O_3 \rightarrow ClO + O_2 \qquad (1.12)$$

$$ClO + O \rightarrow Cl + O_2 \qquad (1.13)$$

$$\textit{net:}\ O + O_3 \rightarrow 2O_2$$

When considering these gas phase reactions, chemical understanding predicts chlorine initiated O_3 destruction to be most efficient at an altitude of around 40km where O atoms are most abundant. However, the bulk of the total ozone column lies in a layer at lower altitudes – around 10 – 20 km below this maximum and so the integrated impact on the total ozone column of this cycle is actually estimated to be small.[20] As a result, the formation of the ozone hole and its size were observed much earlier than expected, a clear indication that significant gaps in the theory existed. The evidence that halogen chemistry, in particular chlorine related chemistry, has been the cause of the bulk of observed polar ozone depletion in recent years is now strong.[21,22] Therefore the misunderstanding lay not in the *source* of the O_3 depletion but how active chlorinated species were able to destroy it at altitudes where the ozone layer typically reaches its maximum concentration. The answer concerns processes involving heterogeneous chlorine chemistry, discussed below.

The chemistry of the atmosphere despite it being a predominantly gas phase medium is not restricted to the homogeneous gas-phase. Heterogeneous reactions – reactions involving species in different phases, occur throughout the atmosphere between gaseous species and airborne particles/droplets known as *aerosols*. Aerosols are suspensions of particles ranging in the size order from the extremely small (0.05 μm) up to the relatively large (1 mm) and consist of solid and/or liquid matter that clouds and other meteorological phenomena are composed of. Polar stratospheric clouds (PSCs) are high altitude clouds, which form in the polar stratosphere during wintertime when temperatures drop below the condensation point for certain trace species in the absence of sunlight. PSCs are typically composed of ice and solid nitric acid trihydrate (NAT) particles which in polar winter night time provide surfaces for the conversion of relatively inert species such as HCl and $ClONO_2$ to Cl_2 and HNO_3:

$$HCl + ClONO_2 \rightarrow Cl_2 + HNO_3 \qquad (1.14)$$

This reaction has a number of consequences, first being the build-up of photolabile chlorine (Cl_2) in the polar stratosphere over winter. Cl_2 is easily photolysed by solar UV radiation from the returning Sun in Springtime and dissociates forming two Cl radicals for every Cl_2 molecule which thereafter destroy ozone:

$$Cl_2 + h\nu \rightarrow Cl + Cl \qquad (1.15)$$

Another consequence is the formation of nitric acid which effectively improves the ozone destroying capacity of chlorine. ClO formed from reaction (1.12) can combine with NO_2 which competes with reaction (1.13), forming the Cl reservoir species $ClONO_2$ thus terminating the radical chain and preventing Cl regeneration:

$$ClO + NO_2 + M \rightarrow ClONO_2 + M \qquad (1.16)$$

Therefore, reaction (1.14) results in a sink for NO_2 as it is bound into nitric acid, thus limiting reaction (1.16). This heterogeneous *denitrification* of the stratosphere also takes place *via* the condensation of HNO_3 onto solid NAT particles during PSC formation and occurs at temperatures considerably higher than the frost point.[20] The overall outcome is a significant perturbation of chlorine reservoir abundances and active species with the partitioning of chlorine in favour of Cl_2 under the conditions of the polar winter. The photolysis of the accumulated Cl_2 in Spring thereafter results in a chlorine 'explosion' resulting in considerable O_3 destruction and an elevated Springtime ClO mixing ratio amplified *via* denitrification by PSCs. Under such enhanced concentrations, the ClO free radical undergoes a pressure dependent self-reaction which results in formation of the thermally and photolytically unstable ClO dimer which may also dissociate in a unimolecular fashion:

$$ClO + ClO + M \rightleftharpoons Cl_2O_2 + M \qquad (1.17)\ (-1.17)$$

However, despite its inherent instability, at the low temperatures prevalent in the stratosphere, the equilibrium between these two reactions lies to the side of the ClO dimer.

As a result of the initial non-recognition of this chlorine activation, the importance of the ClO self-reaction was largely unappreciated in stratospheric modelling until 1987 when Molina and Molina proposed another channel to the destruction of ozone following photolysis of the ClO dimer:[23]

$$Cl_2O_2 + h\nu \rightarrow ClOO + Cl \qquad (1.18)$$

$$ClOO + M \rightarrow Cl + O_2 \qquad (1.19)$$

This ozone loss cycle is now known to be principally responsible for the Springtime polar stratospheric ozone 'holes' observed each year and the rate of reaction (1.17), along with the photolysis of the Cl_2O_2 molecule (reaction (−1.17)), constitute the rate determining processes in this reaction sequence.[24] The rate of reaction (1.17) in particular is proportional of the square of the ClO concentration explaining the severity of polar ozone loss through this process.

1.2.4.2 Tropospheric Ozone: the Origin of Atmospheric Photo Oxidation

Ozone also plays a vital role in the photochemistry of the lower atmosphere. Rather than acting as a significant UV filter, tropospheric ozone acts principally an oxidant source that is essential in the removal of organic pollutants such as methane and the cocktail of volatile organic compounds (VOCs) emitted from the biosphere. Without the oxidising action of the atmosphere these trace gases would accrete thus severely affecting the balance of the global energy budget since most VOCs are significant infrared absorbers. The chemical nature of atmosphere would be also radically different without such oxidation, acutely affecting the biosphere and climate. In the troposphere the principal oxidising agent is the hydroxyl radical, OH, the so-called "detergent of the lower atmosphere". It has gained this reputation because it reacts with hundreds of pollutant gases both natural and anthropogenic, initiating their degradation and eventual removal from the atmosphere. The significance of atmospheric OH oxidation is illustrated when considering it removes a total amount of material estimated to be equal to the total mass of the atmosphere every 1.4 million years[3] (3.7 Gt yr^{-1} of material). Tropospheric O_3 is crucial to atmospheric oxidation and its photochemical loss leads to the formation of the OH radical.[25] O_3 is photolysed by the small amounts of UV radiation that penetrate the stratosphere into the troposphere, liberating O_2 and importantly the reactive (electronically excited) $O(^1D)$ atom. The transient excited $O(^1D)$ atom then reacts with water vapour forming two OH radicals for every molecule of water consumed:

$$O_3 + h\upsilon\ (\lambda < 320\ \text{nm}) \rightarrow O(^1D) + O_2 \tag{1.20}$$

$$O(^1D) + H_2O \rightarrow OH + OH \tag{1.21}$$

These gaseous OH radicals rapidly achieve a steady state with hydroperoxy radicals, HO_2, primarily through reaction of OH with carbon monoxide, CO, and then the subsequent reaction of H atoms with abundant molecular oxygen:

$$OH + CO \rightarrow H + CO_2 \qquad (1.22)$$

$$H + O_2 + M \rightarrow HO_2 + M \qquad (1.23)$$

where M is a buffer species that stabilises the initially formed HO_2 *via* molecular collision. By contrast, OH is reformed from HO_2 *via* a fast reaction with tropospheric ozone:

$$HO_2 + O_3 \rightarrow OH + 2O_2 \qquad (1.24)$$

This rapid interconversion of OH and HO_2 is known as odd hydrogen, HO_x, cycling ($[HO_x] = [OH] + [HO_2]$) and the total concentration of HO_x determines the oxidising capacity of the troposphere: its ability to remove pollutants.[25,26] In addition to CO, OH oxidises NO_2 and SO_2 to give nitric acid (HNO_3) and sulphuric acid (H_2SO_4) respectively. These can go on to form aerosols which may ultimately be lost to the Earth's surface *via* deposition. The OH radical is chiefly responsible for the oxidation and removal of VOCs, thus playing a major role in the carbon cycle and the budget of radiatively active 'greenhouse' gases. OH initiated removal of most organic compounds may proceed by hydrogen abstraction or addition to a double bond, forming an organic radical species. The resultant radical species typically reacts with molecular oxygen (due to its abundance) giving the organoperoxy radical, RO_2. RO_2 species can react further, ultimately producing water and CO_2:

$$OH + RH \rightarrow R + H_2O \qquad (1.25)$$

$$R + O_2 + M \rightarrow RO_2 + M \qquad (1.26)$$

In urban areas where the air is typically polluted *i.e.* regions with significant levels of NO_x, additional reactions occur. Here RO_2 (where R = an organic group) reacts with NO producing RO and NO_2. NO_2 is photolabile and decomposes under visible wavelengths of light below *ca* 400 nm, reforming NO, O atoms and subsequently O_3.[27] It is this process which *in extremis* results in summertime photochemical smog in heavily urbanised areas. Conversely, in unpolluted regions such as the marine boundary layer (MBL), where there are minimal concentrations of short-lived anthropogenic emissions (such as NO_x), the peroxy radicals may combine. The simplest case of this is the hydroperoxy self-reaction:

$$HO_2 + HO_2 \rightarrow H_2O_2 + O_2 \qquad (1.27)$$

The formation of hydrogen peroxide (H_2O_2) results in HO_x loss due to its water solubility despite its potential photo-degradation. The outcome is the "wet deposition" of H_2O_2 which permanently removes HO_x from the system. Thus, reaction (1.27) is a limiting factor of tropospheric HO_x concentrations, and therefore the oxidising capacity of the troposphere. This makes peroxy radical chemistry of atmospheric interest and more detail concerning this chemistry is given later in this thesis.

1.2.5 The Global Energy Budget and Radiative Forcing

It has been discussed that the presence of different oxygen allotropes in the atmosphere is inexorably linked to the chemical nature of Earth's oxidative atmosphere. However, this composition also affects the dynamics of the atmosphere, in particular Earth's radiative balance which concerns the global energy budget of the Earth in terms of energy entering and leaving the Earth system. The Earth receives a fraction of the Sun's radiation, and to a first approximation behaves like a black body by completely absorbing and emitting all incident radiation. For a black body at a given temperature, the intensity of subsequently emitted radiation as a function of wavelength is described by the Planck function, whose maximum shifts to increasingly visible (*i.e.* shorter) wavelengths at higher temperatures. The Stefan-Boltzmann law gives the flux density, F, *i.e.* the total amount of emitted radiation per unit time (W) (the integral of the Planck function over all wavelengths) from a black body at a given temperature:

$$F = \sigma T^4 \qquad (1.2\ \text{iii})$$

where σ is the Stefan-Boltzmann constant which is equal to 5.67×10^{-8} W m^{-2} K^{-4}. Evidently, the Earth only intercepts a fraction of the Sun's output radiation as the energy received is proportional to the inverse square of the mean solar distance which results in a solar constant of 1370 ± 2 W m^{-2} reaching the top of the Earth's atmosphere. This energy is absorbed by the Earth's surface (over a cross sectional area of the solar beam equal to πR_E^2, where R_E = Earth's radius), causing a heating. The Earth then re-emits radiation at different (longer) wavelengths (over an area, the surface area of a sphere, of $4\pi R_E^2$). Therefore the balancing of incoming and outgoing terrestrial fluxes allows calculation of an equilibrium temperature of the Earth. The difference in emission wavelengths of the Sun and Earth is explained by Wien's law which gives the maximum wavelength of light (λ_m) in terms of intensity (in micrometers) emitted at a given temperature:[3]

$$\lambda_m / \mu\text{m} = \frac{2897}{T} \qquad (1.2\ \text{iv})$$

Hence the large temperature difference between the Sun and Earth explains why solar radiation is mainly of the UV, visible and near infrared (near-IR) region of the electromagnetic spectrum whilst terrestrial radiation is principally of the infrared (IR) region. However, not all radiation – solar or terrestrial, is absorbed at the Earth's surface or re-emitted back into space. As was discussed earlier for ozone, not all gases in the atmosphere are transparent to solar radiation and the same is true for outgoing terrestrial radiation. Depending on the location of ozone within the atmosphere (stratospheric or tropospheric), it may act as either a strong effective absorber of UV or IR radiation. Stratospheric ozone principally acts as a UV filter yet the ozone found in the lower troposphere acts a potent greenhouse gas, strongly absorbing IR radiation emitted from the Earth as a result of its proximity to the surface. Figure 1.5 shows the opacity of Earth's atmosphere *i.e.* how much light of a certain wavelength can pass through it, as a function of wavelength. It is clear that the atmosphere is opaque to a significant amount of IR light and this is due to the tropospheric trace species that absorb in the IR such as ozone which are known collectively as greenhouse gases.

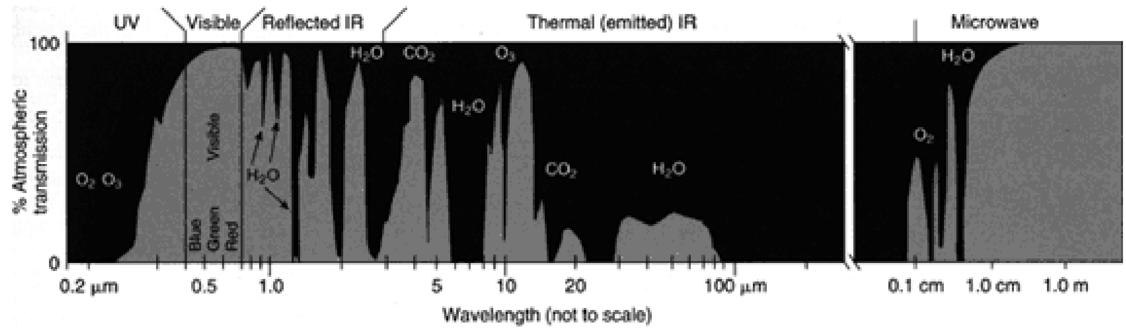

Figure 1.5 *The transparency of Earth's Atmosphere with respect to the electromagnetic spectrum.*[28]

Although it is not a relatively strong IR absorber compared to O_3 and many other trace species, CO_2 is the most significant greenhouse gas due to its atmospheric abundance (currently 0.04 %) over them. The presence of CO_2 in Earth's atmosphere and the subsequent trapping of IR radiation results in a net heating of the lower atmosphere compared to a notional atmosphere that is IR transparent. This is a natural process known as the *global warming effect* and is vital in keeping the biosphere at ambient temperatures *i.e.* above the freezing point of water which is essential for the vast majority of life on Earth. The stability of CO_2 levels and other greenhouse gases such as methane are vital in maintaining the Earth's global energy budget which is key in determining climate as this regulates the amount of energy stored within the Earth system.[29] Changes in climate over the last few decades have been attributed to changes in the global energy budget brought about by changes in the radiative properties of the atmosphere.[2] Perturbations in greenhouse gas concentrations since the start of the industrial revolution and the subsequent change in the behaviour of humans, particularly those in the developed nations, has increasingly been shown to have resulted in anthropogenic climate forcing. Rising levels of greenhouse gases, in particular CO_2 which is by far the most abundant due to its stability, have decreased the transmission of the atmosphere with respect to terrestrial IR radiation causing a positive *radiative forcing*, described below.

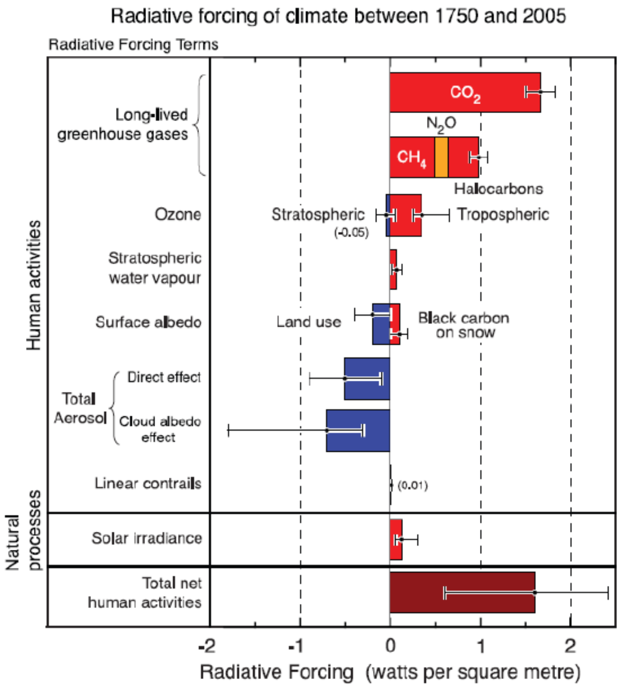

Figure 1.6 *The principal radiative forcings of significance, both anthropogenic and natural. The values represent the forcings in 2005 relative to the start of the industrial era (ca. 1750). The thin black lines represent the ranges in uncertainty.*[2]

A radiative forcing (RF) is an effective change imposed on the planetary solar radiation budget. It is a measure of how the energy balance of the Earth-atmosphere system is influenced when factors that affect climate are altered. The *International Panel on Climate Change* (IPCC) defines it as the "change in net (down minus up) irradiance (solar plus longwave; in W m^{-2}) at the tropopause after allowing for stratospheric temperatures to readjust to radiative equilibrium, but with surface and tropospheric temperatures and states held fixed at unperturbed values." A RF can either be positive or negative *i.e.* the perturbation can have a net heating or cooling effect respectively and Figure 1.6 shows the 4th IPCC report's summary of some of the principal contributions of the RF of climate change.[2] The RFs displayed contribute to the total net RF and originate from both natural sources and anthropogenic activities. As is illustrated below, the most significant positive RF agent is CO_2, which has increased as a result of anthropogenic fossil fuel use in energy generation, transport, agriculture and construction. Other human activities such as cement manufacture and deforestation, among others, have also contributed to further effective CO_2 emissions. Methane, the second most important forcing agent in terms of abundance has also increased due to agriculture, natural gas distribution and landfills from decomposing biomass among other sources.

Current RFs depend on the contemporary concentrations of a forcing agent and in turn depend on historical emissions of that agent and its lifetime. This totalling of the RF for each forcing agent relative to its abundance mainly quantifies the direct radiative effects of an emitted species. Some indirect chemical responses such as the effects of NO_x emissions are included in the IPCC 4th report[2] yet gas-aerosol interactions are currently not. These interactions depend on the availability of oxidants (primarily the OH radical), influencing the rates of formation of aerosol particles from precursor gases (*e.g.* SO_2). As is discussed below the atmospheric oxidative capacity is largely governed by the abundance of methane and ozone precursors (*e.g.* NO_x) linking methane, ozone and aerosols through oxidative chemistry. Therefore altering the emission of a single species could in turn affect the composition of the others. A recent study has calculated atmospheric composition changes, historical radiative forcing, and forcing per unit of emission due to aerosol and tropospheric ozone precursor emissions in a coupled composition-climate model.[30] This study compared the instantaneous RFs of a number of forcing agents (both positive and negative) in terms of abundance-based and emissions-based values. They found that gas-aerosol interactions substantially alter the relative importance of various emissions. In particular, the impact of methane emissions has a larger impact on climate forcing than what is considered in the Kyoto Protocol, thus potentially making the radiative effects of methane even more significant than previously thought.

1.3 Key Atmospheric Radical Reaction Cycles and their Coupling

1.3.1 Peroxy Radical Chemistry

Organoperoxy radicals are important intermediates in the atmospheric oxidation and removal of volatile organic compounds (VOCs). The photochemical removal of VOCs initiated by reaction with the OH radical is far from simple and its mechanism includes a number of possible pathways that take place mainly within the troposphere. The simplest organoperoxy radical is the methyl peroxy radical, CH_3O_2 and is formed by the atmospheric oxidation of methane in an equivalent fashion to reactions (1.25) and (1.26) *i.e. via* H abstraction from methane by OH and subsequent reaction of the newly formed methyl radical with abundant molecular oxygen:

$$OH + CH_4 \rightarrow CH_3 + H_2O \qquad (1.28)$$

$$CH_3 + O_2 + M \rightarrow CH_3O_2 + M \qquad (1.29)$$

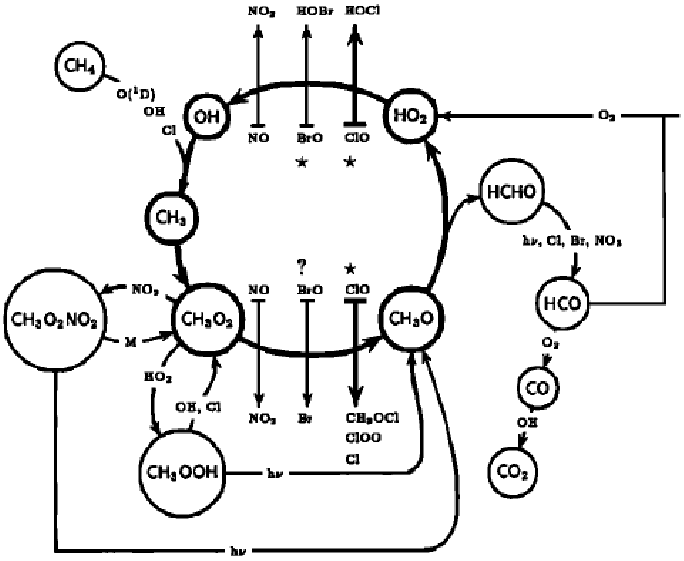

***Figure 1.7** A schematic representation of methane oxidation to its eventual transformation to CO_2.*[31]

This process is well understood and defined.[32] The ensuing chemistry of the methylperoxy radical is complex as summarised in Figure 1.7. Figure 1.7 is a schematic of OH initiated methane oxidation which also encompasses the subsequent chemistry of CH_3O_2.[31] As can be seen, CH_3O_2 is implicated in the HO_x cycle of the unpolluted MBL and it also influences tropospheric ozone production in polluted (high $[NO_x]$) regions. In polluted regions NO_2 photolysis generates ground state $O(^3P)$ oxygen atoms which combine with molecular oxygen forming ozone. Conversely NO_2 is regenerated by the destruction of O_3 by NO.

$$NO_2 + h\nu \rightarrow NO + O(^3P) \quad (1.30)$$

$$O(^3P) + O_2 + M \rightarrow O_3 + M \quad (1.31)$$

$$O_3 + NO \rightarrow NO_2 + O_2 \quad (1.32)$$

This NO_x cycling can be interfered with by peroxy radicals, in particular hydroperoxy and methylperoxy radicals, due to their relative abundance in the troposphere.[27] These radicals react with NO forming NO_2:

$$HO_2 + NO \rightarrow OH + NO_2 \quad (1.33)$$

$$CH_3O_2 + NO \rightarrow CH_3O + NO_2 \quad (1.34)$$

OH can generate another methylperoxy radical and CH_3O reacts rapidly with oxygen to generate another hydroperoxy radical:

$$CH_3O + O_2 \rightarrow HCHO + HO_2 \quad (1.35)$$

Thus the overall effect is the net gain in O_3 as the consumption of O_3 by NO is replaced by reaction with peroxy radicals:

$$\textit{net:}\ CH_4 + 2O_2 \rightarrow H_2O + HCHO + 2O_3 \quad (1.36)$$

Conversely the peroxy radicals can react with each other, resulting in radical termination to stable molecules that might be removed in precipitation thus limiting the formation of ozone:

$$HO_2 + HO_2 \rightarrow H_2O_2 + O_2 \quad (1.37)$$

$$CH_3O_2 + CH_3O_2 \rightarrow \text{Products} \quad (1.38)$$

$$CH_3O_2 + HO_2 \rightarrow \text{Products} \quad (1.39)$$

The formation of tropospheric ozone to a certain degree is a double-edged sword; as discussed above, O_3 is a potent greenhouse gas in addition to its toxicity (O_3 is a strong oxidiser) but it is also vital for the formation of the hydroxyl radical, the principal oxidant of VOCs. Therefore, in polluted regions, the chemistry of the local atmosphere has a greater oxidising capacity than those with "clean" air such as in the ambient marine boundary layer (MBL). Significantly lower levels of NO_x result in radical-radical termination steps being the main sink of peroxy radicals in addition to further OH oxidation of organoperoxy radicals. Therefore, the increases in anthropogenic CH_4 and CO emissions are of concern not just due to their radiative forcing potential but also due to the effect that they have on the stability of tropospheric hydroxyl chemistry. Modelling studies have estimated that the atmospheric OH radical concentration has remained globally stable since the start of the industrial revolution, however this is not the case regionally.[33] The marine troposphere, for example, has shown substantial decreases in OH concentration over the last century whereas OH has increased over polluted continental regions associated with high NO_x levels. Although the NO_x species only have a lifetime of around a few days, the lifetime of the ozone formed as a result of their photochemistry is long enough for it to be transported many thousands of miles away to areas such as the MBL. OH is then generated by reaction of O_3 with HO_2 (generated from reactions (1.41) & (1.40)) to form OH and O_2 (reaction (1.42)) thus compensating low NO_x emission regions with exported OH:

$$OH + CO \rightarrow H + CO_2 \qquad (1.40)$$

$$H + O_2 + M \rightarrow HO_2 + M \qquad (1.41)$$

$$HO_2 + O_3 \rightarrow OH + 2O_2 \qquad (1.42)$$

It appears that the accidental simultaneous emissions of CO and CH_4 (OH depleting) along with NO_x (OH forming) associated with burning fossil fuels have kept the global OH concentrations fairly constant. However, this does not imply long term stability as this trend may change in the future with regions such as South East Asia undergoing abrupt emission changes brought about by rapid land use change (typically rainforest to agriculture) and industrialisation.[34] The degradation of methane and the subsequent chemistry of the methylperoxy radical are therefore important as peroxy-peroxy reactions are ubiquitous in the troposphere and ultimately limit OH concentrations. Therefore, peroxy radicals play a significant role in determining the oxidising capacity of the lower atmosphere, which also affects greenhouse gas concentrations.

In turn, atmospheric models attempting to replicate important trace species concentrations in composition and climate models need accurate kinetic data on key reactive pathways in which peroxy radicals often play a key role. Consequently, accurate experimental work on key peroxy-peroxy reactions is needed to determine vital parameters, notably rate constants and their temperature dependence coupled with an understanding of the mechanistic elements of peroxy radical chemistry.

1.3.2 Halogen Monoxide Radical Chemistry

The halogens are the elements of Group 7 in the periodic table and their chemistry is closely related due to the common electronic configuration of their outer shell. All halogens are reactive in their elemental, diatomic, form due to their highly electronegative nature, making them strong oxidisers. Different forms of halogen species exist in the atmosphere with their speciation being closely linked to their source. The role of chlorine chemistry in the catalytic loss of stratospheric ozone has already been discussed with the source of this chemistry being solely anthropogenic, owing to the chemical and photolytic stability and therefore lifetime of CFCs. Halogen chemistry is also of importance in the troposphere where such compounds play significant roles in processes which again includes the destruction of ozone, changes in the OH/HO_2 and NO/NO_2 ratios, the oxidation of CCN precursors such as dimethyl sulphide as well as the budget of elemental mercury.[35] The majority of these short lived halogen precursors (as distinct from the CFCs) emitted into the troposphere are from natural sources and predominantly from oceanic/coastal regions with the ocean being the largest reservoir of halogens.

The marine boundary layer (MBL) is the atmospheric layer in direct contact with the ocean. In general the strongest source of bromine and chlorine in the MBL is *via* the production of sea-salt aerosol. Heterogeneous chemical processes act upon these aerosol droplets or particles changing their chemical composition and physical nature. In particular, observations of sea-salt aerosols have typically shown a deficit in halide ions Cl^- and Br^- relative to the bulk sea water ratio X^-/Na^+, $X = Cl^-, Br^-$, with depletions particularly noticeable for bromine.[36] A number of heterogeneous processes ranging from acid displacement by HNO_3 to oxidation by OH and O_3 are attributed to releasing halogen species into the marine boundary layer. The atmospheric ageing of such halogen containing salts is believed to account for the elevated levels of active (photolabile) halogen species observed in the ambient marine atmosphere which gas phase chemistry cannot explain alone. Recent atmospheric measurements[37] have shown for example that nitryl chloride ($ClNO_2$) is produced by heterogeneous reactions on sea-salt particles and accumulates during the night. At dawn, the photolysis of nitryl chloride produces a peak concentration of chlorine up to 10^6 atoms cm^{-3}. This source of chlorine seems modest however Cl reacts with VOCs in a similar fashion to OH (*i.e.* through hydrogen abstraction of the organic, forming an alkyl radical), although more efficiently:[38]

$$Cl + RH \rightarrow HCl + R \tag{1.43}$$

The reactivity of Cl towards VOCs and ozone means that Cl may actually represent the dominant dawn time oxidant of the MBL, when concentrations of photolytically produced OH are low.

Along coastal regions with high biological activity, large fluxes of iodine gases to the atmosphere also occur at low tide. It has been shown that the origin of these iodine fluxes arises from bursts of significant quantities of ultrafine particles (~ 3 – 10 nm in diameter), and are the result of the polymerization of iodine oxides.[39] The iodine oxides are then formed from photolysis of precursor gases such as I_2 and iodocarbons which are the products of the original biogenic processes which represent the major source of iodine in the atmosphere.

Ice and snow have also been shown to activate halogens in the Polar boundary layer, providing a significant source of reactive bromine and iodine in particular. The mechanisms behind these emissions are still open to debate as observations linking sea ice/snowpack to active halogen species have been sparse and relatively recent.[40] Initial observations have shown that first year ice coverage may be an important factor in bromine activation. Subsequent work has suggested that the blowing of saline snow over sea ice was subsequently responsible for the heterogeneous activation of bromine on aerosol surfaces. Similarly, iodine observations above the Antarctic marine environment have been made with a proposed mechanism suggesting that the production of inorganic iodine by marine algae within and beneath the sea ice is responsible. Diffusion of iodine through the sea ice and snowpack would therefore trigger this release into the atmosphere.

The reactivity of halogens decreases with increasing mass. Consequently, atomic fluorine is so reactive as to be hard to release from fluorinated precursors and the HF it would form in the troposphere is so secure that it does not partake in any significant atmospheric chemistry.[40] Therefore, when discussing atmospheric halogen chemistry, the focus is on the chemistry of chlorine, bromine and iodine species. As discussed above, atomic chlorine is very reactive towards VOCs. However, bromine atoms also react with selected halocarbons such as aldehydes and dimethyl sulphide, in particular, which is most prevalent in the marine boundary layer, whereas iodine atoms are the least reactive.[40] All atomic halogens do however react with ozone, destroying it in efficient catalytic cycles analogous to reactions (1.8) and (1.9), with a net loss of one ozone molecule per halogen atom per cycle. The halogen monoxide radicals formed upon the initial reaction of a halogen atom and ozone may undergo other chemistry than with atomic oxygen. In regions of relatively elevated halogen concentrations and/or low concentrations of oxygen atoms, halogen oxides undergo reactions with each other *via* self- or cross-halogen monoxide reactions as summarized in Figure 1.8 below.[40,41] These reactions are important as they potentially form species that go on to regenerate halogen atoms thus propagating the potential of further ozone destruction and, under illuminated conditions, are often the rate determining step in the cycle efficiency.

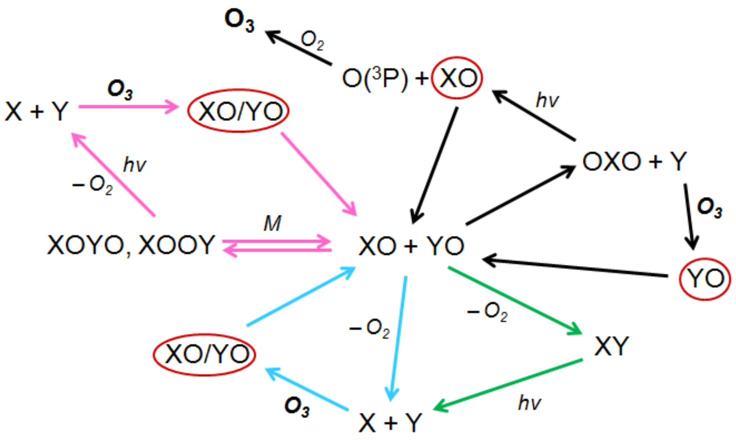

Figure 1.8 *A schematic representation of halogen monoxide cycling involving ozone. The pink cycle is when X = Y = Cl, Br or I.*

As well as the rate of reaction, the product distribution of each XO + YO reaction is also important in determining the ozone destruction cycle efficiency as the competition between direct (shown in the blue and black cycles, above) and indirect photolytic halogen atom regeneration (shown in the green and pink cycles) becomes important. For the ClO self-reaction, the bimolecular channels (*i.e.* non-pink) are relatively slow compared to dimer formation, and the Cl_2O_2 species under tropospheric conditions thermally dissociates back to ClO.[42,43] However, under stratospheric/upper tropospheric conditions, Cl_2O_2 photodissociates readily upon the absorption of UV light.

By contrast, the BrO self-reaction mainly (at ambient *T*) forms two Br atoms per reaction with a minor channel (~ 15 %) forming Br_2. Further, the very fast IO self-reaction forms a mixture dominated by the photolabile dimer (~ 50 %) and dioxide, OIO (~ 40 %), species. Formation of the OXO isomer of a halogen dioxide is dominant in every cross-reaction between halogen monoxide radicals, especially when IO is involved (shown in the black cycle). The next major contributing channel of these bimolecular reactions is the atomic halogen regenerative branch (indicated as the blue cycle) with the formation of the diatomic (shown as the green cycle) halogen species always the minor, although the degree of which varies with each reaction.

The formation of the different photolabile species formed is of consequence as the subsequent photochemistry affects the net capacity of halogens to catalyse ozone destruction. Assuming the formation of XO or YO is the result of the loss of one ozone molecule per X or Y, the formation of the diatomic or dimer species therefore results in the enhanced loss of another two O_3 upon subsequent photodissociation. Conversely, the formation of a ground state O atom upon the photolysis of the halogen dioxide species can result in the formation of an ozone molecule as O combines with O_2, thus partially mitigating the potential ozone loss of each complete cycle. The formation of OIO for example dominates when X or Y = I as it follows a different product channel upon the absorption of a photon, apparently forming molecular oxygen and atomic iodine thus making IO chemistry particularly destructive towards ozone.[39] However, the extent in which a particular XO + YO reaction occurs is also greatly dependent on the relative concentrations of each species which is also a function of their stability and is therefore highly variant both regionally and temporally.

1.3.3 Coupling of Halogen Monoxide and Peroxy Radical Chemistry

While radical reactions can be conveniently categorised into distinct families such as the halogen, HO_x and nitrogen oxide reaction cycles where the chemistry of any one family may dominate particular regions, these cycles can also interact and couple to one another under certain conditions. The implications of this coupling can often change the net outcome of any given radical cycle *e.g.* the modification of the HO_x cycle by nitrogen oxides in polluted regions makes the overall outcome ozone forming as opposed to ozone destroying as in the unpolluted atmosphere. Nitrogen oxides also react with halogen oxides, in particular the reaction of OXO with NO, the rate coefficient of which increases with halogen mass (i.e. I > Br > ClO):[40]

$$OXO + NO \rightarrow XO + NO_2 \qquad (1.44)$$

This limits the potential for O_3 destruction from halogens *via* subsequent O atom regeneration by photolysis of the dioxide. The reaction of the halogen monoxide with nitrogen dioxide may also result in a null cycle for ozone upon photolysis of the products:

$$XO + NO_2 \rightarrow XONO_2 \tag{1.45}$$

$$XONO_2 + h\nu \rightarrow X + NO_3 \tag{1.46}$$

where the subsequent photolysis of NO_3 leads to ozone formation compensating the formation of the halogen atom which results in ozone loss thus forming a null cycle.

In both the troposphere and stratosphere, periods and conditions in which there is a reduction in halogen species concentrations, wherein the coupling of HO_x and halogen monoxide chemistry becomes important,[44] affecting the oxidative capacity of the remote MBL and resulting in substantial ozone destruction:

$$XO + HO_2 \rightarrow HOX + O_2 \tag{1.47}$$

$$HOX + h\nu \rightarrow X + OH \tag{1.48}$$

Analogously, CH_3O_2, arising from methane emissions and subsequent CH_4 oxidation also plays a role in the stratospheric ozone budget through its reaction with ClO, thus competing with the ClO self-reaction:

$$ClO + CH_3O_2 \rightarrow Products \tag{1.49}$$

The potential of this reaction has been appreciated by Crutzen *et al.*[45] who demonstrated that one of the products of this reaction, CH_3OCl, may provide an additional reservoir species for Cl. Once CH_3OCl formed it may be photolysed or react in an analogous fashion to the heterogeneous reaction (1.14):[45,46]

$$HOCl + HCl \rightarrow Cl_2 + H_2O \tag{1.50}$$

The chlorine is therefore reactivated in this process (Cl_2 is photolabile) allowing it to participate in ozone depletion processes.

1.4 Concluding Remarks

The individual components of Earth behave as a single system in which energy and matter are transported throughout at significantly variant rates. Changes to the composition of Earth's atmosphere *via* emissions from the oceanic, lithospheric, biospheric and most recently anthropogenic sources have modified its structure and composition over the eons resulting in the characteristics of the modern atmosphere. The atmosphere and oceans are evidently key to Earth's energy budget in which an equilibrium between incoming UV/visible solar radiation and outgoing infrared terrestrial radiation determines global temperatures. Changes in composition of the contemporary atmosphere have been affected by anthropogenic activities, principally by the industrialisation of nations which in turn has modified the energy budget of the Earth. Ozone depletion in the stratosphere has resulted in some regions being exposed to biologically damaging UV radiation and accelerating emissions of CO_2 are warming the lower atmosphere with potentially severe consequences for the climate and the environment. Understanding of atmospheric chemistry, therefore, has and continues to be vital in elucidating the pathways that lead to such changes in atmospheric composition. The principal drivers of composition change are the short-lived reactive trace species and their chemistry must therefore be well characterised in order to help predict future changes to the Earth system as a whole, achieved through model studies.

Two classes of trace species: the odd hydrogen and related peroxy radicals; and the halogen monoxides species have been identified as being important in determining the oxidative capacity of the troposphere and the ozone budget of the stratosphere. Their individual and coupled reaction cycles are complex but the characterisation of the nature and rates of their elementary steps is needed. This work aims to address some of the issues concerning the reactions of halogen oxides with small peroxy radicals by isolating a selection of these reactions and studying their kinetic behaviour, as discussed in subsequent chapters.

1.5 References

1. Lovelock, J., *Gaia: A New Look at Life on Earth*. 2000, Oxford: Oxford University Press.
2. Forster, P., V. Ramaswamy, P. Artaxo, T. Berntsen, R. Betts, D.W. Fahey, J. Haywood, J. Lean, D.C. Lowe, G. Myhre, J. Nganga, R. Prinn, and M.S.a.R.V.D. G. Raga, in *In: Climate Change 2007:The Physical Science Basis. Contribution of Working Group I to the Fourth Assessment Report of the Intergovernmental Panel on ClimateChange*.
3. J. Wallace, P.H., *Atmospheric Science: An Introductory Survey*. Second Edition. 2006: Elsevier.
4. F. Lutgens, E.T., *The Atmosphere*. Seventh Edition 1998: Prentice Hall.
5. Isaksen, I.S.A., C. Granier, G. Myhre, T.K. Berntsen, S.B. Dalsøren, M. Gauss, Z. Klimont, R. Benestad, P. Bousquet, W. Collins, T. Cox, V. Eyring, D. Fowler, S. Fuzzi, P. Jöckel, P. Laj, U. Lohmann, M. Maione, P. Monks, A.S.H. Prevot, F. Raes, A. Richter, B. Rognerud, M. Schulz, D. Shindell, D.S. Stevenson, T. Storelvmo, W.C. Wang, M. van Weele, M. Wild, and D. Wuebbles, Atmospheric Composition Change: Climate–Chemistry interactions. *Atmospheric Environment*, 2009. **43**(33): 5138-5192.
6. Romankevich, E.A. and A.A. Vetrov, Masses of Carbon in the Earth's Hydrosphere. *Geochemistry International*, 2013. **51**(6): 431-455.
7. Anav, A., P. Friedlingstein, M. Kidston, L. Bopp, P. Ciais, P. Cox, C. Jones, M. Jung, R. Myneni, and Z. Zhu, Evaluating the Land and Ocean Components of the Global Carbon Cycle in the CMIP5 Earth System Models. *Journal of Climate*, 2013. **26**(18): 6801-6843.
8. Le Quere, C., M.R. Raupach, J.G. Canadell, G. Marland, L. Bopp, P. Ciais, T.J. Conway, S.C. Doney, R.A. Feely, P. Foster, P. Friedlingstein, K. Gurney, R.A. Houghton, J.I. House, C. Huntingford, P.E. Levy, M.R. Lomas, J. Majkut, N. Metzl, J.P. Ometto, G.P. Peters, I.C. Prentice, J.T. Randerson, S.W. Running, J.L. Sarmiento, U. Schuster, S. Sitch, T. Takahashi, N. Viovy, G.R. van der Werf, and F.I. Woodward, Trends in the Sources and Sinks of Carbon Dioxide. *Nature Geoscience*, 2009. **2**(12): 831-836.

9. Smith, M.D., An Ecological Perspective on Extreme Climatic Events: A Synthetic Definition and Framework to Guide Future Research. *Journal of Ecology*, 2011. **99**(3): 656-663.
10. Reichstein, M., M. Bahn, P. Ciais, D. Frank, M.D. Mahecha, S.I. Seneviratne, J. Zscheischler, C. Beer, N. Buchmann, D.C. Frank, D. Papale, A. Rammig, P. Smith, K. Thonicke, M. van der Velde, S. Vicca, A. Walz, and M. Wattenbach, Climate Extremes and the Carbon Cycle. *Nature*, 2013. **500**(7462): 287-295.
11. Wood, A.J., G.J. Ackland, J.G. Dyke, H.T.P. Williams, and T.M. Lenton, Daisyworld: A review. *Reviews of Geophysics*, 2008. **46**(1).
12. Villanueva, G.L., M.J. Mumma, R.E. Novak, Y.L. Radeva, H.U. Kaufl, A. Smette, A. Tokunaga, A. Khayat, T. Encrenaz, and P. Hartogh, A Sensitive Search for Organics (CH_4, CH_3OH, H_2CO, C_2H_6, C_2H_2, C_2H_4), Hydroperoxyl (HO_2), Nitrogen Compounds (N_2O, NH_3, HCN) and Chlorine Species (HCl, CH_3Cl) on Mars Using Ground-Based High-Resolution Infrared Spectroscopy. *Icarus*, 2013. **223**(1): 11-27.
13. Atreya, S.K., P.R. Mahaffy, and A.-S. Wong, Methane and Related Trace Species on Mars: Origin, Loss, Implications for Life, and Habitability. *Planetary and Space Science*, 2007. **55**(3): 358-369.
14. A.M. Holloway, R.P.W., *Atmospheric Chemistry*2010: RSC Publishing.
15. DeMore, W.B., S.P. Sander, D.M. Golden, R.F. Hampson, M.J. Kurylo, and A.R.R. C J Howard, C.E. Kolb, and M.J. Molina, *Chemical Kinetics and Photochemical Data for Use in Stratospheric Modeling*. JPL Publication 97-4 ed1997, Pasadena, CA: Jet Propulsion Lab.
16. R. Barry, R.C., *Atmosphere, Weather and Climate* Ninth ed2009: Routledge.
17. Farman, J.C., B.G. Gardiner, and J.D. Shanklin, Large Losses of Total Ozone in Antarctica Reveal Seasonal ClO_x/NO_x Interaction. *Nature*, 1985. **315**(6016): 207-210.
18. Molina, M.J. and F.S. Rowland, Stratospheric Sink for Chlorofluoromethanes – Chlorine Atomic-Catalysed Destruction of Ozone. *Nature*, 1974. **249**(5460): 810-812.
19. Calm, J.M., The Next Generation of Refrigerants – Historical Review, Considerations, and Outlook. *International Journal of Refrigeration-Revue Internationale Du Froid*, 2008. **31**(7): 1123-1133.

20. Montzka, S.A., J.H. Butler, J.W. Elkins, T.M. Thompson, A.D. Clarke, and L.T. Lock, Present and Future Trends in the Atmospheric Burden of Ozone-Depleting Halogens. *Nature*, 1999. **398**(6729): 690-694.
21. Solomon, S., R.R. Garcia, F.S. Rowland, and D.J. Wuebbles, On the Depletion of Antarctic Ozone. *Nature*, 1986. **321**(6072): 755-758.
22. Solomon, S., Stratospheric Ozone Depletion: A Review of Concepts and History. *Reviews of Geophysics*, 1999. **37**(3): 275-316.
23. Molina, L.T. and M.J. Molina, Production of Cl_2O_2 from the Self-Reaction of the ClO Radical. *Journal of physical chemistry*, 1987. **91**(2): 433-436.
24. Boakes, G., W.H.H. Mok, and D.M. Rowley, Kinetic Studies of the ClO + ClO Association Reaction as a Function of Temperature and Pressure. *Physical Chemistry Chemical Physics*, 2005. **7**(24): 4102-4113.
25. Thompson, A.M., The Oxidizing Capacity of the Earth's Atmosphere: Probable Past and Future Changes. *Science*, 1992. **256**(5060): 1157-1165.
26. Hanisco, T.F., E.J. Lanzendorf, P.O. Wennberg, K.K. Perkins, R.M. Stimpfle, P.B. Voss, J.G. Anderson, R.C. Cohen, D.W. Fahey, R.S. Gao, E.J. Hintsa, R.J. Salawitch, J.J. Margitan, C.T. McElroy, and C. Midwinter, Sources, Sinks, and the Distribution of OH in the Lower Stratosphere. *Journal of Physical Chemistry A*, 2001. **105**(9): 1543-1553.
27. Crutzen, P., A Discussion of the Chemistry of Some Minor Constituents in the Stratosphere and Troposphere. *Pure and Applied Geophysics*, 1973. **106**(1): 1385-1399.
28. *http://earthobservatory.nasa.gov/Features/RemoteSensing/remote_04.php*.
29. Trenberth, K.E., J.T. Fasullo, and J. Kiehl, EARTH'S GLOBAL ENERGY BUDGET. *Bulletin of the American Meteorological Society*, 2009. **90**(3): 311-+.
30. Shindell, D.T., G. Faluvegi, D.M. Koch, G.A. Schmidt, N. Unger, and S.E. Bauer, Improved Attribution of Climate Forcing to Emissions. *Science*, 2009. **326**(5953): 716-718.
31. Lary, D.J. and R. Toumi, Halogen-Catalyzed Methane Oxidation. *Journal of Geophysical Research-Atmospheres*, 1997. **102**(D19): 23421-23428.
32. Ravishankara, A.R., Kinetics of Radical Reactions In the Atmospheric Oxidation of CH_4. *Annual Review of Physical Chemistry*, 1988. **39**: 367-394.
33. Lelieveld, J., W. Peters, F.J. Dentener, and M.C. Krol, Stability of Tropospheric Hydroxyl Chemistry. *J. Geophys. Res.*, 2002. **107**(D23): 4715.

34. DalsØRen, S.B., I.S.A. Isaksen, L. Li, and A. Richter, Effect of Emission Changes in Southeast Asia on Global Hydroxyl and Methane Lifetime. *Tellus B*, 2009. **61**(4): 588-601.
35. Monks, P.S., C. Granier, S. Fuzzi, A. Stohl, M.L. Williams, H. Akimoto, M. Amann, A. Baklanov, U. Baltensperger, I. Bey, N. Blake, R.S. Blake, K. Carslaw, O.R. Cooper, F. Dentener, D. Fowler, E. Fragkou, G.J. Frost, S. Generoso, P. Ginoux, V. Grewe, A. Guenther, H.C. Hansson, S. Henne, J. Hjorth, A. Hofzumahaus, H. Huntrieser, I.S.A. Isaksen, M.E. Jenkin, J. Kaiser, M. Kanakidou, Z. Klimont, M. Kulmala, P. Laj, M.G. Lawrence, J.D. Lee, C. Liousse, M. Maione, G. McFiggans, A. Metzger, A. Mieville, N. Moussiopoulos, J.J. Orlando, C.D. O'Dowd, P.I. Palmer, D.D. Parrish, A. Petzold, U. Platt, U. Pöschl, A.S.H. Prévôt, C.E. Reeves, S. Reimann, Y. Rudich, K. Sellegri, R. Steinbrecher, D. Simpson, H. ten Brink, J. Theloke, G.R. van der Werf, R. Vautard, V. Vestreng, C. Vlachokostas, and R. von Glasow, Atmospheric Composition Change – Global and Regional Air Quality. *Atmospheric Environment*, 2009. **43**(33): 5268-5350.
36. Adams, J.W. and R.A. Cox, Halogen Chemistry of the Marine Boundary Layer. *Journal De Physique Iv*, 2002. **12**(PR10): 105-124.
37. Osthoff, H.D., J.M. Roberts, A.R. Ravishankara, E.J. Williams, B.M. Lerner, R. Sommariva, T.S. Bates, D. Coffman, P.K. Quinn, J.E. Dibb, H. Stark, J.B. Burkholder, R.K. Talukdar, J. Meagher, F.C. Fehsenfeld, and S.S. Brown, High Levels of Nitryl Chloride in the Polluted Subtropical Marine Boundary Layer. *Nature Geoscience*, 2008. **1**(5): 324-328.
38. Sander, S.P., J. Abbatt, J. R. Barker, J. B. Burkholder, R. R. Friedl, D. M. Golden, R. E. Huie, C. E. Kolb, M. J. Kurylo, G. and V.L.O. K. Moortgat, P. H. Wine, "Chemical Kinetics and Photochemical Data for Use in Atmospheric Studies, Evaluation No. 17," JPL Publication 10-6, Jet Propulsion Laboratory, Pasadena, 2011 http://jpldataeval.jpl.nasa.gov.
39. Saiz-Lopez, A., J.M.C. Plane, A.R. Baker, L.J. Carpenter, R. von Glasow, J.C. Gómez Martín, G. McFiggans, and R.W. Saunders, Atmospheric Chemistry of Iodine. *Chemical Reviews*, 2011. **112**(3): 1773-1804.
40. Saiz-Lopez, A. and R. von Glasow, Reactive Halogen Chemistry in the Troposphere. *Chemical Society Reviews*, 2012. **41**(19): 6448-6472.
41. Nikitin, I.V., Halogen Monoxides. *Uspekhi Khimii*, 2008. **77**(8): 787-797.

42. Ferracci, V. and D.M. Rowley, The temperature Dependence of the Bimolecular Channels of the ClO + ClO Reaction over the Range T = 298-323 K. *International Journal of Chemical Kinetics*, 2012. **44**(6): 386-397.
43. Ferracci, V. and D.M. Rowley, Kinetic and Thermochemical Studies of the ClO + ClO + M $\rightleftharpoons$ Cl_2O_2 + M Reaction. *Physical Chemistry Chemical Physics*, 2010. **12**(37): 11596-11608.
44. Bloss, W.J., M. Camredon, J.D. Lee, D.E. Heard, J.M.C. Plane, A. Saiz-Lopez, S.J.B. Bauguitte, R.A. Salmon, and A.E. Jones, Coupling of HOx, NOx and Halogen Chemistry in the Antarctic Boundary Layer. *Atmospheric Chemistry and Physics*, 2010. **10**(21): 10187-10209.
45. Crutzen, P.J., R. Muller, C. Bruhl, and T. Peter, On the Potential Importance of the Gas-Phase Reaction CH_3O_2 + ClO → ClOO + CH_3O and the Heterogenous Reaction HOCl + HCl → H_2O + Cl_2 in Ozone Hole Chemistry. *Geophysical Research Letters*, 1992. **19**(11): 1113-1116.
46. Krisch, M.J., L.R. McCunn, K. Takematsu, L.J. Butler, F.R. Blase, and J. Shu, Photodissociation of CH_3OCl to CH_3O + Cl at 248 nm. *Journal of Physical Chemistry A*, 2004. **108**(10): 1650-1656.

Chapter 2: Photochemistry and Gas Kinetics

As described in the previous chapter, the detailed composition of the atmosphere affecting our environment is controlled by the chemistry of trace species. These trace species are highly reactive towards each other both homogeneously and heterogeneously and these reactions are typically initiated by incoming solar radiation. Consequently, in order to characterise the chemistry and composition of Earth's atmosphere fully, an essential understanding of gas phase photochemistry and reaction kinetics is crucial. Therefore a summary of the fundamental principles of these disciplines is provided below.

2.1 Photochemical Processes

The interaction of light with matter is of fundamental interest in all physical and natural sciences. In particular, the interaction of incoming solar and outgoing terrestrial radiation with trace species in the atmosphere, discussed in Chapter 1, is of absolute importance in the control of Earth's temperature through the solar energy budget. Photochemical processes are also key to the understanding of the initiation of photochemical reactions in Earth's Atmosphere and in the laboratory and provide the basis of all spectroscopic techniques. Therefore, the principles that govern the interaction of photons with matter are discussed in this section.

2.1.1 Photoabsorption

Absorption of radiation by a molecule may occur if the incident energy of the photon is equal to the difference between two energy levels of the molecule. The extent of this absorption is determined by the absorption cross section, σ, of the molecule at a given wavelength (*i.e.* energy) of light, λ. This in turn is governed by the oscillator strength of the transition, embodied in the Einstein A coefficient. Considering the extent of absorption, for a sample of infinitesimal thickness, dl, containing absorbing molecules at a concentration of c, the infinitesimal attenuation of intensity, dI, that occurs when light passes through, is given by:

$$dI = -I\sigma.c.dl \tag{2.1 i}$$

Separating the variables and expressing the integral between the limits of l = 0 and l (hence I_0 and I_l respectively) gives:

$$\int_{I_0}^{I_t} \frac{dI}{I} = -\sigma.c \int_0^l dl \tag{2.1 ii}$$

Assuming that the concentration of the absorber is independent of the path length of light, the solution to this equation leads to:

$$\ln\left(\frac{I_0}{I_t}\right) = \sigma.c.l \tag{2.1 iii}$$

The extent of this change in light intensity of a given wavelength upon passing through a sample is known as the absorbance and is given by Beer's Law:

$$A_\lambda = \ln\left(\frac{I_{0,\lambda}}{I_{t,\lambda}}\right) \tag{2.1 iv}$$

Where $I_{0,\lambda}$ is the incident intensity and $I_{t,\lambda}$ the transmitted intensity at wavelength λ. Therefore from equation (2.1 iii) and (2.1 iv), Beer's Law can be re-written to give the Beer-Lambert Law:

$$A_\lambda = \sum_i \sigma_{i,\lambda}.[i].l \tag{2.1 v}$$

Which defines the total absorbance of a sample from all absorbing species labelled, i. Hence, provided the absorption cross sections, wavelength of light and the absorbing path length are known, the concentrations of multiple absorbing species within a sample can be measured. When applied experimentally as in this work (discussed in Chapter 3), equation (2.1 v) forms the basis of the spectroscopic measurements used to quantify the concentration of transient absorbers.

Once absorbed, the energy of a photon results in a transition within a molecule. The energy of the photon determines what transition can occur, typically going from the ground state to an upper state in the electronic, vibrational or rotational (or up to all three) levels. Given this energy level spacing, it follows that the energy required for a particular transition is of the order:

$$E_{\mathrm{electronic}} > E_{\mathrm{vibrational}} > E_{\mathrm{rotational}}$$

Corresponding to the relative energy regions of radiation:

UV/visible > infrared > microwave

which is inversely proportional to wavelength. Hence, the UV/visible absorption of a photon by a molecule as encountered with atmospheric solar radiation and in the laboratory, typically gives rise to an electronic excitation. When considering a simple diatomic species such as ClO, for example, there is a rapid shift in electron density within the molecule causing the initially stationary nuclei to suddenly experience a new force and vibrate. The equilibrium internuclear separation of the upper electronic state is therefore shifted from the ground state. The electronic transition thus occurs between two asymmetric states as a consequence of the vibrating nuclei, hence the term *vibronic transition*. According to the Franck-Condon principle shown schematically in Figure 2.1, the transition from a ground to upper electronic state is many times faster than molecular vibration and so the change in internuclear distance is essentially zero with respect to the transition in potential energy. The principle therefore dictates that the most intense vibronic transition originates from the ground vibrational state to the vibrational state of the upper electronic level of the same internuclear separation. Thus the stationary equilibrium separation of the nuclei in the initial electronic state may become a stationary turning point in the final electronic state. In classical terms, this corresponds to transitions between two states that are most similar geometrically. In the quantum mechanical sense, it is a transition to the upper vibrational electronic state whose wavefunction most closely resembles (overlaps) the wavefunction of the vibrational ground state of the lower electronic state. However, due to the appreciable overlap of the wavefunctions of other vibrational states, there are many accessible states from the ground state upon absorption. Consequently, a vibrational progression results, with the most favourable transitions represented by a peak in absorption as observed experimentally. If the separation in potential energy between the different upper vibrational states is significant enough as to be resolved experimentally, vibronic structure can then be observed in the absorption spectrum.

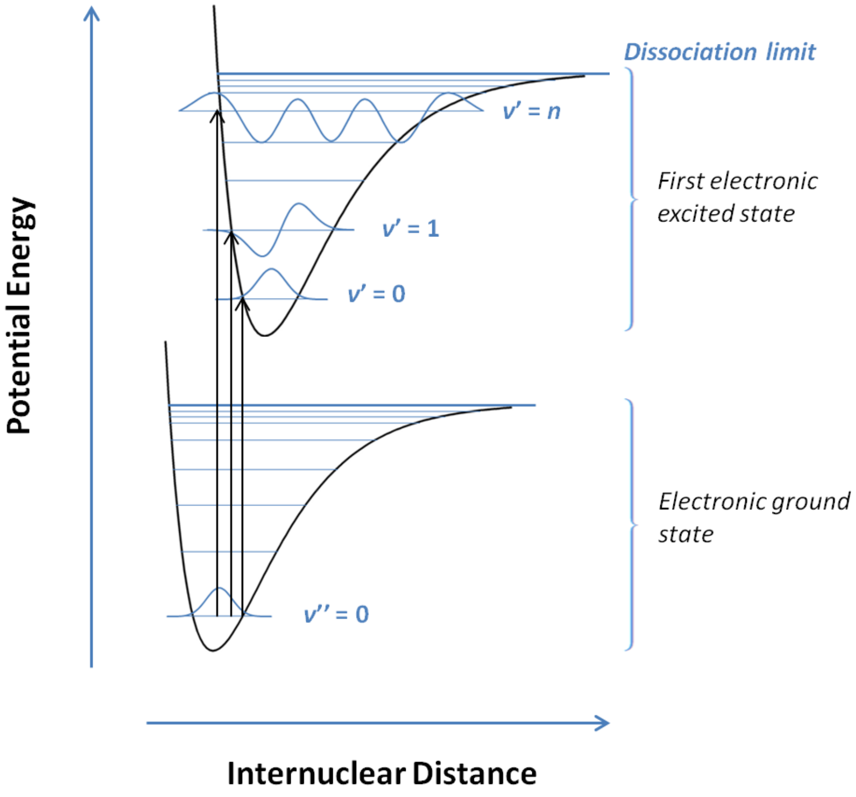

Figure 2.1 *A schematic of the quantum mechanical version of the Franck-Condon principle, illustrating electronic transitions in a diatomic molecule. In this example the greatest wavefunction overlap from the ground electronic state to the upper electronic state is the v' = n state, which would result in the strongest vibronic transition peak.*

One such atmospherically relevant species that this possible for is the ClO radical. As with many other halogen oxides, the ClO absorption spectrum exhibits characteristic vibronic bands, as shown in Figure 2.2, arising from the phenomena described above. The bands come closer together with decreasing wavelength as the vibrational levels converge with increasing energy. The smooth absorption cross sections observed at higher energy result from electronic transitions from the ground state to the upper bound electronic state at an energy that exceeds the vibronic dissociation threshold.

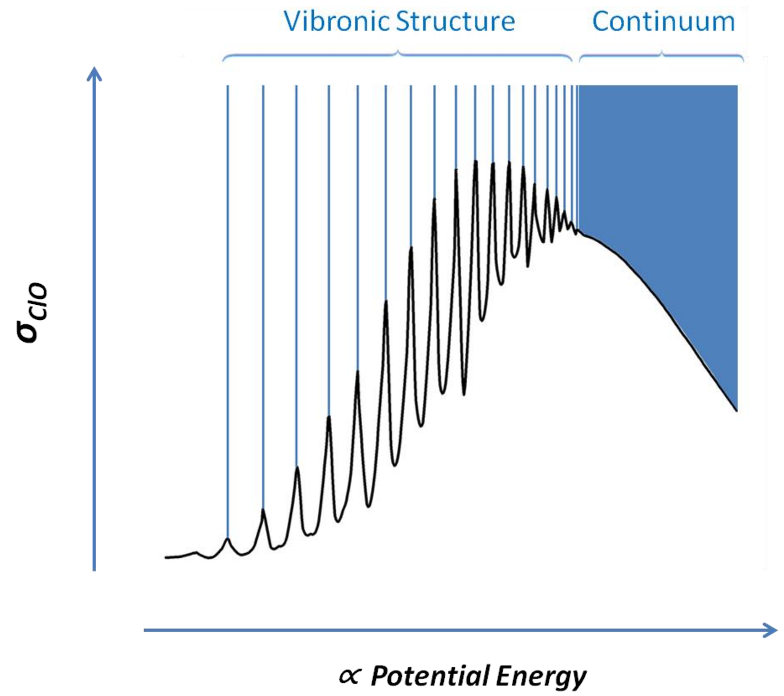

Figure 2.2 *The absorption cross section of ClO plotted as proportional to increasing potential energy (i.e. decreasing λ) highlighting the vibronic transitions from the ground electronic state to the upper electronic state. ClO cross sections are from Sander et al.*[1]

If the excitation results in a transition to an upper unbound state, the unstructured continuum absorption is also observed. In this case, where the upper state is antibonding in character, the molecule disintegrates upon absorption at all wavelengths and the observed absorptions reflect the shape of the ground state wavefunction because the excited states are ultimately represented by the unquantised translational motion of the unbound fragments. This situation is common in larger species including the peroxy radicals, which typically exhibit smooth absorption single peaked absorption spectra.[2]

2.1.2 The Fates of Excited Species

Upon the absorption of a photon possessing sufficient energy, a molecule undergoes almost instantaneous electronic excitation, represented as:

$$AB + h\nu \rightarrow AB^* \qquad (2.1)$$

The energetic excited species can undergo a number of different processes that ultimately determines their fate and the outcome of these processes can have significant atmospheric implications. Figure 2.3 summarises the different fates possible of an excited species AB*.

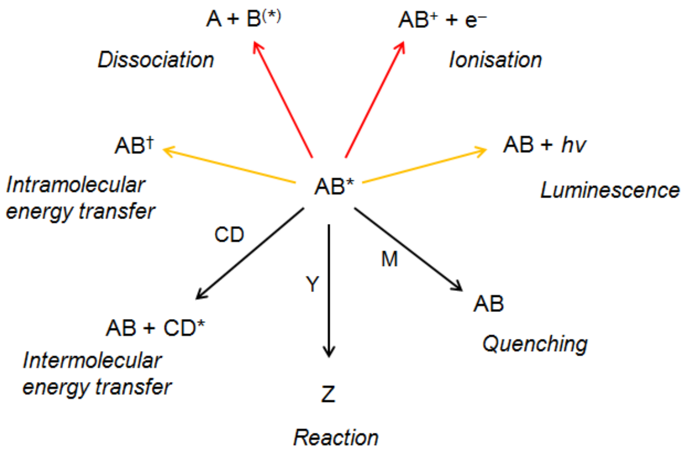

Figure 2.3 *Pathways for loss of electronic excitation that are of importance to atmospheric chemistry. Adapted from Wayne.*[3]

An electronically excited species may lose its excess energy by: re-emitting radiation *via* luminescence (fluorescence or phosphorescence); redistribution of its energy internally *via* non-radiative transitions back to the ground state or another electronic state (internal conversion, IC, or intersystem crossing, ISC); or transferring its newly acquired energy to another molecule *via* collision (*quenching*) bringing about electronic and vibrational relaxation of the molecule.[3] Electronic excitation may also bring about changes in chemical reactivity of the parent molecule either through rate enhancement of previously possible reactions or indeed new chemistry. For example, the formation of $O(^1D)$ compared to $O(^3P)$ in the atmosphere has atmospheric implications since the triplet ground state is unable to react with certain species that the excited singlet state may. For instance, the reactions:

$$O(^3P) + H_2O \rightarrow OH + OH \qquad (2.2)$$

$$O(^1D) + H_2O \rightarrow OH + OH \qquad (2.3)$$

are around 121 kJ mol^{-1} endothermic (2.2) and 69 kJ $mole^{-1}$ exothermic (2.3) respectively. The 190 kJ mol^{-1} difference in energy is the result of the excitation energy of $O(^1D)$ which therefore effectively overcomes the activation energy required for the reaction.

Photodissociation is one of the most important atmospheric processes since this initiates all radical chemistry. As touched upon above, there are two possible dissociation mechanisms for this: *optical* and *pre-dissociation*. Optical dissociation is characterised by the dissociation from the electronic state to which absorption first occurred and, as discussed above, the spectrum of a dissociative absorption appears as a continuum. Pre-dissociation is distinguished from optical dissociation by the involvement of a different electronic state of the molecule that was initially populated upon excitation. The phenomenon arises from the crossing of electronic states and the radiationless transfer between them (*i.e.* IC or ISC). If this transfer occurs near the crossing point of two potential energy surfaces, it can lead to the population of the repulsive state which is unstable with respect to the formation of ground state fragments of the molecule (which are lower in energy than the excited state fragments). Consequently, pre-dissociation provides a route for product formation in an allowed transition at *longer* wavelengths than required to yield excited fragments.

A special case of photodissociation is photoionisation, an important process occurring mainly in the upper atmosphere (regions beyond the scope of this work) in which two charged species are formed (a positive ion and an electron) rather than neutral fragments. The energy of light required to ionise a neutral molecule must be at least equivalent to the ionisation potential of the molecule which is greater in energy required for dissociation. Thus, photoionisation typically occurs in the upper atmosphere due to the low attenuation of the incoming solar radiation at wavelengths in the ionising UV spectral window.

2.1.3 Rates of Photolysis

Aside from the nature of photochemical processes, understanding of the photochemistry of transient species throughout the atmosphere also depends upon the knowledge of the *rate* of photolysis of a given species. The rate constants for photolysis, known as j-values, are effective first order rate constants for photochemical reactions. These are linearly dependent on: the solar flux intensity, I_λ, *i.e.* how much solar light at a particular wavelength is available; the absorption cross section, $\sigma_{x,\lambda}$, of the species, x, of interest; and the quantum yield of the process, $\Phi_{x,\lambda}$, which is defined as the ratio of reactants/products destroyed/formed per number of photons absorbed, having a maximum value of 1. The total quantum yield of all photochemical processes possible for an electronically excited species as shown in Figure 2.3, is always unity. For calculating each j-value, the governing function is integrated over all wavelengths although in practice only UV-visible wavelengths (*ca* 200 – 700 nm) contribute:

$$J_x = \int_0^\infty I_\lambda \sigma_{x,\lambda} \Phi_{x,\lambda} d\lambda \qquad (2.1\ \text{vi})$$

The quantity of light available to molecules in the atmosphere, also known as the actinic flux, is highly region and altitude dependent thus making j-values directly dependent on these parameters. This dependence is also affected by the random scattering and absorption of incoming solar radiation within the atmosphere, the degree of which varies temporally and regionally with altitude.

2.2 Gas Kinetics

Aside from photochemical parameters, the fundamental rates of gas phase reactions are key to atmospheric change. The basis of kinetics is presented here.

The extent of reaction, $\delta\xi$, for a species, Q, in a chemical reaction is given by:

$$\delta\xi = \frac{\delta n_{\mathrm{Q}}}{v_{\mathrm{Q}}} \tag{2.2 i}$$

where δn_{Q} is the change in the number of moles of Q in reaction and v_{Q} is the stoichiometric number for that species in the reaction (defined as negative for a reactant and *vice versa* for a product). Hence for a gas phase chemical reaction of the generic form:

$$\mathrm{aA + bB \rightarrow cC + dD} \tag{2.4}$$

where lower case letters define v. The extent of reaction is therefore:

$$\delta\xi = -\frac{\delta n_{\mathrm{A}}}{\mathrm{a}} = -\frac{\delta n_{\mathrm{B}}}{\mathrm{b}} = \frac{\delta n_{\mathrm{C}}}{\mathrm{c}} = \frac{\delta n_{\mathrm{D}}}{\mathrm{d}} \tag{2.2 ii}$$

The rate of reaction, $\tilde{r}$, is now defined as:

$$\tilde{r} = \frac{d\xi}{dt} = \frac{1}{v_{\mathrm{Q}}}\frac{dn_{\mathrm{Q}}}{dt} \tag{2.2 iii}$$

This is the *extensive* definition of the reaction rate where the stoichiometric number gives a consistent value for $\tilde{r}$ irrespective of which species is temporally monitored. However, it usually more convenient to use the *intensive* definition in which the volume is fixed (removing the size dependence of the system) and the rate of reaction is referred to as r.

$$r = \frac{1}{v_{\mathrm{Q}}}\frac{d}{dt}\left(\frac{n_{\mathrm{Q}}}{V}\right) = \frac{1}{v_{\mathrm{Q}}}\frac{d}{dt}[\mathrm{Q}] \tag{2.2 iv}$$

where [Q] is the *concentration* of any species Q. Hence combining equations (2.2 ii) and (2.2 iv) gives:

$$r = -\frac{1}{\mathrm{a}}\frac{d[\mathrm{A}]}{dt} = -\frac{1}{\mathrm{b}}\frac{d[\mathrm{B}]}{dt} = \frac{1}{\mathrm{c}}\frac{d[\mathrm{C}]}{dt} = \frac{1}{\mathrm{d}}\frac{d[\mathrm{D}]}{dt} \tag{2.2 v}$$

Therefore the rate of reaction (which from now on refers to the intensive quantity) can be defined irrespective of which species involved in the reaction is referred to.

Experimentally it is found that the rate of reaction is given by the product of a constant and the reactant concentrations raised to a certain power:

$$r = k_{\mathrm{obs}}[\mathrm{A}]^{\alpha}[\mathrm{B}]^{\beta} \tag{2.2 vi}$$

Here, k_{obs} is the observed rate coefficient of the reaction, and the orders of reaction with respect to species A and B are α and β respectively. The sum of the power terms is referred to as the overall *order* of reaction, which cannot be predicted *a priori* and may only be determined *via* experiment.

However, a single step reaction *i.e.* a direct reaction without the formation of intermediates is known as an *elementary reaction*. These reactions can be used to predict the kinetics of multistep reactions since the rate at which an elementary reaction proceeds is the product of its rate coefficient and the reactant concentrations raised to the power of their stoichiometric number, termed the *molecularity*. Hence, a reaction involving only one single body is *unimolecular*; a reaction involving two single species colliding is *bimolecular*; and a reaction involving three bodies is *termolecular*.

If reaction (2.4) is known to proceed *via* a multistep mechanism, but comprising of a number of elementary steps, for example:

$$\mathrm{A} + \mathrm{B} \rightarrow \mathrm{AB} \tag{2.5}$$

$$\mathrm{AB} \rightarrow \mathrm{C} + \mathrm{D} \tag{2.6}$$

Then the differential rate equations for the individual species may be expressed as:

$$-\frac{d[\mathrm{A}]}{dt} = -\frac{d[\mathrm{B}]}{dt} = k_{2.5}[\mathrm{A}][\mathrm{B}] \qquad \text{(2.2 vii)}$$

$$\frac{d[\mathrm{AB}]}{dt} = k_{2.5}[\mathrm{A}][\mathrm{B}] - k_{2.6}[\mathrm{AB}] \qquad \text{(2.2 viii)}$$

$$\frac{d[\mathrm{C}]}{dt} = \frac{d[\mathrm{D}]}{dt} = k_{2.6}[\mathrm{AB}] \qquad \text{(2.2 ix)}$$

where the intermediate, AB appears multiple times in the mechanism and the differential (rate) terms are *additive*. If the differential equations such as those given above are soluble, they can be used to express the overall rate constant of the reaction in terms of the rate constants for the elementary steps in the mechanism. However, due to the complicated reaction systems that often arise experimentally, it is frequently the case that the differential equations do not have a classical solution. Subsequent approximations are thus made in order to simplify the situation and derive an overall rate equation. For example, if the rate of removal of an intermediate species, such as AB, far exceeds the rate at which it is produced, then the concentration of AB remains relatively small and becomes predominantly invariant after an initial induction period. That is to say:

$$\frac{d[\mathrm{AB}]}{dt} \approx 0 \qquad \text{(2.2 x)}$$

which when applied to situations where a reactive intermediate is formed, is known as the *steady state approximation*. In this example, combining (2.2 viii) and (2.2 x) gives:

$$k_{2.5}[\mathrm{A}][\mathrm{B}] = k_{2.6}[\mathrm{AB}] \qquad \text{(2.2 xi)}$$

Therefore the rate of product formation can be expressed in terms of the reagent concentrations:

$$\frac{d[\mathrm{C}]}{dt} = \frac{d[\mathrm{D}]}{dt} = k_{2.6}[\mathrm{AB}] = k_{2.5}[\mathrm{A}][\mathrm{B}] \qquad (2.2\ \mathrm{xii})$$

Since AB is removed far quicker than it is formed, the rate of product formation is controlled by the rate of reaction (2.15) and is thus rate limiting. This is known as the *rate determining step*.

2.3 The Temperature Dependence and Theories of Reaction Rates

2.3.1 Temperature Dependence of Reaction Rates

It is well known that most reaction rate ‘constants’ vary greatly with temperature, making them more accurately described as rate ‘coefficients’. The chemist and physicist Svante Arrhenius[4] was the first to empirically derive an equation, along with the work of van’t Hoff, that satisfactorily describes the link of rate coefficients to temperature, incorporating the idea that only activated molecules are those that react upon colliding:

$$k = A\exp\left(\frac{-E_a}{RT}\right) \qquad (2.3\ \mathrm{i})$$

Here E_a is the activation energy, A is the pre-exponential factor and R is the gas constant. This expression is found to be valid for many reactions, providing valuable insight into the energetic, notably the activation barrier, involved for each reaction. A number of theories have been developed to attempt to explain this temperature dependence of the rates of gas phase bimolecular reactions. A brief account of some of these theories is provided below.

2.3.2 Bimolecular Reactions

2.3.2.1 Simple Collision Theory

The simplest approach to predicting rate constants for gas phase bimolecular reactions is by applying simple collision theory (SCT). In this approach, reactants are described as in kinetic theory, *i.e.* as hard spheres undergoing only elastic collisions. Intermolecular forces are not taken into account and reactive collisions only occur provided that a collision exceeds a certain energy threshold. Thus a typical elementary bimolecular reaction of the form:

$$\mathrm{A} + \mathrm{B} \rightarrow \mathrm{Products} \tag{2.7}$$

Has the rate:

$$r_{2.7} = Z_{\mathrm{AB}}.F \tag{2.3 ii}$$

where Z_{AB} is the collision frequency between molecules, A and B, and F is the fraction of molecules with sufficient energy to react upon collision. From kinetic theory, Z_{AB} can be expressed as:

$$Z_{\mathrm{AB}} = V_{\mathrm{col}} L^2 [\mathrm{A}][\mathrm{B}] \tag{2.3 iii}$$

Where L is the Avogadro number and V_{col} is the collision volume *i.e.* the volume swept out by the propagation of a molecule in a given period of time, in which a collision will occur if another molecule (which is considered essentially stationary with respect to the travelling molecule, hence adopting the mean *relative* speed, $\bar{c}_{\mathrm{rel}}$) is to occupy that volume:

$$V_{\mathrm{col}} = \sigma_{\mathrm{AB}} \bar{c}_{\mathrm{rel}} \Delta t \tag{2.3 iv}$$

where σ_{AB} is the collision cross section, defined as a function of the sum of the reactant radii:

$$\sigma_{\mathrm{AB}} = \pi(r_{\mathrm{A}} + r_{\mathrm{B}})^2 \qquad (2.3\ \mathrm{v})$$

The mean relative speed of the molecules is given by:

$$\bar{c}_{\mathrm{rel}} = \left(\frac{8k_{\mathrm{B}}T}{\pi\mu}\right)^{1/2} \qquad (2.3\ \mathrm{vi})$$

where k_{B} is the Boltzmann constant and μ is the reduced mass of the two reacting species. Therefore the total A-B collision frequency, per unit time, becomes:

$$Z_{\mathrm{AB}} = \sigma_{\mathrm{AB}}\left(\frac{8k_{\mathrm{B}}T}{\pi\mu}\right)^{1/2} L^2[\mathrm{A}][\mathrm{B}] \qquad (2.3\ \mathrm{vii})$$

The fraction of molecules that are able to react *i.e.* the fraction possessing at least a threshold energy to react, ε, is determined by a normalised Boltzmann distribution of energies, $f(E)$:

$$f(E) = \frac{1}{k_{\mathrm{B}}T}\exp\left(\frac{-E}{k_{\mathrm{B}}T}\right) \qquad (2.3\ \mathrm{viii})$$

Integrating the above for energies limited by ε to infinity gives the fraction of molecules that have sufficient energy to react at a given temperature:

$$F = f(E > \varepsilon) = \frac{1}{k_{\mathrm{B}}T}\int_{\varepsilon}^{\infty} \exp\left(\frac{-E}{k_{\mathrm{B}}T}\right)dE = \exp\left(\frac{-\varepsilon}{k_{\mathrm{B}}T}\right) \qquad (2.3\ \mathrm{ix})$$

Hence, combining this equation with that for Z_{AB} (2.3 vii) and F gives the theoretical rate of reaction:

$$r_{2.7} = \sigma_{\mathrm{AB}}\bar{c}_{\mathrm{rel}}L^2[\mathrm{A}][\mathrm{B}]\exp\left(\frac{-\varepsilon}{k_{\mathrm{B}}T}\right) \qquad (2.3\ \mathrm{x})$$

which may be directly compared to the form of equation (2.2 vi). Given this comparison, the observed rate constant for a bimolecular reaction is therefore predicted to exhibit the following form, which compares well with the Arrhenius equation commonly observed experimentally:

$$k = \sigma_{\mathrm{AB}} \bar{c}_{\mathrm{rel}} L^2 \exp\left(\frac{-\varepsilon}{k_{\mathrm{B}} T}\right) \qquad (2.3\ \mathrm{xi})$$

In this way SCT allows the broad features of a reaction (*e.g.* the experimental T dependence of k) to be predicted, working best for atomic or small molecular reactions in which the hard sphere assumption is most viable. However, due to this unrealistic depiction of all molecules being perfectly spherical, steric and orientation factors are not accounted for. There is also a lack of consideration in this theory for internal energy distributions within the reactants/products and an assumption that particles do no interact in space outside of the collision volume. This typically results in overestimated rate constants being derived using this theory compared to those found experimentally. Therefore a higher level of theory is required.

2.3.2.2 Transition State Theory

Transition state theory (TST) or activated complex theory (ACT) has been applied to address some of the limitations of SCT. TST is based on the recognition that the changes in molecular structure and electronic distribution brought about by a reaction are *not* instantaneous but actually occur over a finite period of time and that reaction rates may be energy dependent. The total energy of the reactants and products of an elementary reaction is a function of all the atomic reaction coordinates of the species involved. In the simplest instance, for the co-linear bimolecular reaction:

$$\mathrm{A} + \mathrm{BC} \rightarrow \mathrm{AB} + \mathrm{C} \qquad (2.8)$$

the coordinates of this reaction are described by TST as a trajectory across a three dimensional potential energy surface (PES) of the reaction, as shown schematically in Figure 2.4. The PES in this case is a function of both the A…B and B…C reaction coordinates (*versus* potential energy) and as the reaction proceeds the A…B distance decreases as the B…C increases. As the separation between A and B shortens (as A approaches B) the B-C bond weakens and lengthens and there is an increase in potential energy. When the atomic distances become almost equidistant there is a maximum in potential energy on both sets of coordinates. This maximum on the PES is known as the saddle point and is where the activated complex, denoted [$ABC^{\ddagger}$], consisting of both reactants and products, resides. The activated complex is at a transition state in energy where the A…B coordinate begins to resemble a bond and the B…C distance increases on crossing the energy maximum.

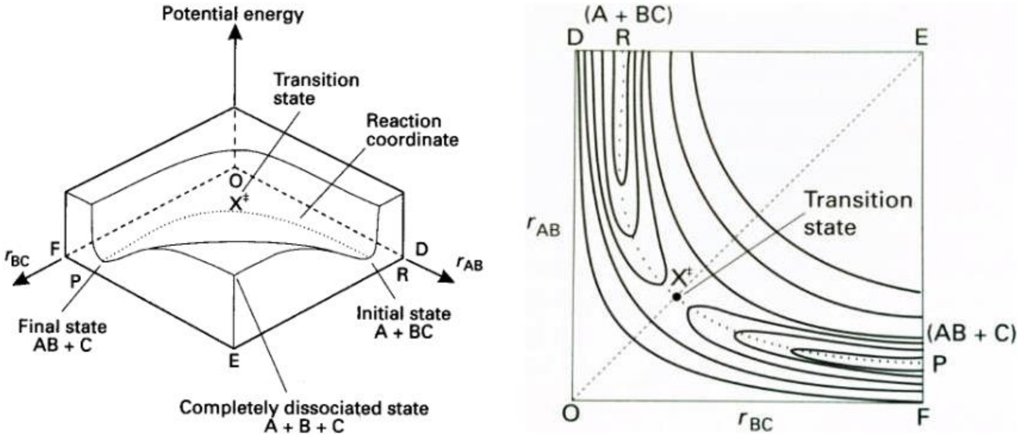

Figure 2.4 The PES for the bimolecular collinear reaction (2.8). The left panel shows the 3D nature of the reaction coordinate as a function of potential energy. The right panel is a contour plot of the same reaction, showing clearly the saddle point on which the transition state species is formed. Taken from Pilling and Seakins.[5]

TST interprets this motion across the PES by postulating a system in equilibrium between the reactant species and the activated complex which decomposes irreversibly to products:

$$A + BC \rightleftharpoons ABC^{\ddagger} \qquad (2.9)$$

$$ABC^{\ddagger} \rightarrow AB + C \qquad (2.10)$$

The rate of the overall reaction is then effectively predicted from the notional concentration of the activated complex and the rate of decomposition of it into product fragments:

$$\frac{d[\mathrm{AB}]}{dt} = \frac{d[\mathrm{C}]}{dt} = k_{2.10}[\mathrm{ABC}^{\ddagger}] \qquad (2.3\ \mathrm{xii})$$

By the assumption of equilibrium, the concentration of the activated complex may be expressed in terms of the equilibrium constant and the equilibrium concentrations of the reactants and of the activated complex:

$$K^{\ddagger} = \frac{[\mathrm{ABC}^{\ddagger}]}{[\mathrm{A}][\mathrm{BC}]} \qquad (2.3\ \mathrm{xiii})$$

Therefore rearranging the above and substituting into (2.3 xii) gives:

$$\frac{d[\mathrm{AB}]}{dt} = \frac{d[\mathrm{C}]}{dt} = k_{2.10}[\mathrm{ABC}^{\ddagger}] = k_{2.10}K^{\ddagger}[\mathrm{A}][\mathrm{BC}] \qquad (2.3\ \mathrm{xiv})$$

The first order rate constant for the decomposition of the activated complex into products is interpreted in terms of the frequency of the critical bond-breaking vibration that takes it over the saddle point, ν, multiplied by a transmission coefficient, κ, which accounts for the fraction of critical vibrations that lead to product formation:

$$k_{2.10} = \kappa\nu \qquad (2.3\ \mathrm{xv})$$

From statistical mechanics, the equilibrium constant between reactants and the activated complex can be expressed in terms of the total partition functions for species A, BC and $\mathrm{ABC}^{\ddagger}$:

$$K^{\ddagger} = \left(\frac{\mathrm{Q}_{\mathrm{ABC}^{\ddagger}}}{\mathrm{Q}_{\mathrm{A}}\mathrm{Q}_{\mathrm{BC}}}\right)\exp\left(-\frac{\Delta\varepsilon_0}{k_{\mathrm{B}}T}\right) \qquad (2.3\ \mathrm{xvi})$$

where $\Delta\varepsilon_0$ is the energy difference between the reactant ground states and that of the activated complex, Q_i is the total partition function for any species i and k_B is the Boltzmann constant. The partition function for the transition state species can be split into two separate components: q, the total partition function for the reactive vibration and $Q'_{\mathrm{ABC}^\ddagger}$, the total partition function of $\mathrm{ABC}^\ddagger$ excluding q:

$$\mathrm{Q}_{\mathrm{ABC}^\ddagger} = qQ'_{\mathrm{ABC}^\ddagger} \tag{2.3 xvii}$$

q can be approximated to:

$$q = \frac{k_\mathrm{B}T}{hc\omega_e} \tag{2.3 xviii}$$

Where h and c are Planck's constant and the speed of light respectively, ω_e is the vibrational frequency and $c\omega_e$ is equal to the dissociative vibrational frequency in equation (2.3 xv).

Incorporating the above into equation (2.3 xvi) returns the expression:

$$K^\ddagger = \frac{k_\mathrm{B}T}{hc\omega_e}\left(\frac{Q'_{\mathrm{ABC}^\ddagger}}{\mathrm{Q_A Q_B}}\right)\exp\left(-\frac{\Delta\varepsilon_0}{k_\mathrm{B}T}\right) \tag{2.3 xix}$$

Therefore, the rate equation to describe the elementary process of the formation of AB and C is:

$$\frac{d[\mathrm{AB}]}{dt} = \frac{d[\mathrm{C}]}{dt} = \kappa\nu\frac{k_\mathrm{B}T}{hc\omega_e}\left(\frac{Q'_{\mathrm{ABC}^\ddagger}}{\mathrm{Q_A Q_B}}\right)\exp\left(-\frac{\Delta\varepsilon_0}{k_\mathrm{B}T}\right)[\mathrm{A}][\mathrm{BC}] \tag{2.3 xx}$$

Which is of the form rate = k[X][Y] and the above can be simplified and rearranged to predict the bimolecular rate coefficient:

$$k_\mathrm{bimolec} = \kappa\frac{k_\mathrm{B}T}{h}\frac{Q'_{\mathrm{ABC}^\ddagger}}{\mathrm{Q_A Q_B}}\exp\left(-\frac{\Delta\varepsilon_0}{k_\mathrm{B}T}\right) \tag{2.3 xxi}$$

TST generally models experimental rate coefficients very well, with exceptions that result from, for example quantum tunnelling or reactions with pre-reactive association complexes. Accordingly, several attempts to improve TST have been invoked in recent years, such as variational TST. TST has also been improved immeasurably by the developments in quantum mechanics and statistical mechanics as a result of theoretical *e.g. ab initio* methods (briefly discussed later). For atmospheric purposes the decomposition and association of radicals also needs to be considered, as discussed from a theoretical viewpoint in the following section.

2.3.3 Unimolecular and Termolecular Reactions

While the majority of reactions in the atmosphere take place as simple bimolecular processes with no significant pressure dependence (as evidenced for example, from the magnitude of data tables in the latest JPL NASA kinetic data evaluation[6]) there are other chemical processes that lead to a deviation from simple second order behaviour. For instance, if a molecule acquires enough energy to isomerise or decompose such as in the case of photodissociation then its rate of decomposition may be first order. However, complications arise from interpreting such thermal unimolecular reactions which typically exhibit second order behaviour at low pressures and first order at high pressures. Lindemann was the first to provide a basic rationalisation of such reactions by proposing that these reactions were not elementary but in fact consisted of a mechanism of three reactions.[7] For instance:

$$AB + M \rightleftharpoons AB^{\dagger} + M \qquad (2.11)\ (-2.11)$$

$$AB^{\dagger} \rightarrow A + B \qquad (2.12)$$

where M is any other participating molecule which could be AB itself or a bath gas. If reaction (−2.11), $AB^{\dagger}$ deactivation, dominates the $AB^{\dagger}$ loss over dissociation, then AB and its activated form will generally exist in thermal equilibrium. Reaction (2.12) is the rate determining step and dominates the overall loss kinetics as first order. However, if the concentration of M is low *i.e.* the system is at low pressure, then the deactivation of $AB^{\dagger}$ will be the limiting step. In this case the overall kinetics become second order with respect to AB. The change in reaction order of unimolecular reactions can be accounted for qualitatively by applying the steady state equation to $\mathrm{AB}^{\dagger}$, an intermediate species by definition:

$$\frac{d[\mathrm{AB}^{\dagger}]}{dt} = k_{(2.12)}[\mathrm{AB}][\mathrm{M}] - k_{(-2.11)}\left[\mathrm{AB}^{\dagger}\right][\mathrm{M}] - k_{(2.12)}\left[\mathrm{AB}^{\dagger}\right] \approx 0 \tag{2.3 xxii}$$

Thus

$$\left[\mathrm{AB}^{\dagger}\right] = \frac{k_{(2.11)}[\mathrm{AB}][\mathrm{M}]}{k_{(2.12)} + k_{(-2.11)}[\mathrm{M}]} \tag{2.3 xxiii}$$

The rate of loss of AB can then be described by the rate of $\mathrm{AB}^{\dagger}$ deactivation:

$$-\frac{d[\mathrm{AB}]}{dt} = k_{(2.12)}\left[\mathrm{AB}^{\dagger}\right] \tag{2.3 xxiv}$$

Substituting equation (2.3 xxiii) into the above gives:

$$-\frac{d[\mathrm{AB}]}{dt} = k_{(2.12)}\frac{k_{(2.11)}[\mathrm{AB}][\mathrm{M}]}{k_{(2.12)} + k_{(-2.11)}[\mathrm{M}]} \tag{2.3 xxv}$$

Here, the $k_{(-2.11)}[\mathrm{M}]$ term explains the observed change in rate order as when [M] approaches zero (in the limit of low pressure) $k_{(-2.11)}[\mathrm{M}]] << k_{(2.11)}$, the denominator approximates to $k_{(2.11)}$ and the reaction becomes second order overall. When the reverse is true *i.e.* $k_{(-2.11)}[\mathrm{M}] >> k_{(2.11)}$, the $k_{(-2.11)}[\mathrm{M}]$ term dominates and equation (2.3 xxv) simplifies to first order loss:

$$-\frac{d[\mathrm{AB}]}{dt} = \frac{k_{(2.12)}k_{(2.11)}}{k_{(-2.11)}}[\mathrm{AB}] \tag{2.3 xxvi}$$

Consideration of pressure effects on chemistry of atmospheric interest are also frequently met in the form of termolecular processes. These do not occur on the unlikely event of three molecules colliding in unison to react but when there is excess energy within a newly formed species upon initial bond formation in a bimolecular reaction which in this case is dissipated by collision. For example, the recombination of two oxygen atoms (discussed in Chapter 1) leads to the initial formation of an excited oxygen molecule which must be quenched *via* collision with another body to give a stable oxygen species which would otherwise redissociate. This process may be depicted generally for the association of A and B by the following scheme:

$$\mathrm{A} + \mathrm{B} \rightarrow \mathrm{AB}^{\dagger} \qquad (2.13)$$

$$\mathrm{AB}^{\dagger} \rightarrow \mathrm{A} + \mathrm{B} \qquad (2.14)$$

$$\mathrm{AB}^{\dagger} + \mathrm{M} \rightarrow \mathrm{AB} \qquad (2.15)$$

In this case the kinetic formation of the stable product may be described by again treating $\mathrm{AB}^{\dagger}$ as an intermediate and applying SSA which yields:

$$\frac{d[\mathrm{AB}]}{dt} = k_{(2.15)}[\mathrm{M}]\left(\frac{k_{(2.13)}[\mathrm{A}][\mathrm{B}]}{k_{(2.14)} + k_{(2.15)}[\mathrm{M}]}\right) \qquad (2.3\ \mathrm{xxvii})$$

As with unimolecular reactions, the order of reaction is dependent on the relative importance of the term $k_{(2.15)}[\mathrm{M}]$ hence pressure. Therefore at high pressures, this theory predicts:

$$\frac{d[\mathrm{AB}]}{dt} = k_{(2.13)}[\mathrm{A}][\mathrm{B}] \qquad (2.3\ \mathrm{xxviii})$$

i.e. second order overall, whereas at low pressures, equation (2.3 xxvii) becomes:

$$\frac{d[\mathrm{AB}]}{dt} = \frac{k_{(2.15)}k_{(2.13)}}{k_{(2.14)}}[\mathrm{A}][\mathrm{B}][\mathrm{M}] \qquad (2.3\ \mathrm{xxix})$$

For both unimolecular and termolecular reactions, the pressure dependence of the rate of reaction can be defined as having low and high pressure limiting values from expressions (2.3 xxviii) and (2.3 xxix) respectively. These effective rate constants are typically represented by k_0 and k_∞ for the low and high pressure limits respectively. Thus for the termolecular rate constant k_{ter}:

$$k_{\mathrm{ter}} = \frac{k_\infty k_0[\mathrm{M}]}{k_\infty + k_0[\mathrm{M}]} \qquad (2.3\ \mathrm{xxx})$$

The form that this pressure dependence takes is shown schematically below in Figure 2.5.

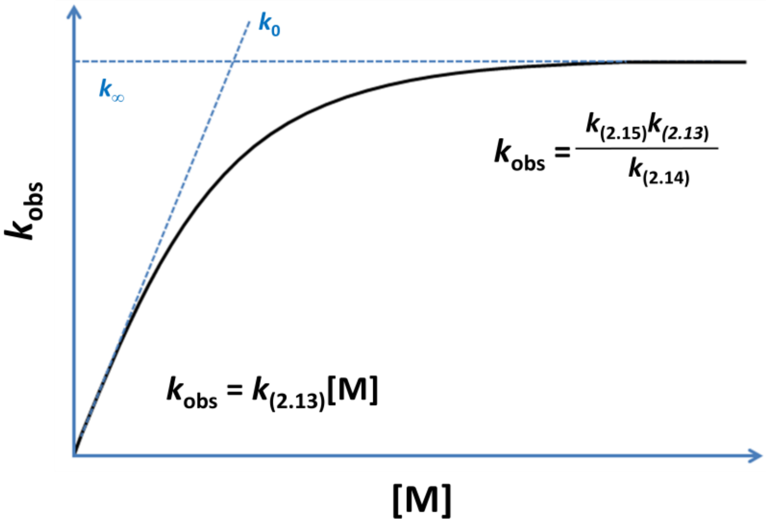

Figure 2.5 *Schematic diagram of the observed first order rate coefficient, k_{obs}, as a function of number density [M].*

While equation (2.3 xxx) represents the experimental variation of k_{ter} depicted above, it often does not explicitly match experimental observations and its application is unsuitable at intermediate pressures between the upper and lower pressure limits. The reasons for this are principally due to shortcomings of the Lindemann mechanism which does not recognise, for example, that rates of formation of the energised molecule $\mathrm{AB}^\dagger$ are dependent on its internal degrees of freedom. Modifications by the work of Rice, Ramsperger, Kassel and Marcus to the Lindemann mechanism, appropriately named RRKM theory, have been used to successfully predict rate coefficients that are in good agreement with experimental data.[8-10] RRKM theory includes a weighted sum of the rate coefficients with respect to population, for each vibrational and rotational energy level of the energised species. These parameters provide a rigorous *a priori* calculation of the overall rate constant, provided that reliable thermodynamic data constants can be acquired for a given species. However, application of RRKM theory to actual atmospheric processes has also proven difficult owing to the lack of readily available accurate thermodynamic data for atmospheric species. To resolve this issue, Troe[11] demonstrated a much simpler approach in determining k_{ter} that has subsequently become almost universally adopted. Incorporating a "broadening factor", *F*, as a multiplicative factor in the right hand side of equation (2.3 xxx), it follows that:

$$k_{\text{Troe}} = \frac{k_\infty k_0[\text{M}]}{k_\infty + k_0[\text{M}]}.F \qquad \text{(2.3 xxxi)}$$

where:

$$F = F_c^{\,x^{-1}} \qquad \text{(2.3 xxxii)}$$

F_c itself is dependent on the specific reaction, although for the majority of atmospheric species a value of 0.6 returns a reasonable representation of k_{ter} as recommended by the JPL NASA panel for data evaluation.[6] The *x* term is a function of equation (2.3 xxx) itself:

$$x = 1 + \left[\log_{10}\left(\frac{k_\infty k_0[\text{M}]}{k_\infty + k_0[\text{M}]}\right)\right] \qquad \text{(2.3 xxxiii)}$$

2.3.4 Deviation from Arrhenius Behaviour

Whilst the theories outlined in sections 0 and 2.3.3 for the rationalisation and prediction of bimolecular, unimolecular and termolecular rate coefficients are reasonable, there are certain experimental rate observations that defy simple explanation. Particular examples are the deviation from Arrhenius behaviour (*i.e.* non-linear *T* dependence) and the observation of negative *T* dependencies for rate coefficients.

The temperature dependence of the rate coefficient of a reaction will, according to the Arrhenius expression (equation (2.3 i)), typically give a linear plot of ln k *versus* T^{-1}:

$$\ln k = \ln A - \frac{E_a}{R} T^{-1} \tag{2.3 xxxiv}$$

where $\ln A$ and $-E_a/R$ are the intercept and gradient of this plot respectively. Therefore, the observed rate coefficients for reactions that follow this are said to be “Arrhenius” in behaviour. However, there are reported cases in which reactions do not obey this rule. These cases typically arise at the extremes of high or low temperatures and are indicated by a curvature in the trend, deviating from the broadly linear correlation over intermediate temperatures. Quantum tunnelling through a potential energy barrier by a particle means that a particle can appear on the other side of this without being energetic enough to surmount it. However, the tunnelling rate only becomes comparable to the reaction rate at extremely low temperatures. At such temperatures, the reaction may proceed faster than predicted by theory, resulting in a positive deviation in the Arrhenius plot.[5] However, the probability of tunnelling depends inversely exponentially on the mass of the particle involved and so this particular non-Arrhenius behaviour has been principally observed in reactions involving light species, notably hydrogen atoms.[12,13]

Further non-Arrhenius behaviour can be explained by examining the pre-exponential factor, A. The partition functions in expression (2.3 xvi) are each the product of translational, rotational and vibrational partition functions thus each also has a specific dependence on temperature. Importantly, this temperature dependence follows a power law and equation (2.3 xxi) can be rewritten as:

$$k = T^n A' \exp\left(\frac{-E_a}{RT}\right) \tag{2.3 xxxv}$$

where A' is the temperature independent component of the pre-exponential function and n is an exponent chosen according to the size/structure of the reactants. From (2.3 i) and the above, the pre-exponential factor, A, is therefore temperature dependent, which if this dependence is significant enough over a given range of T, the expression will be non-linear. However, for the majority of reactions of atmospheric importance, the temperature dependence of *A* is weak compared to that of the exponential term which dominates the overall temperature dependence of the reaction.

2.3.5 Non-Arrhenius and Negative Temperature Dependence

A great number of processes involving free radicals, in particular radical-radical association reactions, appear to exhibit non-Arrhenius behaviour *via* an apparent "negative" activation energy with the reaction, thus becoming more efficient with decreasing temperature. These reactions are said to have a negative temperature dependence where *k* increases as *T* decreases. As discussed above for a bimolecular collision, when two stable species approach each other there is a deviation in their potential energy of interaction compared to when they are completely separate. For thermochemical reactions, this deviation is typically positive *i.e.* the potential energy increases forming an activation energy barrier. Thus, to overcome this barrier, the reactants must be sufficiently thermally energetic to cross the saddle point on the potential energy surface. A larger proportion of molecules will possess this minimum energy at elevated temperatures and so the rate of reaction typically increases with increasing temperature.

However, when considering chemical processes such as the reaction between two free radicals, this deviation can be negative. Radical species are typically highly reactive and, therefore, relatively unstable owing to their lone outer shell electron. When a pair of reacting radicals approaches one another, depending on their orientation, they can form an energetically favourable intermediate complex upon collision that is lower in energy than the two lone radicals, forming thereafter a negative reaction energy barrier. This intermediate/transition state can be vibrationally excited, meaning stabilisation by a third body is potentially required. However, if the newly formed species is sufficiently large, this excess energy may be dissipated throughout other vibrational modes prior to quenching and/or dissociation back to reactants. The lower the thermal energy of the reactants, the less internal vibrational energy is stored and the lifetime of the complex/transition state becomes significant. Therefore at lower temperatures, product formation becomes increasingly favourable; ergo the rate of reaction increases as the temperature decreases.

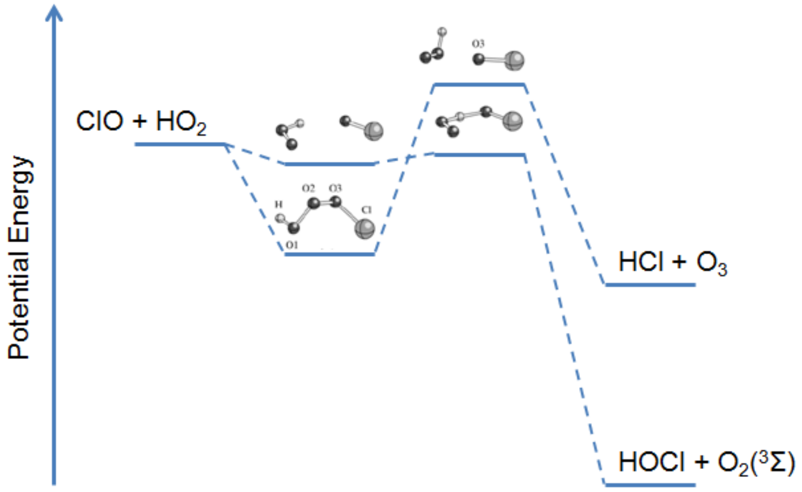

Figure 2.6 *A schematic potential energy diagram of the two most energetically favourable product channels of the* $ClO + HO_2$ *reaction. Adapted from Kaltsoyannis and Rowley.*[14]

The reaction of halogen oxides with hydroperoxy radicals typically exhibit negative temperature dependencies. One such example is the reaction of ClO with HO_2 which is discussed in detail in Chapter 4. Here, a qualitative view is provided to illustrate this prototypical reaction and to aid visualisation of the mechanistic approach to such elementary reactions. A schematic potential energy diagram shown in Figure 2.6 gives the relative energies of the reactants, minima, transition states and products of the reaction derived from previous laboratory and theoretical studies. It shows the routes of the two lowest energy product pathways which are the most likely to occur. The reaction proceeds either through the highly exothermic H-abstraction of HO_2 to give HOCl or *via* the formation of the energetic HOOOCl intermediate which requires collisional quenching before dissociating to give HCl and O_3. It can be seen that the initial H-bond in the HOCl-forming channel leads to a decrease in the overall potential energy and the subsequent transition state leads to a maximum below the initial potential energy level of the reactants. The formation of HOOOCl, by contrast, results in a much lower potential energy minimum although the subsequent transition state is slightly higher in potential energy than the reactants. Also, the HOOOCl product formed in this case would be expected to be vibrationally excited and to require a third body collision to stabilise it. The HOCl pathway is the dominant product channel as verified by experiment although the HCl channel is predicted to give rise to a pressure dependent element and a branching of the total rate constant.

Multiple product channels of atmospherically relevant reactions are common. The relative probability of products formed in such reactions can have consequences in the atmosphere depending on their reactivity/photochemistry. For instance, the probability of HCl *versus* HOCl formation in the ClO + HO_2 reaction has a direct effect on ozone destruction: HCl is a reservoir species of atomic chlorine preventing further ozone loss (indeed ozone is also co-produced) whereas the photolabile HOCl leads to the loss of two O_3 molecules upon photolysis and subsequent chemistry. As a result, the outcome of this reaction can vary from ozone forming to ozone destroying. Therefore the relative rates of formation for each product pathway are of particular significance. The branching ratio of a particular reaction channel, f_{a}, is defined by the ratio of the rate coefficient of that channel, k_{a} over the total rate coefficient of the reaction which is a sum of all the rate coefficients of the possible reaction channels:

$$f_{\mathrm{a}} = \frac{k_{\mathrm{a}}}{k_{\mathrm{total}}} = \frac{k_{\mathrm{a}}}{k_{\mathrm{a}} + k_{\mathrm{b}} + k_{\mathrm{c}} \ldots} \qquad \text{(2.3 xxxvi)}$$

2.4 Computational Methods

The discussion on the theories of gas phase kinetics in the preceding sections of this chapter and their subsequent mechanistic interpretation allow the determination of rate ‘constants’ from physical experimental data. However, these theories can be potentially applied to any elementary reaction thus the dynamics and therefore kinetics of such systems may be simulated from these first principles. Computational investigations, so called *theoretical studies*, have become increasingly insightful in elucidating the mechanisms of reactions that are particularly difficult to investigate experimentally and are complementary to laboratory studies in particular (*e.g.* as in

Figure 2.6). A detailed description of these theoretical techniques is beyond the scope of this current work, however, a brief summary of the approach that these methods are based on is given here.

Classically, any attempt at a full scale theory of elementary reactions should incorporate three stages:[15] (i) the calculation of the PES for the system should be made; (ii) the dynamics of individual molecular events (*e.g.* collision, translation, *etc*) should be solved; (iii) and the results of (ii) should be averaged appropriately in order for the results to be suitably compared to experiment *i.e.* using (i) and (ii) to determine reaction cross sections/rate constants.

Traditionally, the *ab initio* calculation of accurate rate constants has been extraordinarily difficult owing to the quantum mechanical chemical calculation of the PES.[16] The repetitious nature of solving of the Schrödinger equation, which itself is limited to the simplest of molecular systems, for the many points required needed for the PES to retain the necessary accuracy is computationally expensive. For the sizeable systems which are usually representative of atmospheric species, suitable approximations *via* the assemblage of the linear combination of mathematical functions that approximate the electronic structure of the system (the basis set). The accuracy of the PES depends on the size of the basis set used which itself must be compromised with the computational time available. Thus the level of theory selected must be both the most cost-effective and accurate to avoid shortcomings in the calculation of the PES.[17] Other techniques such as *density functional theory* are more cost effective as the use of functionals to calculate regions of electron density are more cost effective, although there are still limitations with regards to properly describing intermolecular forces. *Semi-empirical* methods often drastically reduce the calculational task of forming PES's as they use empirical analogy *i.e.* experimental data. By the interpolation/extrapolation of known sets of molecular properties, semi-empirical methods can estimate detailed properties of the transition state by analogy with known chemical species.[16]

Once a suitable PES has been chosen, the dynamics are treated by the simulation of individual molecular collisions by computationally solving the classical equations for the relative motions of the nuclei (across the PES).[15] For classical trajectories, the selection is made on the basis of the internal energies being allowed a continuous range of values. By using TST (section 2.3.2.2), the geometry of the activated complex can be obtained by locating the saddle point on the PES. Furthermore, the shape of the PES at the saddle point itself can be used to determine the vibrational frequencies of the activated complex.[5] Quasiclassical trajectories can also be utilised to determine rate constants, where collisions are simulated by solving the classical equations for the relative motions of the nuclei where the starting positions are selected. Averaging is built into the selection of the initial values of the position and momentum coordinates of the nuclei using pseudo random techniques.

As discussed above, TST is not without limitations and deviations from Arrhenius behaviour can lead to deviations in reported rate constants between theoretical and experimental studies if quantum effects and others, including pressure, are not accounted for.[12] Also, if potential species/pre-reactive complexes are formed and not accounted for in theoretical calculations, deviations can also arise.[18] However, this can be beneficial, since these deviations can imply shortcomings in the proposed mechanism of a reaction and help identify other possible elementary reactions.

2.5 Concluding Remarks

The theories of gas phase photochemistry and thermochemistry have been summarised and their main assumptions discussed. These theories provide the basis of gas phase kinetic studies, most specifically relevant to the study of gas phase atmospheric chemistry. Chemical mechanisms of atmospheric processes and species can be built from these theories and tested. However in order to test these models, *experiments* must be performed in which concentrations of transient species much be generated and their behaviour monitored. The principles of pursuing such experiments are discussed in the following chapter.

2.6 References

1. Sander, S.P. and R.R. Friedl, Kinetics and Product Studies of the Reaction ClO + BrO Using Flash Photolysis Ultraviolet Absorption. *Journal of physical chemistry*, 1989. **93**(12): 4764-4771.
2. Tyndall, G.S., R.A. Cox, C. Granier, R. Lesclaux, G.K. Moortgat, M.J. Pilling, A.R. Ravishankara, and T.J. Wallington, Atmospheric Chemistry of Small Organic Peroxy Radicals. *J. Geophys. Res.*, 2001. **106**(D11): 12157-12182.
3. Wayne, R.P., *Chemistry of Atmospheres* 1985, Oxford: Oxford University Press.
4. Arrhenius, S., *Zeitschrift für Physikalische Chemie*, 1889. **4**: 226.
5. M.J. Pilling and P.W. Seakins, *Reactions Kinetics* 1995, Oxford, United Kingdom: Oxford University Press.
6. Sander, S.P., J. Abbatt, J. R. Barker, J. B. Burkholder, R. R. Friedl, D. M. Golden, R. E. Huie, C. E. Kolb, M. J. Kurylo, G. and V.L.O. K. Moortgat, P. H. Wine, "Chemical Kinetics and Photochemical Data for Use in Atmospheric Studies, Evaluation No. 17," JPL Publication 10-6, Jet Propulsion Laboratory, Pasadena, 2011 http://jpldataeval.jpl.nasa.gov.
7. Lindemann, F.A., S. Arrhenius, I. Langmuir, N.R. Dhar, J. Perrin, and W.C. McC. Lewis, Discussion on "the Radiation Theory of Chemical Action". *Transactions of the Faraday Society*, 1922. **17**(0): 598-606.
8. Rice, O.K. and H.C. Ramsperger, Theories of Unimolecular Gas Reactions at Low Pressures. *Journal of the American Chemical Society*, 1927. **49**(7): 1617-1629.
9. Kassel, L.S., Studies in Homogeneous Gas Reactions. I. *The Journal of Physical Chemistry*, 1927. **32**(2): 225-242.
10. Marcus, R.A., Unimolecular Dissociations and Free Radical Recombinaiton Reactions. *Journal of Chemical Physics*, 1952. **20**(3): 359-364.
11. Troe, J., Predictive Possibilities of Unimolecular Rate Theory. *Journal of physical chemistry*, 1979. **83**(1): 114-126.
12. Zhu, R.S., E.G.W. Diau, M.C. Lin, and A.M. Mebel, A Computational Study of the OH(OD) + CO Reactions: Effects of Pressure, Temperature, and Quantum-Mechanical Tunneling on Product Formation. *Journal of Physical Chemistry A*, 2001. **105**(50): 11249-11259.

13. Nguyen, T.L., B.C. Xue, R.E. Weston, J.R. Barker, and J.F. Stanton, Reaction of HO with CO: Tunneling Is Indeed Important. *Journal of Physical Chemistry Letters*, 2012. **3**(11): 1549-1553.
14. Kaltsoyannis, N. and D.M. Rowley, *Ab initio* Investigations of the Potential Energy Surfaces of the XO + HO_2 reaction (X = Chlorine or Bromine). *Physical Chemistry Chemical Physics*, 2002. **4**(3): 419-427.
15. M.J. Pilling and I.W.M. Smith, *Modern Gas Kinetics: Theory, Experiment and Application* 1987, Oxford, United Kingdom: Blackwell Scientific Publications.
16. Kaufman, F., Rates of Elementary Reactions – Measurement and Applications. *Science*, 1985. **230**(4724): 393-399.
17. Chan, B. and L. Radom, Approaches for Obtaining Accurate Rate Constants for Hydrogen Abstraction by a Chlorine Atom. *Journal of Physical Chemistry A*, 2012. **116**(14): 3745-3752.
18. Weston, R.E., T.L. Nguyen, J.F. Stanton, and J.R. Barker, HO + CO Reaction Rates and H/D Kinetic Isotope Effects: Master Equation Models with *ab initio* SCTST Rate Constants. *Journal of Physical Chemistry A*, 2013. **117**(5): 821-835.

Chapter 3: Laboratory Studies of Atmospheric Chemical Reactions: Strategies and Techniques

3.1 Introduction

Strategies in undertaking the research of atmospheric science require the application of a range of scientific disciplines ranging from the physical to the biological, reflecting the complex interdependencies of the Earth System (discussed in Chapter 1) and the pivotal role the atmosphere plays within it. Atmospheric chemistry, a key part in the defining characteristics of the atmosphere, also requires a multi-disciplined approach in tackling the problem of knowing what chemical reactions are happening and what their features are. Due to the nature of the reactive, often intermediate, trace chemical species, monitoring them and elucidating their chemical transformations has been and continues to be a challenge. Over the course of the latter half of the 20th Century, the practice of atmospheric chemistry was founded and has relied greatly on the tools provided by the physical and chemical sciences and with a significantly increasing computational aspect in recent decades, owing to the rapid development of more powerful processors.[1] Consequently, the approach to studying atmospheric chemistry is underpinned by 3 distinct fields (Figure 3.1) which may be defined as: *Field Observations* where species/reactions are directly or indirectly monitored in the atmosphere *via in situ* measurements or through remote sensing; *Laboratory Studies* where the kinetics, thermochemistry, photochemistry and/or product distributions of atmospherically relevant reactions are measured under controlled conditions (which is the basis of this thesis) and *Modelling* where the atmosphere is modelled as a function of altitude, latitude, longitude and time, with the aim of linking and assessing the knowledge provided by what is observed in the field and what is predicted by laboratory studies. Other approaches to atmospheric research use techniques similar to more than one of the above fields such as smog chamber studies which can be thought of as pseudo laboratory-field studies.[2] Further, the use of computer models in simulating complex reaction mixtures in kinetic studies, although much simpler compared to their atmospheric cousins, is also common.[3] Other computational methods that are becoming more accurate in predicting rate coefficients and product distributions involve the dynamical study of reactions using techniques such as *ab initio* and *semi-empirical* approaches, discussed above in Chapter 2.

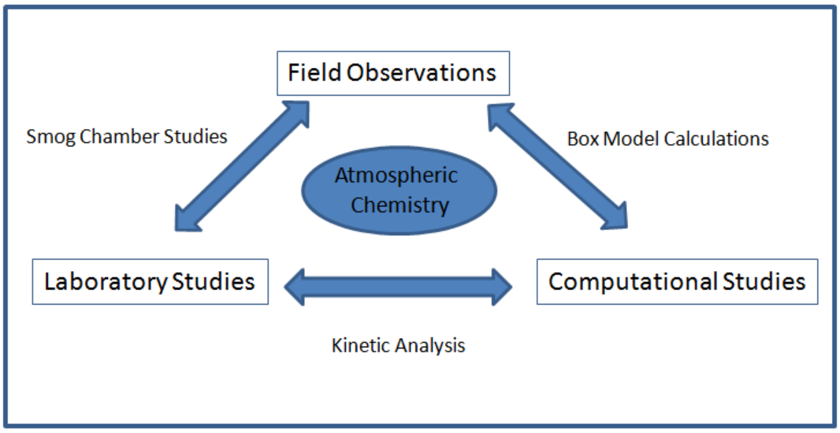

Figure 3.1 *A schematic representation of the different strategies employed to research the chemistry of Earth's Atmosphere.*

This thesis is based on work conducted in a laboratory setting and so will principally focus on the comparison of this work with other similar laboratory studies. The other methods used, upon which our current understanding of the reactions studied in this work is based on, will also be discussed to provide a more complete picture in interpreting the results. The following section will provide a summary of the techniques typically used in laboratory studies and the principles of the experiments employed in this work which is focussed on gas phase radical reactions.

3.2 Experimental Methods

There are two general types of experimental approaches applied in the study of gas phase radical reactions. Fundamentally, both are concerned in measuring the changes of at least one or more reactant or product species as a function of time and then deducing rates of loss which are applicable to real life situations such as atmospheric or, for example, combustion chemistry. Understanding the sensitivity of these rate coefficients to temperature and pressure is vital and these dependencies are pursued experimentally and theoretically often by many groups in order to find a consensus that also reflects what is simulated compared to what is observed in the field. While today a host of techniques is available to laboratory based groups to probe these reactions, they all are based on one of two separate principles developed around the middle of the previous century. These are the flash photolysis (FP) technique, based on the Nobel Prize winning work of Porter and Norrish,[4] and the discharge-flow (DF) tube reactor technique, which is the remote offspring of the separate work of Wood[5,6] and Bonhoeffer.[7,8] These two techniques offer two rather different methods of studying the same chemistry and ultimately measuring the same quantity, the rate coefficient of a given gas phase reaction, k. While comparing them can induce the impression of the two techniques vying for superiority over the other, the reality is that the two experimental methods are complementary to one another as this chapter hopes to highlight.

3.2.1 Real Time *versus* Elapsed Time Monitoring

Fundamental to studying any chemical reaction is measuring how the concentration of a chemical species changes with time. Real time is conceptually the simplest mode to understand, where the passage of experimental time is the same as the time in which the reaction proceeds *i.e.* the formation and subsequent decay of the reactants is observed and recorded as it actually happens. This mode of time is employed by the FP technique making it the preferred method of choice as it allows direct measurement of species concentration (depending on the detection method) in real time and the results can be readily analysed. Through an intense pulse of radiation, radicals may be formed *via* photolysis of photolabile molecules, generating the species of interest directly or indirectly through subsequent reactions. Here, an essential requirement of FP for its efficacy in accurately obtaining k for a reaction is in the relative rapidity of radical formation and subsequent decay. In order for the decay kinetics of a reaction not to be convoluted by any opposing (preceding) formation kinetics, the formation of the reactant species must be sufficiently rapid to ensure that the largest possible portion of reactants formed must be formed before any significant decay *i.e.* the effective $r_{formation}$ >> the effective r_{decay}. This requirement essentially decouples the formation and decay kinetics of the reactive species of interest, allowing the pure decay kinetics to be investigated. However, a corollary and a disadvantage to the real time monitoring of a reaction is the rapidity in which short-lived radical reactions occur. In order to carry out real time studies, the time resolution of the detection apparatus must be sufficiently high enough to monitor rapid changes in concentration. Indeed, the time response of the detection system employed in flash photolysis studies can often be the limiting factor in the ability to investigate a given reaction. Furthermore, the typically small radical concentrations often encountered in FP studies (ppmv or smaller) require high sensitivity of detection. This is coupled with the temporal requirement. Increasing the radical concentration to preclude sensitivity issues usually leads to a more rapid radical decay, which thereby compromises the detection limits.

Elapsed time monitoring removes this potential problem of time response and sensitivity of a detection system as the reaction time is decoupled from the observed experimental time. By applying suitable conditions that permit the reaction time to be interpreted as a physical distance, the reaction time can be deduced. This scenario can be thought about by preparing reactant species separately, usually in fast gas flows, and monitoring them at a fixed time after their interaction (mixing). The elapsed time of reaction is then given by the simple relationship:

$$t = d / v \tag{3.2 i}$$

where time, $t = t_n - t_0$, and distance, $d = d_n - d_0$, are the reaction time and distance respectively defined by the point in reaction space (therefore time) where the reactant gases of interest are detected (t_n and d_n) minus the point where they first interact *i.e.* mix (defining t_0 and d_0). v is the linear flow velocity. For this to be achieved experimentally, the situation must be set up whereby the reactants must be formed and flowed continually to form a steady-state abundance at a given position within a reactor as shown schematically in Figure 3.2. Radicals are typically produced continuously using a microwave discharge forming a constant flow of species which are either used directly as reactants or as reactant precursors (hence the term “discharge-flow”). The reactants are kept physically separated from one another until they are mixed in the flow reactor at which point defining t_0 as the reaction of interest is initiated. The concentrations observed downstream are stationary under these circumstances with respect to experimental time, removing the constraint of the detection system time response. The distance between mixing and detection may then be changed to build up the temporal profile of reactant/product concentration. Many different methods may be applied in detecting the reactant/product species making the DF approach a versatile technique. However, DF is not without its limitations as the relationship of distance with time is often less trivial than indicated in equation (3.2 i). Most rigorously a transport equation must be solved which, depending on the flow regime, can introduce significant uncertainty into t_n and t_0. This may be exacerbated by a poorly defined mixing time. Further, heterogeneous loss of species onto the reactor surface, especially at low pressures which are often needed to accommodate fast gas flows and are especially significant at low temperatures, must be accounted for and can pose problems if the processes are not minimised or they are poorly understood.[6,9]

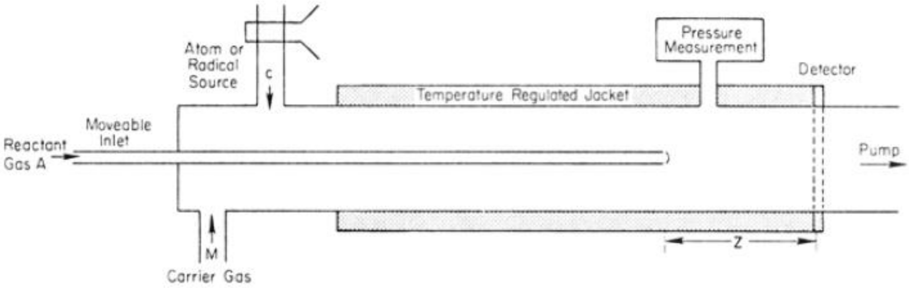

Figure 3.2 *A schematic diagram of a generic DF experimental set up.*[6]

3.3 The Flash Photolysis Technique

The term *flash photolysis* is essentially a description of the mode of radical production. The technique typically involves a short-lived but intense burst of light from, originally, a high voltage discharge lamp or, as is more typical today, a pulsed laser light source to initiate a reaction. This light must be sufficiently intense to result in the photolysis of a suitable proportion of a given precursor gas mixture. The rapid generation of radical species initiates the reaction of interest either directly or indirectly, with real time monitoring of reactants and/or products as discussed above. Bimolecular radical reactions typically occur with rate constants of the order of $k = 10^{-11} - 10^{-13}$ cm^3 molecules^{-1} s^{-1}. Detectors need to be able to have suitably short time responses and be able to distinguish typically small changes in concentration (typically sub ppmv).

Spectroscopy is a powerful, direct method of investigating concentrations; thereafter providing insight into the mechanisms, kinetics and thermodynamics of chemical reactions. Spectroscopy also gives detailed information on the nature and structure of reactive intermediates, such as gaseous free radicals. Absorption spectroscopy in particular is well suited for kinetic studies as concentrations of absorbing species can be monitored unequivocally and reactions can be studied non-invasively. This differs from emission spectroscopy in which emission bands generated either by flame or discharge tubes necessarily involve extreme conditions to create electronic transitions. Free radicals are particularly well suited for absorption spectroscopy as the majority of simple radicals have electronic transitions involving the ground state to an easily accessible first electronically excited state. Thus, the UV/visible spectrum provides a sensitive method of detection.[10] However, for absorption spectroscopy to be effective, relatively large concentrations of the free radicals compared to those that are typically encountered in the atmosphere are needed. Furthermore, because of overlapping absorptions of different species, the measured absorption is often a composite of all absorbances present.

3.3.1 A Brief History of Flash Photolysis

The flash photolysis technique was first developed by Porter, Norrish and co-workers in the late 1940s and early 1950s.[4,11] Reactions were initiated by photolytic pulses emitted by a rare-gas flashlamp with a second, delayed pulse from a different flashlamp used to monitor the species generated using UV absorption spectroscopy. Experimental transmission spectra were recorded on photographic plates; a part of one photographic plate per photolytic pulse was used which was aligned in the dispersive plane of a spectrograph which the probe light, transmitted through the reactor, was focussed onto. Absorptions were calculated manually by measuring the degree of darkening of the exposed flashed plate relative to that of a non-flashed exposed plate giving an absorption spectrum recorded at a fixed point in time. To build up a temporal profile of these flashlamp initiated reactions, different delay times after the photolytic flash were used and the changes in absorption measured. While the method was laborious; slow and work intensive, this technique was pioneering and thereby used to produce some of the first experimental evidence for gas phase free radicals.[10] Furthermore, its advent was a major development for gas phase kinetics. The contribution Porter and Norrish's technique has made to gas phase kinetics was recognised in 1967 when they were awarded the Nobel Prize in chemistry.

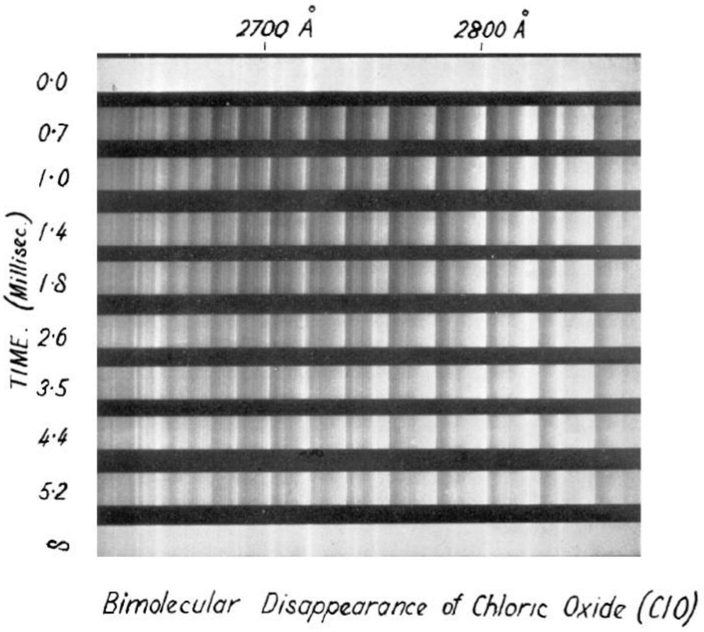

Figure 3.3 *A photographic plate made in 1953 showing the first recorded absorptions of the ClO radical.*[12]

The emergence of electronic photodetectors in the 1960s was the next major development associated with the flash photolysis technique.[13] Photomultiplier tubes (PMTs) enabled the first continuous real time monitoring of reactive systems recording light intensities on the order of microseconds. This significantly reduced the challenge of such experiments and facilitated the inclusion of multiple repeated experiments, since a complete temporal decay profile of transmitted light intensity initiated by a single photolysis pulse could be observed. However, the absorption data recorded by PMTs are single wavelength due to their inability to distinguish between photons arriving at different positions of the detector window, preventing the simultaneous measurement of wavelength resolved absorptions in the dispersive plane of a typical spectrograph. Therefore the reactive species in this instance are monitored by selecting a single wavelength, typically near the maximum absorption of the absorbing species of interest, using a monochromator rather than a spectrograph. Consequently the absorption for each species is inferred and then the concentration is calculated by subtracting the contributions from the coincident absorbers, leaving the species of interest. Despite being limited to single wavelengths, the use of multiple PMTs (with multiple monochromators) can enable the monitoring of multiple species and the use of PMTs has been effective.[14] Therefore it is unsurprising that the inclusion of this method in flash photolysis systems is still widespread today.[4,15]

The advent of photodiode arrays in recent years has permitted the simultaneous time and wavelength resolved monitoring of light intensity electronically. These detectors comprise rows of small, light sensitive elements (pixels), which can be aligned along the dispersive axis of a spectrograph. The broad wavelength coverage allows entire absorption bands to be monitored rather than single wavelengths, meaning the unequivocal determination of species concentrations is possible, making this a more accurate method than that provided by the use of PMTs. However the temporal resolution of a photodiode array is dictated by the readout time of the device. With a single output amplifier, signal from the pixels in the array is read out sequentially. With a typical timescale of milliseconds, the effectiveness of photodiode array detection for reactions occurring on faster timescales, as many free radical reactions do, is therefore limited. One solution to this issue consists of coupling the array with fast electronic time gating, allowing the recording of a “snapshot” spectrum at a certain delay time after photolysis. Analogous to the pioneering procedure used with photographic plates, repeated experiments with different delay times may then be employed in order to assemble the variation of wavelength-resolved transmission (and therefore absorption) as a function of time.

The application of charge-coupled device (CCD) detectors in flash photolysis experiments was pioneered by Rowley and co-workers in Cambridge in the mid-1990s.[16] Combining the advantages of the rapid temporal resolution of PMTs *and* the spectral resolution of photodiode arrays, CCD detectors overcome the limitations associated with previous detectors. Similar to photodiode arrays, CCDs consist of light sensitive pixels that convert incident light into photocharge. However, they differ in that CCDs comprise of a *two*-dimensional array of pixels in which the recorded photocharge may be rapidly and efficiently transferred across the device to a storage region, allowing continuous, rapid acquisition of spectral data throughout a whole experiment. Full readout of the device only occurs when the entire device has been filled with signal and real-time data acquisition has stopped. Consequently, the readout process can take place on a slower timescale than the reaction of interest and the temporal resolution of the experiment is therefore dictated by the rate of charge transfer (typically on the order of microseconds). Data recorded *via* CCD detection in FP experiments are therefore both spectrally *and* temporally resolved, thus optimising the quality and quantity of information obtained from each photolysis experiment.

3.3.2 Principles of CCD Operation and Application to the Flash Photolysis Technique

Whilst laser flash photolysis with time resolved absorption spectroscopy is now a well-established technique, the incorporation of a charge coupled device (CCD) detector – a two dimensional, light sensitive detector array, is unique to this laboratory. The CCD allows rapid real time monitoring of transmitted light intensities simultaneously in *both* temporal and wavelength regimes as shown schematically in Figure 3.4. Crucially, the CCD has the ability to shift rows of photogenerated signal (as charge) rapidly along one axis of the array. Thus by imaging a spectrum of transmitted light intensities perpendicular to this charge transfer axis, charge transfer within the device can be used to record sequential spectra from an illuminated region of the CCD to an optically concealed one. The CCD device itself consists of a grid of linearly coupled metal oxide semiconductor pixels embedded in a silicon substrate. These pixels convert incident light into photocharge which is stored in an electrically generated potential well within the pixel. The quantum efficiency (QE) – the percentage of photons hitting the photoreactive surface that produce an electron-hole pair – peaks at incident wavelengths around 700 nm, with a value at approximately 60 %. At wavelengths below 400 nm the QE is somewhat less and is therefore enhanced by application of a thin phosphor coating (approximately 0.3 μm) which fluoresces at visible wavelengths resulting in an effective QE of about 20 %.[16] The fluorescence lifetime of the coating is of the order of nanoseconds and so does not distort the time resolution of the device. Similarly, cross talk between the pixels is negligible due to the comparatively large pixel size (22.5 μm^2), compared to the thickness of the optical coating. Application of suitably phased voltages to a series of electrodes on the device induces transfer of photocharge from pixel to pixel. These are aligned perpendicular to the axis of transfer of photocharge as shown in Figure 3.4. Charge transfer efficiency is exceedingly high at > 99.9999 % and rates of charge transfer at up to 1 MHz or a 1 μs row-shifting time are readily attained.

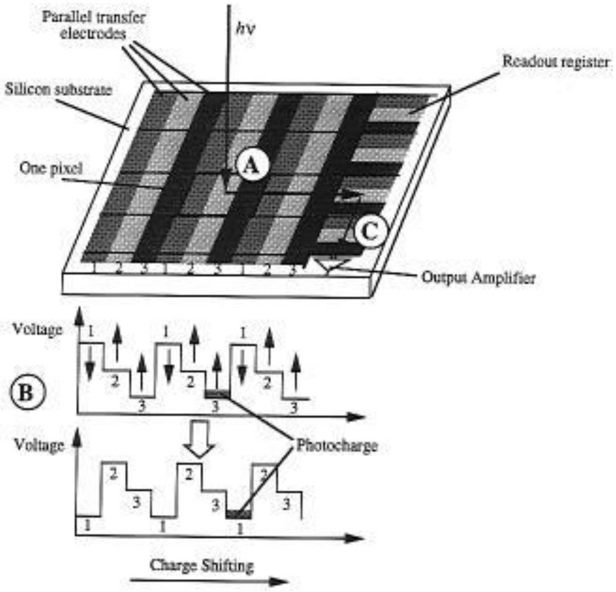

Figure 3.4 *A schematic of a CCD detector demonstrating charge shift throughout the device. (A) incident light is converted to photocharge and stored in a potential well. (B) The electrodes are charged to maintain potential gradient across the device. (C) The photocharge is read out from the device. Taken from Rowley et al.*[16]

There are two major sources of noise associated with CCD detection. The principal source arises from the so called "dark" current formed upon the thermal excitation of charge carriers within the device. This must be recorded for each pixel prior to exposure and subtracted from experimental intensities. However this effect is minimised through Peltier cooling of the CCD and by thermally insulating it in a vacuum enclosure. The other source of noise is photonic noise and is an inherent property of the incident light intensity. Due to the photon flux exhibiting a Poisson distribution, the photonic noise is typically equivalent to the square root of the number of photons detected at each pixel of the CCD. Thus, for a typical full pixel capacity of 2×10^6 photoelectrons, the associated photonic noise is about ± 0.07 %. Of course the effective noise can be reduced through the co-addition and averaging of experiments described and applied below.

A schematic representation of the CCD used in this work is shown below in Figure 3.5. The top few (31) rows of the CCD device are exposed to wavelength resolved light from the spectrograph while the rest of the CCD is optically masked. The CCD affords light to charge conversion within these exposed rows and then charge routines rapidly and efficiently shift the photocharge row by row down the device. This allows transmission spectra of the gas mixture to be continuously acquired until the entire length of the CCD has been traversed by signal. The shift time or “clocking rate” is selected prior to the experiment, hence the clocking axis represents the time resolved axis of the detector. Using CCD detection has the advantage of duplicating the ability of a diode array by recording a range of wavelengths of absorption without compromising the capacity to monitor rapidly and continuously, as with a photomultiplier tube. The result is unequivocal detection of absorbing species as a function of time which is discussed later in this chapter, and evidenced in subsequent chapters.

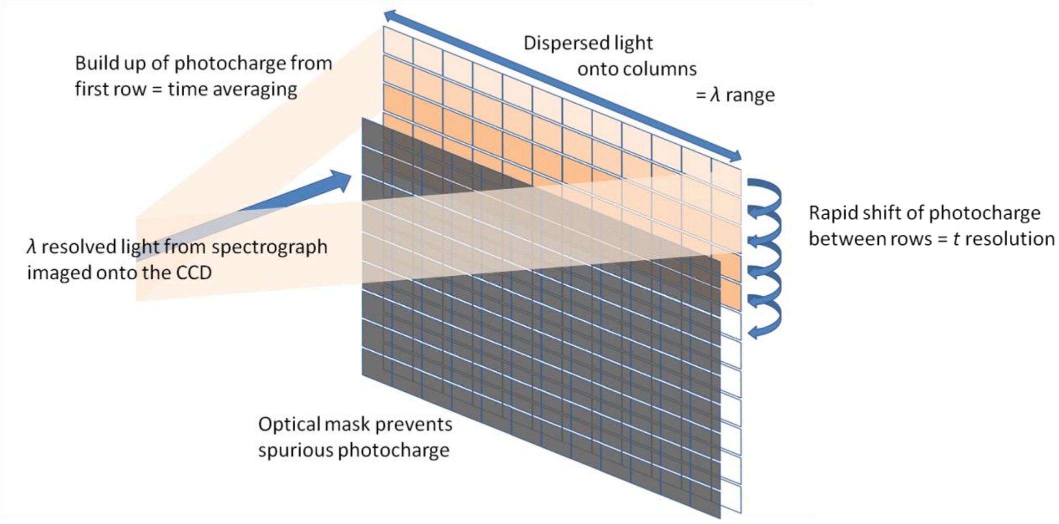

Figure 3.5 *A schematic representation of CCD operation: the top of the detector is illuminated by wavelength resolved light, generating photocharge that is subsequently rapidly transferred down the CCD continuously. Only the top 31 rows are illuminated.*

3.4 Description of the Apparatus

A schematic representation of the apparatus used in this work is shown in Figure 3.6. Described below is a summary of how the different components of the experimental setup used in this work were practically carried out.

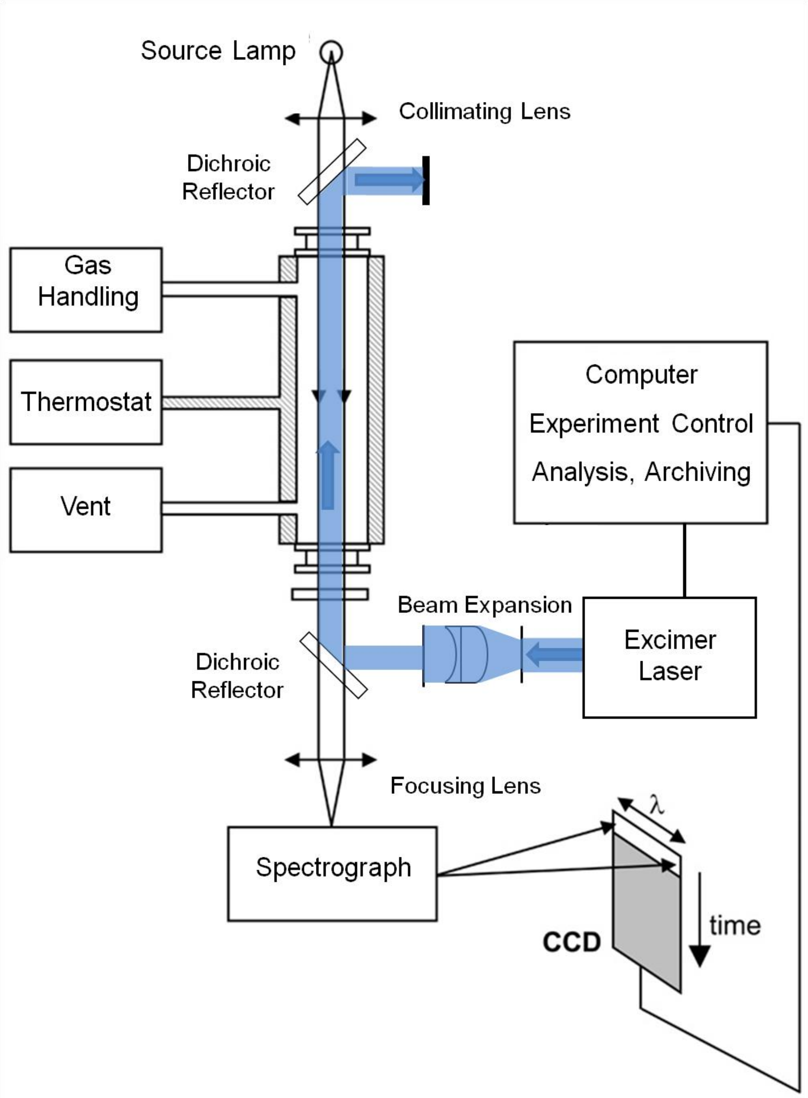

Figure 3.6 *A schematic of the flash photolysis set up employed in this work. Adapted from Bloss et al.*[17]

3.4.1 Gas Handling

Precursor gases were mixed upstream of the reaction vessel, prior to their arrival, in a Pyrex mixing line. Equipped with Teflon valves (Young and Co.), the mixing line consisted of a cylindrical carrier gas vessel punctuated with gas injectors facing against the flow of the carrier gas to augment thorough gas mixing. Non-corrosive gases were routed to the mixing line *via* calibrated mass flow controllers (MKS), regulated by a digital readout controller (MKS). The flow rates of corrosive gases, such as Cl_2, were monitored by flowing them through calibrated glass ball-rotameters (Appendix I). Gases were introduced directly to the mixing line from pure or diluted mixtures as provided and for condensed-phase reagents at ambient conditions, their vapours were entrained by a known flow of an inert gas (typically N_2) which was passed through appropriate bubblers or traps containing the reagent.

The premixed gases were transported to the reaction vessel *via* Teflon tubing. The reaction vessel consisted of a spectrosil quartz tube, 98.2 cm in length with a 1.48 cm internal diameter which was double jacketed with the inner jacket connected to a thermostat unit (Huber CC180). The unit pumped an inert perfluorinated liquid (Galden, HT110) recirculating and regulating its temperature, thus enabling temperature control of the reactor. The outer jacket was evacuated to inhibit condensation onto the reactor walls when operating at low temperatures. Similarly, the windowed end pieces of the reaction cell were double walled and evacuated to impede condensation on the surfaces thus improving optical measurements. The internal temperature of the reactor was checked using a ceramic enclosed Pt-100 resistance thermometer (Farnell) that resided in the gas flow. The temperature of the gases could be controlled to ± 0.5 K over the range T = 206 to 373 K (requiring a change of the thermostat fluid).

Gases were continuously flowed through the reaction vessel at a typical total gas flow rate of 900 SCCM (standard cm^3 per minute). This flow rate was employed to ensure a fresh gas fill approximately every 10 seconds. This ensured that a fresh supply of precursor gas was provided for each laser flash, allowing the experiment to run continuously. The total gas flow took place on timescales much longer than the reactions investigated and so the effect of this flow rate on the elucidated kinetics were negligible. Nonetheless, flow was considered in the analytical procedure when undertaking kinetic analysis. The pressure of the cell was continuously monitored with a capacitance monitor (MKS Baratron).

3.4.2 Radical Generation: Laser *versus* Flashlamp Photolysis

As discussed above, the original, historic, flash photolysis experimental apparatus employed the use of pulsed radiation from flashlamps. Typically these would be xenon filled arc lamps, situated adjacent and parallel to the reaction vessel and powered by a large capacitor (charged to ~ 20 kV). The high voltage causes the spontaneous electrical breakdown in the lamp thereby flashing it and so providing the radiation to induce photodissociation within the reaction vessel. The use of a laser in place of a flashlamp, as in this work, presents a number of advantages. While both sources provide sufficient energy per pulse to initiate photolysis, the timescale in which these packets of energy are delivered differs by orders of magnitude with laser photolysis occurring ~1000 times faster (laser pulse timescale ~ 10 ns). Both flash sources initiate photolysis rapidly enough as to not interfere with the subsequent reaction kinetics but the efficiency of the laser flash also facilitates a more distinct reactant concentration maximum. Therefore a more accurate determination of the initial “time zero” concentrations for reactants can be derived which is important when conducting the kinetic analysis of a decay trace. Another benefit to laser photolysis is the spectral output of the pulse: flashlamps produce broadband spectral output, whereas lasers are monochromatic. Selectivity in the photolysis of the gas mixture both maximises specific reactant yields and minimises the contribution of any flash-initiated secondary reactions that can convolute the primary kinetics. This selectivity is therefore enabled by pre-selecting a suitable wavelength to maximise photodissociation of the principal radical precursor gases. Finally, the quality of the traces obtained by laser photolysis are often superior to those afforded from flashlamp photolysis. This is because generation of the laser pulse typically requires much smaller voltages thereby minimising unavoidable radiofrequency interference which affects the signal to noise ratios. Furthermore, the laser offers a higher pulse repetition rate enabling a greater number of trace co-additions which also improves the average quality of the data and so making the experiment more time efficient.

Radicals of interest were generated directly from photolysis or *via* radical-molecule chemical reactions following the laser UV photolysis of precursor gas mixtures. An excimer laser (Lambda Physik COMPex 201) operating at λ = 351 nm with a Xe/F_2/Ne gas fill was employed, delivering a pulse of energy, typically 110 mJ/pulse within 10 ns. Automated laser operation was afforded *via* the control computer through a fibre optic cable connected to a trigger module (EG&G, TM11A). The beam exiting the laser unit was expanded using a pair of fused silica cylindrical lenses (Exitech Ltd) as to exceed the cross sectional area of the reaction vessel and was then collimated through an iris to match it. A dichroic reflector (Elliot Scientific) directed the beam along the length of the reactor, propagating counter to the beam of the UV-visible light source used for analysis (see Species Monitoring, discussed below), thus illuminating its entire volume. The alignment of the laser and optics was routinely tested using a co-propagated He-Ne laser beam.

A potential negative consequence of the longitudinal alignment of the photolysis beam through the reaction cell is the formation of a non-uniform concentration profile of the reactants along the length of the reaction volume. If the precursor mixture absorbs too strongly at the laser wavelength, most of the photolysing photons will be absorbed in the initial portion of the reaction vessel encountered by the laser beam. This would lead to a significant concentration gradient of photolysis products throughout the reaction cell with a much higher concentration of radicals formed at the optical entrance than the exit due to the attenuation of the laser beam. This longitudinal gradient is non-linear and in turn may give rise to spuriously enhanced observed reaction rates as observed by line-of-sight absorption if it is sufficiently pronounced. Therefore simulations of the optical depth of each precursor mixture employed in this work were routinely carried out to investigate the potential laser attenuation and the consequent distortion of the apparent kinetic parameters was assessed. All experiments were designed as to ensure the optical density of the precursor gas mixture at the laser wavelength suitably low as to keep the longitudinal concentration gradient was at an insignificant level. Again this was accounted for in the analysis.

3.4.3 Species Monitoring

Transient molecules and radicals generated within the reaction vessel were identified and monitored by UV/visible absorption spectroscopy. Spectroscopic measurements were made continuously, both pre- and post-laser flash. A 70 W continuous xenon arc lamp (Hamamatsu L2174) provided the broad band light source for this absorption over a broad wavelength range 200 – 700 nm. The lamp output was collimated along the length of the reactor cell and then focused onto the entrance slit of a spectrograph using a pair of spectrosil quartz lenses. The spectrograph, a 25 cm focal length astigmatic Czerny-Turner spectrograph (Chromex 250IS), subsequently imaged the dispersed light onto the top rows of the CCD detector. The principles of operation of the CCD are described above. The particular CCD employed in this work consisted of a 298 by 1152 array of light sensitive pixels mounted in a Peltier cooled camera head (EEV CCD05-10-0-202, Wright Instruments Ltd). An optical shutter was installed, aligned perpendicular to the longitudinal optical path, as to prevent the accumulation of photocharge on the detector between each experiment. To prevent any potential damage to the detector from back-scattered laser radiation, an optical filter absorbing at the laser wavelength was also placed over the spectrograph entrance slit.

The spectrograph was fitted with three interchangeable diffraction gratings, ruled with 150, 300 and 600 grooves mm^{-1} respectively. When coupled to the detector, these settings gave rise to spectral windows (coverages) of approximately 120, 60 and 30 nm respectively (with a dispersion of approximately 0.45, 0.22 and 0.11 nm/pixel respectively). The resolution of the spectrograph was determined as the full-width half-maximum (FWHM) of the peak of the principal emission line produced by a “pen ray” mercury lamp (Appendix II). Each spectral window was also calibrated from the pen ray lamp using several emission peaks, finding a linear relationship with the gradient giving the dispersion (Appendix I).

3.4.4 Operating Procedure

Operation of the CCD, shutter and laser were controlled by a PC and the course of a typical experiment is given in the flow chart in Figure 3.7 below, summarizing the above.

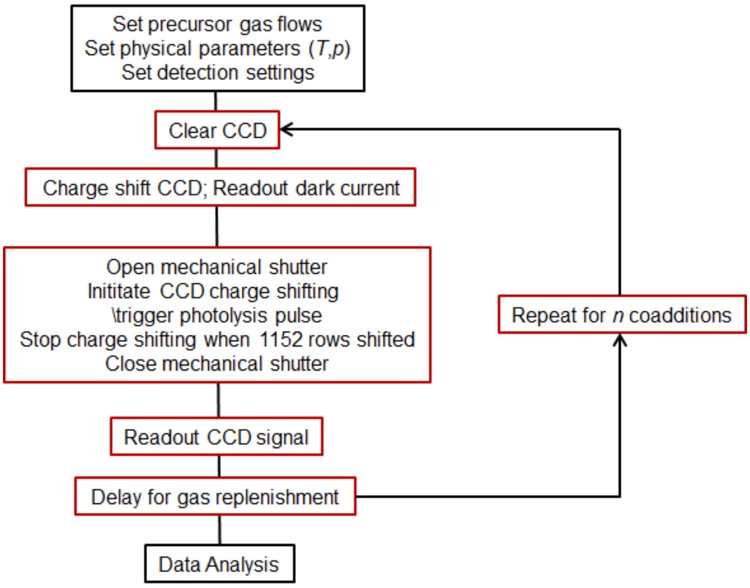

Figure 3.7 *Flowchart describing the operation of a typical flash photolysis experiment.*

To maximise the signal to noise ratio, each experiment typically consisted of the co-addition of a run of several photolysed/background exposures which were then averaged. The repetition rate was dictated by the flow out time of the reactor so that each flash event used fresh gases. Experiments were often carried out in groups of triplets *i.e.* three successive runs in the order of “flashed,” “non-flashed,” “flashed” which was done to account for the build-up of dark current in the CCD in the intervening experiment. The three dimensional data obtained by the CCD was transferred to a separate PC for analysis which is described below.

3.5 Analysis Procedures

3.5.1 Determination of Absorbances

The recorded light intensity at a given wavelength at a given time is related to the absorbance by Beer's Law:

$$A_{t,\lambda} = \ln\left(\frac{I_{0,\lambda}}{I_{t,\lambda}}\right) \tag{3.5 i}$$

Where $I_{0,\lambda}$ is the initial intensity or "pre-flash" light intensity *i.e.* the intensity of transmitted light through the reaction mixture before photolysis and $I_{t,\lambda}$ is the post flash intensity at any given time, *t*, during the experiment. Thus, the absorption spectra recorded exhibited the measured *change* in light intensity of transmitted light through a gas mixture that resulted from laser photolysis. When conducting non-kinetic spectroscopic measurements of the non-flashed gas mixtures, $I_{\mathrm{t},\lambda}$ is simply the transmitted light through the mixture whereas $I_{0,\lambda}$ is the transmitted light intensity through the mixture with the absorber(s) of interest absent. In these circumstances, the time resolution can be made arbitrarily long.

As discussed above, the accumulation of dark current as photocharge traverses the CCD is a potential problem in the kinetic experiments because the charge transfer of each row gives the temporal resolution. Therefore, the extra charge each pixel acquires as it is shifted would be interpreted as an increase in apparent absorbance if unaccounted for thus skewing the kinetic information obtained from the analysis of the time resolved spectra. Non-flashed experiments were therefore carried out intervening the flashed experiments (hence the triplet procedure) so experimental conditions were as close to identical between these runs as possible. Subtracting the non-flashed absorbance from the flashed therefore cancelled any accumulative apparent absorptive contribution resulting from the dark current:

$$A_{t,\lambda} = \ln\left(\frac{I_{0,\lambda}}{I_{t,\lambda}}\right)_{\text{flashed}} - \ln\left(\frac{I_{0,\lambda}}{I_{t,\lambda}}\right)_{\text{non-flashed}} \tag{3.5 ii}$$

Figure 3.8 below shows a time resolved series of sequentially recorded uncalibrated absorption spectra of the ClO radical from Chapter 4 below, demonstrating the three-dimensional nature of the data recorded by the CCD. The recorded uncalibrated absorption spectra of a particular species were wavelength calibrated (Appendix I) and then its concentration determined at each time point, as described below.

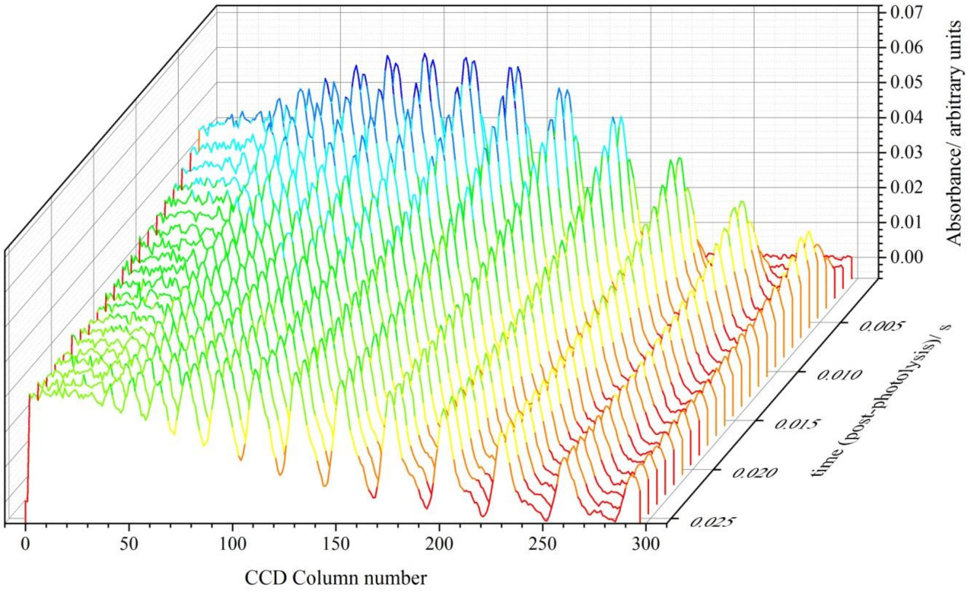

Figure 3.8 *A series of observed experimental absorbance spectra of the post-photolysis decay of the ClO radical as a function of time and wavelength (photolysis at t = 0), from Chapter 4.*

3.5.2 Determination of Species Concentrations

The absorbance of a mixture of gases is related to the contribution from the sum of its components *via* the Beer-Lambert Law:

$$A_{t,\lambda} = \sum_{i}^{[\mathrm{X}]} \sigma_{i,\lambda}[\mathrm{X}]_{i,t} l \qquad (3.5\ \text{iii})$$

Where $A_{t,\lambda}$ is the total absorbance at time t and wavelength λ, $\sigma_{i,\lambda}$ is the absorption cross section of species i at wavelength λ, $[\mathrm{X}]_{i,t}$ is the concentration of i at time t and l is the length of the absorption path. Using equation (3.5 iii), the spectroscopic determination of precursor gas concentrations could be carried out by fitting reference absorption cross sections to the experimental absorption spectra. When measuring the concentration of a single absorber or a mixture of non-spectrally overlapping absorbers simple scaling of a given cross section of that species to absorption spectra was possible. However in cases when absorbers overlapped, multiple cross sections were required, one for each absorbing species contributing to the total absorbance at a given wavelength. These equations were solved simultaneously to derive absolute concentrations of the UV absorbing gases present.

The transient absorbers that were formed *via* photolysis and then monitored in this work had absorption cross sections that typically overlapped with those of their parent gases. This posed potential problems in elucidating accurate concentrations of the radical species generated due to significant differences in the relative concentrations between them and the predominant species in the precursor mixture. As the concentration of the transient and precursor species differed by several orders of magnitude, any uncertainty in the precursor cross sections could be transposed to the derived concentrations of the radicals of interest. However, the halogen monoxides studied in this work possess spectrally structured absorption cross sections characteristic to each species that result from vibronic transitions (Figure 3.8). Since the appearance of these highly structured absorption features post-photolysis were attributed solely to these species, unequivocal monitoring the halogen monoxides was possible.

By applying a ‘differential’ fitting procedure to the temporal absorbance spectra, the technique of which is summarised in Figure 3.9 below, the contribution of any overlapping featureless absorbers was subtracted leaving the sole absorbance of the structured species. To do this, the structured region of both the absorption spectra and the reference cross sections was high pass filtered thus removing the smooth contributions and leaving the differential structure. The smoothing was achieved by the fitting and subsequent subtraction of a polynomial function that replicated the featureless absorptive input to the spectra/cross sections or *via* a sliding average routine. The remaining differential absorbance was then scaled to the differential reference cross sections *via* a least-squares routine resulting in the unequivocal and accurate determination of concentration. Furthermore, spectral subtraction of the "differentially-quantified" structured absorber and further fitting potentially facilitated the subsequent spectral deconvolution and quantification of underlying absorbers.

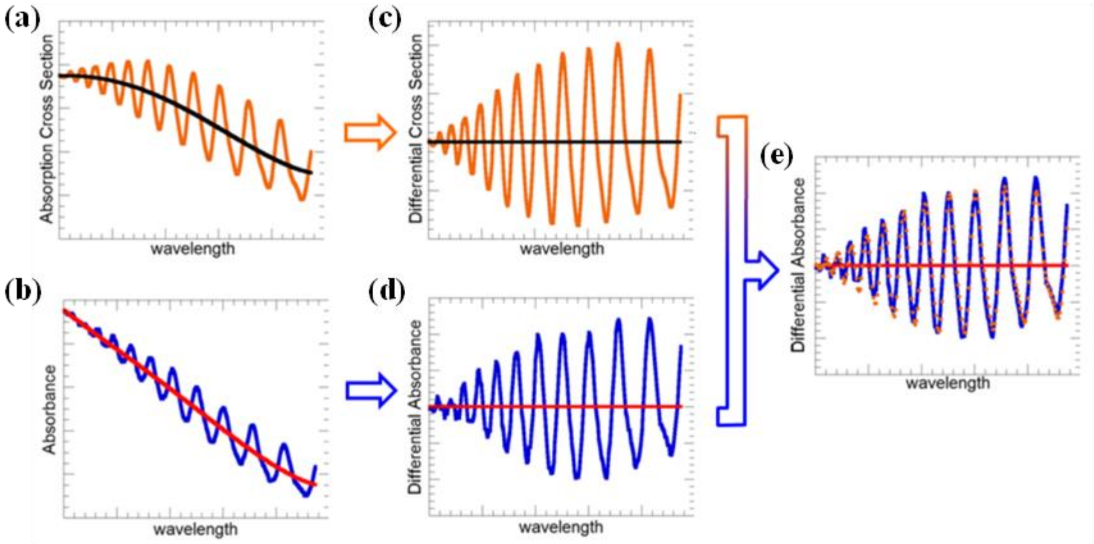

Figure 3.9 *The Principles of differential fitting: the experimentally recorded absorbance spectra and the corresponding reference absorption cross sections are high-pass filtered (panels (a) and (b) respectively) ultimately leaving the 'differential' vibronic structure (panels (c) and (d)). The differential cross sections are then fitted to the differential absorbance (panel (e)), determining species concentration via the Beer-Lambert law. From the PhD Thesis of V. Ferracci.*[18]

Structured spectral features including the vibronic bands of halogen monoxide radicals are strongly dependent on the instrumental spectral resolution. Consequently the resolution of the reference cross sections must also match that of the experimental spectra. When available, reference cross sections of structured absorbers recorded at higher resolutions than those employed in this work were employed and smoothed to ensure that their resolution matched that of the experimental spectra (Appendix II) which is discussed in the relevant subsequent chapters.

Temporal evolution of transient absorbers in the flash photolysis experiment was monitored by applying the chosen fitting routine to each row of data from the CCD and thereby giving rise to concentration *versus* time profiles from which kinetic data could be extracted.

3.5.3 Kinetic Analysis: Extraction of Kinetic Parameters

The experimental kinetic traces (concentrations as a function of time) derived from the procedure described above were fitted to classical kinetic solutions wherever possible. In the occurrence of an insoluble differential equation, as was often the case owing to the complexity of the reaction mechanism due to secondary chemistry, a commercial numerical integration and fitting package FACSIMILE[3] was used. Models for each reaction system studied were built in FACSIMILE with the inclusion of all known reactions occurring in the cell as well as physical processes such as gas flowout. The programme allows the fitting of simulated concentrations to the experimental traces to extract kinetic parameters. In the fitting procedure, simulated concentrations calculated from classical solutions or the FACSIMILE model were fitted to the observed concentrations *via* a least squares routine by varying the rate constants of the reactions of interest and, typically, the initial concentration of the species monitored. Each FACSIMILE model was also used to conduct sensitivity studies to aid experimental design in advance of kinetic experiments.

Sensitivity analyses were also carried out *following* each kinetic study to assess the effects of secondary radical chemistry on the observed kinetic parameters. This method typically involved the analysis of a simulated trace using the FACSIMILE model from which the experimental rate coefficients and parameters were derived. The rate coefficients of secondary reactions were sequentially perturbed (either positively or negatively) by a factor of two and the effect on the derived parameters from re-fitting recorded. Another form of sensitivity analysis assessed the effect of the uncertainties in the concentrations of precursor species and other experimental parameters on the extracted kinetic values. Details of each sensitivity analysis carried out are given in the appropriate results chapters, below.

As discussed previously, the illuminated region of the CCD comprised of 31 rows of pixels, implying that each row of data actually recorded transmitted light intensity for a duration of 31 times the actual charge shift time. Therefore an absorption spectrum resulting from a single output row on the CCD is actually an average of the true absorption spectrum over a period of time, the duration of which is equal to the total exposure of that row of signal to the probe light. Consequently the effect of the simultaneous illumination of these 31 rows results in a slight distortion of the experimental kinetic traces obtained from the Beer-Lambert law. However, by applying a 31-point sliding averaging function to the simulated time dependent concentrations prior to the fitting procedure, this effect is readily accounted for as demonstrated in Figure 3.10 below.

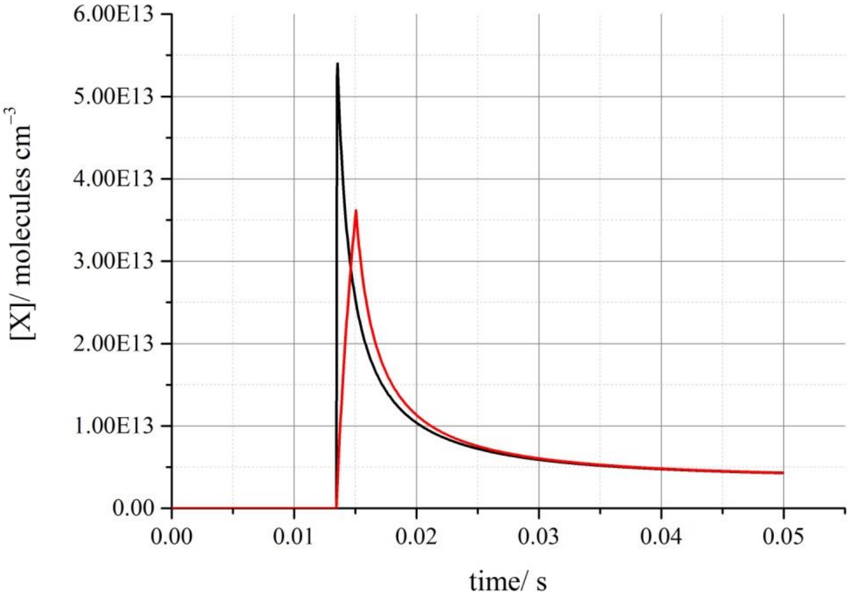

Figure 3.10 *A simulated concentration trace of species X as a function of time (black) and a the same simulated trace but accounting for the temporal distortion through the averaging of the top 31 rows arising from their simultaneous illumination (red).*

Another unavoidable consequence of the experimental set up is the continuous flow of precursors and reactants in/out of the reaction vessel during the timescale of a kinetic experiment. While the effect is largely insignificant due to the timescale of the reactions studied, the gas flow-out was accounted for as a zeroth order decay superimposed on to the temporal behaviour of the species monitored.

3.6 Concluding Remarks

Several approaches to studying the kinetics of short-lived gaseous species have been discussed and compared. In particular, flash photolysis/time resolved UV absorption spectroscopy is a powerful method when applied to such kinetic studies. The novel use of CCD detection included in the experimental setup of this work provides a more accurate determination of kinetic parameters compared to previous UV absorption spectroscopic methods. This is due to the wide range of the spectral and temporal regimes that CCD detection makes possible as is hoped to be evidenced in the following results chapters.

3.7 References

1. Bauer, S.H., Comments on Current Aspects of Chemical Kinetics. *International Journal of Chemical Kinetics*, 1990. **22**(2): 113-133.
2. Doyle, G.J., Design of a Facility (Smog Chamber) for Studying Photochemical Reactions Under Simulated Tropospheric Conditions. *Environmental Science & Technology*, 1970. **4**(11): 907-&.
3. Curtis, A.R., FACSIMILE – Computer-Program for Simulation and Optimization. *Biochemical Society transactions*, 1976. **4**(2): 364-371.
4. Norrish, R.G.W. and G. Porter, Chemical Reactions Produced by Very High Light Intensities. *Nature*, 1949. **164**(4172): 658-658.
5. Wood, R.W., LVIII. The Fluorescence of Sodium Vapour and the Resonance Radiation of Electrons. *Philosophical Magazine Series 6*, 1905. **10**(59): 513-525.
6. Howard, C.J., Kinetic Measurments Using Flow Tubes. *Journal of physical chemistry*, 1979. **83**(1): 3-9.
7. Bonhoeffer, K.F., Chemical luminescence with active hydrogen. *Zeitschrift Fur Physikalische Chemie--Stochiometrie Und Verwandtschaftslehre*, 1925. **116**(5/6): 391-400.
8. Bonhoeffer, K.F., The Conduct of Active Hydrogen. *Zeitschrift Fur Physikalische Chemie--Stochiometrie Und Verwandtschaftslehre*, 1924. **113**(3/4): 199-219.
9. Leather, K.E., A. Bacak, R. Wamsley, A.T. Archibald, A. Husk, D.E. Shallcross, and C.J. Percival, Temperature and Pressure Dependence of the Rate Coefficient

for the Reaction Between ClO and CH_3O_2 in the Gas-Phase. *Physical Chemistry Chemical Physics*, 2012. **14**(10): 3425-3434.

10. Porter, G., Flash Photolysis and Spectroscopy a New Method for the Study of Free Radical Reactions. *Proceedings of the Royal Society of London Series a-Mathematical and Physical Sciences*, 1950. **200**(1061): 284-&.
11. Thrush, B.A., The Genesis of Flash Photolysis. *Photochemical & photobiological sciences*, 2003. **2**(5): 453-454.
12. Porter, G. and F.J. Wright, Studies of Free Radical Reactivity by the Methods of Flash Photolysis – The Photochemical Reaction between Chlorine and Oxygen. *Discussions of the Faraday Society*, 1953(14): 23-&.
13. Commitee, H.P.K.K.E., *Photomultiplier Tubes: Basics and Applications*, ed. I. Word Technical Writing2006: Hamamatsu Photonics K.K. Electron Tube Division.
14. Mauldin, R.L., A. Wahner, and A.R. Ravishankara, Kinetics and Mechanism of the Self-Reaction of the BrO Radical. *Journal of physical chemistry*, 1993. **97**(29): 7585-7596.
15. Li, H., L. van 't Hag, Y.A. Yousef, T.B. Melo, and K.R. Naqvi, Single Shot Laser Flash Photolysis with a Fibre-Coupled Reference Beam Monitor. *Photochemical & photobiological sciences*, 2013. **12**(2): 404-406.
16. Rowley, D.M., M.H. Harwood, R.A. Freshwater, and R.L. Jones, Novel Flash Photolysis UV Absorption System Employing Charge-Coupled Device (CCD) Detection: A Study of the BrO + BrO Reaction at 298 K. *Journal of physical chemistry*, 1996. **100**(8): 3020-3029.
17. Bloss, W.J., D.M. Rowley, R.A. Cox, and R.L. Jones, Rate Coefficient for the BrO + HO_2 Reaction at 298 K. *Physical Chemistry Chemical Physics*, 2002. **4**(15): 3639-3647.
18. Ferracci, V., *Kinetic Studies of Gaseous Halogen Oxide Radical Reactions Implicated in Ozone Depletion*, PhD in *Chemistry* 2012, University College London: London.

Chapter 4: The Kinetics of the ClO + HO_2 Reaction

4.1 Introduction

The work in this chapter concerns the kinetics of the atmospherically relevant reaction:

$$\mathrm{ClO} + \mathrm{HO_2} \rightarrow \text{Products} \qquad (4.1)$$

which is a cross-reaction between the two separate radical reaction families of ClO_x and HO_x discussed in Chapter 1. As discussed in the introduction, stratospheric ozone loss has been reported for several decades and is of environmental concern, directly affecting the solar UV exposure of all ecosystems.[1] In the Polar Springtime when ClO abundances are high, the ClO self-reaction is particularly efficient at driving the formation of photolabile chlorinated species:

$$\mathrm{ClO} + \mathrm{ClO} + \mathrm{M} \rightleftharpoons \mathrm{Cl_2O_2} + \mathrm{M} \qquad (4.2)\ (-4.2)$$

The formation of the ClO ‘dimer’ and its subsequent photolysis is implicated in severe ozone loss events, since the forward reaction (4.2) may become rate-limiting with a rate proportional to the square of [ClO].[2] As was also discussed above, heterogeneous chemistry can drive the formation of active chlorinated species from inactive reservoir species in the dark Polar Wintertime leading to the observed elevated [ClO] upon solar illumination in Spring.

By contrast, at mid-latitudes and in the tropics, where the oscillation between day and night is more regular throughout the year compared to the Poles, stratospheric ozone destruction through pure chlorine chemistry is much less pronounced. This is because the accumulation of HOCl and Cl_2 through *heterogeneous* processes is inhibited and so ClO concentrations remain relatively low. However, ozone loss is observed in middle-latitude regions predominantly near the tropopause, spanning the upper troposphere (UT) and lower stratosphere (LS).

A catalytic ozone loss cycle involving the formation and solar photolysis of HOCl has been recognised as an important mechanism for mid-latitude ozone loss in the upper troposphere/lower stratosphere (UT/LS) region,[3] competing with heterogeneous processes occurring on ice particles, for example, in cirrus clouds:

$$ClO + HO_2 \rightarrow HOCl + O_2 \qquad (4.1a)$$

$$HOCl + h\nu \rightarrow OH + Cl \qquad (4.3)$$

$$Cl + O_3 \rightarrow ClO + O_2 \qquad (4.4)$$

$$OH + O_3 \rightarrow HO_2 + O_2 \qquad (4.5)$$

$$\textit{net:}\ 2O_3 \rightarrow 3O_2$$

The formation of HOCl *via* reaction (4.1a) is significant in not only being the rate determining step in this catalytic cycle (in sunlight) but since this reaction also couples stratospheric chlorine chemistry to tropospheric odd hydrogen (HO_x) chemistry. HO_x is formed in the stratosphere principally by the interaction of excited oxygen atoms, $O(^1D)$, with stratospheric H_2O, which itself is transported there *via* wet tropospheric air mixing with dry stratospheric air or is formed *in situ via* the oxidation of CH_4, the other products of which can also form additional HO_x.[4,5] The mixing of wet tropospheric air is ordinarily expected not to hydrate the stratosphere through the 'cold trap' process in which the water vapour rapidly condenses out of the rising air at the tropopause.[6] However, recent studies suggest that this process may be actually less efficient than previously believed and that there *is* a moistening of the stratosphere through 'geysers' of ice crystals which pass the tropopause and subsequently sublime.[7] This phenomenon is now believed to be common over tropical regions and may be significant in providing stratospheric water, and consequently HO_x, up to altitudes of ~ 20 km.[8]

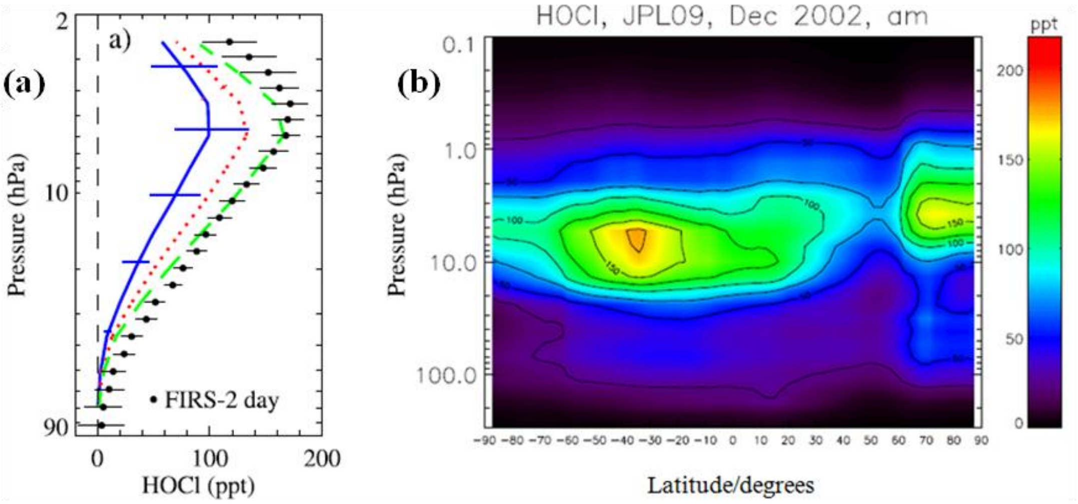

Figure 4.1 *(a) Comparison of the observed (black dots) and simulated mixing ratio of HOCl using different values of* $k_{(4.1)}(T)$ *(blue = JPL NASA 2006 recommendation; red = JPL NASA 2000; green = Stimpfle et al.*[12] *as a function of pressure. (b) Modelled HOCl mixing ratios as a function of pressure and latitude using the 2009 JPL NASA recommendation for* $k_{(4.1)}$*, the current recommendation of which is unchanged.*[11] *Adapted from Kovalenko et al.*[9] *and von Clarmann et al.*[10] *respectively.*

As a consequence of the importance of chlorine oxide chemistry and odd-hydrogen chemistry in the stratosphere, the ClO + HO_2 reaction is of particular interest. A number of studies have accordingly recently highlighted the importance of the ClO + HO_2 reaction by the comparison of atmospheric model predictions with field observations of HOCl.[9,10] Discrepancies between observations and models arising from the differences between the current JPL NASA[11] recommendation for the temperature dependence of the kinetics of reaction (4.1) and the rate constants reported by individual laboratory studies (*e.g.* those of Stimpfle *et al.*[12]) have also been found to have a large impact in the model simulation of HOCl abundances.[9,10] Figure 4.1 (a) shows the discrepancies between modelled HOCl mixing ratios using previous JPL NASA recommendations to field observations at midlatitudes. The values of the JPL NASA recommendation have historically changed in accordance with available data from new laboratory studies. These studies are discussed in detail in the following section but the earliest, the Stimpfle *et al.*[12] study, has so far provided the highest values for the rate constant $k_{(4.1)}$ as a function of temperature which appear to simulate HOCl in accordance with observations.[9] Figure 4.1 (b), however, shows the modelled mixing ratios of HOCl from a simulation, as a function of pressure (*i.e.* altitude) as well as latitude, which applied the most recent JPL NASA recommended evaluation of $k_{(4.1)}$ which is smaller than that reported by Stimpfle *et al.*[12] Comparing the midlatitude region of panel (b) with panel (a) in Figure 4.1, there are clear similarities despite the comparably different values of $k_{(4.1)}$ and furthermore, the von Clarmann *et al.*[10] study shown in panel (b) found that the Stimpfle *et al.*[12] parameterisation leads to an overestimation of measured HOCl.

A recent study by Anderson *et al.*[13] for example, has also highlighted the potential for significant ozone loss over the US in summertime following deep convective injection of water vapour into the stratosphere. In this particular region, where nitrogen oxide abundances are also typically high, the enhanced ozone loss through partitioning of inactive chlorine reservoirs into more active species is somewhat sensitive to heterogeneous (cloud) chemistry. However, in the mid-latitude regions of the lower stratosphere the dominant source of HOCl is believed to be through gas-phase sources, principally reaction (4.1) driven by the availability of ClO.[10] Further, a recent study from von Hobe *et al.*[14] has found evidence for significant heterogeneous chlorine activation in the tropical UT/LS on ice particles in cirrus clouds under both conditions of high and low denitrification. The relative importance of this heterogeneous activity in partitioning inactive chlorine to active species is directly dependent on the rate of the ClO + HO_2 reaction *via* the production of HOCl, as shown in Figure 4.2 below. In order to quantify this in models, knowledge of the kinetics of reaction (4.1) are therefore important in determining abundances of HOCl and the amount to which the HOCl cycle contributes to overall observed ozone losses at mid-latitudes, through a variety of direct and indirect mechanisms delineated above.

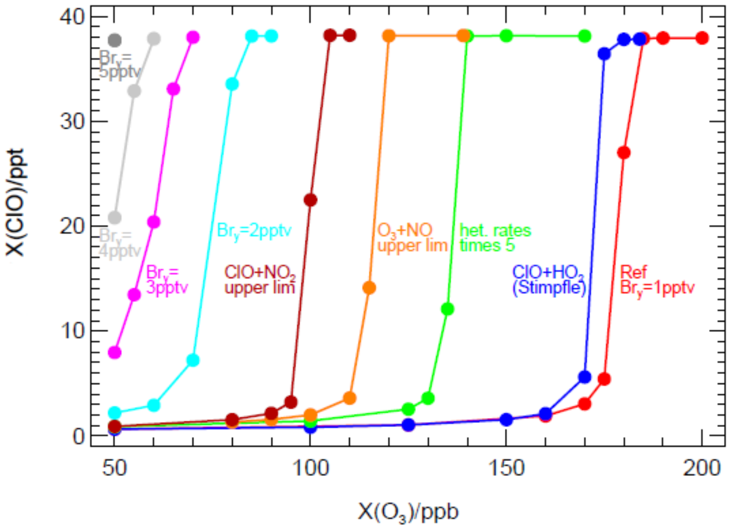

***Figure 4.2** The sensitivity of modelled ClO mixing ratios as a function of O_3 mixing ratios to individual reactions. The step functions are representative of the threshold of $[O_3]$ required for full chlorine activation. The red plot is the reference simulation using the current JPL NASA recommendations for all reactions and each plot is the accumulative change after perturbing the kinetic values of each individual reaction in turn as labelled.*[14]

4.1.1 Previous Studies of the ClO + HO_2 Reaction

4.1.1.1 ClO + HO_2 Kinetics

There are a number of previous laboratory studies of the ClO + HO_2 reaction, reporting ambient temperature rate constants that range between $k_{(4.1)} = (3.8 - 8.26) \times 10^{-12}$ cm^3 $molecule^{-1}$ s^{-1} (Table 4.1). However, when considering the reported uncertainties in these determinations, there is reasonable agreement between the studies with the exception of those of Reimann and Kaufman[15] (discharge-flow/resonance fluorescence over $p = 2 - 3$ Torr at $T = 298$ K), Leck *et al.*[16] (discharge-flow/mass-spectrometry over $p = 2 - 6$ Torr, $T = 298$ K) and Burrows and Cox[17] (molecular modulation/ultraviolet absorption at $p = 760$ Torr, $T = 300$ K). Therefore the current JPL NASA[11] and IUPAC[18] 298 K recommendations, which are based on the average of the ambient temperature data of Hickson *et al.*[19] (discharge-flow resonance-fluorescence at *ca.* $p = 1.5$ Torr, over the temperature range $T = 220 – 336$ K), Nickolaisen *et al.*[20] (flash photolysis/ultraviolet absorption over $p = 50 – 700$ Torr, $T = 203 – 364$ K), Knight *et al.*[21] (discharge-flow/mass-spectrometry over $p = 1.1 – 1.7$ Torr, $T = 215 – 298$ K), and Stimpfle *et al.*[12] (discharge-flow/laser magnetic resonance over $p = 0.8 – 3.4$ Torr, $T = 235 – 393$ K) (JPL NASA[11]) and Stimpfle *et al.*[12], Cattell and Cox[22] (molecular modulation/ultraviolet absorption over $p = 50 – 760$ Torr at $T = 308$ K), Nickolaisen *et al.*[20] and Knight *et al.*[21] (IUPAC) are in agreement. Of the results of the studies summarised in Table 4.1, Cattell and Cox[22] and Nickolaisen *et al.*[20] performed experiments as a function of pressure from $p = 50 – 760$ Torr. Neither of these studies found any significant trend in $k_{(4.1)}$ with pressure implying there is pressure independence in the ClO + HO_2 reaction. Accordingly, when the data are grouped into low pressure studies ($p < 50$ Torr)[12,15,16,21] and high pressure ($p > 50$ Torr)[17,20,22] and averaged, there is no discernible difference when considering the combined uncertainties.

Study	T / K	$k_{(4.1)}$/ cm^3 molecule^{-1} s^{-1}
Reimann and Kaufman[15]	298	$(3.8 \pm 0.7) \times 10^{-12}$
Stimpfle *et al.*[12]	298	$(6.43 \pm 0.96) \times 10^{-12}$
	235 – 393	$3.3 \times 10^{-11} \exp(850/T) +$ $4.5 \times 10^{-12} (T/300)^{-3.7}$
Leck *et al.*[16]	298	$(4.5 \pm 0.9) \times 10^{-12}$
Burrows and Cox[17]	300	$(5.4 \pm 3.0) \times 10^{-12}$
Cattell and Cox[22]	308	$(6.2 \pm 1.5) \times 10^{-12}$
Nickolaisen *et al.*[20]	299	$(7.79 \pm 0.83) \times 10^{-12}$
	203 – 364	$2.84 \times 10^{-12} \exp[(312 \pm 60)/T]$
Knight *et al.*[21]	294	$(7.1 \pm 1.8) \times 10^{-12}$
	215 – 298	$7.1 \times 10^{-12} \exp[-(16 \pm 17)/T]$
Hickson *et al.*[19]	296	$(6.4 \pm 1.6) \times 10^{-12}$
		$1.75 \times 10^{-12} \exp[(368 \pm 78)/T]$
IUPAC[18]	298	$(6.9 \pm 1.6) \times 10^{-12}$
	230 – 300	$2.20 \times 10^{-12} \exp[(340 \pm 350)/T]$
JPL NASA[11]	298	6.9×10^{-12} (error factor = 1.2)
		$1.75 \times 10^{-12} \exp[(290 \pm 78)/T]$

Table 4.1 *Previous studies of* $k_{(4.1)}$ *at ambient temperature and as a function of temperature.*

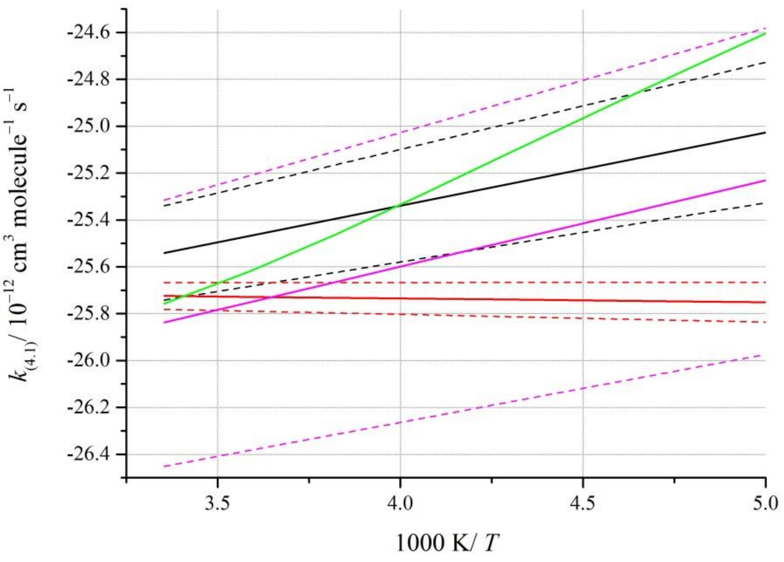

Figure 4.3 *Arrhenius plot of the parameterised determinations of* $k_{(4.1)}$*: Green = Stimpfle et al.;*[12] *Pink = Hickson et al.;*[19] *Black = Nickolaisen et al.;*[20] *Red = Knight et al.*[21] *the dotted lines show the upper and lower limits of each corresponding study.*

The earliest kinetic study of ClO + HO$_2$ by Stimpfle *et al.*[12] found a strong negative temperature dependence and – interestingly – recorded non-Arrhenius behaviour for $k_{(4.1)}$ at sub-ambient temperatures. This was attributed to complex formation involving a third body in the reaction mechanism. However, no other subsequent study of the ClO + HO$_2$ has observed this phenomenon, although the results from the two other studies performed at similarly low pressures may not rule this out. Knight *et al.*[21] do not agree on the sign of the temperature dependence recorded by the Stimpfle *et al.*[12] study, while the relatively large uncertainty associated with the Arrhenius expression obtained by Hickson *et al.*[19] encompasses all of the previously published Arrhenius parameters reported for this reaction. This highlights the appreciably poor agreement between the temperature dependent studies of reaction (4.1) which is illustrated in Figure 4.3. Apart from the findings of Knight *et al.*,[21] it is generally agreed that the ClO + HO$_2$ reaction exhibits a negative temperature dependence, although the extent of this is unclear, *i.e.* the value of (E/R) varies considerably between each study. Consequently, between the four previously reported temperature dependence studies, the temperature dependence ranges from strongly negative (Stimpfle *et al.*[12]), to slightly positive (Knight *et al.*[21]) with Hickson *et al.*[19] and Nickolaisen *et al.*[20] reporting E/R values in between. The values of $k_{(4.1)}$ reported by Nickolaisen *et al*.[20] lie closest to the average of these four studies from which JPL NASA[11] has based their current recommendation.

4.1.1.2 ClO + HO_2 Product Channels

The ClO + HO_2 reaction is radical terminating with two reported channels:[11]

$$ClO + HO_2 \rightarrow HOCl + O_2 \qquad (4.1a)$$

$$\rightarrow HCl + O_3 \qquad (4.1b)$$

Experimentally it is found that reaction (4.1a) is dominant (> 95 %) with reaction (4.1b) contributing to a maximum of < 5 % of the total reaction yield at temperatures below $T = 250$ K[23] and even lower at room temperature (0.3 – 2 %)[16,21,24]. Aside from HOCl, there is no direct evidence for any other product formation from reaction (4.1) between $T = 210 – 300$ K.

These product studies are supported by the extensive computational studies performed of which a detailed review can be found in Hickson *et al.*[19] In general, the computational studies show that the ClO + HO_2 reaction predominantly follows a direct H-abstraction pathway on the triplet potential energy surface through a weakly hydrogen bonded complex, forming HOCl + $^3O_2$ as the sole product at $T = 298$ K. At lower temperatures, complex formation through two possible stable isomers of HO_2OCl through a termolecular process may also occur on the singlet potential energy surface. These excited intermediates are expected to produce HO + ClOO; HCl + $^1O_3$; HOCl + $^1O_2$ and HO + OClO products upon dissociation *via* multistep processes. The findings of the most recent theoretical study, from Zhu *et al.*[25] further support the previous computational work and these authors were also able to estimate rate constants for both the total rate constant and also the relative importance of the direct H-abstraction pathway *versus* the stabilization of the potentially stable HOOOCl intermediate, formation of which might be expected to be strongly pressure dependent. For the total rate constant, there is general agreement from the computational studies with the experimental data of the previous temperature dependent studies albeit given the error bounds of the recommendation for this rate constant as a function of temperature.

Given the importance of the ClO + HO_2 reaction in (particularly) mid-latitude ozone loss and the considerable uncertainty in $k_{(4.1)}$ as a function of temperature, the current work aimed to determine $k_{(4.1)}$ as a function of temperature, using an experimental system uniquely suited to monitoring ClO radicals as demonstrated by, for example, Ferracci and Rowley.[26]

4.2 Experimental

4.2.1 Principles of the Kinetic Approach

The ClO + HO_2 reaction was studied using laser flash photolytic radical generation coupled with time-resolved ultraviolet absorption spectroscopy for radical monitoring, described in detail in Chapter 3. In this work, ultraviolet absorption was monitored using a charge-coupled device (CCD) detector[27] which enabled simultaneous wavelength and rapid time-resolved recording of spectra and the accurate and unambiguous determination of ClO radical concentrations as a function of time using 'differential' spectroscopy. The principle of these experiments was that ClO radicals were principally initially generated from reactions of photolytically generated chlorine atoms. In subsequent experiments, the addition of methanol vapour to the precursor gas mixture led to a competition for these Cl atoms which, in the presence of excess oxygen, thereafter produced HO_2 radicals (which could not be monitored) rapidly and stoichiometrically. The perturbed ClO signal under these conditions, showing a lower initial ClO concentration (attributed to HO_2 production) and a faster decay of the ClO radicals (attributed to the ClO + HO_2 reaction) then exhibited sensitivity to the ClO + HO_2 reaction, which was analysed to extract kinetic parameters.

4.2.2 Radical Formation

Precursor gas mixture concentrations were first designed using numerical integration simulations of the expected immediate post-photolysis chemistry. Gas mixtures were prepared, in a continuous flow of either oxygen or synthetic air, using flows of precursor gases determined by mass flow controllers (MKS). For corrosive chlorine gas (supplied as diluted, 5 % in nitrogen), flows were controlled using a PTFE needle valve and measured using a glass ball flowmeter. For the introduction of methanol vapour, a flow of nitrogen was passed through a bubbler containing liquid methanol held at a known and constant temperature, typically $T = 0$ °C, in an ice/water bath. All flow controllers and meters were routinely calibrated, and the degree of saturation of the methanol vapour flow was determined in separate experiments (and found to be at least 95 % saturated) using cryogenic collection of the methanol vapour and gravimetry, as has been discussed previously.[28] The total flow rate of gases was such that the flowout of species from the reaction vessel during an experiment was negligible on the timescale of the kinetic processes under study, and was in any case accounted for in the analytic procedures.

ClO radicals were generated following laser photolysis of Cl_2/Cl_2O mixtures in an oxygen or synthetic air bath gas flow. Cl_2O was generated *in situ* using the method initially described by Hinshelwood and Pritchard:[29] a known flow of Cl_2 was passed through a trap containing dried mercuric (II) oxide.

$$2Cl_2(g) + HgO(s) \rightarrow Cl_2O(g) + HgCl_2(s) \qquad (4.6)$$

The principal source of ClO radicals resulted from the photolysis of molecular chlorine and the subsequent reaction of Cl atoms with an excess of dichlorine monoxide, Cl_2O:

$$Cl_2 + h\nu \rightarrow 2Cl \qquad (4.7)$$

$$Cl + Cl_2O \rightarrow Cl_2 + ClO \qquad (4.8)$$

Direct photolysis of Cl_2O also contributed a minor source of ClO, given the smaller cross section of Cl_2O compared to Cl_2 at the 351 nm photolysis laser wavelength (σ_{Cl_2} (351 nm) = 1.8×10^{-19} cm^2 molecule^{-1}, σ_{Cl_2O}(351 nm) = 7.0×10^{-21} cm^2 molecule^{-1}).[11] A T-junction was placed upstream of the HgO trap in order to partially bypass it and a needle valve allowed the control of the amount of Cl_2 passed through the trap in order to optimise the initial ClO concentration.

For the generation of HO_2, chlorine atoms were reacted (competitively) with an excess of methanol vapour, in the presence of a large excess of molecular oxygen:

$$Cl + CH_3OH \rightarrow HCl + CH_2OH \tag{4.9}$$

$$CH_2OH + O_2 \rightarrow HCHO + HO_2 \tag{4.10}$$

Typical precursor concentrations were: [Cl_2] = 2.5 – 5.0 × 10^{16} molecules cm^{-3}; [Cl_2O] = 1.5 – 5.0 × 10^{15} molecules cm^{-3} (measured spectroscopically, see appendices I and III); [CH_3OH] = 0.4 – 1.1 × 10^{16} molecules cm^{-3} with the carrier gas balanced to 1 atm. These concentrations were such that photolytically generated Cl atoms were always rapidly (on the timescale of subsequent chemistry) and stoichiometrically consumed to produce either ClO or HO_2 radicals. Typical initial (immediately post-photolysis) radical concentrations were in the range (1 – 2) × 10^{14} molecules cm^{-3}.

4.2.3 Radical Monitoring

The radical species generated in the reaction vessel were monitored using UV spectroscopy as also described in Chapter 3. Figure 4.4 shows the absorption cross sections of the main absorbers present in the experimental post-photolysis gas mixtures. As it can be seen, the strongest HO_2 absorption is separated by around 70 nm from the fingerprint ClO vibronic absorption. This makes the simultaneous spectroscopic measurement of both ClO and HO_2 species impossible due to the unavoidable decrease in resolution of the recorded ClO spectra if such a wide spectral window were adopted. Furthermore, the absorptions of other species present overlap with the HO_2 cross section making deconvolution of the experimental absorption spectra problematic. Therefore the monitoring of ClO was prioritised over HO_2, the concentration of which was determined indirectly as discussed below.

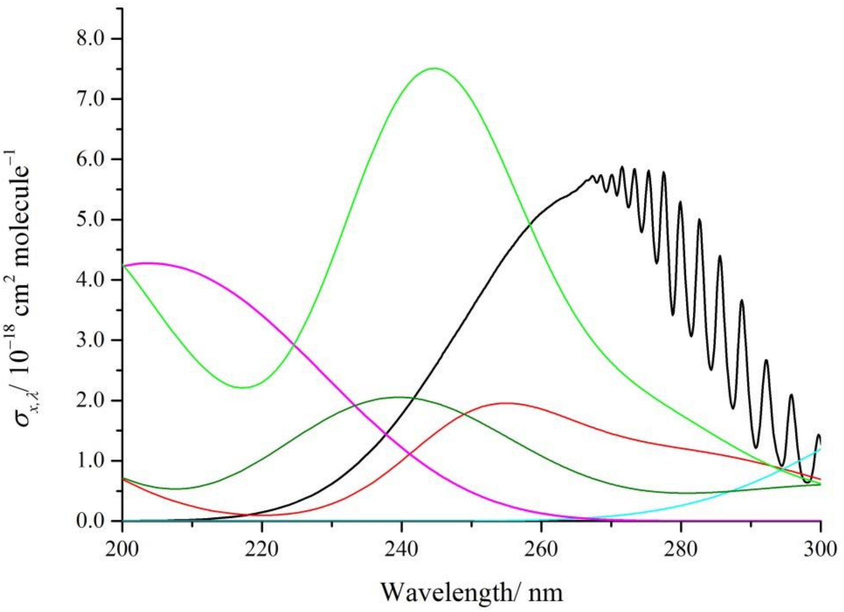

Figure 4.4 *Absorption cross sections of the key absorbing species, σ_x, of the photolysed $Cl_2/Cl_2O/CH_3OH/O_2$ system: Black = ClO; Pink = HO_2; Light green = Cl_2O_2; Red = Cl_2O; Light blue = Cl_2 × 10; Green = HOCl × 10. Taken from JPL NASA.*[11]

Following exploratory experiments, the spectrograph was set with a diffraction grating of 600 grooves/mm and an entrance slit width of 112 μm. The spectra were consequently recorded over a wavelength range of 262.9 – 296.2 nm at a spectral resolution of 0.8 nm full width half-maximum (FWHM). Wavelength calibration and spectral resolution were verified in separate experiments, by Gaussian fitting the measured peaks of the emission spectrum of a mercury ‘pen-ray’ lamp (Appendix II). Experiments were performed recording typically 1000 time resolved spectra before, during and after laser photolysis over a total timescale of 15 – 100 μs/spectrum. Typically, 15 – 20 photolysis experiments were conducted and the results co-added for each determination of $k_{(4.1)}$ and at least six determinations were conducted at each experimental temperature.

The data recorded by the CCD consisted of a matrix of 1152 (rows) × 298 (columns) of signal representing transmitted intensity through the reaction vessel. Each row of data therefore corresponded to a transmission spectrum at a particular time and each column to a time resolved transmission at a particular wavelength. Recorded transmissions were converted into wavelength and time resolved absorbances relative to the pre-photolysis transmitted intensities using Beer's Law as described in Chapter 3. The recorded absorbances therefore represent *changes* in absorption brought about by laser photolysis and subsequent gas phase chemistry.

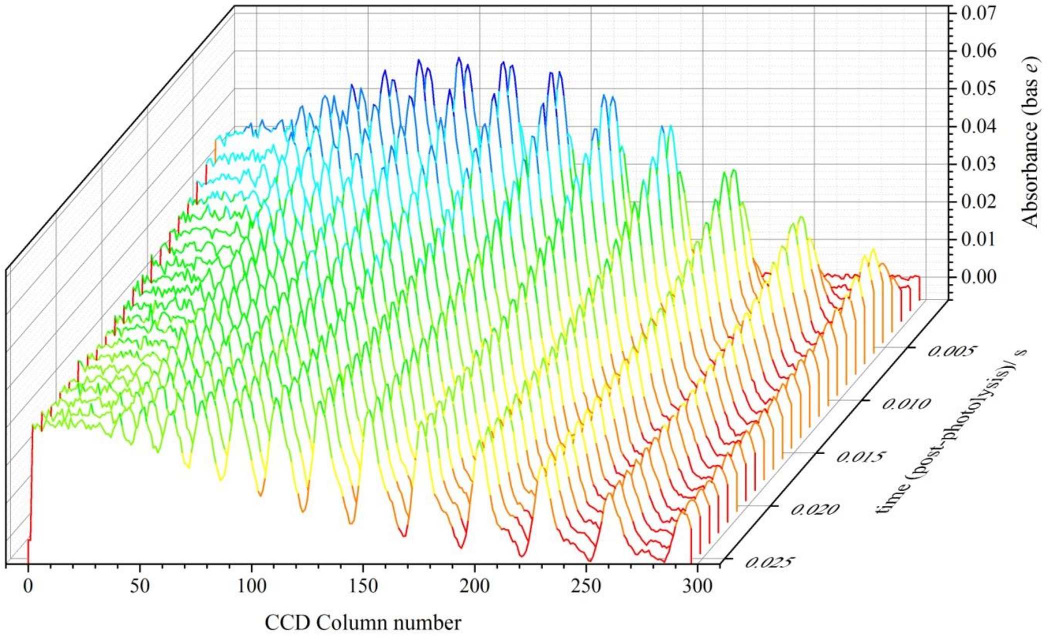

Figure 4.5 *Sequential (uncalibrated) post-laser flash absorption spectra obtained from experimental pre-flash and post-flash intensities recorded by the CCD (CCD column number* $\propto$ *wavelength).*

Figure 4.5 shows a series of typical post-flash (uncalibrated) absorption spectra (each recorded over an average of 1 ms), from a run of 15 $Cl_2/Cl_2O_2/O_2$ photolysis experiments under methanol free conditions. Evident is a rapid increase followed by a subsequent decay in the absorption signal which is spectrally characteristic of the ClO radical. The absorption spectra were subsequently calibrated, enabling the determination of time resolved ClO concentrations using 'differential' spectroscopy as described in the following section.

4.2.4 Determination of ClO Concentrations

The concentration of the ultraviolet absorbing species in the reaction vessel is directly related to their absorbance by the Beer-Lambert law as discussed in Chapter 3. Therefore knowledge of the ClO absorption cross section in accurately determining ClO concentrations is vital. In particular, in the spectral region in which ClO exhibits vibronic transitions the structure of the ClO cross section is both temperature and instrumental resolution dependent.

In the present work, over the wavelength range monitored, several UV absorbing species, including precursor gases, radicals and reaction products were present. For many of these species, the UV absorption spectra are spectrally structureless, and whilst in principle their contributions to the total absorption could be deconvoluted, in practice the similarities in the spectra precluded this. By contrast, ClO radicals exhibit distinctive spectral structure attributed to the ($A^2\Pi \leftarrow X^2\Pi$) vibronic transition.[11] This structure was exploited to determine ClO concentrations using ‘differential’ spectroscopy. Briefly, in this procedure the recorded absorption spectrum exhibiting the ClO spectral structure is high-pass filtered. A suitable reference spectrum of ClO is then analogously filtered and the filtered spectrum fitted to the experimental spectrum, minimising the sum of squares of residuals to determine the ClO species concentration using the Beer-Lambert law as described in detail previously in Chapter 3. In this way, the ClO concentration as a function of time could be accurately and unequivocally extracted from the time resolved spectra recorded on the CCD, despite the presence of many other absorbing species in the spectral window studied. Critical to this spectral fitting is that the instrumental resolution adopted is identical to that at which the structured ClO absorption cross sections are available, since the ClO cross sections are a strong function of instrumental resolution. In this work, a spectral resolution of 0.8 nm FWHM was chosen. This resolution is identical to that employed by Ferracci *et al.*[26] and Boakes *et al.*[30] from which the extensively studied ClO absorption cross sections, and their temperature dependence were taken. Furthermore, these studies employed near identical conditions on the same apparatus used in this study to investigate the kinetics and thermochemistry of reactions (4.2) and (−4.2). The temperature dependent ‘differential’ absorption cross sections for the representative (12 – 0) vibronic band of ClO, corresponding to the difference between the peak at λ = 275.2 nm minus the accompanying trough at λ = 276.4 nm were given by:[26]

$$\sigma_{ClO\ diff} / \mathrm{cm^2\ molecule^{-1}} = (1.07 \pm 0.33) \times 10^{-17} - \{(2.46 \pm 1.1) \times 10^{-20}.(T/\mathrm{K})\} \qquad (4.2\ \mathrm{i})$$

Whilst these two wavelengths were selected to quantify the ClO differential absorbance, it should be emphasised that the entire spectrum of each experiment was calibrated using the above expression. Subsequently the following expression was applied to each recorded absorption spectrum:

$$\sigma_{\mathrm{ClO}} = A_\lambda \times \frac{\sigma_{\mathrm{ClO\ diff\ (12,0)}}}{A_{\mathrm{diff\ (12,0)}}} \qquad (4.2\ \mathrm{ii})$$

A fully calibrated ClO spectrum was therefore generated for analysis of every experimental spectrum obtained at each temperature. A spectrum recorded over the entire spectral range (*ca.* 260 – 296 nm) was recorded at *each* time point and that the spectral fitting adopted the whole range in determining $[\mathrm{ClO}]_t$, the analysis of which is described in the following section.

4.3 Results and Kinetic Analysis

4.3.1 Temporal Profiles of [ClO] Recorded in the Absence and Presence of CH_3OH

A typical time-averaged post-photolysis (relative to pre-photolysis) absorption spectrum recorded from a Cl_2/Cl_2O/ carrier gas mixture is shown in Figure 4.6. The distinctive spectral structure of ClO is apparent, which was confirmed by the fit of calibrated reference differential absorption cross sections to the experimental absorption spectra. Also shown in Figure 4.6 is the analogous spectrum recorded under identical conditions except for the inclusion of methanol vapour ($[CH_3OH]$ = 1.1×10^{16} molecules $\mathrm{cm^{-3}}$) showing a clear reduction in the average ClO absorbance.

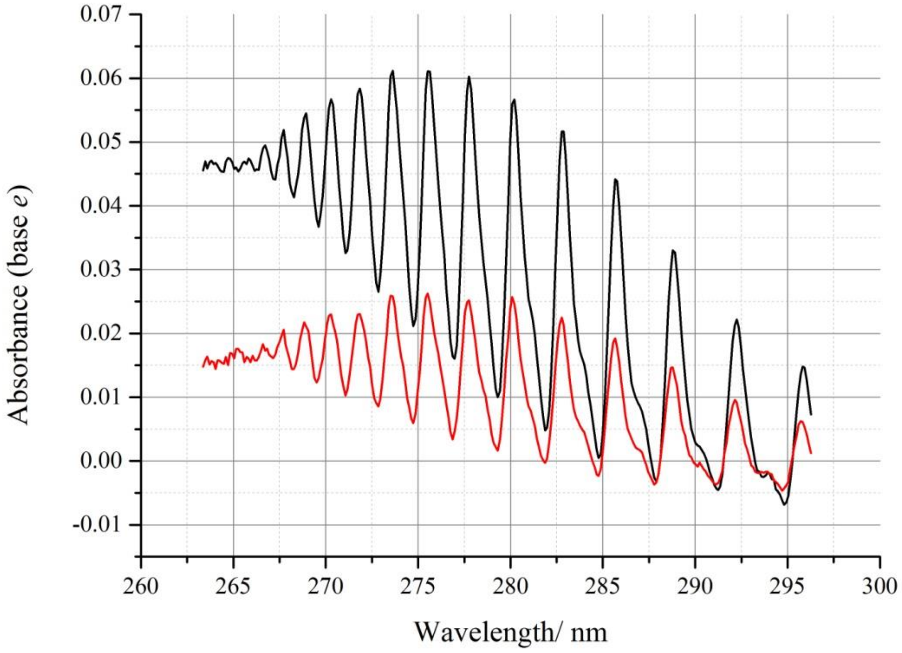

Figure 4.6 *The measured time averaged post-photolysis absorbance of ClO recorded under methanol free conditions (black) and with [CH_3OH] = 1.1×10^{16} molecules cm^{-3} (red) at T = 298 K.*

Two temporal profiles of ClO radical concentration, obtained from the differential fitting of each time resolved absorption spectrum sequentially recorded throughout a given experiment and both recorded in the absence of methanol, are given in Figure 4.7 (a). Also shown is a temporal profile of ClO recorded in the presence of methanol, which was obtained in an experiment carried out intervening those without CH_3OH present, under otherwise identical conditions. This clearly shows that the ClO concentration is reduced in the presence of methanol, but then recovers almost exactly to its original level once the source of methanol has been removed. Figure 4.7 (a) also shows kinetic fits to the ClO traces recorded in the absence of methanol. These fits were based solely upon the analytical solution to a two-reaction model involving the termolecular association of ClO radicals (4.2) and the thermal decomposition of Cl_2O_2 (−4.2).[30] The fitting optimised the initial concentration of ClO, but also accounted for a temporal averaging inherent to the illumination of multiple rows on the CCD detector, described in Chapter 3.[26] The forward reaction rate constants $k_{(4.2)}$ and $k_{(-4.2)}$ were also optimised.

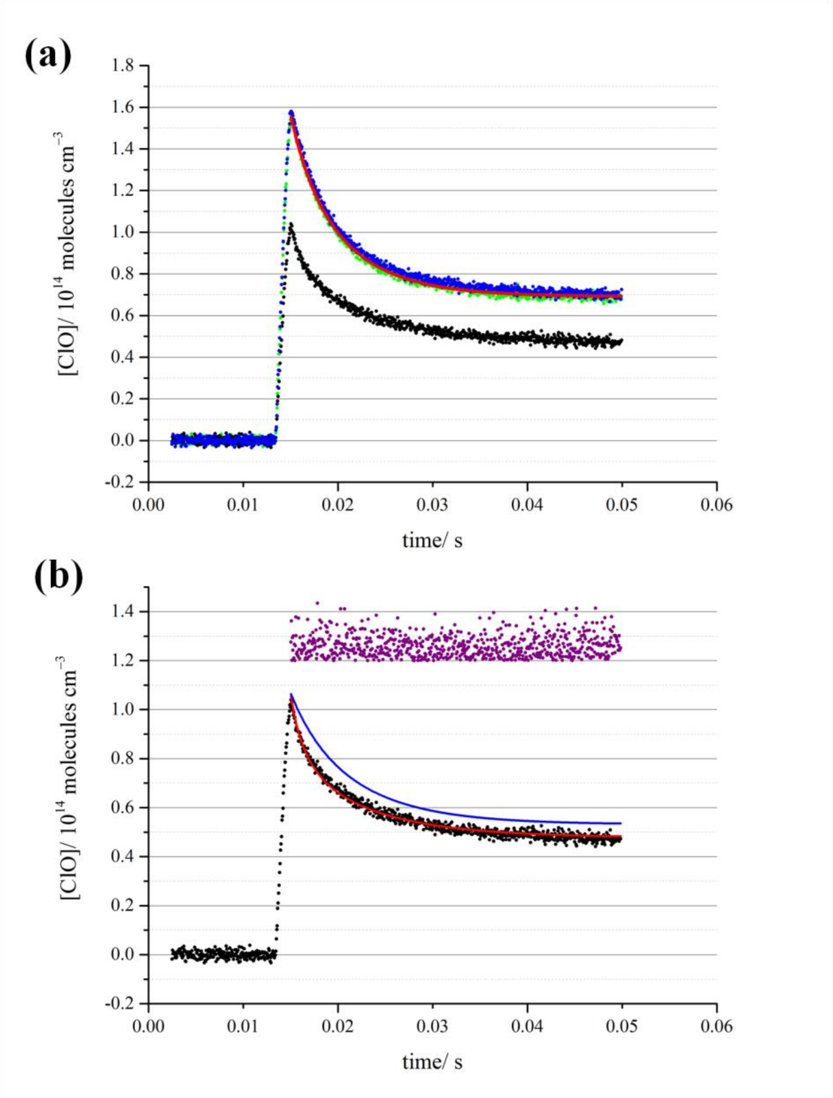

Figure 4.7 *(a) Three separate kinetic experiments showing* $[ClO]_t$ *traces before addition of* CH_3OH *to the system (green), with* CH_3OH *in the system (black) and with* CH_3OH *subsequently removed from the system (blue) with a simulated trace from an optimised model of a ClO dimerisation-only mechanism (red). (b) A [ClO] temporal trace (black) where* $[CH_3OH] = 7.2 \times 10^{15}$ *molecules* cm^{-3} *recorded at* $T = 298$ *K with a simulated trace from an optimised model including ClO +* HO_2 *chemistry (red) and a simulated* $[ClO]_t$ *trace from a ClO dimerisation-only mechanism using the same* $[ClO]_{max}$ *(blue). The offset residuals × 5 are shown above (purple).*

The values of $k_{(4.2)}$ and $k_{(-4.2)}$ derived from these particular fits to the individual experiments were (4.35 ± 0.05) × 10^{-13} cm^3 molecule^{-1} s^{-1} and (40.4 ± 0.44) s^{-1} respectively (initial experiment) and (4.27 ± 0.05) × 10^{-13} cm^3 molecule^{-1} s^{-1} and (40.1 ± 0.44) s^{-1} respectively (post-methanol experiment) at T = 298 K, p = 760 Torr (*i.e.* at a total number density of ~ 2.40 × 10^{19} molecules cm^{-3}). Similarly, the initial ClO concentrations derived from these fits lay within ~ 3 % of each other. Temporal traces of ClO were obtained for each photolysis experiment performed at a given temperature. The traces typically showed the same general behaviour as above which was dependent on the [CH$_3$OH] present. For each temporal trace of [ClO] with zero methanol, $k_{(4.2)}$ and $k_{(-4.2)}$ were obtained as outlined above. The ensemble of kinetic parameters recorded in the absence of methanol vapour are reported below in Table 4.2 and are comparable with results of previous studies investigating the kinetics of $k_{(4.2)}$ and $k_{(-4.2)}$.[26,30]

T / K	$[\text{ClO}]_0{}^a$ / 10^{14}	$k_{(4.2)}{}^b$ / 10^{-13}	$k_{(-4.2)}{}^c$
298.15	1.59 – 2.02	(3.89 ± 0.21)	39.98 ± 0.83
278.65	1.70 – 2.18	(5.97 ± 0.09)	6.39 ± 0.37
261.55	2.08 – 2.94	(6.62 ± 0.22)	0.54 ± 0.25
246.45	1.71 – 2.61	(8.63 ± 1.13)	0.16 ± 0.06
232.95	1.63 – 2.20	(10.2 ± 0.23)	0.08 ± 0.15
210.05	1.50 – 2.25	(12.2 ± 0.16)	0.00

[a]*units of molecules cm*$^{-3}$, [b]*units of cm*^{3} *molecule*$^{-1}$ *s*$^{-1}$, [c]*units of s*$^{-1}$

***Table 4.2** Kinetic parameters recorded for reversible ClO association in the absence of methanol, before and after introduction of methanol. Errors are 1σ statistical only.*

Given the robustness of the results of the ClO self-reaction kinetics derived from the methanol free experiments, shown in Figure 4.7 (a), a simulation of a [ClO] temporal profile was made from a model that incorporated the same derived parameters of $k_{(4.2)}$ and $k_{(-4.2)}$ but was re-optimised with a lower maximum [ClO] to match the intermediary experiment recorded in the presence of methanol and is shown in Figure 4.7 (b) above. Clearly, the observed kinetics of ClO decay are not reproduced by a ClO reversible dimerisation only scheme. Further, even allowing $k_{(4.2)}$ and $k_{(-4.2)}$ to subsequently vary within the model to optimise the fit could not reproduce the form of the observed ClO temporal behaviour, and in any case led to rate coefficients for ClO association which gave significantly enhanced kinetic values for the forward dimerisation reaction rate constant $k_{(4.2)}$, incompatible with any known third body enhancement for ClO association which may have resulted from the presence of methanol.

As a consequence of this evident enhancement in ClO decay upon addition of methanol, a series of analogous experiments were therefore carried out monitoring ClO in the absence of methanol, and then with methanol present but now over a *range* of methanol concentrations (between (0.41 – 1.13) × 10^{16} molecules cm^{-3}). After each addition of methanol, an experiment was performed in which the methanol vapour trap was bypassed to revert to pure Cl_2/Cl_2O photolysis. A selection of the resulting ClO temporal traces is presented in Figure 4.8. The maximum [ClO] concentrations, $[ClO]_{max}$, recorded in these experiments are presented in Table 4.3, confirming the systematic dependence of the maximum ClO concentration as a function of the added methanol concentration.

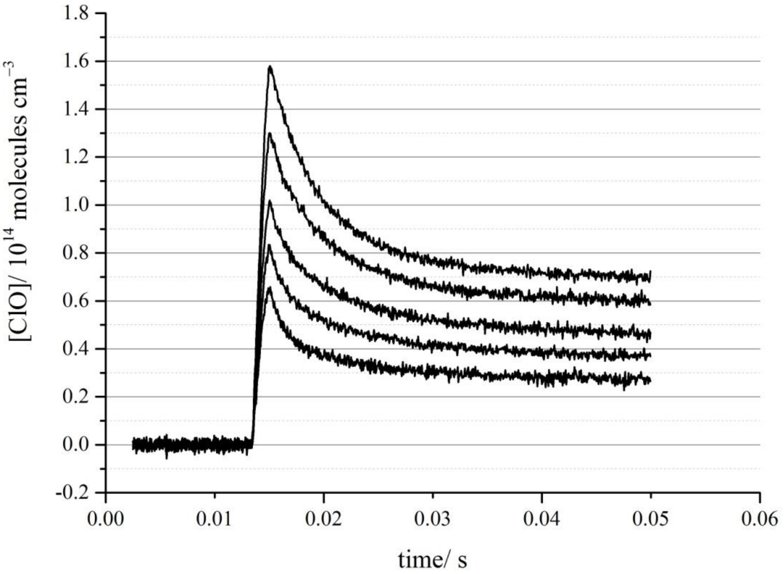

Figure 4.8 *[ClO] temporal traces showing the effect of added [CH_3OH] on $[ClO]_{max}$. $[ClO]_{max}$ decreases with increasing [CH_3OH], whereas the rate of loss of ClO increases. Starting with the largest $[ClO]_{max}$, the [CH_3OH]/ 10^{16} molecules cm^{-3} present for each trace (top to bottom) was: 0.41; 0.57; 0.72; 0.88; and 1.13.*

$[CH_3OH]^a$	$[ClO]_{max}{}^a$	$-\left(\frac{d[ClO]}{dt}\right)_{0,exp}^{b}$	$-\left(\frac{d[ClO]}{dt}\right)_{0,\text{"ClO only"}}^{b}$
4.11×10^{15}	1.58×10^{14}	1.72×10^{16}	1.67×10^{16}
5.67×10^{15}	1.30×10^{14}	1.48×10^{16}	1.17×10^{16}
7.23×10^{15}	1.05×10^{14}	1.30×10^{16}	7.87×10^{15}
8.79×10^{15}	8.08×10^{13}	1.17×10^{16}	4.78×10^{15}
7.23×10^{15}	9.44×10^{13}	1.19×10^{16}	6.42×10^{15}
1.03×10^{16}	7.17×10^{13}	1.13×10^{16}	3.79×10^{15}
1.13×10^{16}	6.52×10^{13}	1.14×10^{16}	3.16×10^{15}

[a]Units of molecules cm^{-3}, [b]units of cm^{3} molecule^{-1} s^{-1}

Table 4.3 *The experimental maximum ClO radical concentration and the initial rates of change of ClO concentration recorded as a function of methanol vapour concentration at T = 298 K. In addition, the simulated initial rates of change of ClO concentration in the absence of methanol, "ClO only," using the same maximum ClO concentration as found in the experiments. Errors have been omitted for clarity.*

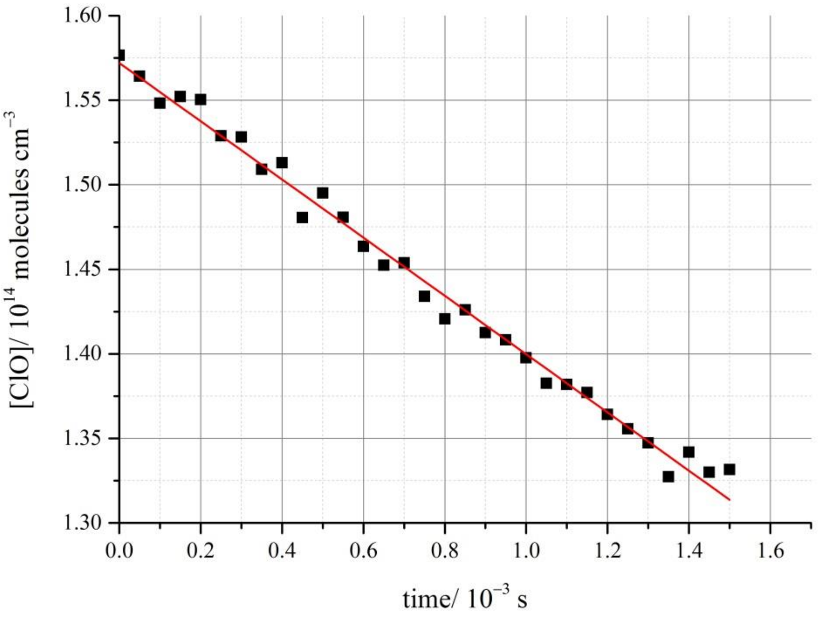

Figure 4.9 *An example of the initial decay of [ClO] (black squares) and a linear fit to the data (red).*

In addition to the direct recording of initial post-photolysis $[ClO]_{max}$, Figure 4.9 above shows that over a short timescale (compared to the overall decay), the initial decay of ClO is approximately linear and can be fit to determine not only the maximum post-photolysis [ClO] but also the initial loss rate of ClO radicals, $-\left(\frac{d[\mathrm{ClO}]}{dt}\right)_{0,\mathrm{exp}}$.

These initial rates of loss of ClO radicals were calculated for ClO temporal traces such as those shown in Figure 4.9. These data are also presented in Table 4.3 and shown graphically, as a function of the initial (maximum) ClO concentration in Figure 4.10 below. Also shown in Figure 4.10 are simulated initial rates of ClO decay calculated under methanol free conditions at the same initial concentrations of ClO as was recorded in the experiments carried out with methanol. The parameters for these simulations were taken from the kinetic experiments carried out before and after the inclusion of methanol, which, as discussed above, exhibited excellent reproducibility. These initial rates of equivalent initial ClO concentrations, in the presence and absence of methanol, clearly show that the loss rate of ClO is enhanced in the presence of methanol despite the lower initial concentrations of ClO that are recorded when methanol is present, indicating the operation of an additional ClO loss channel.

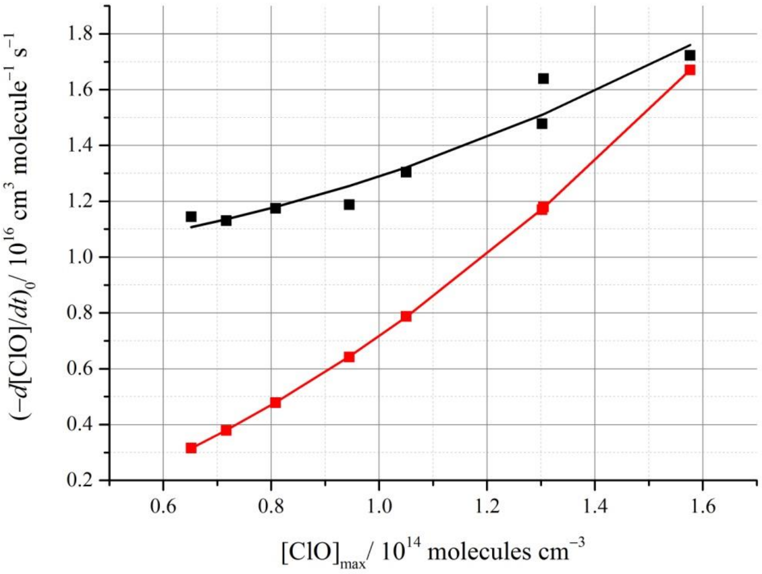

__Figure 4.10__ A plot of the initial rate of change in $[ClO]_t$ with the corresponding experimental $[ClO]_{max}$ for: experimental $[ClO]_t$ (black); and simulated $[ClO]_t$ (red), modelled on the basis of ClO dimerisation-only kinetics.

The inference from the analysis of the ClO temporal traces recorded in the presence of methanol, and supported by numerical modelling, is that the reduction in $[ClO]_{max}$ is due to competitive loss of chlorine atoms with methanol (reaction (4.9)). This is supported by Figure 4.11 below, showing the decrease in the experimental $[ClO]_{max}$ as a function of increasing methanol concentration which is attributed to the competition of Cl between Cl_2O and CH_3OH. What is more, the presence of a large excess of oxygen as applied to these experiments is expected to produce HO_2 radicals from CH_2OH radicals formed in reaction (4.9) stoichiometrically through reaction (4.10), as a direct result of this competitive chemistry. The ClO traces recorded in the presence of methanol were therefore analysed using a variety of assumptions, discussed below.

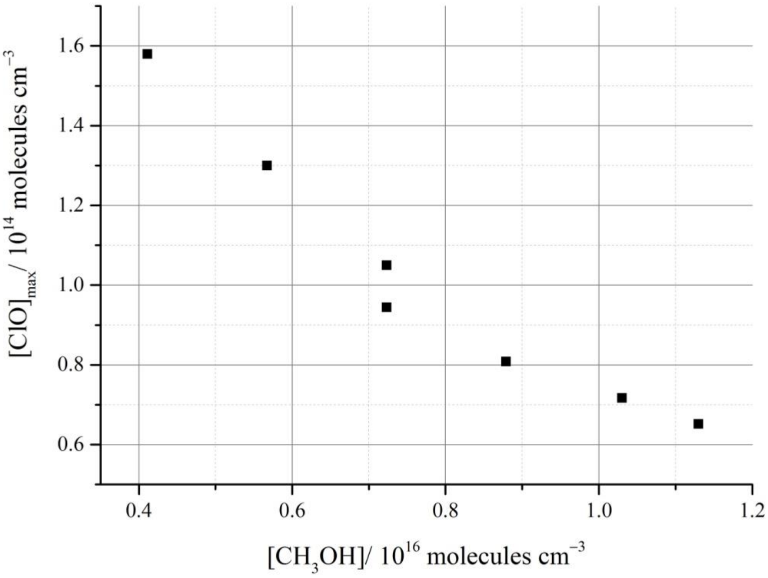

Figure 4.11 *Experimental maximum ClO concentrations as a function of methanol concentration, from the data in Table 4.3.*

4.3.2 Analysis of the $[ClO]_t$ Profiles Recorded in the Presence of CH_3OH: Part 1

Most simplistically, the reduction in the initial post-photolysis ClO concentration upon the addition of methanol to the $Cl_2/Cl_2O/O_2$ system could be assigned to a rapid and stoichiometric production (from Cl atoms, *via* reactions (4.9) and (4.10)) of HO_2 radicals. Thus, for analysis of these temporal traces, the total radical concentration (as determined under CH_3OH free conditions), $[TR]_0$, was initially fixed in the numerical model, the initial ClO concentration, $[ClO]_0$, re-optimised to fit to that of the observed ClO trace and the initial HO_2 concentration, $[HO_2]_0$, therefore effectively stipulated in the model as being the difference between the two. An additional (terminating) reaction, that of ClO + HO_2, was incorporated into this model, and its rate constant optimised. An example of the resulting fits from this analysis at $T = 298$ K is shown in Figure 4.7 (b). A consistent ClO + HO_2 rate constant was obtained from this analysis except at the highest methanol concentrations used when HO_2 is in excess over ClO. This result is unsurprising, since this analysis does not account for the known self-reaction of HO_2 radicals which will become increasingly significant as $[HO_2]_0$ is increased:[28]

$$HO_2 + HO_2 \rightarrow H_2O_2 \qquad (4.11)$$

This analysis does however demonstrate that the inclusion of methanol and excess oxygen to the reaction system is consistent with the formation of an additional species (and self-reacting) radical, namely HO_2, which also provides an additional termination reaction for ClO radicals.

A second method wherein the initial concentrations of ClO and HO_2 were allowed to vary in optimising the fits to ClO traces was also carried out. In this case, the fits to data were as equally good as found previously, and the rate constants at high $[ClO]_0/[HO_2]_0$ ratios were remarkably consistent with the results from analysis constraining the total radical concentration. In this case, the rate constant enhancement at low $[ClO]_0/[HO_2]_0$ ratios was not as significant as in the preceding analysis, but rather the total radical concentration indicated an apparent shortfall of radicals compared to the expected total concentration inferred from experiments carried out without methanol. Again this implies a significant loss of HO_2 through the known HO_2 self-reaction.

These initial analytic procedures gave considerable insight into the nature of the reactive system employed and the flux of photolytically generated atoms and radicals through the various potential channels. In light of this, a more comprehensive analysis was carried out, using a model with all known gas phase chemistry and physical processes such as gas flowout from the reaction vessel. Additionally, a degree of constraint on the data fitting was also applied as discussed after consideration of the provenance of the radicals formed which is below. Details of the chemical mechanism of this model are presented in Table 4.4 below.

	Reaction and Label	Rate constant ($k(T)$ at p = 760 Torr)[a]
	Formation Chemistry	
k_{1f}	$Cl + Cl_2O \rightarrow Cl_2 + ClO$	$6.20 \times 10^{-11} \exp(130/T)$
k_{2f}	$Cl + CH_3OH \rightarrow CH_2OH + HCl$	5.5×10^{-11}
k_{3f}	$CH_2OH + O_2 \rightarrow HCHO + HO_2$	9.1×10^{-11}
	Principal Reaction	
k_{4f}	$ClO + HO_2 \rightarrow HOCl + O_2$	$2.6 \times 10^{-12} \exp(290/T)$
	ClO Competing Chemistry	
k_{5fD}	$ClO + ClO + M \rightarrow Cl_2O_2 + M$	$k_0 = 1.60 \times 10^{-32} \times (T/300)^{-4.5b}$
k_{5rD}	$Cl_2O_2 + M \rightarrow ClO + ClO + M$	$k_\infty = 3.00 \times 10^{-12} \times (T/300)^{-2}$
		$K_{eq} = 1.72 \times 10^{-27} \exp(8649/T)^c$
k_{6fa}	$ClO + ClO \rightarrow Cl_2 + O_2$	$1.00 \times 10^{-12} \exp(-1590/T)$
k_{6fb}	$ClO + ClO \rightarrow OClO + Cl$	$3.50 \times 10^{-13} \exp(-1370/T)$
k_{6fc}	$ClO + ClO \rightarrow ClOO + Cl$	$3.00 \times 10^{-11} \exp(-2450/T)$
k_{7f}	$Cl + O_2 + M \rightarrow ClOO + M$	$k_0 = 2.20 \times 10^{-33} \times (T/300)^{-3.1b}$
k_{7r}	$ClOO + M \rightarrow Cl + O_2 + M$	$k_\infty = 1.80 \times 10^{-10} \times (T/300)^0$
		$K_{eq} = 6.60 \times 10^{-25} \exp(2502/T)^c$
k_{8f}	$ClOO + ClOO \rightarrow ClO + ClO + O_2$	1.60×10^{-11}
k_{9f}	$ClOO + Cl_2 \rightarrow Cl_2O + ClO$	3.40×10^{-12}
k_{10f}	$ClO + OClO + M \rightarrow Cl_2O_3 + M$	$k_0 = 1.60 \times 10^{-32} \times (T/300)^{-4.7b}$
k_{10r}	$Cl_2O_3 + M \rightarrow ClO + OClO + M$	$k_\infty = 3.00 \times 10^{-11} \times (T/300)^{-1.1}$
		$K_{eq} = 1.50 \times 10^{-27} \exp(7140/T)^c$
	$CH_2OH + Cl_2 \rightarrow Cl + ClCH_2OH$	2.90×10^{-11}
	HO_2 Competing Chemistry	
k_{11f}	$HO_2 + HO_2 \rightarrow H_2O_2 + O_2$	$3.00 \times 10^{-13} \exp(460/T) + 5.17 \times 10^{-14} \exp(920/T)$
k_{12f}	$HO_2 + CH_3OH \rightarrow HO_2.CH_3OH$	$2.80 \times 10^{-15} \exp(-1800/T)$
k_{12r}	$HO_2.CH_3OH \rightarrow HO_2 + CH_3OH$	$K_{eq} = 1.10 \times 10^{-24} \exp(4093/T)^c$
k_{13f}	$HO_2 + HO_2.CH_3OH \rightarrow H_2O_2 + CH_3OH + O_2$	$5.40 \times 10^{-11} \exp(-410/T)$
k_{14f}	$HO_2 + H_2O \rightarrow HO_2.H_2O$	$2.80 \times 10^{-15} \exp(-1800/T)$

k_{14r}	$HO_2.H_2O \rightarrow HO_2 + H_2O$	$K_{eq} = 2.40 \times 10^{-25}\exp(4350/T)^c$
k_{15f}	$HO_2 + HO_2.H_2O \rightarrow H_2O_2 + H_2O + O_2$	$5.40 \times 10^{-11}\exp(-410/T)$
k_{16fa}	$HO_2 + Cl \rightarrow HCl + O_2$	$1.40 \times 10^{-11}\exp(270/T)$
k_{16fb}	$HO_2 + Cl \rightarrow OH + ClO$	$3.60 \times 10^{-11}\exp(-375/T)$
k_{17f}	$Cl + H_2O_2 \rightarrow HCl + HO_2$	$1.10 \times 10^{-11}\exp(-980/T)$
	Secondary Chemistry	
k_{18f}	$HOCH_2O_2 \rightarrow HO_2 + HCHO$	$9.70 \times 10^{-15}\exp(-625/T)$
k_{18r}	$HO_2 + HCHO \rightarrow HOCH_2O_2$	$2.40\times10^{12}\exp(7000/T)$
k_{19f}	$HOCH_2O_2 + HO_2 \rightarrow HOCH_2OOH + O_2$	$(0.6) \times 5.60\times10^{-15}\exp(-2300/T)$
k_{20f}	$HOCH_2O_2 + HO_2 \rightarrow O_2 + HC(O)OH + H_2O$	$(0.4) \times 5.60\times10^{-15}\exp(-2300/T)$
k_{21fa}	$HOCH_2OOH + Cl \rightarrow HCOOH + OH + HCl$	1.00×10^{-10}
k_{21fb}	$HOCH_2OOH + Cl \rightarrow HOCH_2O_2 + HCl$	5.00×10^{-10}
k_{22f}	$HOCH_2O_2 + HOCH_2O_2 \rightarrow HOCH_2O + HOCH_2O + O_2$	$5.70 \times 10^{-14}\exp(750/T)$
k_{23f}	$HOCH_2O_2 + O_2 \rightarrow HCOOH + HO_2$	3.50×10^{-14}
k_{24f}	$Cl + HCHO \rightarrow HCl + HCO$	$8.10 \times 10^{-11}\exp(-30/T)$
k_{25f}	$HCO + O_2 \rightarrow CO + HO_2$	$3.50 \times 10^{-12}\exp(140/T)$
k_{26f}	$HCO + Cl_2 \rightarrow HCOCl + Cl$	$6.10 \times 10^{-12}\exp(-36/T)$

[a]Units are cm^3 molecule^{-1} s^{-1} unless otherwise stated [b]units of cm^6 molecule^{-2} s^{-1} and [c]units of cm^3 molecule^{-1}

Table 4.4 *Reaction scheme used for numerical modelling with rate coefficient expressions taken principally from the JPL NASA data evaluation.*[11]

4.3.3 Analysis of Radical Production Routes

The total concentration of the chlorine containing species (Cl_2 and Cl_2O) in the precursor gas mixture was governed by the flow rate of (diluted) Cl_2 into the carrier flow, and the degree of conversion of Cl_2 into Cl_2O upon passing through the trap containing mercuric oxide (reaction (4.6)). With the entire flow of Cl_2 passing through the HgO trap, this conversion was typically high (70 – 80 % removal of Cl_2) as confirmed by spectroscopic measurements. In practice however, a degree of control (reduction) over this conversion was afforded using a tube bypassing the HgO trap, flow through which was controlled by a PTFE needle valve.

If the fractional conversion of Cl_2 into Cl_2O in the precursor gas arrangement is defined as α, and the total concentration of Cl_2 introduced to the system, as determined from calibrated flow rates is $[Cl_2]_{total}$ (the concentration of Cl_2 that would result in the *absence* of flow through the mercuric oxide trap), then the actual concentrations of Cl_2O and Cl_2 in the precursor gas mixture may be expressed as:

$$[Cl_2]_0 = (1 - \alpha)\,[Cl_2]_{total} \qquad (4.3\text{ i})$$

$$[Cl_2O]_0 = (\alpha / 2)\,[Cl_2]_{total} \qquad (4.3\text{ ii})$$

taking account of the stoichiometry of the Cl_2 to Cl_2O conversion (reaction (4.6)).

Upon laser photolysis, the initial (immediate post-photolysis) concentrations of Cl atoms and ClO radicals, from the photolysis of Cl_2 and Cl_2O (which yields exclusively Cl + ClO at λ = 351 nm[11]) are then given by:

$$[Cl]_0 = 2\,f(Cl_2)\,[Cl_2]_0 + f(Cl_2O)\,[Cl_2O]_0 \qquad (4.3\text{ iii})$$

$$[ClO]_0 = f(Cl_2O)\,[Cl_2O]_0 \qquad (4.3\text{ iv})$$

Where $f(Cl_2)$ and $f(Cl_2O)$ are defined as the respective fractions of the Cl_2 and Cl_2O gases that are photolysed.

Subsequently, in the absence of methanol, and with Cl_2O in excess, all of the initial photolytically generated Cl atoms react rapidly and exclusively with Cl_2O forming ClO in reaction (4.8):

$$Cl + Cl_2O \rightarrow Cl_2 + ClO \qquad (4.8)$$

$k_{(4.8)}$ (T = 298 K) = 9.6×10^{-11} cm^3 $molecule^{-1}$ s^{-1}.[11] Thus, the effective instantaneous post-photolysis concentration of ClO radicals is in this case given by:

$$[\mathrm{ClO}]_0 = 2\,f(\mathrm{Cl_2})\,[\mathrm{Cl_2}]_0 + 2\,f(\mathrm{Cl_2O})\,[\mathrm{Cl_2O}]_0 \qquad (4.3\ \mathrm{v})$$

which from (4.3 i) and (4.3 ii) gives:

$$[\mathrm{ClO}]_0 = \{[2\,f(\mathrm{Cl_2})\,(1-\alpha)] + [f(\mathrm{Cl_2O})\,\alpha]\}[\mathrm{Cl_2}]_{\mathrm{total}} \qquad (4.3\ \mathrm{vi})$$

Now, assuming that the ratio of the fractional photolyses of Cl_2 and Cl_2O in the precursor gas mixture is equal to the ratio of the absorption cross sections of these species at the laser wavelength of 351 nm (this is the case since the photolysis quantum yield for both molecules are unity at λ = 351 nm[11]), the immediate post-photolysis ClO concentration may be expressed as:

$$[\mathrm{ClO}]_0 = \{[2\,\beta\,f(\mathrm{Cl_2O})\,(1-\alpha)] + [f(\mathrm{Cl_2O})\,\alpha]\}[\mathrm{Cl_2}]_{\mathrm{total}} \qquad (4.3\ \mathrm{vii})$$

where β is defined here as $\{f(\mathrm{Cl_2}) / f(\mathrm{Cl_2O})\} = \{\sigma(\mathrm{Cl_2}) / \sigma(\mathrm{Cl_2O})\}_{\lambda\,=\,351\ \mathrm{nm}}$, giving $\beta = 8.53 \times 10^{-2}$ from the latest JPL NASA evaluation.[11]

Thus, measurement of the immediate post-photolysis concentrations of ClO, provided by kinetic fitting to the ClO temporal traces recorded in the absence of methanol, constrains $f(\mathrm{Cl_2O})$ and therefore $f(\mathrm{Cl_2})$ (from β) for a given value of the Cl_2 to Cl_2O conversion, α. This parameter was also constrained separately, through independent measurements of the Cl_2 and Cl_2O absorption spectra in the precursor gas mixture at a fixed position of the needle valve on the HgO trap bypass. Therefore experiments carried out in the absence of methanol gave considerable insight into the initial Cl atom and ClO radical concentrations immediately post-photolysis.

Upon the introduction of methanol into the precursor gas mixture, in experiments that intervened those without methanol, the methanol competes with Cl_2O for the initial photolytically generated Cl atoms *via* reaction (4.9). In the presence of excess oxygen, the CH_2OH radicals formed thereafter then react rapidly and exclusively to generate HO_2 radicals in reaction (4.10), thereby leading to prompt HO_2 formation along with the ClO radicals, immediately post-photolysis. As Figure 4.7 (a) demonstrates, roughly the same number density of Cl/ClO radicals can readily be formed (*i.e.* approximately the same $[\mathrm{TR}]_0$) post-photolysis between each run of zero methanol experiments. Therefore, it is implied that the initial concentration of HO_2 could be inferred from the difference between the initial post-photolysis [ClO] recorded in the presence and absence of methanol.

Furthermore, the parameters extracted in equation (4.3 vii) from the experiments conducted in the absence of methanol provide information on the initial total radical number density (*i.e.* $[TR]_0$) post-photolysis. Thus, the immediate post-photolytic concentration of HO_2 could be inferred, along with that of ClO, which was directly measured. For clarity, this radical formation scheme is also presented diagrammatically in Figure 4.12 below.

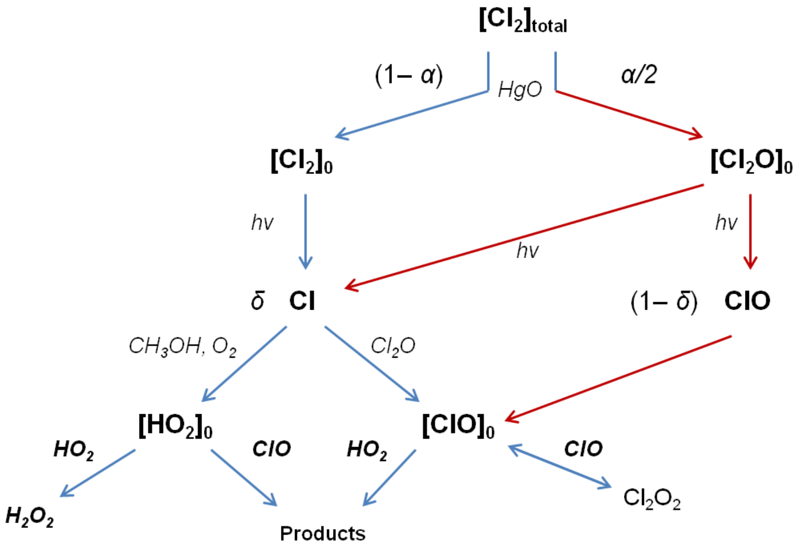

Figure 4.12 *A schematic representation of the chemical reactions in the photolysed $Cl_2/Cl_2O/O_2/CH_3OH$ mixtures.*

4.3.4 Analysis of ClO Temporal Traces Recorded in the Presence of CH_3OH: Part 2

The [ClO] temporal traces recorded in the presence of methanol vapour were analysed through the fitting of simulated ClO profiles based upon the model presented in Table 4.4. The initial post-photolysis ClO concentration, and the rate constant for the ClO + HO_2 reaction were varied to optimise the fit, along with a third parameter, δ, which effectively partitioned the modelled initial Cl atom and ClO radical concentrations as described by equations (4.3 iii) and (4.3 iv), along with the constraint to these concentrations provided using the parameter β and expressed by equation (4.3 vii). In this way, the only varied parameter in addition to the initial radical concentration and the ClO + HO_2 rate constant was effectively the parameter α, the fractional conversion of Cl_2 to Cl_2O, which reflected the efficacy of the HgO trap and the degree to which it was bypassed in the gas flow which was specific to a given experiment. An example of a typical fit is shown in Figure 4.13 at T = 298 K with [CH_3OH] = 7.2×10^{15} molecules cm^{-3}.

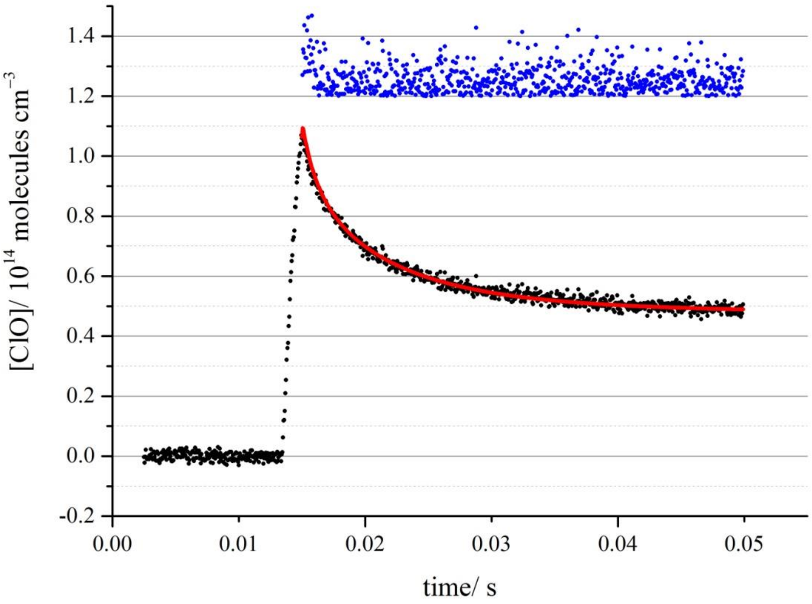

Figure 4.13 *An example of a typical fit between experimental* $[ClO]_t$ *(black dots) and a simulated* $[ClO]_t$ *trace using optimised parameters from the FACSIMILE fitting procedure. The blue dots are the offset residuals* $\times 5$.

The parameters extracted from the analysis of the ClO traces recorded in the presence of methanol are summarised in Table 4.5. The initial post-photolysis concentrations of ClO, *i.e.* $[ClO]_0$, reflected the competition for chlorine atoms between methanol and Cl_2O according to the current JPL NASA[11] recommendations for these rate coefficients as a function of temperature.

T/ K	$[\mathrm{ClO}]_0{}^a$/ 10^{14}	$[\mathrm{ClO}]_0/[\mathrm{TR}]_0$	$[\mathrm{CH_3OH}]_0{}^a$/ 10^{15}	δ	$k_{(4.1)}{}^b$/ 10^{-11}
298.15	1.0 – 1.5	0.54 – 0.72	3.0 – 8.8	0.2 – 0.6	0.847 ± 0.231
278.65	1.0 – 1.5	0.61 – 0.77	3.2 – 9.7	0.4 – 0.7	1.50 ± 0.33
261.55	1.4 – 1.6	0.60 – 0.66	6.7 – 9.7	0.6	1.22 ± 0.15
246.45	1.1 – 1.8	0.57 – 0.68	2.5 – 8.3	0.3 – 0.6	2.52 ± 1.66
232.95	1.1 – 1.3	0.65 – 0.82	4.2 – 8.8	0.4 – 0.6	2.34 ± 0.81
210.05	1.1 – 1.8	0.20 – 0.53	10 – 14.7	0.4 – 0.7	3.43 ± 2.34

[a]*Units of molecules* cm^{-3}, [b]*units of* cm^3 *molecule*$^{-1}$ s^{-1}

Table 4.5 *Kinetic parameters obtained for reaction (4.1) along with ranges of initial ClO and added methanol concentrations. The parameter* $[ClO]_0/[TR]_0$ *represents the fraction of ClO radicals to total radical concentrations. The parameter* δ *represents the partitioning of initial Cl and ClO concentrations.*

The rate constants for the ClO + HO$_2$ reaction obtained in this work are shown in Arrhenius form in Figure 4.14 below. The results show a negative temperature dependence for the overall rate constant, with linear Arrhenius behaviour, described by:

$$k_{(4.1)}\left(T/\mathrm{K}\right) = (4.07 \pm 3.55) \times 10^{-13}\, e^{\left(\frac{(949 \pm 197)}{T}\right)} \mathrm{cm^3\ molecule^{-1}\ s^{-1}} \qquad (4.3\ \mathrm{viii})$$

where errors are 1σ, from the Arrhenius fit to all data.

In principle, given the nature of the broadband UV absorption spectroscopy adopted in this work, the time resolved concentrations of HO$_2$, in addition to those of ClO, could have been monitored. However, in practice, the presence of several strongly absorbing species in the reaction mixture (Cl_2O, ClO, and Cl_2O_2) and the absence of any distinctive spectral structure for the absorptions of these species, or indeed for HO$_2$, precluded this monitoring. Thus, the HO$_2$ concentrations were inferred as discussed above. A detailed sensitivity analysis was therefore also performed to examine the integrity of these assumptions, and to quantify the potential effect of uncertainty in the kinetic and physical parameters used in the analytic model, as discussed below.

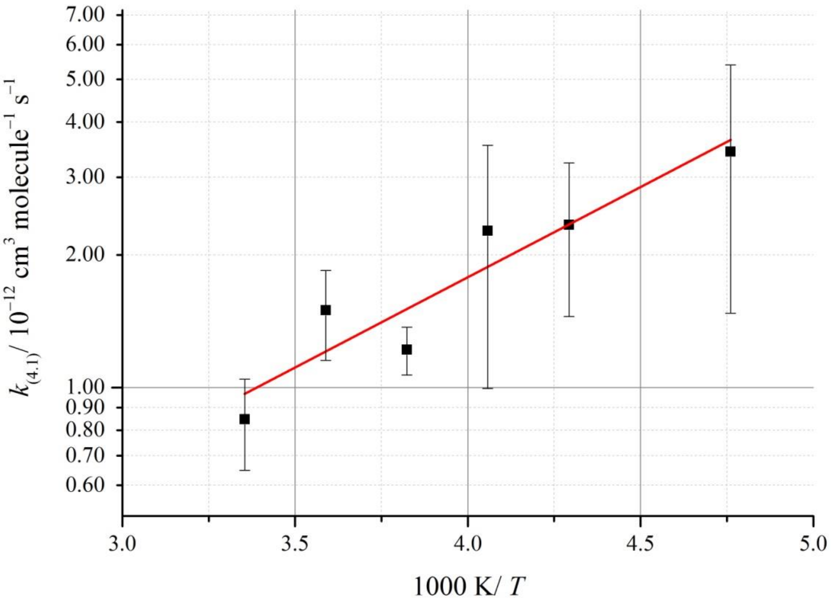

Figure 4.14 *Arrhenius plot of the temperature dependence of $k_{(4.1)}$ as found in this work (black squares) and the corresponding Arrhenius optimisation (red line). Errors are 1σ, statistical only.*

4.4 Discussion

4.4.1 Sensitivity Analysis

To investigate the sensitivity of the ClO + HO_2 rate constant extracted from the [ClO] traces recorded from Cl_2O/Cl_2 photolysis in the presence of methanol vapour and excess oxygen, the kinetic model used in deriving $k_{(4.1)}$ was systematically perturbed and the effect on the extracted rate constant recorded. Specifically, each of the rate constants for the chemistry summarised in Table 4.4 were altered, in turn, by ± 50 % in the model (which is typically larger than the recommended uncertainty). The perturbed model was then used to re-evaluate the rate constant for ClO + HO_2 and the parameter δ from representative traces, at T = 298 K and at T = 210 K, the lower limit of the temperature range over which this reaction was studied, the results of which are shown in Figures 4.14 (a) through to 4.14 (d). The label for each rate constant in Figure 4.14 corresponds to the reactions as labelled in the numerical model in Table

4.4. However, reactions that caused any significant perturbations in the retrieved parameters are identified. For the majority of reactions included in the model, the perturbation of the rate constant by ± 50 % (which is typically somewhat greater than the recommended uncertainty) led to a returned rate constant for ClO + HO_2 within ~ 3 % of that obtained using the unperturbed model at T = 298 K and ~ 4 % at T = 210 K. Specific reactions affecting the ClO + HO_2 rate constant, $k_{(4.1)}$, at T = 298 K were: the ClO + HO_2 reaction itself (labelled $k_{4\mathrm{f}}$ in the model); the ClO self-reaction chemistry (labelled $k_{5\mathrm{fD}}$, $k_{5\mathrm{rD}}$ and $k_{6\mathrm{f}}$) with the reversible dimerisation reaction, reactions (4.2) and (−4.2) (*i.e.* $k_{5\mathrm{fD}}$ and $k_{5\mathrm{rD}}$) being particularly important; and the HO_2 self-reaction, reaction (4.11) (labelled $k_{11\mathrm{f}}$). The sensitivity to the self-reaction chemistry of both reactants is unsurprising since the experiments were designed as such that it is assumed that these species are the dominant radicals formed upon photolysis. Therefore, aside from the principal reaction investigated which is radical terminating, the dominant source of secondary chemistry involved ClO and HO_2, both of which self-react efficiently. In particular, this highlights the importance of characterising the ClO dimerisation kinetics at each temperature in the absence of methanol. Aside from determining the initial total radical concentration (thus enabling the inference of [HO_2] in the methanol experiments), the optimisation of $k_{(4.2)}$ and $k_{(-4.2)}$ means that $k_{(4.1)}$ is essentially optimised from the enhanced rate of loss of ClO relative to the methanol free experiments. Consequently, this demonstrates that although the experimentally derived rate constants for ClO dimerisation are not exactly equal the JPL NASA recommendation,[11] they are consistent with the methanol experiments which are particularly sensitive to $k_{(4.2)}$ and $k_{(-4.2)}$. Thus the use of the experimentally obtained values of $k_{(4.2)}$ and $k_{(-4.2)}$ in the model used to optimise $k_{(4.1)}$ is justified. Again, at T = 210 K the model is most sensitive to ClO dimerisation, although not to the reverse reaction, the rate of which becomes insignificant below T = 250 K. There is no value plotted for when the rate constant for reaction (4.2) was halved as in this case the model failed to converge on an optimised value, implying that an accurate value of $k_{(4.2)}$ is crucial at lower temperatures which is unsurprising since the rate of reaction (4.2) is proportional to the square of $[\mathrm{ClO}]_t$.

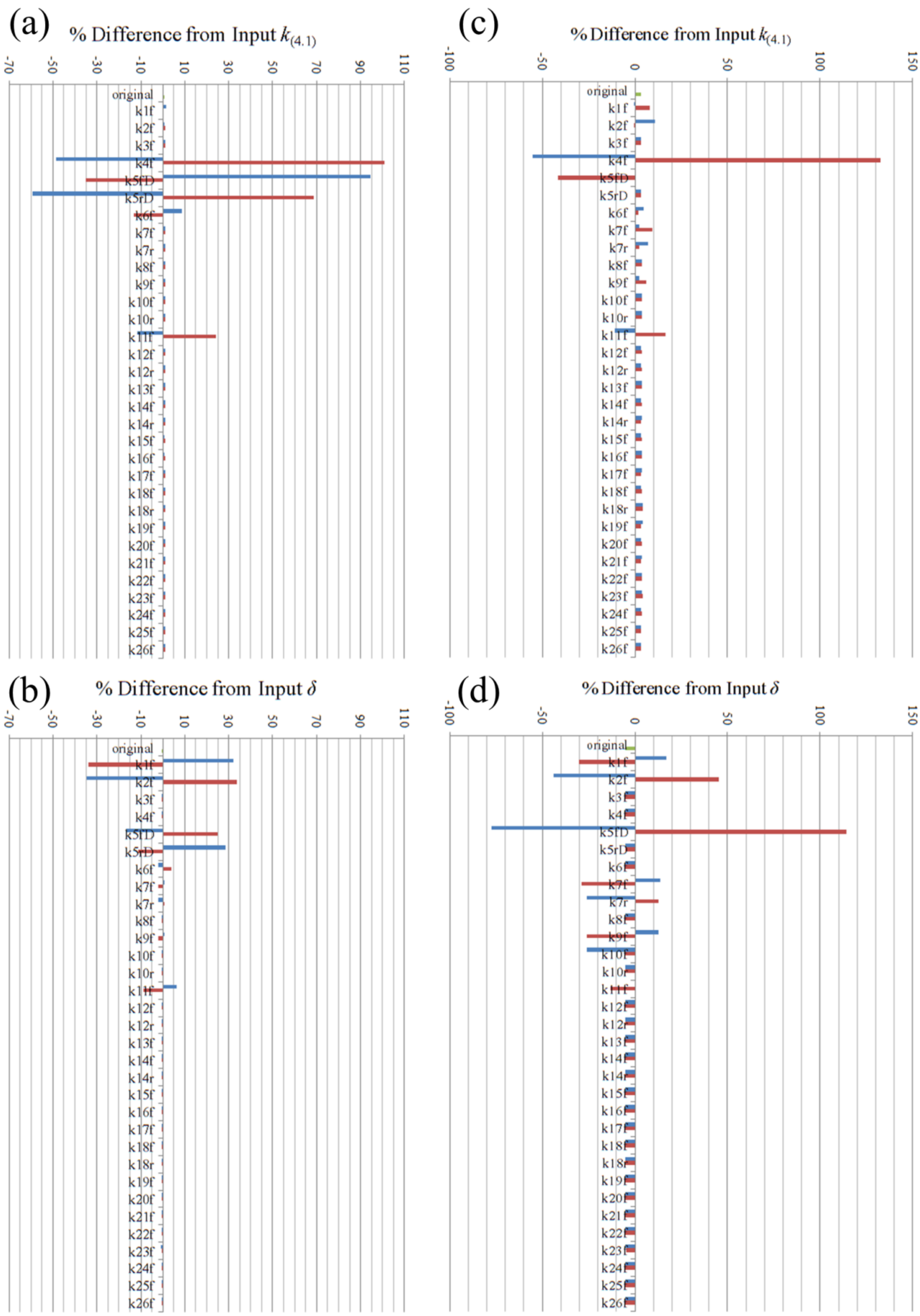

Figure 4.15 *The sensitivity of the output optimised values of $k_{(4.1)}$ and δ to each reaction in the numerical model in Table 4.4, at T = 298 K (a) and (b) and T = 210 K (c) and (d). The results are presented as the percentage difference between the input and output values found in the*

fitting procedure used in FACSIMILE. The following input values for each corresponding figure were: (a) $k_{(4.1)}$ *(*T *= 298 K), =* 6.88×10^{-12} *cm*^{3} *molecules*$^{-1}$ *s*$^{-1}$*; (b)* δ *= 0.71 at 298 K; (c)* $k_{(4.1)}$ *(*T *= 210 K) =* 1.03×10^{-11} *cm*^{3} *molecules*$^{-1}$ *s*$^{-1}$*; (d)* δ *= 0.71 at* T *= 210 K. The green bar represents the optimised result of the "original" unperturbed model. The blue bars represent the halving of a particular rate constant whereas the red bars represent a doubling. The reactions are labelled as in Table 4.4.*

By comparison, the returned values of the parameter δ are in general less precise than for those of $k_{(4.1)}$ upon perturbing the rate constants in the model. Comparing the optimised values of δ in the unperturbed model it is clear the model performs slightly better at T = 298 K than at T = 210 K. The sensitivity to the formation chemistry of either reactant, reactions (4.8) and (4.10) (labelled in the model k_{1f} and k_{2f} respectively) in particular and at T = 210 K the reactions involving the species ClOO (which becomes more stable with decreasing temperature) can be rationalised through the intrinsic link δ has with the initial [Cl] and [ClO]. Therefore it is unsurprising that perturbing the chemistry involving Cl in particular, affected the output value of δ. The results of the sensitivity analysis suggest that the kinetic model is robust under the experimental conditions employed in this work and that the value of $k_{(4.1)}$ is largely unaffected by the uncertainty of the majority of the reactions utilised. What is more, the perturbations in the retrieved values of δ suggest that the variation of this parameter permits a degree of freedom in the fitting procedure that buffers $k_{(4.1)}$ from the uncertainty in the formation chemistry in particular.

In a similar fashion, the effect of potential uncertainties in the other key parameters on the optimised values of $k_{(4.1)}$ and δ were explored. These parameters, namely: the initial total radical concentration, $[TR]_0$; the methanol concentration, $[CH_3OH]$; the partitioning of Cl_2/Cl_2O, α; and the partitioning of Cl/ClO post-photolysis, δ, were perturbed in a similar fashion to the above sensitivity analysis. The parameters were changed in turn and simulated traces for each model were generated. The unperturbed model was fitted to these perturbed traces, again varying $k_{(4.1)}$ and δ. The degree in which each parameter was perturbed in the sensitivity analysis was believed to be larger than any corresponding deviation in the actual experimental conditions. The results are presented in Figure 4.16, showing the percentage difference between the input and output parameters of $k_{(4.1)}$ and δ for each scenario at T = 298 K. It can be seen that changes in all of the parameters above lead to significant differences in the returned values of δ. However, aside from the initial total radical concentration, deviations in the other parameters have a minimal affect on the optimised $k_{(4.1)}$. Similarly at T = 210 K, in Figure 4.17, the same can be seen. Again this demonstrates the robustness of the model and the suitability in varying δ in addition to $k_{(4.1)}$.

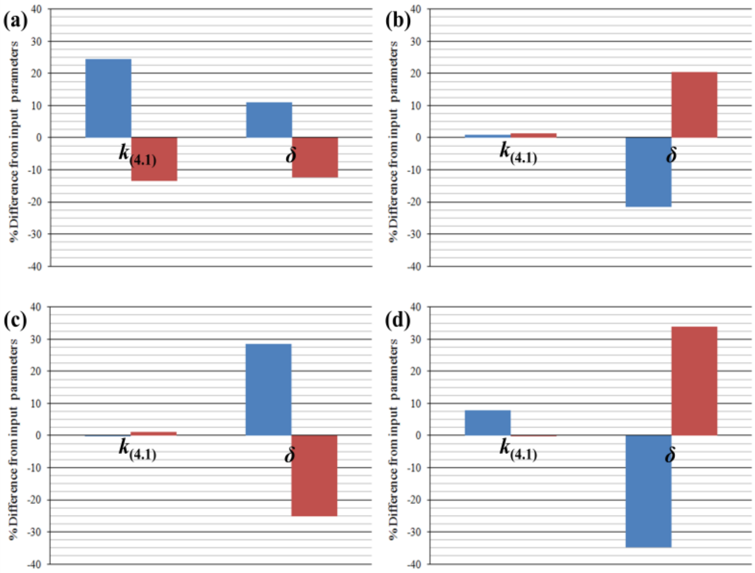

Figure 4.16 *The sensitivity of the optimised model in Table 4.4 to the input parameters: (a)* $[TR]_0$ *(+/–20 %); (b)* δ *(+/–20 %); (c)* α *(+/–50 %); (d)* $[CH_3OH]$ *(halved/doubled), at* T = *298K. The blue bars correspond to a decrease in a given parameter (compared to the original model) and the red bars correspond to an increase.*

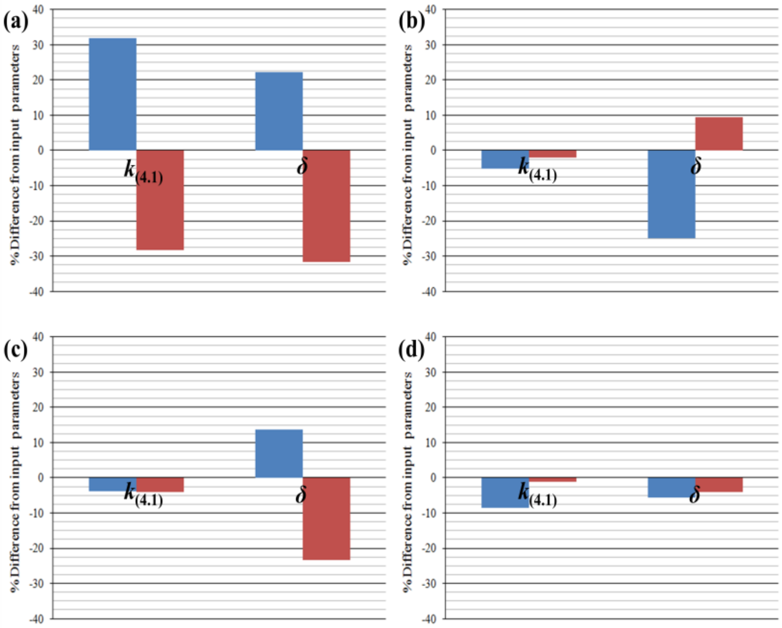

Figure 4.17 *The sensitivity of the optimised model in Table 4.4 to the input parameters: (a) $[TR]_0$ (+/–20 %); (b) δ (+/–20 %); (c) α (+/– 50 %); (d) $[CH_3OH]$ (halved/doubled), at T = 210K. The blue bars correspond to a decrease in a given parameter (compared to the original model) and the red bars correspond to an increase.*

A subsequent flux analysis of the principal reactants of the chemical system, ClO and HO_2, showed that the relative importance of these rate constants could be rationalised. This analysis demonstrated that under experimental conditions, the vast majority of ClO and HO_2 formed react almost exclusively *via* reactions (4.1), (4.2), (−4.2) and the HO_2 self-reaction. The importance of the ClO or HO_2 self-reaction chemistry in particular, was therefore evidently dependent upon the relative amount of $[ClO]_0$ and $[HO_2]_0$.

Systematic errors and their effect on the sensitivity of the kinetic model were considered in the form of the uncertainty associated with the ClO differential absorption cross section used in determining ClO concentrations. Alteration of σ_{ClO} to the upper and lower bounds of uncertainty as derived from in equation (4.2 i) led to a change in the maximum concentrations by a factor of 1.8 which led to differences in the extracted forward reaction rate constant for ClO + ClO of *ca.* ± 40. However, the subsequent change in the extracted ClO + HO_2 was smaller (*ca.* ± 10 %), as the rate of this reaction was essentially measured *relative* to the ClO self-reaction (reactions (4.2) and (−4.2)) and the rate of reaction is not dependent on the square of [ClO].

4.4.2 Assumptions of the Kinetic Analysis

Aside from the sensitivity to kinetic and spectral parameters discussed above, the fundamental assumption employed in this work was that the photolytically generated Cl atoms produced exclusively ClO in the absence of methanol, which was indeed observed explicitly, but also HO_2 radicals when methanol and excess oxygen were present. This was supported by numerical integration simulations using all known gas phase chemistry[11] and the well-established concentrations of precursor species present. Methanol and oxygen mixtures are commonly used as a source of HO_2 radicals in the presence of photolytically produced Cl atoms.[28] The systematic variation of $[ClO]_0$ with added methanol concentration was also consistent with a competition for Cl atoms either reacting with Cl_2O or CH_3OH. Further, the systematic reproducibility of the ClO temporal traces recorded before and after the addition of methanol vapour in successive experiments also supports the robustness of this chemistry.

4.4.3 Comparison with Previous Work

The present work reports an ambient temperature (T = 298 K) value of $k_{(4.1)} = (8.47 \pm 2.31) \times 10^{-12}$ cm^3 molecule^{-1} s^{-1}, taken from typically four determinations of $k_{(4.1)}$ at each methanol concentration used and, at this temperature, a total of 8 different methanol concentrations in the range stipulated above. Errors are 1σ, statistical only. Comparing this to the other previous reports of $k_{(4.1)}$, shown in Figure 4.18, this shows that the present work reports the highest average value for $k_{(4.1)}$ at T = 298 K, albeit within the error limit of several of the previous studies, and particularly in agreement with those studies carried out at high pressure ($p >$ *ca.* 50 Torr).

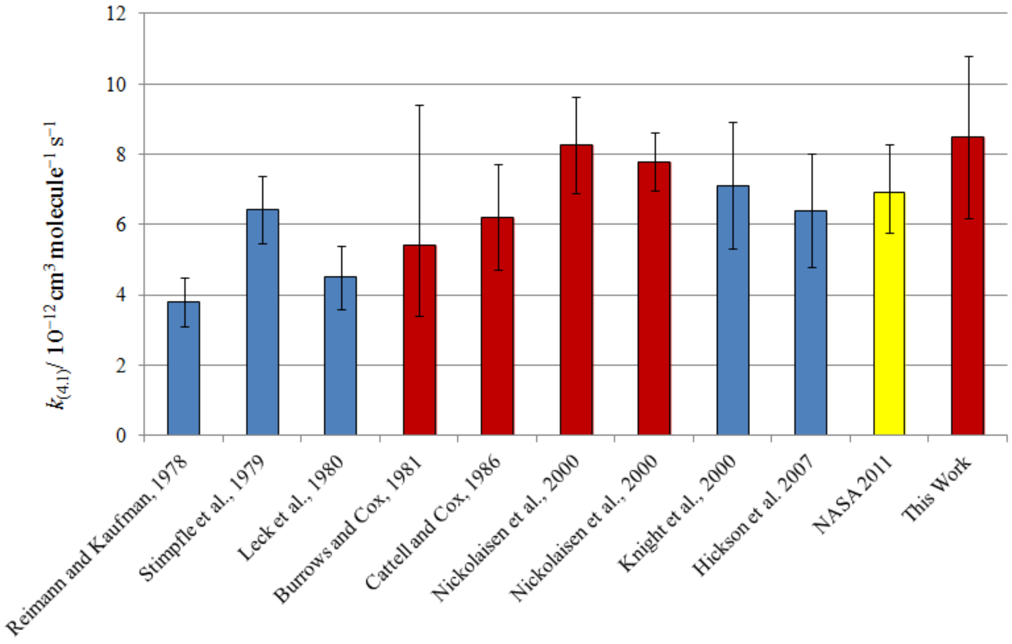

Figure 4.18 *Histogram plot of all previous determinations of* $k_{(4.1)}$ *at* T = *298 K with their associated errors. Blue bars refer to low pressure (* $p <$ *10 Torr), typically from flow tube, measurements. Red bars refer to high pressure (*$p \geq$ *50 Torr), typically from static or flash photolysis measurements. The yellow bar refers to the current recommended JPL NASA evaluation.*[11]

For the temperature dependence of $k_{(4.1)}$, shown in Figure 4.19 in comparison with the results of previous work, this study reports a stronger negative temperature dependence (E/R) = (−949 ± 197) K than previously observed, consequently resulting in a greater value for $k_{(4.1)}$ = (3.43 ± 2.34) × 10^{-11} cm^3 molecule^{-1} s^{-1} at the lowest temperature studied in the present work (T = 210 K). As with the ambient temperature results, the values of $k_{(4.1)}$, and their temperature dependence, most closely resemble previous determinations of $k_{(4.1)}$ recorded in experiments conducted at high (p > *ca.* 50 Torr) pressures.

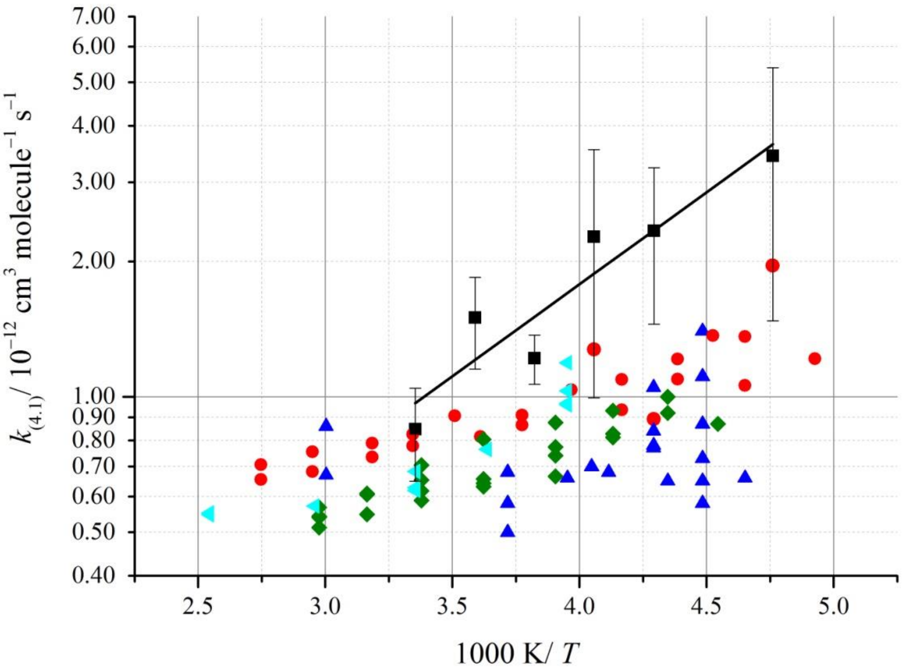

Figure 4.19 *Arrhenius plot for determinations of* $k_{(4.1)}$*: Red circles = Nickolaisen et al.;*[20] *Dark blue triangles = Knight et al.;*[21] *Green diamonds = Hickson et al.;*[19] *Light blue triangles = Stimpfle et al.*[12] *and black squares = this work. Error bars are 1σ, statistical only.*

Considering the approach taken for the present work, compared with previous studies, at T = 298 K and as a function of temperature, several studies have also had to rely upon somewhat indirect measurements to infer the concentrations of ClO and/or HO_2 radicals. Considering first the low pressure (p < *ca.* 50 Torr) studies, the earliest ambient temperature study, that of Reimann and Kaufmann[15] detected HO_2 following its conversion to OH (*via* reaction with NO) and subsequent laser induced fluorescence of OH. As subsequently noted and accounted for in the analysis by Hickson *et al.*,[19] this procedure may have been compromised by a reduction in stoichiometry in this conversion as a result of, for example, secondary chemistry of HO_2 such as the HO_2 self-reaction or heterogeneous losses of radicals which are endemic to flow tube studies and which therefore have to be accounted for. In the Reimann and Kaufmann study, the concentrations of ClO were also not directly measured, but obtained from inference and extrapolation of the Cl atom signal recorded. In similar fashion, the study of Leck *et al.*,[16] which used mass spectrometric detection of species sampled from a flow tube, inferred ClO radical concentrations from the depletion of the precursor species Cl_2 when the microwave discharge used to generate radicals was operated.

Considering the high pressure ensemble of ambient temperature studies of $k_{(4.1)}$, those of Burrows and Cox[17] and Cattell and Cox[22] used continuous photolysis of precursor gas mixtures in one case analogous to those used in the present work, Cl_2 with Cl_2O[17] and in the other with a chlorine, hydrogen, oxygen mixture[22] to generate radicals. This photolysis was modulated over several seconds and UV spectroscopy was used to monitor a composite radical and product signal, which was then fitted using numerical integration to extract the value of $k_{(4.1)}$. This approach, whilst noteworthy and pioneering, does however carry the risk that not only the initial reactants but then the subsequent products may be photolysed, leading to extensive and potentially complex secondary chemistry and a subsequent reduction in sensitivity to the reaction of interest. Further, the single wavelength UV absorption monitoring gives a time-resolved signal containing contributions from all potential UV absorbing species present. By contrast, Nickolaisen *et al.*[20] employed pulsed flashlamp photolysis/ultraviolet absorption to monitor (principally) HO_2 (at λ = 210 nm) and ClO (in a dual wavelength set-up at λ = 275.2 nm and λ = 276.4 nm) from a variety of precursor sources including (F_2, H_2, O_2, Cl_2O) and (Cl_2, Cl_2O, CH_3OH, O_2) in common with the present work. The recorded absorbance traces obtained at λ = 210 nm were modelled to infer the HO_2 concentration, in the presence of a number of other absorbing species. The differential signal at the two higher wavelengths was used as a direct measure of the ClO absorbance.

Considering the studies of $k_{(4.1)}$ as a function of temperature, Stimpfle *et al.*[12] measured both HO_2 and ClO concentrations using laser magnetic resonance, at low pressures ($0.8 \leq p$/ Torr ≤ 3.4) following their microwave generation in a flow tube. Uniquely, these authors recorded a non-linear temperature dependence for $k_{(4.1)}$, which they attributed to a more than one form of the HO_3Cl association complex in the reaction, potentially leading to the different product channels (4.1a)(4.1b) and (4.1b). Subsequently, the study of Nickolaisen *et al.*[20] reported a linear negative temperature dependence for $k_{(4.1)}$, albeit with absolute values for the rate constant close to those reported by Stimpfle *et al.*[12] The other two studies of $k_{(4.1)}$ carried out as a function of temperature were reported by Knight *et al.*[21] and Hickson *et al.*,[19] both using flow tubes at low pressure. Knight *et al.*[21] used multiple radical sources for the reaction (albeit with ClO always in excess), and reported a near-zero temperature dependence for $k_{(4.1)}$. By contrast, Hickson *et al.*[19] reported a negative, linear, temperature dependence to $k_{(4.1)}$, using a variety of radical precursors and experimental arrangements, with the temperature trend of (E/R) in $k_{(4.1)}$ close to that in gradient, although smaller in absolute magnitude of the results of Nickolaisen *et al.*[20]

The results recorded in the present work were analysed under a number of different scenarios, discussed above, which gave insight into the provenance of the two radicals involved and which gave consequent constraint on the numerical model assumptions of which were in any case tested through sensitivity analysis. The final temperature dependence for $k_{(4.1)}$ recorded here shows considerable scatter, reflected in the statistical error in the Arrhenius parameters reported. However, the data here exhibit a clear negative temperature dependence in agreement with previous high pressure studies of $k_{(4.1)}$. As indicated by several previous theoretical studies,[25,31,32] this might imply the collisional stabilisation of a HO_3Cl moiety at high pressures, in addition to “bimolecular” channels predominating at low pressures. This may imply, as has also been proposed previously,[31] that the HO_3Cl, specifically HOOOCl, species might form in the lower stratosphere and therefore the potential photolysis channels of this molecule would govern its atmospheric impact. At the very least, the data reported in the present study confirm and quantify the efficiency of the HO_2 + ClO reaction and its key role in midlatitude ozone loss.

4.4.4 Atmospheric Implications

The strong negative temperature dependence of this work for reaction (4.1) predicts that this reaction is more efficient at all tropospheric temperatures down to stratospheric when compared to previous work. As a mechanism in partitioning active Cl and HO_2 into relatively inactive reservoir species through the formation of HOCl, the relative importance of reaction (4.1) is enhanced when comparing this work to the competing Cl reservoir forming heterogeneous chemistry occurring on cirrus clouds in the UT/LS region at low latitudes. Furthermore, this work suggests that the importance of this chemistry may not be restricted to the remote marine boundary layer in the troposphere where mixing ratios of NO_x, BrO and IO are low which all react with ClO efficiently. In particular, reaction (4.1) could perhaps be more effective as a loss of ClO around coastal areas at high latitudes than currently thought. However, the large mixing ratios of BrO and IO in these regions probably precludes this but if the efficiency of reaction (4.1) is as significant as shown here, the range in which this reaction is important throughout the atmosphere is increased.

4.5 Conclusions

The present study represents a study of the ClO decay chemistry in the presence of HO_2, with a technique (CCD monitoring and multiwavelength/time resolved spectroscopy) that is especially suited to ClO monitoring. The ClO traces recorded in the absence of methanol, and therefore HO_2 were readily fit to a two reaction model with only small perturbations for physical processes, giving confidence in this monitoring. In the subsequent presence of CH_3OH and excess oxygen, well-established chemistry was used to generate HO_2 and the ClO decay traces exhibited temporal behaviour consistent with a termination reaction of ClO + HO_2. Rate constants reported in this work were higher and exhibited a stronger negative temperature dependence than those reported previously. Several of these studies were carried out at low pressure, thus the present work is perhaps indicative of a pressure dependent contribution to reaction (4.1).

4.6 References

1. WMO, *(World Meteorological Organization), Scientific Assessment of Ozone Depletion: 2010, Global Ozone Research and Monitoring Project-Report No. 52, 516 pp., Geneva, Switzerland, 2011*, 2010.
2. Anderson, J.G., D.W. Toohey, and W.H. Brune, Free Radicals within the Antarctic Vortex - the Role of CFCs in Antarctic Ozone Loss. *Science*, 1991. **251**(4989): 39-46.
3. Johnson, D.G., W.A. Traub, K.V. Chance, K.W. Jucks, and R.A. Stachnik, Estimating the Abundance of ClO from Simultaneous Remote Sensing

Measurments of HO_2, OH and HOCl. *Geophysical Research Letters*, 1995. **22**(14): 1869-1871.

4. Wuebbles, D.J. and K. Hayhoe, Atmospheric methane and global change. *Earth-Science Reviews*, 2002. **57**(3-4): 177-210.
5. Hanisco, T.F., E.J. Lanzendorf, P.O. Wennberg, K.K. Perkins, R.M. Stimpfle, P.B. Voss, J.G. Anderson, R.C. Cohen, D.W. Fahey, R.S. Gao, E.J. Hintsa, R.J. Salawitch, J.J. Margitan, C.T. McElroy, and C. Midwinter, Sources, sinks, and the distribution of OH in the lower stratosphere. *Journal of Physical Chemistry A*, 2001. **105**(9): 1543-1553.
6. Danielsen, E.F., A Dehydration Mechanism for the Stratosphere. *Geophysical Research Letters*, 1982. **9**(6): 605-608.
7. Khaykin, S., J.P. Pommereau, L. Korshunov, V. Yushkov, J. Nielsen, N. Larsen, T. Christensen, A. Garnier, A. Lukyanov, and E. Williams, Hydration of the lower stratosphere by ice crystal geysers over land convective systems. *Atmospheric Chemistry and Physics*, 2009. **9**(6): 2275-2287.
8. Pommereau, J.P., Troposphere-to-Stratosphere Transport in the Tropics. *Comptes Rendus Geoscience*, 2010. **342**(4-5): 331-338.
9. Kovalenko, L.J., K.W. Jucks, R.J. Salawitch, G.C. Toon, J.F. Blavier, D.G. Johnson, A. Kleinbohl, N.J. Livesey, J.J. Margitan, H.M. Pickett, M.L. Santee, B. Sen, R.A. Stachnik, and J.W. Waters, Observed and Modeled HOCl Profiles in the Midlatitude Stratosphere: Implication for Ozone Loss. *Geophysical Research Letters*, 2007. **34**(19).
10. von Clarmann, T., B. Funke, N. Glatthor, S. Kellmann, M. Kiefer, O. Kirner, B.M. Sinnhuber, and G.P. Stiller, The MIPAS HOCl climatology. *Atmospheric Chemistry and Physics*, 2012. **12**(4): 1965-1977.
11. Sander, S.P., J. Abbatt, J. R. Barker, J. B. Burkholder, R. R. Friedl, D. M. Golden, R. E. Huie, C. E. Kolb, M. J. Kurylo, G. and V.L.O.a.P.H.W. K. Moortgat, "Chemical Kinetics and Photochemical Data for Use in Atmospheric Studies, Evaluation No. 17," JPL Publication 10-6, Jet Propulsion Laboratory, Pasadena, 2011 http://jpldataeval.jpl.nasa.gov.
12. Stimpfle, R.M., R.A. Perry, and C.J. Howard, Temperature Dependence of the Reaction of ClO and HO_2 Radicals. *Journal of Chemical Physics*, 1979. **71**(12): 5183-5190.

13. Anderson, J.G., D.M. Wilmouth, J.B. Smith, and D.S. Sayres, UV Dosage Levels in Summer: Increased Risk of Ozone Loss from Convectively Injected Water Vapor. *Science*, 2012. **337**(6096): 835-839.
14. von Hobe, M., J.U. Grooss, G. Gunther, P. Konopka, I. Gensch, M. Kramer, N. Spelten, A. Afchine, C. Schiller, A. Ulanovsky, N. Sitnikov, G. Shur, V. Yushkov, F. Ravegnani, F. Cairo, A. Roiger, C. Voigt, H. Schlager, R. Weigel, W. Frey, S. Borrmann, R. Muller, and F. Stroh, Evidence for heterogeneous chlorine activation in the tropical UTLS. *Atmospheric Chemistry and Physics*, 2011. **11**(1): 241-256.
15. Reimann, B. and F. Kaufman, Rate Constant of Reaction HO_2 + ClO → HOCl + O_2. *Journal of Chemical Physics*, 1978. **69**(6): 2925-2926.
16. Leck, T.J., J.E.L. Cook, and J.W. Birks, Studies of Reactions of Importance in the Stratosphere 3: Rate constant ans Products of the Reaction Between ClO and HO_2 Radicals at 298 K. *Journal of Chemical Physics*, 1980. **72**(4): 2364-2373.
17. Burrows, J.P. and R.A. Cox, Kinetics of Chlorine Oxide Radical Reactions Using Modulated Photolysis 4. The Reactions of Cl + Cl_2O Cl_2 + ClO and HO_2 + ClO - Products Studied at 1 atm and 300 K. *Journal of the Chemical Society-Faraday Transactions I*, 1981. **77**: 2465-2479.
18. Atkinson, R., D.L. Baulch, R.A. Cox, J.N. Crowley, R.F. Hampson, R.G. Hynes, M.E. Jenkin, M.J. Rossi, and J. Troe, Evaluated kinetic and photochemical data for atmospheric chemistry: Volume III - gas phase reactions of inorganic halogens. *Atmospheric Chemistry and Physics*, 2007. **7**: 981-1191.
19. Hickson, K.M., L.F. Keyser, and S.P. Sander, Temperature dependence of the HO_2 + ClO reaction. 2. Reaction kinetics using the discharge-flow resonance-fluorescence technique. *Journal of Physical Chemistry A*, 2007. **111**(33): 8126-8138.
20. Nickolaisen, S.L., C.M. Roehl, L.K. Blakeley, R.R. Friedl, J.S. Francisco, R.F. Liu, and S.P. Sander, Temperature dependence of the HO_2 + ClO reaction. 1. Reaction kinetics by pulsed photolysis-ultraviolet absorption and *ab initio* studies of the potential surface. *Journal of Physical Chemistry A*, 2000. **104**(2): 308-319.
21. Knight, G.P., T. Beiderhase, F. Helleis, G.K. Moortgat, and J.N. Crowley, Reaction of HO_2 with ClO: Flow tube studies of kinetics and product formation between 215 and 298 K. *Journal of Physical Chemistry A*, 2000. **104**(8): 1674-1685.

22. Cattell, F.C. and R.A. Cox, Pressure-Dependence of the Reactions of HO_2 with Cl and ClO. *Journal of the Chemical Society-Faraday Transactions II*, 1986. **82**: 1413-1426.
23. Finkbeiner, M., J.N. Crowley, O. Horie, R. Muller, and G.K. Moortgat, Reaction Between HO_2 and ClO - Product Formation Between 210 AND 300 K. *Journal of physical chemistry*, 1995. **99**(44): 16264-16275.
24. Leu, M.T., Product Distribution for the Reaction of HO_2 with ClO. *Geophysical Research Letters*, 1980. **7**(2): 173-175.
25. Zhu, R.S. and M.C. Lin, *Ab initio* chemical kinetics for ClO reactions with HO_x, ClOx and NOx (x=1, 2): A review. *Computational and Theoretical Chemistry*, 2011. **965**(2-3): 328-339.
26. Ferracci, V. and D.M. Rowley, Kinetic and thermochemical studies of the ClO + ClO + M reversible arrow Cl_2O_2 + M reaction. *Physical Chemistry Chemical Physics*, 2010. **12**(37): 11596-11608.
27. Rowley, D.M., M.H. Harwood, R.A. Freshwater, and R.L. Jones, Novel flash photolysis UV absorption system employing charge-coupled device (CCD) detection: A study of the BrO + BrO reaction at 298 K. *Journal of physical chemistry*, 1996. **100**(8): 3020-3029.
28. Stone, D. and D.M. Rowley, Kinetics of the gas phase HO_2 self-reaction: Effects of temperature, pressure, water and methanol vapours. *Physical Chemistry Chemical Physics*, 2005. **7**(10).
29. Hinshelwood, C.N. and C.R. Prichard, A homogeneous gas reaction - The thermal decomposition of chlorine monoxide Part I. *Journal of the Chemical Society*, 1923. **123**: 2730-2738.
30. Boakes, G., W.H.H. Mok, and D.M. Rowley, Kinetic studies of the CIO + CIO association reaction as a function of temperature and pressure. *Physical Chemistry Chemical Physics*, 2005. **7**(24): 4102-4113.
31. Kaltsoyannis, N. and D.M. Rowley, Ab initio investigations of the potential energy surfaces of the XO + HO_2 reaction (X = chlorine or bromine). *Physical Chemistry Chemical Physics*, 2002. **4**(3): 419-427.
32. Xu, Z.F., R.S. Zhu, and M.C. Lin, *Ab initio* studies of ClO_x reactions: VI. Theoretical prediction of total rate constant and product branching probabilities for the HO_2 + ClO reaction. *Journal of Physical Chemistry A*, 2003. **107**(19): 3841-3850.

Chapter 5: The Kinetics of the ClO + CH_3O_2 Reaction

5.1 Introduction

As discussed in Chapter 1, the separate halogen oxide and peroxy radical families partake in a number of atmospherically important reaction cycles throughout the troposphere and stratosphere. In particular, the coupling of chlorine monoxide, ClO, chemistry with the hydroperoxy radical, HO_2, was discussed in the previous chapter. It was found that these two species react very efficiently with one another, increasingly so at the low temperatures which correlate to certain regions in the atmosphere where these species are most likely to come into contact with one another. This chapter will present experimental work investigating the kinetic behaviour of another halogen oxide-peroxy radical reaction; the stratospherically relevant reaction of chlorine monoxide with the methylperoxy radical:

$$ClO + CH_3O_2 \rightarrow Products \qquad (5.1)$$

Organoperoxy radicals (RO_2) play significant roles in determining the oxidative capacity of the troposphere. As with HO_2, organoperoxy radicals also react with a number of other important trace atmospheric species. For example, the conversion of NO to NO_2 by RO_2 ultimately leads to ozone formation in polluted regions and the self and cross-reactions of peroxy radicals lead to a number of different product channels which can be either radical terminating or propagating. The presence of methane in the atmosphere, through its relatively high abundance over other reduced carbon species, represents the source of the most abundant organoperoxy, the methylperoxy radical, CH_3O_2. As a consequence of the atmospheric lifetime of methane (~ 8 years), it is also able to cross the tropopause and enter the stratosphere. On reaching the stratosphere, CH_4 degradation is initiated by a number of possible reactions: by reaction with the hydroxyl radical; the abundant electronically excited $O(^1D)$ atoms; or by chlorine atoms:

$$CH_4 + X \rightarrow XH + CH_3 \qquad (5.2)$$

where X = OH, $O(^1D)$ or Cl. The resultant methyl radical subsequently reacts with abundant molecular oxygen, forming the methyl peroxy radical:

$$CH_3 + O_2 + M \rightarrow CH_3O_2 + M \qquad (5.3)$$

where M is a third body. The reaction of stratospheric CH_3O_2 with ClO in the Polar regions is believed to play a significant role in converting the reservoir species HCl to the active Cl species[1,2] which is inextricably linked to the annual Springtime "ozone hole" observed in Antarctica and increasingly in the Arctic.[3-5] This is due to the occurrence of several different product channels, one of which leads to the intermediate ClOO species which can rapidly decompose thermally, even at stratospheric temperatures, to give Cl:

$$ClOO + M \rightarrow Cl + O_2 + M \qquad (5.4)$$

Therefore, an understanding of reaction (5.1) is of importance as the kinetics of ClOO and the consequent Cl formation has implications for understanding the ozone destruction observed in the Wintertime Polar vortices. Similarly the co-products of reaction (5.1) may lead to direct effects upon stratospheric ozone levels.

5.1.1 Previous Studies of ClO + CH_3O_2

There have been a number of previous studies of reaction (5.1), investigating the kinetics and product distribution as a function of temperature. Unlike the analogous reaction of ClO with HO_2, there exists for (5.1) a possible radical non-terminating channel:

$$ClO + CH_3O_2 \rightarrow ClOO + CH_3O \qquad (5.1a)$$

$$\rightarrow CH_3OCl + O_2 \qquad (5.1b)$$

$$\rightarrow HCHO + HCl + O_2 \qquad (5.1c)$$

The products of (5.1a) lead to the formation of Cl *via* the subsequent thermal decomposition of ClOO. Further, the reaction of CH_3O with oxygen results in the formation of HO_2. Thus the branching of reaction (5.1) has atmospheric implications concerning both the stratospheric ozone and HO_x budgets.

The kinetics and product branching of the ClO + CH_3O_2 reaction were first studied at ambient temperature by Simon *et al.*[6] employing the broadband photolysis of $Cl_2/Cl_2O/CH_4/O_2$ mixtures, using molecular modulation UV absorption spectroscopy detection at around p = 310 mbar. Subsequently Helleis *et al.*[7,] investigated the absolute rate coefficient and later in a separate study[8] the branching ratio, $k_{(5.1a)}/k_{(5.1)}$, as a function of temperature (T = 215 – 295 K) and pressure (p = 2.3 – 4.0 mbar) using a flow tube technique with mass spectrometric detection. A study from Kenner *et al.*[9] in the same year measured the absolute rate coefficient only of reaction (5.1) at T = 293 K and p = 2.5 mbar again using a flow tube technique with mass spectrometric detection. Kukui *et al.*[10] measured $k_{(5.1a)}/k_{(5.1)}$ and the absolute rate coefficient from T = 233 – 300 K in a flow tube using at p = 5 – 6 mbar, monitoring both parent ions *via* mass spectrometry. Another two separate flow tube investigations of the branching $k_{(5.1a)}/k_{(5.1)}$ at room temperature (T = 298 K) were reported by Biggs *et al.*[11] and Daele and Poulet[12] at p = 2.7 mbar and p = 1.3 mbar respectively. Both studies used both mass spectrometry and laser induced fluorescence to detect ClO and CH_3O respectively. The most recent study of reaction (5.1) was by Leather *et al.*[13] who measured the absolute rate coefficient $k_{(5.1)}$ as a function of pressure (p = 100 – 200 Torr) and temperature (T = 298 – 223 K) using a turbulent flow technique with a chemical ionisation mass spectrometry detection system.

There is general agreement that channels (5.1a) and (5.1b) are the only significant pathways operating for the title reaction at stratospheric temperatures.[7-11,13] However, there is considerable disagreement concerning the relative importance of these two channels with a number of studies reporting conflicting findings as to which one is the dominant pathway. As a result of this discrepancy, JPL NASA[14] do not recommend a branching ratio at any temperature. Simon *et al.*[6], Helleis *et al.*[7], Kukui *et al.*[10] and Helleis *et al.*[8] all report channel (5.1a) being the dominant pathway at T = 298 K whereas later studies from Biggs *et al.*[11] and Daele and Poulet[12] report it as being the minor.

Study	T / K	$k_{(5.1)}{}^{a}$	A factor^{a}	E/R/ K
Simon *et al.*[6]	300	$(3.1 \pm 1.7) \times 10^{-12}$	-	-
Helleis *et al.*[7]	295	$(2.2 \pm 0.1) \times 10^{-12}$	3.25×10^{-12}	114 ± 38
Kenner *et al.*[9]	293	$(1.9 \pm 0.4) \times 10^{-12}$	-	-
Kukui *et al.*[10]	300	$(2.5 \pm 0.3) \times 10^{-12}$	2.0×10^{-12}	-80 ± 50
Leather *et al.*[13]	294	$(2.4 \pm 0.1) \times 10^{-12}$	$(2.2^{+0.28}_{-0.24}) \times 10^{-12}$	626 ± 35
JPL NASA[14]	298	$(3.3 \pm 1.6) \times 10^{-12}$	$(2.2 \pm 1.1) \times 10^{-12}$	115
IUPAC[15]	298	$(2.2 \pm 0.4) \times 10^{-12}$	$(2.4 \times 10^{-12}$	-20 ± 200

^{a}*Units in* cm^3 *molecule*$^{-1}$*s*$^{-1}$

***Table 5.1** Literature results of the overall rate constant for reaction (5.1).*

The work of Simon *et al.*[6] is the only study to use absorption spectroscopic detection of radicals in reaction (5.1) rather than laser induced fluorescence or mass spectrometry. The Simon *et al.*[6] study used modulated photolysis of $Cl_2/CH_4/Cl_2O/O_2$ mixtures with absorption spectroscopy in the IR and UV regions at ambient temperature. However changes in optical density rather than direct measurements of concentrations and extensive modelling had to be used in evaluating the overall rate constant, $k_{(5.1)}$. Helleis *et al.*,[7] and Kukui *et al.*[10] evaluated $k_{(5.1)}$ at room temperature as well as Kenner *et al.*[9] and these values are given in Table 5.1 along with those of Simon *et al.*[6] and the most recent determination from Leather *et al.*[13] The temperature dependence of reaction (5.1) has also been evaluated by Helleis *et al.*,[7] Kukui *et al.*[10] and Leather *et al.*[13] Both Helleis *et al.*[7] and Kukui *et al.*[10] report only a slight temperature dependence but they disagree with one another on the direction of this temperature dependence with Helleis *et al.*[8] reporting a positive dependence and Kukui *et al.*[10] a negative (Table 5.1). However the recent pressure and temperature kinetic study on reaction (5.1) by Leather *et al.*[13] found a much stronger, positive, temperature dependence, with a reported *E/R* value over 5 times that reported by Helleis *et al.*[8] The previous literature temperature parameterisations and ambient temperature determinations of (5.1) are shown in Figure 5.18***Figure 5.19*** and 5.19 in the discussion.

Computational studies shed further light on the mechanism and generally corroborate with experimental studies on the possible product channels of the title reaction. A recent computational characterization of the reaction between methylperoxy radicals and ClO has been carried out by Kosmas *et al.*[16] The calculations suggest a potential mechanism for the existence of the two important channels observed experimentally, leading to CH_3O + ClOO (5.1a) and CH_3OCl + O_2 (5.1b) products. More specifically, this comprehensive re-evaluation of the exothermicity of channel (5.1a) using spin-restricted methods, describes satisfactorily the experimental evidence about the significance of this channel as the most important pathway. The methyl hypochlorite production channel (5.1b), is also shown to be significant and thermodynamically possible through either the singlet or the triplet potential energy surface. Reaction channel (5.1c) was also investigated and found to be thermodynamically accessible, with the HOOCl product expected to readily dissociate to HCl and O_2 (Figure 5.1).

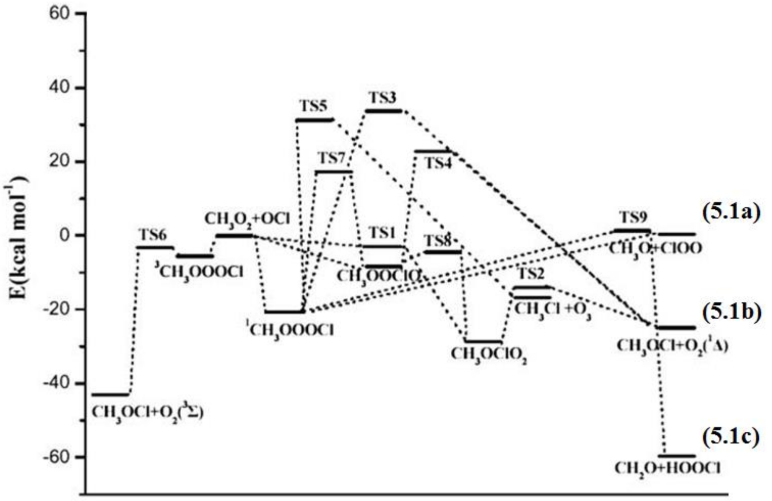

Figure 5.1 *A potential energy diagram showing the energy maxima and minima of the predicted transition states of the reaction channels for reaction (5.1). From Kosmas et al.*[16]

5.2 Experimental

5.2.1 Principles of the Experiment

The ClO + CH_3O_2 reaction was studied *via* the laser flash photolysis of suitable precursor gas mixtures coupled with time-resolved UV absorption spectroscopy to detect the radical species generated. The absorption of ultraviolet radiation was monitored using a charge-coupled-device (CCD) detector[17] as discussed in Chapter 3. This enabled the simultaneous broadband wavelength and rapid time-resolved recording of the analysis light which was passed through the temperature controlled photolysis gas mixture, which in turn, allowed the accurate and unambiguous determination of ClO radical concentrations as a function of time using ‘differential’ spectroscopy discussed in Chapter 3. Analogously to the work reported in Chapter 4, in the study of the ClO + HO_2 reaction, the principle of these experiments was that ClO radicals were principally generated from reactions of initially photolytically generated chlorine atoms. In subsequent experiments, the addition of methane gas to the precursor gas mixture led to a competition for the initial Cl atoms which, in the presence of excess oxygen, subsequently produced CH_3O_2 radicals both rapidly and stoichiometrically. Similarly to the HO_2 radicals described in Chapter 4, CH_3O_2 could not be directly monitored spectroscopically. However, the presence of CH_3O_2 could be inferred from the perturbed ClO signal during these experiments (compared to experiments carried out in the absence of CH_4), showing a lower initial ClO concentration (attributed to CH_3O_2 production) and a faster decay of the ClO radicals (attributed to the ClO + CH_3O_2 reaction) which exhibited sensitivity principally to the ClO + CH_3O_2 reaction. Temporal traces of ClO concentration were then analysed to extract kinetic parameters. The products of reaction (5.1) are also spectrally unstructured absorbers in the UV, hence they were unable to be monitored under the experimental conditions employed in this work.

5.2.2 Experimental

The kinetics of the ClO + CH_3O_2 reaction was studied using the laser flash photolysis/UV absorption spectroscopy apparatus described in detail in Chapter 3. Precursor gas mixture concentrations were first designed using numerical integration simulations of the expected and generally well known immediate post-photolysis chemistry. Gas mixtures were prepared, in a balanced continuous carrier flow of typically oxygen, using flows of the precursor gas CH_4 which were both set using calibrated mass flow controllers (MKS). For the corrosive chlorine gas (supplied as diluted, 5% in nitrogen), flows were controlled using a PTFE needle valve and measured using a calibrated glass ball flow meter. The total flow rate of gases in the reactor, was such that the loss of species *via* flowout during an experiment was insignificant on the timescales of the kinetic processes under investigation and accounted for in the analytic procedures. Reactions in this work were all performed at ambient atmospheric pressure, (p = 760 ± 20 Torr) as determined using a capacitance manometer (MKS Baratron). Radicals were principally formed from atomic species themselves, generated from laser photolysis, as discussed in previous chapters. As also discussed in Chapters 3 and 4, the species in the reaction vessel were monitored using time resolved ultraviolet absorption spectroscopy.

5.2.3 Radical Formation

ClO radicals were generated *via* laser photolysis of Cl_2/Cl_2O mixtures in an oxygen or synthetic air carrier flow as in Chapter 4. The principal source of ClO radicals resulted from the reaction of Cl atoms with an excess of dichlorine monoxide (formed by reaction 5.5, as in Chapter 4), Cl_2O, and ClO radicals were therefore principally initially formed by the photolytic breakdown of molecular chlorine:

$$2Cl_2(g) + HgO(s) \rightarrow Cl_2O(g) + HgCl_2(s) \tag{5.5}$$

$$Cl_2 + h\nu \rightarrow 2Cl \tag{5.6}$$

$$Cl + Cl_2O \rightarrow Cl_2 + ClO \tag{5.7}$$

The direct photolysis of Cl_2O also contributed a minor source of ClO, given the smaller cross section of Cl_2O compared to Cl_2 at the 351 nm photolysis laser wavelength (σ_{Cl_2} (351 nm) = 1.8 × 10^{-19} cm^2 $molecule^{-1}$, σ_{Cl_2O}(351 nm) = 7.0 × 10^{-21} cm^2 $molecule^{-1}$).[14] A T-junction was placed upstream of the HgO trap as to potentially bypass it and a needle valve allowed the control of the amount of Cl_2 passed through the trap in order to optimise the initial ClO concentration under methane free conditions.

For the generation of CH_3O_2, atomic chlorine reacted (competitively) with varied amounts of methane within the precursor mixture, in the presence of a large excess of molecular oxygen:

$$Cl + CH_4 \rightarrow HCl + CH_3 \qquad (5.8)$$

$$CH_3 + O_2 + M \rightarrow CH_3O_2 + M \qquad (5.9)$$

Precursor concentrations were: $[Cl_2] = (2.5 - 3.5) \times 10^{16}$ molecules cm^{-3}; $[Cl_2O] = (1.0 - 2.0) \times 10^{15}$ molecules cm^{-3} (measured spectroscopically); $[CH_4] = (0.2 - 1.1) \times 10^{19}$ molecules cm^{-3} with the carrier gas balanced to a total flow rate of 810 SCCM (1 atm). These concentrations ensured that the photolytically generated Cl atoms were always rapidly (on the timescale of subsequent chemistry) and stoichiometrically consumed, principally producing either ClO or CH_3O_2 radicals. Typical initial (immediately post-photolysis) radical concentrations were in the range $(0.7 - 1.5) \times 10^{14}$ molecules cm^{-3}.

5.2.4 Monitoring of Species

The radical species generated in the reaction vessel were monitored using UV spectroscopy as described in Chapter 3 and in an identical fashion as described in Chapter 4. Figure 5.2, below, shows the absorption cross sections of the main absorbers present in the experimental post-photolysis gas mixtures.

This figure shows that the strongest CH_3O_2 absorptions are separated by around 30 nm from the 'fingerprint' ClO vibronic transitions. Therefore, the simultaneous spectroscopic monitoring of both transient species, using the high resolution settings, is possible in theory as the spectral window with such settings on the spectrograph is around 65 nm. However, the number of significant absorbers in this system, both transient and stable, is far greater in this photolysis system than that of Chapter 4, owing to the extent of secondary chemistry that inevitably occurs (discussed below). Hence, the number of spectrally smooth absorbers arising from principally HO_2 chemistry, would be expected to optically mask CH_3O_2 absorption owing to their cumulative absorption, which is dependent on the abundance and/or size of the relative absorption cross sections of any given species. Therefore only ClO, the only absorbing species with identifiable vibronic structure, was chosen to be monitored during a photolysis experiment and other radical concentrations were inferred, analogously to those described in the preceding chapter.

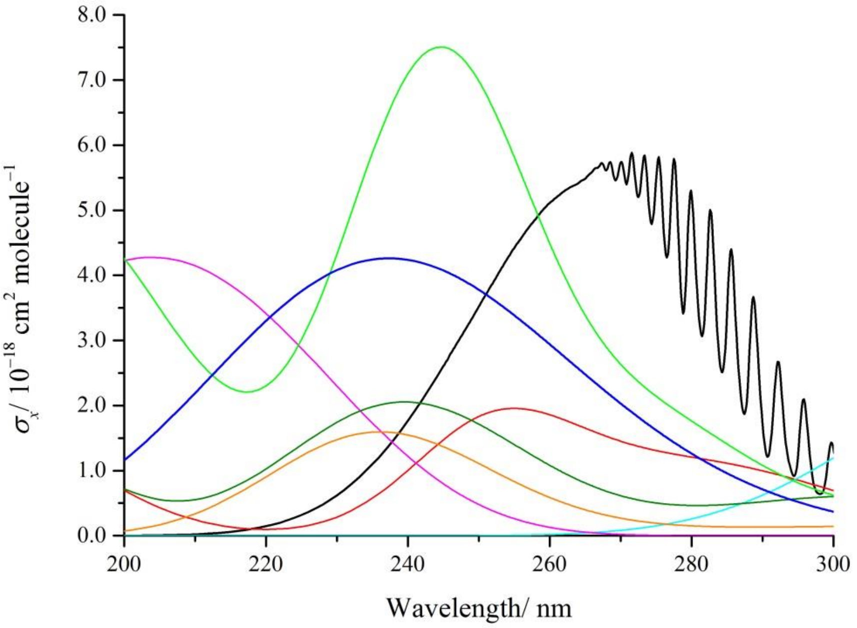

Figure 5.2 *Absorption cross sections, σ_x, of the key absorbing species in the photolysed Cl_2/Cl_2O/CH_4/O_2 system: ClO (black); CH_3O_2 (blue); HO_2 (pink); Cl_2O_2 (light green); Cl_2O (red); Cl_2 × 10 (light blue); HOCl × 10 (green); CH_3OCl × 10 (orange).*[14]

For the kinetic experiments, the spectrograph was principally set with a diffraction grating or 600 grooves/mm and an entrance slit width of 112 μm as in the experiments described in Chapter 4. The spectra were recorded over a wavelength range of λ = 262.9 – 296.2 nm with a spectral resolution of 0.8 nm full-width half-maximum (FWHM). Wavelength calibration and spectral resolution were verified in separate experiments recording the emission spectrum from a mercury ‘pen-ray’ lamp (Appendices I & II). Experiments were performed recording time resolved spectra before, during and after laser photolysis over a total timescale of typically 100 μs/spectrum. Typically, for each determination of $k_{5.1}$, 10 – 50 photolysis experiments were conducted with the results co-added and at least six determinations were conducted at each experimental temperature.

Figure 5.3 illustrates the differences in ClO absorption between photolysis experiments in the absence or presence of methane. The extent of the difference between the averaged absorption spectra of a photolysis experiment performed in the absence of methane, to those recorded in the presence of methane in the same series of experiments, was clearly dependent on the amount of methane present. Hence the presence of methane resulted in changes in the overall optical density of the photolysed mixtures, which further implies there were changes in the resultant photochemistry.

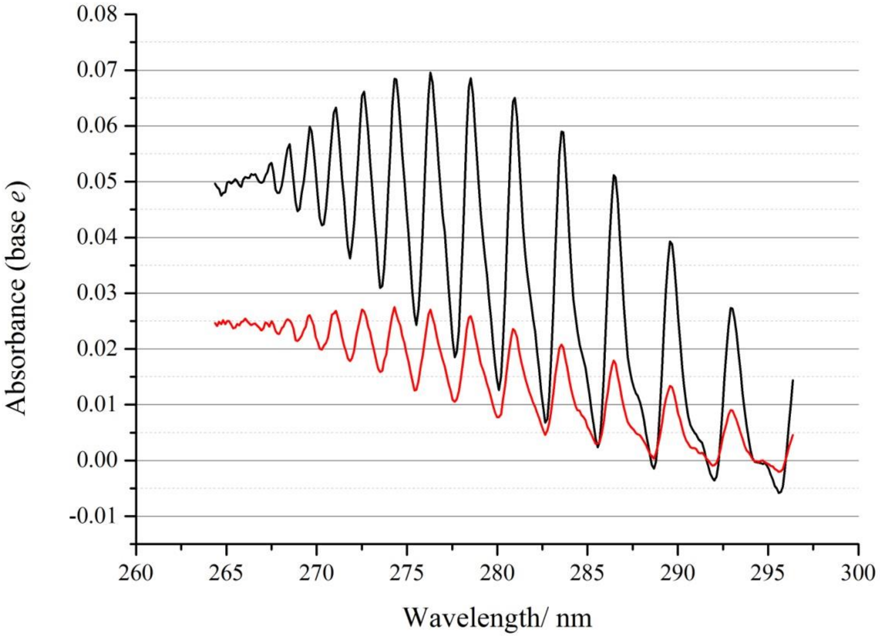

Figure 5.3 *A typical example of time averaged absorption spectra for photolysis experiments for $Cl_2/Cl_2O/O_2/N_2$ in the absence of methane (black) and in the presence of methane (red).*

5.2.5 Determination of ClO Concentrations

ClO was the only reactant or product of reaction (5.1) monitored in this work thus accurate knowledge of its absolute concentration as a function of time was essential to the analysis of the kinetics of said reaction. Crucial to this work was the application of 'differential' spectroscopy *i.e.* the filtering of the absorptions of overlapping smooth absorbers from each absorption spectrum which left the sole structured absorptions originating from the vibronic transitions of ClO. The same spectral resolution was used in these experiments as in Chapter 4, thus the identical temperature dependent ‘differential’ absorption cross sections for the representative 12–0 vibronic band of ClO was used, corresponding to the difference between the peak at around λ = 275.2 nm minus the trough at λ = 276.4 nm.[19]

These calibrated spectra were then fit to the time resolved spectra differentially, an example of which is given below in Figure 5.4, to generate [ClO] *versus* time profiles as described in Chapter 4. These temporal traces of [ClO] were subsequently analysed as discussed in the next section.

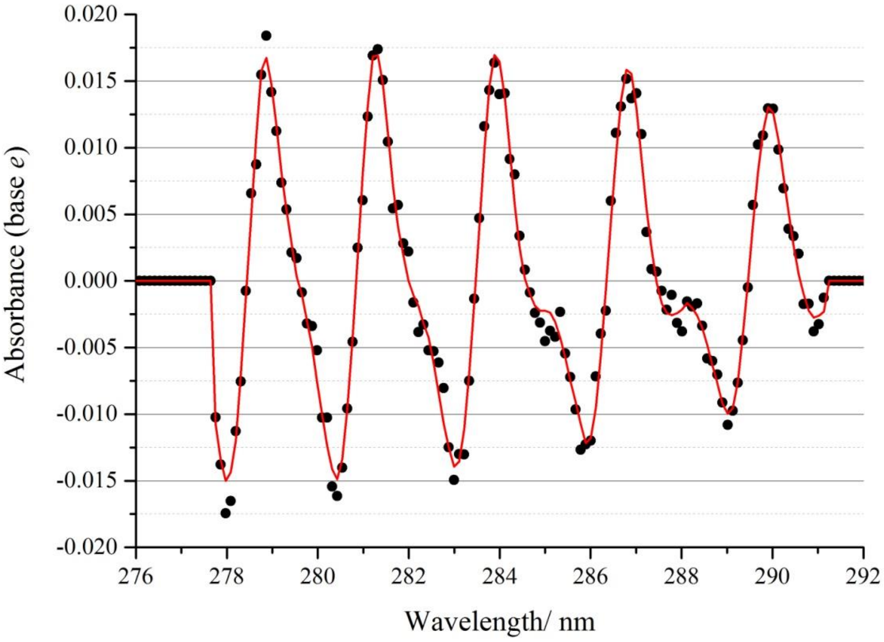

***Figure 5.4** Differential fitting to a ClO spectrum at T = 298 K, t = 0.013 s post flash. The black dots represent the recorded spectrum and the red line is the scaled ClO differential cross section.*

5.3 Results and Kinetic Analysis

5.3.1 Temporal Profiles of [ClO] Recorded in the Absence and Presence of CH_4

Temporal traces of ClO concentration were obtained as described above. At each temperature, measurements of [ClO] were made from photolysed precursor gas mixtures in the absence of methane. Separate [ClO] measurements were subsequently recorded under identical conditions except with the addition of methane into the precursor gas mixture. Under these conditions it was expected that additional chemical processes would take place principally *via* reaction (5.1), thus affecting the temporal behaviour of ClO compared to that recorded under methane-free conditions. Figure 5.5 below, shows a series of typical ClO traces obtained from five separate photolysis experiments carried out under near identical conditions except for the amount of methane present at T = 287 K. The initial trace, shown in black, was carried out under methane free conditions. For the subsequent experiments, depicted as the blue, red and green traces, an increasing flow of methane was added to the precursor mixture in each experiment accordingly. The final experiment shown in this series, in yellow, was carried out after the methane had been removed and was therefore under methane free conditions once more. These experiments exhibit the general features of each set of experiments carried out at each temperature in this study. It is clear that for each experiment, the temporal ClO behaviour is strongly dependent on the level of methane present. Most noticeable is the drop in the maximum initial ClO concentration post-photolysis, $[ClO]_{max}$, compared to the ClO traces in which there is no methane. Importantly, the traces of the first and last experiments with each series, performed under methane free conditions, are very similar to one another showing that there was only a small drift in experimental conditions over the time frame in which the series of experiments was recorded and this was typical for most temperatures.

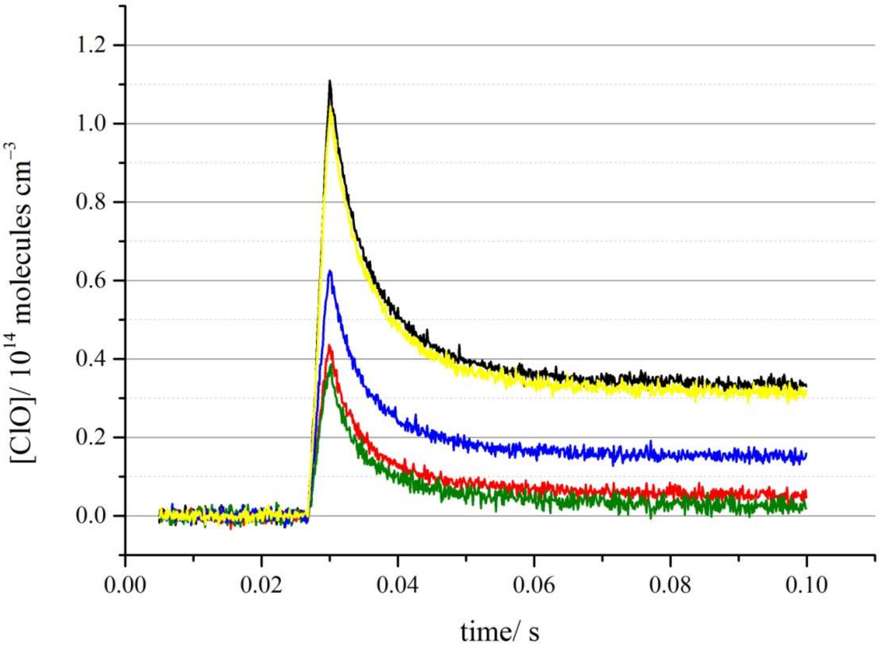

Figure 5.5 *$[ClO]_t$ from a series of photolysis experiments performed at T = 287 K as a function of $[CH_4]$/ molecules cm^{-3}: $[CH_4]$= 0 (black); $[CH_4] = 3.10 \times 10^{18}$ (blue); $[CH_4] = 5.25 \times 10^{18}$ (red); $[CH_4] = 7.40 \times 10^{18}$ (green); and $[CH_4] = 0$ (yellow).*

As with the inclusion of methanol in experiments described in Chapter 4 for the analogous ClO + HO_2 study, there was a clear decrease in $[ClO]_{max}$ when methane was present in the reactor. This divergence of $[ClO]_{max}$ from CH_4 free conditions became more significant at higher $[CH_4]$ as shown below in Figure 5.6. This behaviour was attributed to the competition of Cl atoms between Cl_2O and CH_4, in which there was a decrease in the fraction of Cl formed post-photolysis reacting to form ClO, *i.e.* reaction (5.7) became less significant with increasing $[CH_4]$. As discussed in Chapter 4, there is also a relative enhancement in the initial rate of ClO loss as compared to the expected initial loss of ClO under CH_4 free conditions with similar $[ClO]_{max}$ (Figure 5.7).

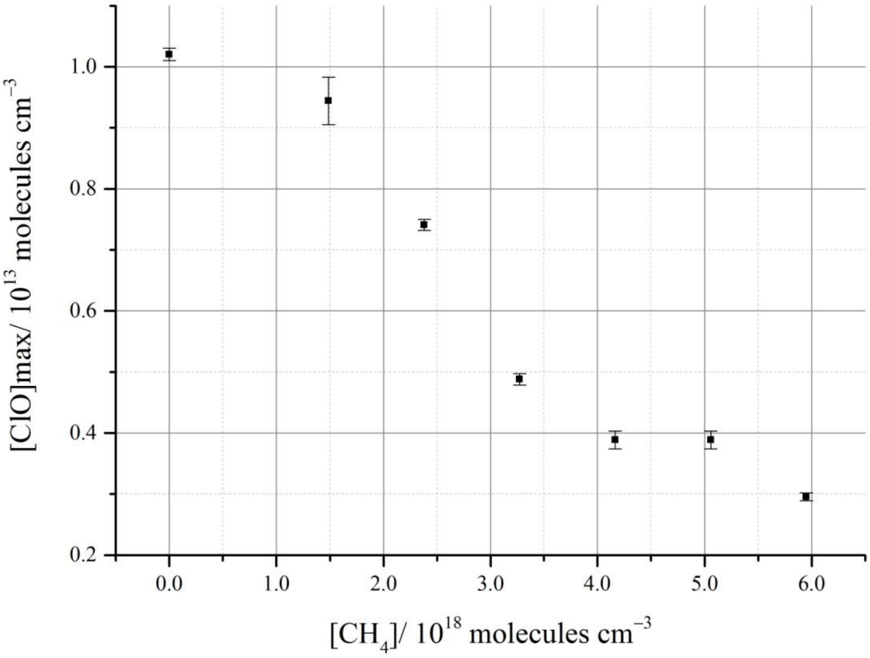

Figure 5.6 *A plot of $[ClO]_{max}$ as a function of $[CH_4]$ at T = 298 K.*

As can be seen in Figure 5.7 below, there is a significant enhancement of the rate of ClO loss when methane is present in the photolysis mixture compared to a simulated decay of ClO from the same $[ClO]_{max}$ under methane free conditions. ClO equilibrium concentrations, $[ClO]_{eq}$, defined by the observed level of [ClO] at which it remains effectively constant post-decay, were also recorded and the fraction of ClO lost was calculated:

$$\text{Fraction of [ClO] lost} = \frac{([\text{ClO}]_{\text{max}} - [\text{ClO}]_{\text{eq}})}{[\text{ClO}]_{\text{max}}} \qquad (5.3\text{ i})$$

The same analysis was carried out for simulated $[ClO]_t$ traces using pure ClO dimerisation kinetics using the same $[ClO]_{max}$ as the experimental values and compared, the results of which are displayed in Figure 5.8. For experiments performed in the presence of methane, a greater proportion of ClO is lost upon reaching equilibrium than predicted from the corresponding methane free conditions. What is more, the extent of this loss vastly increases as $[ClO]_{max}$ decreases which correlates with increasing $[CH_4]$ experimentally.

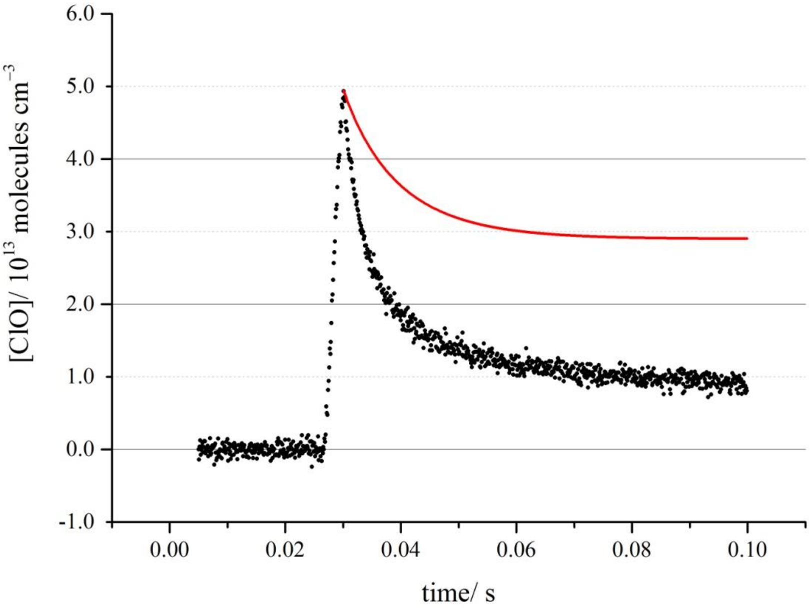

Figure 5.7 *A $[ClO]_t$ trace in the presence of methane (black points) and a simulated trace (red line) of $[ClO]_t$ recorded under methane free conditions from the same $[ClO]_0$ at T = 298 K.*

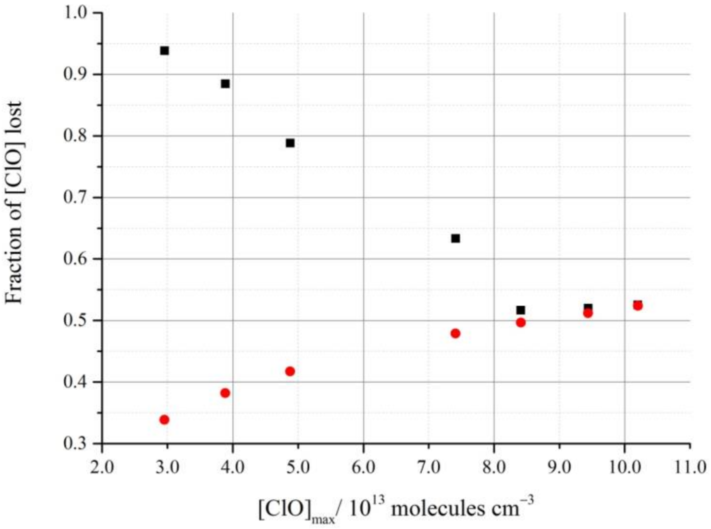

Figure 5.8 *A plot of the fraction of [ClO] lost as a function of experimental $[ClO]_{max}$ at T = 298 K for: the experimental $[ClO]_t$ (black squares); and simulated $[ClO]_t$ under methane free conditions but equivalent experimental $[ClO]_{max}$.*

Thus, the effect of increasing the amount of methane in the $Cl_2/Cl_2O/O_2$ photolysis mixtures serves to decrease the amount of ClO formed initially following photolysis and increases the relative amount that irreversibly reacts than might be assumed from ClO self-reaction chemistry alone. This in turn changes the temporal behaviour of [ClO], the kinetics of which are quantified in the following sections.

5.3.2 Analysis of the [ClO] Temporal Profiles Recorded in the Absence of CH_4

The photolysis of $Cl_2/Cl_2O/O_2$ gas mixtures in the absence of methane indicated experimental conditions in which the dominant chemistry was governed by ClO dimerisation and the reverse, thermal unimolecular decay of the dimer, Cl_2O_2, back into ClO were prevalent:

$$ClO + ClO + M \rightleftharpoons Cl_2O_2 + M \qquad (5.10)\ (-5.10)$$

This reaction has been studied extensively in this laboratory previously. Therefore, by optimising the experimental $[ClO]_t$ traces, the kinetics of reactions (5.10) and (−5.10) could be used as an actinic calibration for measuring the total radical number density, $[TR]_0$, formed upon photolysis:

$$[TR]_0 = [Cl]_0 + [ClO]_0 \qquad (5.3\ ii)$$

where $[Cl]_0$ and $[ClO]_0$ are the initial atomic chlorine and chlorine monoxide radical concentrations formed directly *via* Cl_2 and Cl_2O laser photolysis respectively.

Traces of $[ClO]_t$ were fit using a model incorporating ClO self-reaction kinetics under methane free conditions in an identical manner as described in Chapter 4. $[TR]_0$, $k_{(5.10)}$ and $k_{(-5.10)}$ were optimised accordingly at each temperature and an example of a typical fit at T = 298 K is shown in Figure 5.9, illustrating the quality of the fit between the experimental and optimised traces. The results of $[TR]_0$, $k_{(5.10)}$ and $k_{(-5.10)}$ for each temperature are presented in Table 5.2.

T / K	$[TR]_0{}^a$ / 10^{14}	$k_{(5.10)}{}^b$ / 10^{-13}	$k_{(-5.10)}{}^c$	$K_c{}^d$ / 10^{-13}	$K_p{}^e$ / 10^7
298.15	1.00 – 1.30	(5.63 ± 0.20)	36.06 ± 0.44	0.152	0.0373
287.05	(1.39 ± 0.06)	(6.96 ± 0.02)	14.46 ± 0.35	0.481	0.123
276.85	(1.33 ± 0.23)	(7.53 ± 0.62)	4.84 ± 0.06	1.56	0.413
270.1	(0.53 ± 0.02)	(11.18 ± 0.67)*	1.24 ± 0.07	9.01	2.45
267.25	(1.19 ± 0.05)	(9.15 ± 0.38)	1.49 ± 0.06	6.14	1.69
263.1	(0.49 ± 0.07)	(11.73 ± 0.60)*	0.03 ± 0.01	599	167
258.3	(1.48 ± 0.11)	(9.83 ± 0.34)	0.40 ± 0.01	24.5	6.96
249.95	(1.22 ± 0.04)	(10.00 ± 0.74)	0.10 ± 0.03	105	30.7

[a]Units of molecules cm^{-3}, [b]units of cm^3 molecule^{-1} s^{-1}, [c]units of s^{-1}, [d]units of , [e]units of atm^{-1}

Table 5.2 *Results of the kinetics and equilibrium constants of ClO dimerisation as a function of temperature.* Indicates a spurious result.*

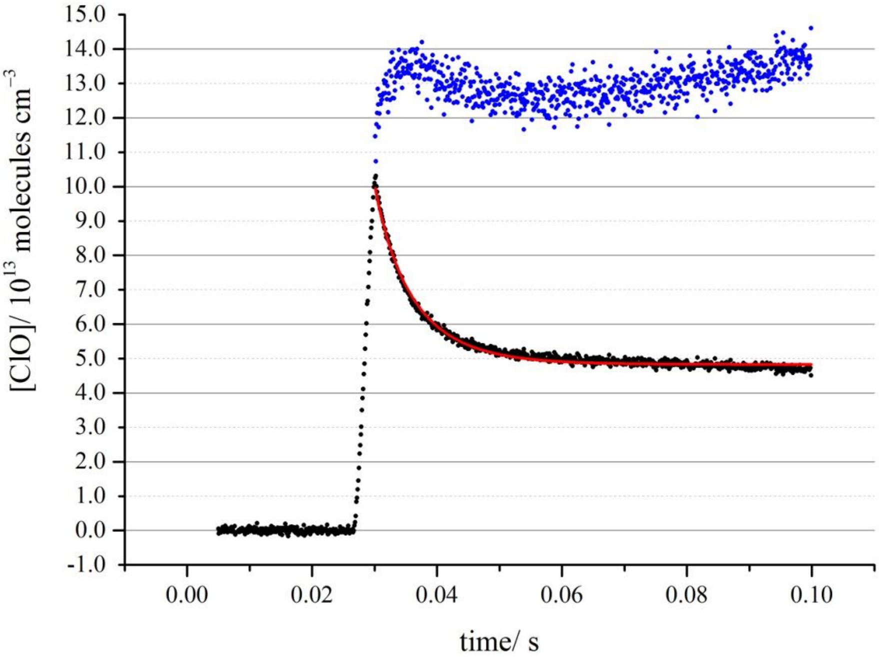

Figure 5.9 *A plot of a [ClO]$_t$ trace (black circles) with the corresponding optimised [ClO]$_t$ trace (red line) and the offset residual × 5 (blue dots).*

The equilibrium between ClO and Cl_2O_2 is clearly defined by the effective zero change in $[ClO]_t$ from around 0.06 s shown in Figure 5.9 below. The equilibrium concentration of ClO is related to the equilibrium constant, K_c, defined as:

$$K_c = \frac{[Cl_2O_2]_{eq}}{[ClO]_{eq}^2} = \frac{k_{(5.10)}}{k_{(-5.10)}} \qquad (5.3\ iii)$$

Thus the temperature dependence of K_c could be calculated and compared to previous work, irrespective of the absolute values of $k_{(5.10)}$ and $k_{(-5.10)}$. What is more, by converting K_c into K_p, which is the equilibrium constant in units of reciprocal pressure:

$$K_p/\ \text{atm}^{-1} = 101325 \times 10^{-6} \,.\, K_c \,.\, (k_B T)^{\Delta n} \qquad (5.3\ iv)$$

the experimentally determined equilibrium constant could be related to the standard Gibbs free energy change of reaction:

$$\Delta_r G° = -\,RT \ln K_p \qquad (5.3\ v)$$

$\Delta_r G°$ is itself related to the standard enthalpy of change of reaction and the standard entropy change of reaction, $\Delta_r H°$ and $\Delta_r S°$ respectively:

$$\Delta_r G° = \Delta_r H° - T\Delta_r S° \qquad (5.3\ vi)$$

Thus combining equations (5.3 v) and (5.3 vi) gives the van’t Hoff equation, linking K_p to T^{-1}:

$$\ln K_p = -\,\frac{\Delta_r H°}{R}\,T^{-1} + \frac{\Delta_r S°}{R} \qquad (5.3\ vii)$$

Hence a plot of ln K_p *versus* T^{-1} will result in a straight line of gradient $-\frac{\Delta_r H°}{R}$ and intercept $\frac{\Delta_r S°}{R}$ as shown below in Figure 5.10 where the data from this work are compared to that of Ferracci *et al.*[19] Using linear regression, the values of $\Delta_r H°$ and $-\Delta_r S°$ were found to be (86.9 ± 5.0) kJ mol^{-1} and (185.4 ± 17.5) J K^{-1} mol^{-1}

respectively, which is in agreement with Ferracci *et al.*[19] in which $\Delta_r H°$ and $-\Delta_r S°$ were found to be (80.7 ± 2.2) kJ mol^{-1} and (168.1 ± 7.8) J K^{-1} mol^{-1} when considering uncertainty.

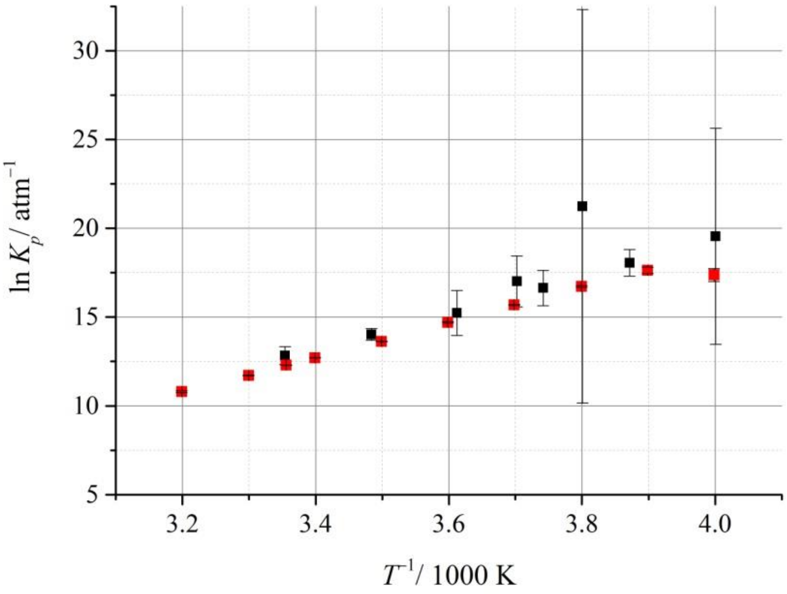

Figure 5.10 *A van't Hoff plot of the temperature dependence of K_p from: this work (black squares); and the work of Ferracci et al.*[19] *(red squares).*

The method above could have also been applied to the previous ClO self-reaction results in Chapter 4. However, the temperature range applied in this work is more suitable in deriving equilibrium constants (therefore thermodynamic data) than that of the previous chapter. This is because below T = 250 K the rate of ClO loss resulting from the ClO self-reaction essentially becomes second order due to the thermal stability of Cl_2O_2 below this temperature.[19] Thus this dataset provides a more rigorous analysis of ClO self-reaction thermochemistry since a greater number of temperatures have been studied, the lowest of which is around 250 K.

5.3.3 Analysis of Radical Production Routes

In Chapter 4, the total initial radical concentration formed upon photolysis of $Cl_2/Cl_2O/O_2$ gas mixtures was defined as:

$$[\text{TR}]_0 = ([2\,\beta\, f(\text{Cl}_2\text{O})\,(1-\alpha)] + [f(\text{Cl}_2\text{O})\,\alpha])[\text{Cl}_2]_{\text{total}} \qquad (5.3\ \text{viii})$$

Where α is the partitioning between Cl_2 and Cl_2O resulting from (in this case) reaction (5.1) and β is defined as the ratio of the fraction of Cl_2 photolysed compared to the fraction of Cl_2O photolysed, $f(Cl_2)/f(Cl_2O) = \sigma(Cl_2)/\sigma(Cl_2O)$ which gives $\beta = 8.53 \times 10^{-2}$ from the latest JPL NASA[14] evaluation at $\lambda = 351$ nm. The first term is equal to $[Cl]_0$ and the second, $[ClO]_0$. Thus the partitioning of $[Cl]_0$ and $[ClO]_0$ can be given by the fraction δ:

$$\delta = \frac{[\text{Cl}]_0}{[\text{TR}]_0} \qquad (5.3\ \text{ix})$$

Analogous to the fate of the newly liberated Cl atoms described in Chapter 4, there is a competition for atomic chlorine between reactions (5.7) and (5.8) in the presence of methane to ultimately form ClO and CH_3O_2:

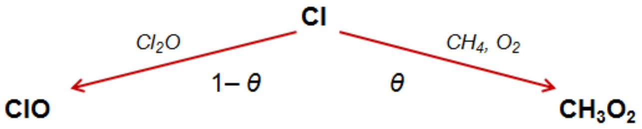

The branching between ClO and CH_3O_2 is dependent on the function, θ, which is equal to:

$$\theta = \frac{k_{(5.8)}[\text{CH}_4]}{k_{(5.8)}[\text{CH}_4] + k_{(5.7)}[\text{Cl}_2\text{O}]} \qquad (5.3\ \text{x})$$

Thus assuming $[TR]_0$ is constant between consecutive experiments of methane free conditions and intervening experiments carried out in the presence of methane, the initial total (*i.e.* summed) concentrations of ClO and CH_3O_2 (which under the experimental conditions employed here is approximately equal to their maximum concentration following rapid reactant formation) can be constrained and is dependent on the relative concentrations of CH_4, Cl_2O and Cl_2.

5.3.4 Analysis of [ClO] Temporal Traces Recorded in the Presence of CH_4 (and O_2)

As discussed above, the $[\mathrm{ClO}]_t$ traces recorded in the presence of methane were markedly different from those recorded in the absence of methane under otherwise essentially identical conditions. Fitting the traces recorded with methane to the kinetics of ClO dimerisation only, yielded spurious rate constants for $k_{(5.10)}$ and $k_{(-5.10)}$ compared to those found and reported in Chapter 4. Thus, a simple numerical model was initially constructed, expanding the scope of ClO decay by including an additional radical terminating loss term for ClO. This source of ClO loss was attributed to the bimolecular reaction of ClO with CH_3O_2, the temporal behaviour of which was also included in the model:

$$-\frac{d[\mathrm{ClO}]}{dt} = k_{(5.10)}[\mathrm{ClO}][\mathrm{ClO}] - 2\,k_{(-5.10)}[\mathrm{Cl_2O_2}] - k_{(5.1)}[\mathrm{ClO}][\mathrm{CH_3O_2}] \qquad (5.3\ \mathrm{xi})$$

$$-\frac{d[\mathrm{CH_3O_2}]}{dt} = -\,k_{(5.1)}[\mathrm{ClO}][\mathrm{CH_3O_2}] \qquad (5.3\ \mathrm{xii})$$

The initial concentrations of ClO and CH_3O_2 were then constrained by the parameters described above using the experimental concentrations of CH_4, Cl_2O and Cl_2 and the parameters of $[\mathrm{TR}]_0$, $k_{(5.10)}$ and $k_{(-5.10)}$, optimised here from ClO methane free traces, using equation (5.3 xi) and $[\mathrm{CH_3O_2}]_0$ set to zero. Values of $k_{(5.1)}$ were optimised from experimental $[\mathrm{ClO}]_t$ traces at a number of different temperatures and the results are shown below in Figure 5.11, in the form of an Arrhenius plot. The results show that using this simple model, in which there is no secondary chemistry incorporated aside from reactions (5.10) and (−5.10), leads to a significant negative temperature dependence for the observed $k_{(5.1)}$. What is more, there is a definite methane enhancement to the observed rate of ClO decay that is proportional to the $[\mathrm{CH_4}]$ used experimentally shown in Figure 5.12 which also appears to increase with decreasing temperature, values of $k_{(5.1)}$ of which were obtained using the same method above.

These preliminary results were not surprising, considering the simplicity of the model used to optimise the kinetics of reaction (5.1) is unrealistic as it is believed to have a dominant radical chain carrying reaction channel, (5.1a). In addition CH_3O_2 is also known to self-react and again, not all products formed in this reaction are radical terminating:

$$CH_3O_2 + CH_3O_2 \rightarrow CH_3O + CH_3O + O_2 \qquad (5.11a)$$

$$\rightarrow HCHO + CH_3OH + O_2 \qquad (5.11b)$$

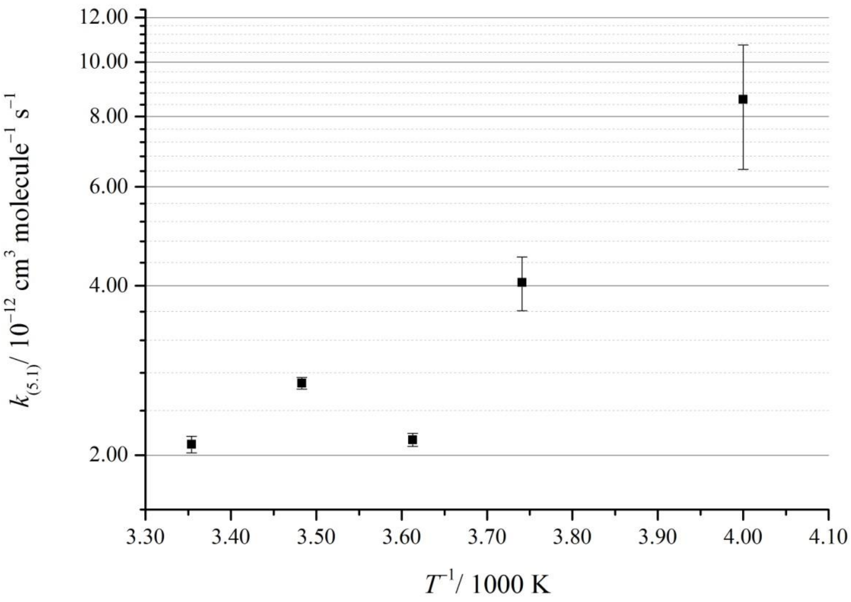

Figure 5.11 *An Arrhenius plot of* $k_{(5.1)}$ *obtained by fitting* $[ClO]_t$ *in the* $Cl_2/Cl_2O/O_2/CH_4$ *decay to a simple numerical model.*

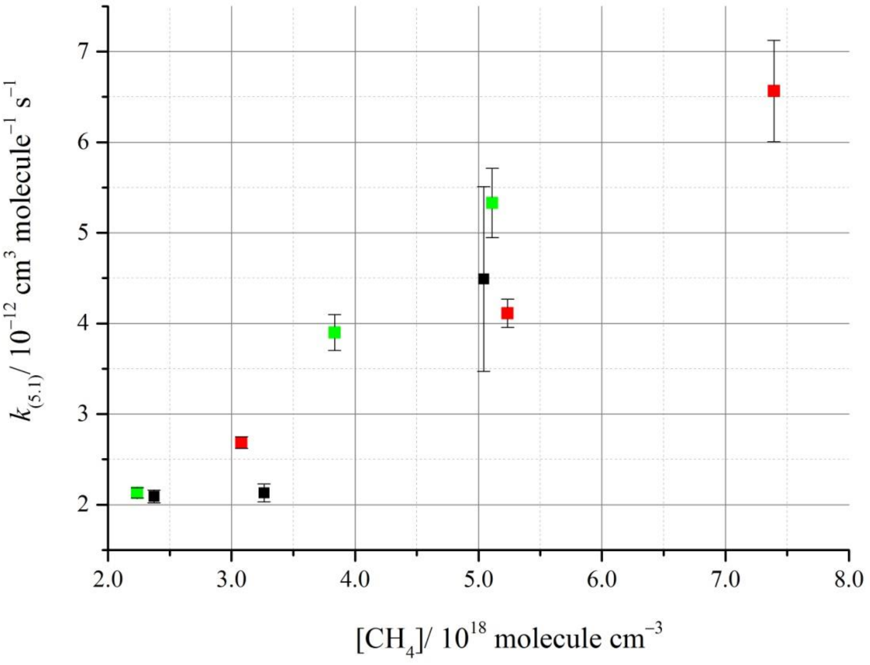

Figure 5.12 *Derived values of $k_{(5.1)}$ as a function of methane at: T = 298.1 K (black); T = 287.1 K (red); and T = 276.9 K (green). Errors are 1σ, statistical only.*

The minor channel of the CH_3O_2 self-reaction channel is (5.11a), forming the methoxy radical, CH_3O which, under experimental conditions (excess oxygen), leads to the formation of HO_2:

$$CH_3O + O_2 \rightarrow HO_2 + HCHO \tag{5.12}$$

HO_2 reacts rapidly with both ClO and CH_3O_2 and although the products of these are radical terminating, these channels would be expected to enhance ClO loss:

$$ClO + HO_2 \rightarrow Products \tag{5.13}$$

$$HO_2 + CH_3O_2 \rightarrow HO_2 \tag{5.14}$$

In addition, the HO_2 undergoes reaction with itself:

$$HO_2 + HO_2 (+ M) \rightarrow H_2O_2 (+ M) \tag{5.15}$$

Thus, the chemical mechanism, expanded to include just the minimal secondary chemistry arising from the formation of CH_3O through reactions (5.1a) and (5.11a), becomes far more complex as shown schematically in Figure 5.13.

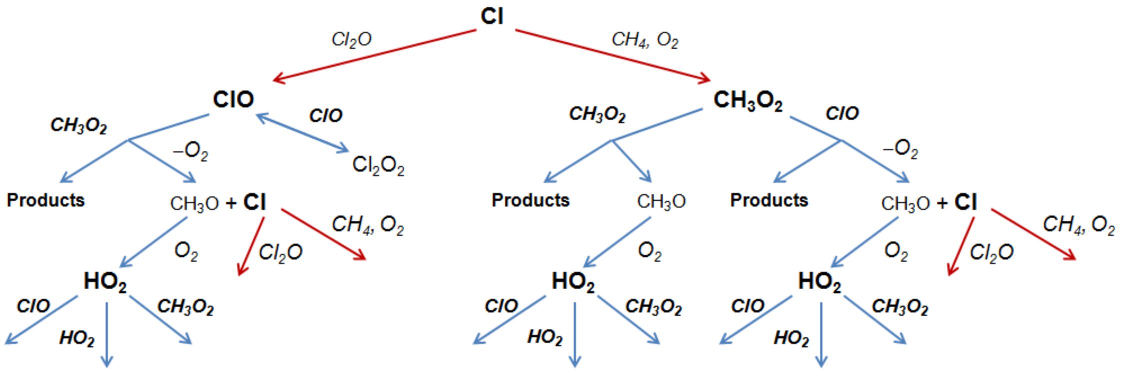

Figure 5.13 *A schematic representation of the main reactive pathways of Cl, ClO, CH_3O_2 and HO_2 following the photolysis of $Cl_2/Cl_2O/CH_4/O_2/N_2$ mixtures.*

	Reaction	Rate coefficient ($k(T)$ at 760 Torr)[a]
	Principal Reaction	
k_{af}	$ClO + CH_3O_2 \rightarrow ClOO + CH_3O$	$2.40 \times 10^{-12} \exp(-20/T)$
k_{bf}	$ClO + CH_3O_2 \rightarrow CH_3OCl + O_2$	$k_{af}/k_f = 1.51 \exp(-218/T)$
	Cl Chemistry	
k_{1f}	$Cl + Cl_2O \rightarrow Cl_2 + ClO$	$6.20 \times 10^{-11} \exp(130/T)$
k_{2fD}	$ClO + ClO \rightarrow Cl_2O_2$	$k_0 = 1.60 \times 10^{-32} \times (T/300)^{-4.5 b}$
k_{2rD}	$Cl_2O_2 \rightarrow ClO + ClO$	$k_\infty = 3.00 \times 10^{-12} \times (T/300)^{-2}$
		$K_{eq} = 1.72 \times 10^{-27} \exp(8649/T)^{c}$
k_{2fa}	$ClO + ClO \rightarrow Cl_2 + O_2$	$1.00 \times 10^{-12} \exp(1590/T)$
k_{2fb}	$ClO + ClO \rightarrow OClO + Cl$	$3.50 \times 10^{-13} \exp(1370/T)$
k_{2fc}	$ClO + ClO \rightarrow ClOO + Cl$	$3.00 \times 10^{-11} \exp(2450/T)$
k_{3f}	$Cl + O_2 \rightarrow ClOO$	$k_0 = 2.20 \times 10^{-33} \times (T/300)^{-3.1 b}$
k_{3r}	$ClOO \rightarrow Cl + O_2$	$k_\infty = 1.80 \times 10^{-10} \times (T/300)^{0}$
		$K_{eq} = 6.60 \times 10^{-25} \exp(2502/T)^{c}$
k_{4f}	$ClO + HO_2 \rightarrow HOCl + O_2$	$2.60 \times 10^{-12} \exp(290/T)$
k_{5f}	$ClOO + ClOO \rightarrow ClO + ClO + O_2$	1.60×10^{-11}
k_{6f}	$ClOO + Cl_2 \rightarrow Cl_2O + ClO$	3.40×10^{-12}
k_{38f}	$ClO + OClO \rightarrow Cl_2O_3$	$k_0 = 5.80 \times 10^{-33} \times (T/300)^{-4.7 b}$
k_{38r}	$Cl_2O_3 \rightarrow ClO + OClO$	$k_\infty = 2.40 \times 10^{-11} \times (T/300)^{-1.1}$
		$K_{eq} = 1.50 \times 10^{-27} \exp(7140/T)^{c}$
k_{45f}	$Cl + Cl_2O_2 \rightarrow Cl + Cl_2 + O_2$	1.00×10^{-10}
	CH_3O Chemistry	
k_{7f}	$CH_3O + CH_3O \rightarrow HCHO + CH_3OH$	3.80×10^{-11}
k_{8f}	$CH_3O_2 + CH_3O \rightarrow HCHO + CH_3OOH$	5.00×10^{-13}
k_{9f}	$CH_3O + ClO \rightarrow HOCl + HCHO$	3.40×10^{-11}
k_{10f}	$CH_3O + HO_2 \rightarrow HCHO + H_2O_2$	5.00×10^{-13}
k_{11f}	$CH_3O + O_2 \rightarrow HO_2 + HCHO$	$3.90 \times 10^{-14} \exp(-900/T)$
k_{12f}	$CH_3O + CH_4 \rightarrow CH_3OH + CH_3$	$2.61 \times 10^{-13} \exp(-4450/T)$
	CH_3O_2 Chemistry	
k_{13f}	$Cl + CH_4 \rightarrow HCl + CH_3$	$7.30 \times 10^{-12} \exp(-1280/T)$
k_{14f}	$CH_3 + O_2 \rightarrow CH_3O_2$	$k_0 = 4.00 \times 10^{-31} \times (T/300)^{-3.6 b}$
		$k_\infty = 1.20 \times 10^{-12} \times (T/300)^{1.1}$
k_{15fa}	$CH_3O_2 + CH_3O_2 \rightarrow CH_3O + CH_3O + O_2$	$9.50 \times 10^{-14} \exp(390/T)$
k_{15fb}	$CH_3O_2 + CH_3O_2 \rightarrow HCHO + CH_3OH + O_2$	k_{15fb} / k_{15f}
		$k_{15f} / (26.2 \exp(-1130/T) + 1)$

k_{16f}	$HO_2 + CH_3O_2 \rightarrow CH_3OOH + O_2$	$4.10 \times 10^{-13} \exp(750/T)$
k_{17fa}	$Cl + CH_3O_2 \rightarrow ClO + CH_3O$	3.845×10^{-11}
k_{17fb}	$Cl + CH_3O_2 \rightarrow HCl + CH_2O_2$	3.85×10^{-11}
	HO_2 Chemistry	
k_{18f}	$HO_2 + HO_2 \rightarrow H_2O_2 + O_2$	$3.00 \times 10^{-13} \exp(460/T) + 5.17 \times 10^{-14} \exp(920/T)$
k_{19f}	$HO_2 + CH_3OH \rightarrow HO_2.CH_3OH$	$2.80 \times 10^{-15} \exp(-1800/T)$
k_{19r}	$HO_2.CH_3OH \rightarrow HO_2 + CH_3OH$	$K_{eq} = 1.10 \times 10^{-24} \exp(4093/T)^{c}$
k_{20f}	$HO_2 + HO_2.CH_3OH \rightarrow H_2O_2 + CH_3OH + O_2$	$5.40 \times 10^{-11} \exp(-410/T)$
k_{21f}	$HO_2 + H_2O \rightarrow HO_2.H_2O$	$2.80 \times 10^{-15} \exp(-180/T)$
k_{21r}	$HO_2.H_2O \rightarrow HO_2 + H_2O$	$K_{eq} = 2.40 \times 10^{-25} \exp(4350/T)^{c}$
k_{22f}	$HO_2 + HO_2.H_2O \rightarrow H_2O_2 + H_2O + O_2$	$5.40 \times 10^{-11} \exp(-410/T)$
k_{23fa}	$HO_2 + Cl \rightarrow HCl + O_2$	$1.40 \times 10^{-1} \exp(270/T)$
k_{23fb}	$HO_2 + Cl \rightarrow OH + ClO$	$3.60 \times 10^{-11} \exp(-375/T)$
k_{24f}	$Cl + H_2O_2 \rightarrow HCl + HO_2$	$1.10 \times 10^{-11} \exp(-980/T)$
k_{25f}	$Cl + CH_3OH \rightarrow CH_2OH + HCl$	5.50×10^{-11}
k_{26f}	$CH_2OH + O_2 \rightarrow HCHO + HO_2$	9.10×10^{-11}
	Secondary Chemistry	
k_{27f}	$Cl + CH_3Cl \rightarrow CH_2Cl + HCl$	$2.17 \times 10^{-11} \exp(-1130/T)$
k_{28f}	$CH_2Cl + O_2 \rightarrow CH_2ClO_2$	$k_0 = 1.90 \times 10^{-30} \times (T/300)^{-3.2b}$ $k_\infty = 2.90 \times 10^{-12} \times (T/300)^{1.1}$
k_{29f}	$CH_2ClO_2 + HO_2 \rightarrow CH_2ClOOH + O_2$	$3.30 \times 10^{-13} \exp(820/T)$
k_{30f}	$CH_3 + Cl_2 \rightarrow CH_3Cl + Cl$	$1.61 \times 10^{-12} \exp(64/T)$
k_{31f}	$CH_3 + Cl \rightarrow CH_3Cl$	6.11×10^{-11}
k_{32f}	$HO_2 + HCHO \rightarrow HOCH_2O_2$	$9.70 \times 10^{-15} \exp(-625/T)$
k_{32r}	$HOCH_2O_2 \rightarrow HO_2 + HCHO$	$2.40 \times 10^{12} \exp(7000/T)$
k_{33fa}	$HOCH_2O_2 + HO_2 \rightarrow HOCH_2OOH + O_2$	$5.60 \times 10^{-15} \exp(-2300/T)$
k_{33fb}	$HOCH_2O_2 + HO_2 \rightarrow O_2 + HC(O)OH + H_2O$	$k_{33fa} / k_{33f} = 0.6$
k_{34fa}	$HOCH_2OOH + Cl \rightarrow HCOOH + OH + HCl$	1.00×10^{-10}
k_{34fb}	$HOCH_2OOH + Cl \rightarrow HOCH_2O_2 + HCl$	5.00×10^{-10}
k_{35fa}	$HOCH_2O_2 + HOCH_2O_2 \rightarrow HOCH_2O + HOCH_2O + O_2$	$5.70 \times 10^{-14} \exp(750/T)$ 5.50×10^{-12}
k_{35fb}	$HOCH_2O_2 + HOCH_2O_2 \rightarrow HCOOH + CH_2O_2H_2 + O_2$	3.50×10^{-14}
k_{36f}	$HOCH_2O_2 + O_2 \rightarrow HCOOH + HO_2$	2.41×10^{-23}
k_{37f}	$CH_3 + CH_4 \rightarrow CH_4 + CH_3$	5.35×10^{-11}
k_{40f}	$CH_3 + CH_3 \rightarrow C_2H_6$	5.91×10^{-11}

k_{41f}	$CH_3OOH + Cl \rightarrow HCl + CH_2OOH$	$8.10\times 10^{-11}\exp(30/T)$
k_{42f}	$Cl + HCHO \rightarrow HCl + HCO$	$3.50 \times 10^{-12}\exp(140/T)$
k_{43f}	$HCO + O_2 \rightarrow CO + HO_2$	$6.10 \times 10^{-12}\exp(-36/T)$
k_{44f}	$HCO + Cl_2 \rightarrow HCOCl + Cl$	

[a]Units are cm^3 molecule^{-1} s^{-1} unless otherwise stated [b]units of cm^6 molecule^{-2} s^{-1} and [c]units of cm^3 molecule^{-1}

Table 5.3 *The chemical mechanism used in the FACSIMILE numerical model for deriving $k_{(5.1)}$. The rate constants are from JPL NASA.*[14]

Reactions (5.11) and (5.13) – (5.15) all exhibit negative temperature dependences which partly explains the observed behaviour of $k_{(5.1)}$ shown in Figures 5.11 and 5.12; the loss of ClO and CH_3O_2 through secondary chemistry increases with increasing $[CH_4]$ and decreasing temperature.

Hence an expanded chemical model incorporating the formation chemistry, the above chemistry and a number of other possible secondary reactions that could also occur was developed in the numerical integration software package FACSIMILE. The reaction scheme shown in Table 5.3 resulted from systemically following the radical chain carrier reactions and then cross referring any subsequent potential reactions with other species in the system.

Given initial estimates for the parameters to be optimised, FACSIMILE was able to iterate its integration procedure a number of times, varying the parameter values of interest, until it found the optimal values which simulated $[ClO]_t$ traces closest to the experimental traces. The parameters of interest which were varied in the model were the two dominant reaction pathways for the ClO + CH_3O_2, (5.1a) and (5.1b), whose branching is given by the IUPAC[15] recommendation. IUPAC[15] also recommends a third branch, assumed to form generic non-radical products to account for the remaining fraction of the total rate constant after channels (5.1a) and (5.1b) are accounted for which was added on as a component in the branching of (5.1b). The fitting procedure yielded rate constant values $k_{(5.1a)}$ and $k_{(5.1b)}$ which were totalled to give the overall $k_{(5.1)}$. As no products were monitored, no accurate information on the branching was obtainable. In addition to $k_{(5.1)}$, the parameter δ was also varied as this gave the model an extra degree of freedom in the case of any drift in the experimental conditions during a given series of photolysis experiments.

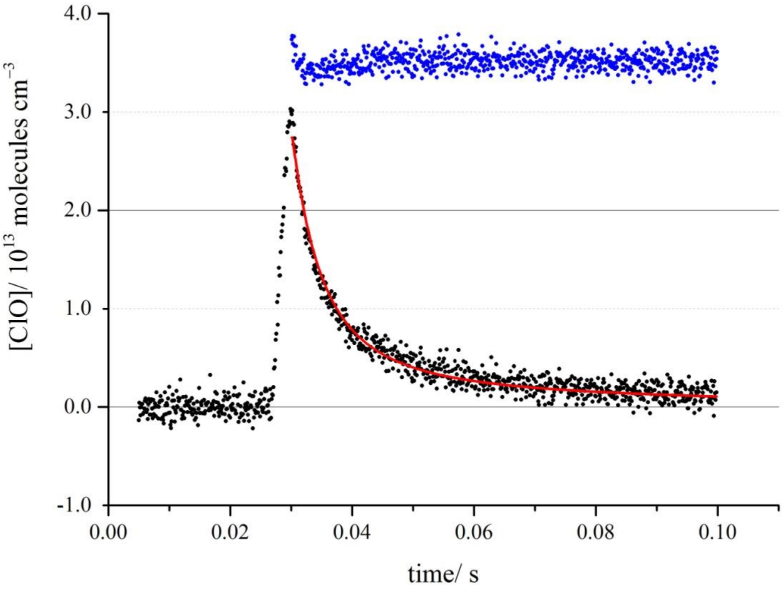

Figure 5.14 *An experimental [ClO]$_t$ trace with [CH_4] = 6.0 × 10^{18} molecules cm^{-3} (black circles) with the corresponding optimised trace using the expanded FACSIMILE model (red line) and the offset residual between the two (blue circles).*

Figure 5.14 above shows the typical quality of the fit between experimental and optimised traces using the model presented in Table 5.3. It can be seen that the model is able to satisfactorily replicate the temporal behaviour of [ClO] by allowing FACSIMILE to optimise the chosen parameters in the fitting procedure. Values of $k_{(5.1)}$ and δ were found for every single [ClO]$_t$ trace recorded at each temperature investigated and the final results, averaged for each temperature, are presented in Table 5.4 below. The sensitivity of the fitting procedure is discussed in Section 5.4.1. At lower temperatures some anomalous results were returned when δ was floated thus it was fixed at the measured value of 0.71 which is in agreement with the values of δ at the higher temperatures. Values of 0.78 were also used at the lower temperatures, reflecting the range in δ found at the higher temperatures.

T / K	$k_{(5.1)}{}^{a}$ / 10^{-12}	δ	$[CH_4]_0{}^{b}$ / 10^{18}
298.15	(2.73 ± 0.46)	0.74 ± 0.07	2.4 – 6.0
287.05	(2.30 ± 0.07)	0.79 ± 0.16	3.1 – 7.4
276.85	(2.48 ± 0.67)	0.72 ± 0.17	2.2 – 8.0
270.1	(1.52 ± 0.62)	0.29 ± 0.14*	3.3 – 6.6
267.25	(2.57 ± 1.00)	0.87 ± 0.08*	4.6 – 10.2
263.1	(1.91 ± 0.47)	0.45 ± 0.14*	6.7
258.3	(2.06 ± 0.45)	-*	5.8 – 12.0
249.95	(2.14 ± 0.97)	-*	7.1 – 12.4

*^{a}Units of cm^{3} molecule^{-1} s^{-1} ,^{b}units of molecules cm^{-3} *fixed during optimisation at 0.71 and 0.78 per trace for final results*

Table 5.4 *The results of $k_{(5.1)}$ as a function of temperature and the range of experimental $[CH_4]$.*

The results of $k_{(5.1)}$ are plotted in Arrhenius form in Figure 5.15 along with the corresponding parameterisation obtained by linear regression, which was described by:

$$k_{(5.1)}\left(T/\mathrm{K}\right) = 2.20^{+3.40}_{-1.30} \times 10^{-11}\, e^{\left(\frac{-(642\,\pm 253)}{T}\right)} \mathrm{cm}^3\ \mathrm{molecule}^{-1}\ \mathrm{s}^{-1} \qquad (5.3\ \mathrm{xiii})$$

where errors are 1σ. These results are in reasonable agreement with the JPL NASA[14] and IUPAC[15] recommendations when combining uncertainty, which are respectively:

$$k_{(5.1)}\left(T/\mathrm{K}\right) = 3.3 \times 10^{-12}\, e^{\left(\frac{-115}{T}\right)} \mathrm{cm}^3\ \mathrm{molecule}^{-1}\ \mathrm{s}^{-1}\ (\mathrm{JPL\ NASA}^{14}) \qquad (5.3\ \mathrm{xiv})$$

$$k_{(5.1)}\left(T/\mathrm{K}\right) = (2.40 \pm 0.15) \times 10^{-11}\, e^{\left(\frac{-(20\,\pm 200)}{T}\right)} \mathrm{cm}^3\ \mathrm{molecule}^{-1}\ \mathrm{s}^{-1}\ (\mathrm{IUPAC}^{15}) \qquad (5.3\ \mathrm{v})$$

The recommended parameterisations above are based on the temperature dependence studies of Helleis *et al.*[7] and Kukui *et al.*[10] with the results from Leather *et al.*[13] yet to be reviewed. As with this work, Leather *et al.*[13] found a much stronger positive temperature dependence for reaction $k_{(5.1)}$ than the current recommendation, reasons for which and the subsequent implications of this are discussed below.

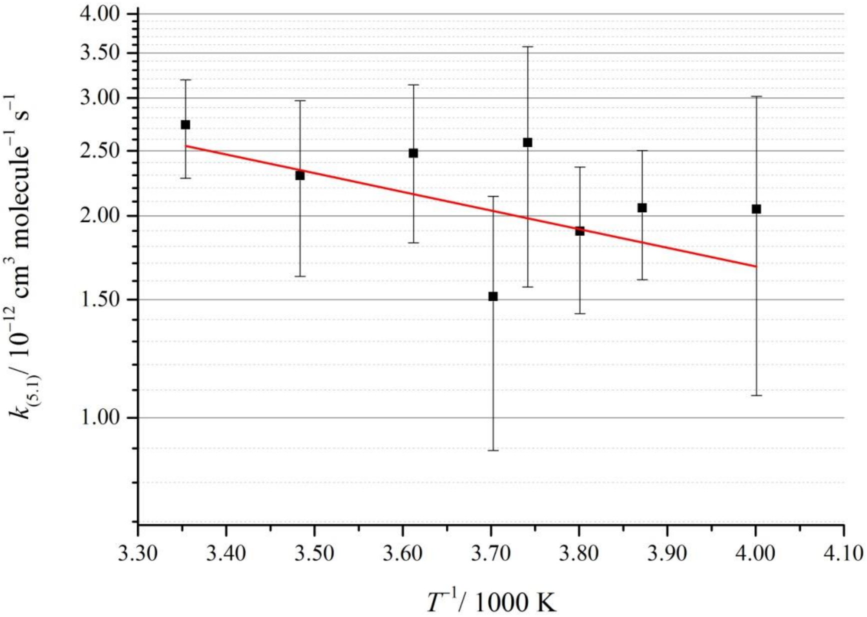

Figure 5.15 *An Arrhenius plot of the temperature dependence of* $k_{(5.1)}$ *found in this work (black squares) and the corresponding optimised parameterisation (red line).*

5.4 Discussion

5.4.1 Sensitivity Analysis

As has been discussed above, the chemical system employed in the study of reaction (5.1) features significant, unavoidable secondary chemistry due to the formation of many radical chain-carrier products. Therefore a comprehensive sensitivity analysis was performed on the chemical mechanism utilised in deriving $k_{(5.1)}$ and the parameters the fitting procedure relies on. A simulated trace of $[ClO]_t$ was generated using the same model used in the fitting procedure in FACSIMILE and then $k_{(5.1)}$ and δ were optimised by fitting to this trace, which gave the same output values as the input to within 1 %. Following this, each rate constant was halved or doubled in an iterative fashion, while holding the initial conditions constant for each optimisation. The output parameters were then recorded and compared to the input values. The percentage difference between the input $k_{(5.1)}$ and output as a result of each rate coefficient perturbed is shown in Figure 5.16 (a) and (b). The model showed greatest sensitivity to reaction (5.1) (labelled k_f in the model) which go beyond the scale of the y-axis for each plot. The change in $k_{(5.1)}$ was also proportional, with the output values equal to ~ 50 % and ~ 100 % for a perturbation of the principal reaction in the simulated traces of half and double the original value at both temperatures.

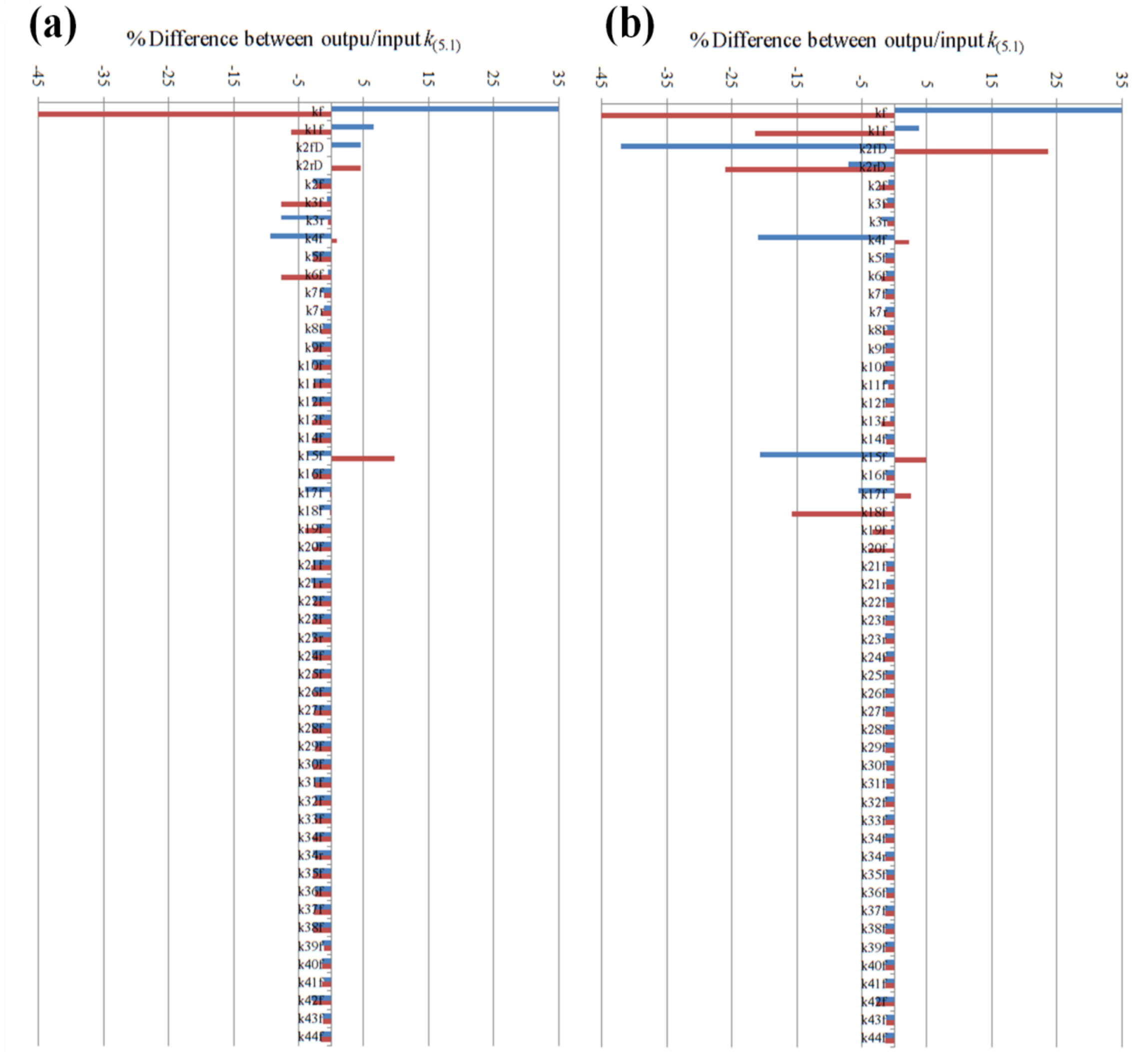

Figure 5.16 *The zoomed in view of the results of the sensitivity analysis of the kinetics of reaction (5.1) to the other reactions used in the chemical mechanism for: (a) T = 298 K; and (b) T = 249 K. Each reaction is identified by its FACSIMILE label given in Table 5.3.*

The self-reaction chemistry of ClO dimerisation (k_{2fD} and k_{2rD}) was found to be particularly important as experimental conditions were such that the $[ClO]_0/[CH_3O_2]_0$ was typically greater than 1 and the kinetics of reactions (5.10) and (−5.10) are consequently efficient. The importance of K_c was particularly important at T = 249 K and caused the model to break down entirely upon doubling as the rate of forward reaction is proportional to the square of [ClO]. The temporal behaviour of [ClO] decay resulting from reaction (5.1) in the current work was therefore measured *relative* to this chemistry. Thus the uncertainty in $k_{(5.1)}$ resulting from the rate coefficients of reactions (5.10) and (−5.10) is small as they were also measured in this work, the results of which were consistent with Boakes *et al.*[21] and Ferracci *et al.*[19] As with the work of Boakes *et al.*[21] and Ferracci *et al.*,[19] systematic error in the determination of $k_{(5.10)}$ and $k_{(-5.10)}$ (hence K_c) arose from the uncertainty in the differential absorption cross section used which was propagated through to the temporal ClO concentrations by equation (4.2 ii) (Chapter 4). The systematic error in the differential cross section of *ca.* ± 16 % at $T = 298$ K reported by Boakes *et al.*[21] results in a scaling of the [ClO] temporal trace by the same extent. The effect of the extracted rate constants for ClO dimerisation and in turn reaction (5.1) were analogous to that in Chapter 4 where the effect on returned value of $k_{(5.1)}$ was smaller than on the forward reaction constant of the ClO self-reaction.

The initial formation chemistry of both the principal reactants ClO and CH_3O_2 was important as perturbations in k_{f1} and k_{f15} affects the effective branching of the Cl atom reactivity which is important upon the initial formation of atomic chlorine post-photolysis as well as the subsequent secondary chemistry involving Cl regeneration. As was found from the results of the simple analysis of the $[ClO]_t$ traces, secondary chemistry is particularly important in the observed kinetics of reaction (5.1). This is also reflected in the sensitivity analysis results where the model is also sensitive with respect to the reactions of HO_2 with ClO and CH_3O_2 (k_{4f} and k_{18f}). HO_2 is inevitably formed following CH_3O formation and its subsequent reaction with O_2. HO_2 reacts efficiently with both ClO and CH_3O_2, increasingly so at lower temperatures (as discussed in Chapter 4 for ClO + HO_2), thus the doubling of these rate coefficients led to smaller output values for $k_{(5.1)}$.

A flux analysis was also conducted to complement the sensitivity analysis of $k_{(5.1)}$ with respect to the individual reactions in the model. Figure 5.17 (a) and (b) show the simulated flux of ClO and CH_3O_2 decay under similar conditions as were used experimentally as a function of methane. The flux of either reactant through reaction (5.1) evidently varies accordingly to the amount of methane for a given concentration of precursor Cl_2O. In Figure 5.17 (a), the fraction of ClO reacting with CH_3O_2 increases with larger [CH_4] attributed to a decreasing $[ClO]_0/[CH_3O_2]_0$ which is also highlighted by the corresponding decrease in ClO regeneration as the branching of Cl atom reactivity is increasingly steered towards CH_3O_2 formation (Figure 5.17 (b), shown by the pink dots). Consequently, the increase in CH_3O_2 results in competition for ClO at the expense of the ClO self-reaction. Conversely, at higher [CH_4], the fraction of CH_3O_2 self-reaction and the extent of reaction of CH_3O_2 with HO_2 increase. However, this is at the expense of the total fraction of CH_3O_2 reacting through (5.1). Fractions of CH_3O_2 reacting with ClO apparently above unity are due to reactant regeneration which contributes to an effective negative decay and balances on summation (shown by the green dots). The proportion of ClO reacting with HO_2 (which reacts more efficiently with ClO than CH_3O_2) initially increases with increasing [CH_4] but then decreases as $[ClO]_0/[CH_3O_2]_0$ decreases. The reason for the total proportion of ClO decay being below unity in Figure 5.17 (a) is because the slower bimolecular contributions of the ClO self-reaction were not included.

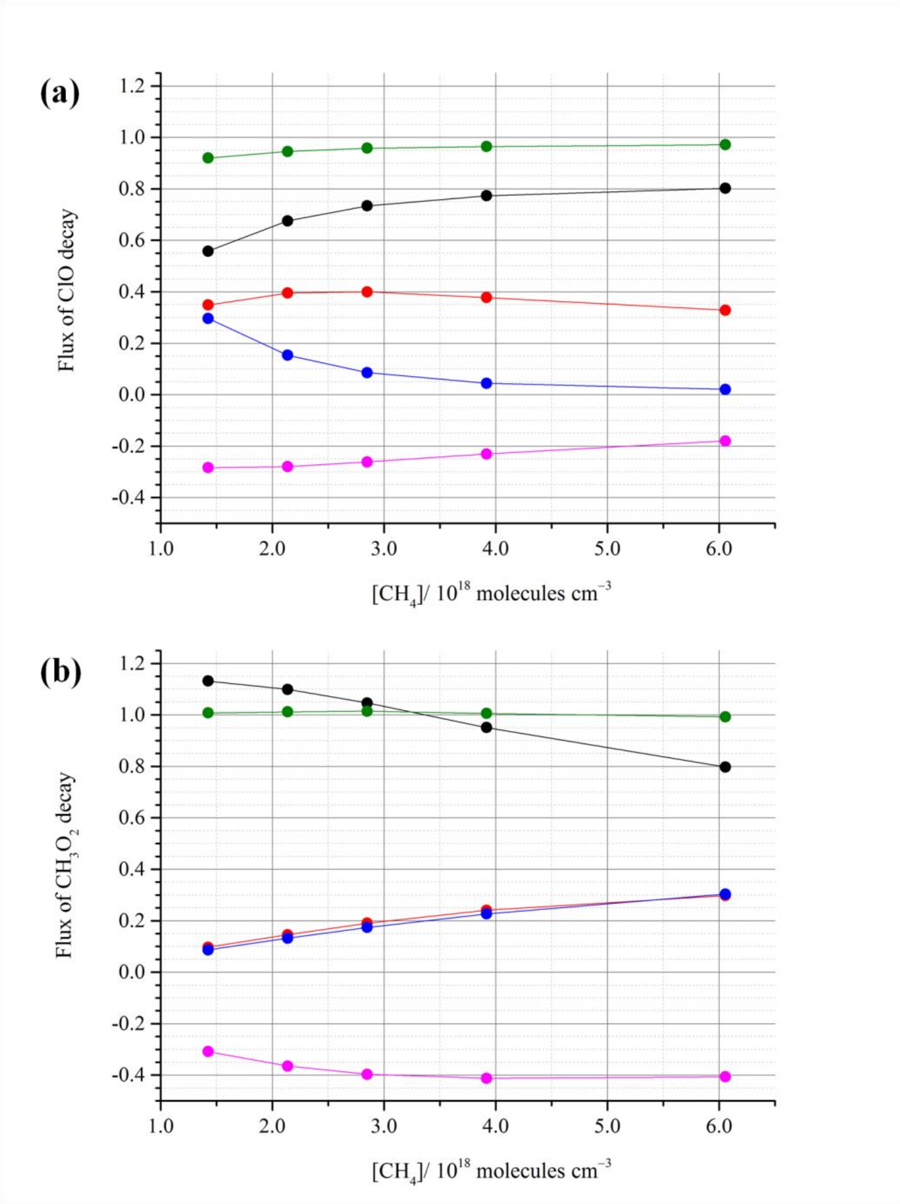

Figure 5.17 *The flux of: (a) ClO; and (b) CH_3O_2 reactivity as a function of methane concentration, presented as a proportion relative to the overall decay of a given reactant in reaction (5.1). Each point represents the simulated flux through: ClO + CH_3O_2 (black); reaction with HO_2 (red); self-reaction (blue); reactant generation (pink); and the sum of the above fluxes (green).*

Similar to the sensitivity analysis in Figure 5.16 (a) and (b), the input parameters $[TR]_0$, $[CH_4]_0$, α and δ were also perturbed by: ± 50 %; ± 50 %; divided and multiplied by a factor of 2; and ± 25 % respectively. The model was most sensitive to the change in $[TR]_0$ which, when underestimated in the fitting model, resulted in a difference in $k_{(5.1)}$ of ~ 50 % and approximately −28 % when overestimated. Similarly, an overestimation of $[CH_4]_0$ and α led to changes in around −25 % each but around 15 % when underestimated. The perturbations in δ led to only minimal changes in the output values of $k_{(5.1)}$ by comparison, resulting in a maximum difference of around 1.5 %. In reality, the uncertainty in each of these parameters was somewhat smaller than what was assumed experimentally with $[TR]_0$ varying typically by no more than ~ 5 % per series of experiments as shown, for example, in Figure 5.5. However on several occasions, $[TR]_0$ did decrease up to 20 %. For these series of experiments, it was assumed that the decrease was linear with experimental (laboratory) time and the $[TR]_0$ of a given experiment in the presence of methane was calculated in accordance with the time that the individual photolysis experiment took place between the two methane free experiments carried out either side of it. Thus the greatest source of uncertainty is likely to lie in deviations in $[TR]_0$ as proportionally it introduces the most uncertainty in $k_{(5.1)}$.

The sensitivity to the optimised value of δ was also found to depend, crucially, on the above parameters and certain reactions. These included the reactant forming reactions of ClO and the reaction of Cl with methane; the ClO dimer forming/decaying reactions in particular and the reversible dissociation of ClOO:

$$\mathrm{ClOO\ (+\ M) \rightleftharpoons Cl + O_2\ (+\ M)} \qquad (5.4)\ (-5.4)$$

The extent of the sensitivity to this reaction also increased at lower temperature, reflecting the efficacy of reaction 5.13.

5.4.2 Comparison with Previous Work

Starting at room temperature, T = 298 K, the results from this work agree most with those of Kukui *et al.*[10] and Leather *et al.*[13] as shown below in Figure 5.18. These authors who report values of $(2.5 \pm 0.3) \times 10^{-12}$ cm^3 $molecule^{-1}$ s^{-1} and $(2.4 \pm 0.3) \times 10^{-12}$ cm^3 $molecule^{-1}$ s^{-1} respectively, compared to $(2.7 \pm 0.5) \times 10^{-12}$ cm^3 $molecule^{-1}$ s^{-1} in the present work. When combining the uncertainty, Simon *et al.*[6], Helleis *et al.*[7] and Kenner *et al.*[9] also agree with the findings presented here. Simon *et al.*,[6] who report the largest room temperature result of $k_{(5.1)} = (3.1 \pm 1.9) \times 10^{-12}$ cm^3 $molecule^{-1}$ s^{-1} is the only other work on reaction (5.1) to date that has used absorption spectroscopy to measure ClO (UV region) and HO_2 (IR region). Prior to this work, the Simon *et al.*[6] investigation was the highest pressure study at p = 240 Torr, which when compared to the low pressure work of the other studies, it has been asserted that the relatively large reported value of $k_{(5.1)}$ may be indicative of a pressure dependence. However, the most recent study prior to this one has not found a pressure dependence between p = 100 – 200 Torr.[13] When compared to this work, which operated around three times the pressure of Simon *et al.*,[6] there is no discernible difference between this study and the other, low pressure work. Consequently it appears that any $[CH_3OOOCl]^*$ energised intermediate believed to be formed in reaction (5.1) is too short lived at all atmospheric pressures to exert a pressure dependence to (5.1) at room temperature.

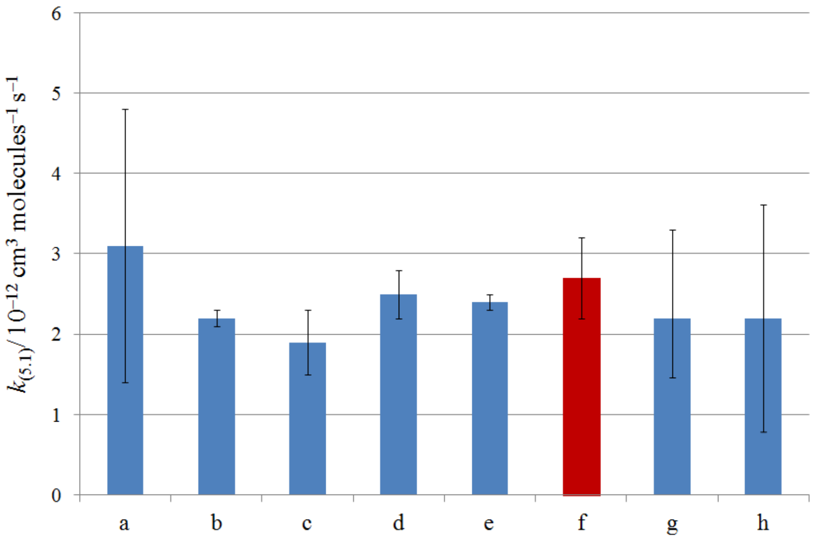

Figure 5.18 *The literature values of $k_{(5.1)}$ compared to the present work at ambient temperature: (a) Simon et al.;[6] (b) Helleis et al.;[7] c) Kenner et al.;[9] (d) Kukui et al.;[10] (e) Leather et al.;[13] (f) this work (T = 298 K); (g) JPL NASA;[14] and (h) IUPAC.*[15]

The discrepancies between the previous studies and those of Simon *et al.*[6] most likely arise from the concentration profiles of ClO derived in their work, in which ClO absorption was measured at λ = 292.2 nm at the (6,0) band head of the ClO vibronic transitions. As their photolysis was modulated rather than flashed, OClO was detected additionally which is also spectrally structured and overlaps with ClO absorptions.

Overlapping absorptions from HO_2, which absorbs more strongly over the same UV region as CH_3O_2, and other absorbers might also have introduced uncertainty into the $[CH_3O_2]_t$ profiles. This is compared to the broadband UV spectroscopic measurements made in the present work. While CH_3O_2 was unable to be directly monitored here, the [ClO] measurements were unequivocal, utilising most of the ClO vibronic absorption spectrum and using differential spectroscopy to filter out any smooth overlapping absorbers. What is more, the potential for secondary chemical effects on the observed rate constant is much higher in the Simon *et al.*[6] study than in this work owing to the relatively non-selective photolysis of the gas mixtures in the Simon *et al.*[6] study which also lasted several minutes. As was shown by the initial use of an overly simplistic chemical mechanism in this work, secondary chemistry effects on the determined $k_{(5.1)}$ may lead to an overestimation if omitted from the analytical procedure. While this was accounted for by the application of an extensive model as in the current study, several of the T = 298 K rate constants have been updated since the time of the Simon *et al.*[6] including the important peroxy radical reactions involving HO_2 and CH_3O_2.

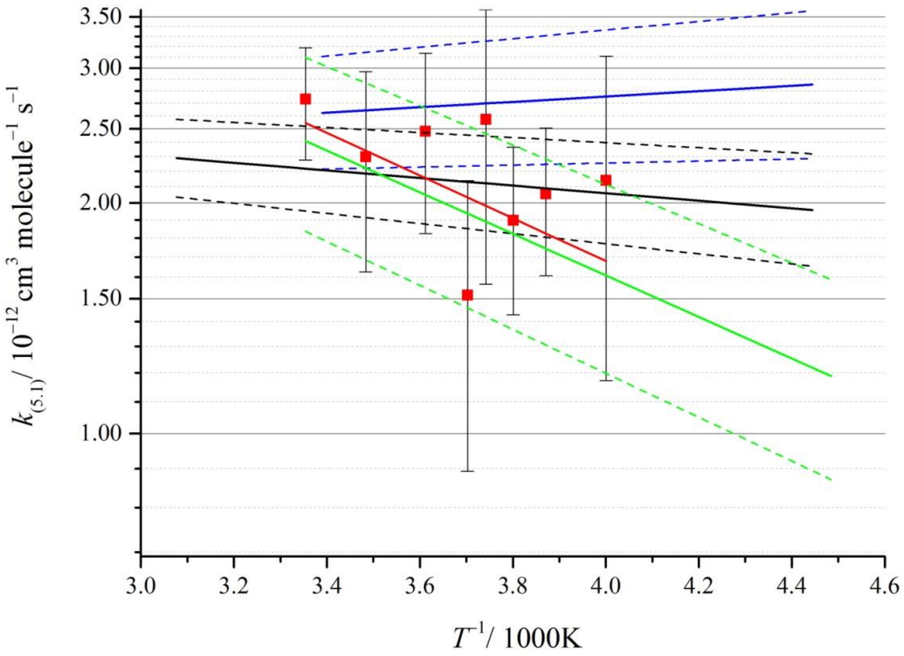

Figure 5.19 *Arrhenius plot of the experimental data of this work (red squares) and the parameterisations of the work reported by: Helleis et al.*[7]*(black); Kukui et al.*[10] *(blue); Leather et al.*[13]*(green); and this work (red).*

The work reported here represents the first reported determination of the kinetics of reaction (5.1) as a function of temperature at atmospheric pressure, employing the flash photolysis technique with UV absorption spectroscopy. The three previous temperature dependence studies of reaction (5.1) all used the discharge-flow tube method making direct comparisons with the current work inappropriate if any pressure dependence to reaction (5.1) actually exists. As shown above in Figure 5.19, there is considerable disagreement in the parameterised temperature dependences (*i.e.* E/R) between these studies with only two agreeing on a positive temperature dependence (Helleis *et al.*[7] and Leather *et al.*[13]). The agreement ends there as there is a considerable discrepancy in the strength of this temperature dependence. However, this work is in good agreement with the most recently published work of Leather *et al.*[13] There are a number of differences in the experimental setup of the Leather *et al.*[13] work and the two earlier studies of Helleis *et al.*[7] and Kukui *et al.*[10] which may explain the discrepancies. Leather *et al.*[13] give a detailed account of the possible reasons for these differences and a summary is provided here.

Firstly, the two earlier studies of reaction (5.1) employed low pressures, $p = 2 - 5$ Torr, compared to $p = 100 - 200$ Torr in Leather *et al.*[13] and $p = 760$ Torr in this work. Thus the low pressure regimes were open to significant secondary chemistry effects owing principally to the incomplete conversion of the methyl radical, CH_3, into CH_3O_2 through the known pressure dependent reaction (5.9). This is evidenced by the observed formation of C_2H_6 and CH_3OH upon CH_3O_2 production in the work of Kukui *et al.*[10] The CH_3 radical can also react with ClO, potentially introducing spurious loss of ClO, to give CH_3O and regenerate Cl:

$$ClO + CH_3 \rightarrow Cl + CH_3O \qquad (5.16)$$

At the low pressures and relatively low $[O_2]$ used in the early studies, the CH_3O formed is also likely to have reacted with ClO:

$$ClO + CH_3O \rightarrow HOCl + HCHO \qquad (5.17)$$

and therefore has consequences of spurious product formation if unaccounted for. What is more, both of the early studies employ the use of F atoms generated by a microwave discharge which react with CH_4 in an analogous fashion to reaction (5.8). However unlike in the present work, where effectively all the CH_3 generated reacts with O_2, there is up to a 40 % loss of F-to-CH_3O_2 conversion reported by Kukui *et al.*,[10] implying there is significant and in some cases unidentified secondary chemistry taking place.

The different ion sources employed in the mass spectrometric detection may also help account for the reported differences between the earlier studies and those of Leather *et al.*[13] Leather *et al.*[13] used time of flight chemical ionisation mass spectrometry (TOF CIMS) which is a more sensitive method of ionisation and detection compared to electron impact (EI) ionisation with quadrapole mass detection. What is more, CIMS is a softer ionisation technique compared to EI, which can often result in the fragmentation of parent ions into several fragments. This may be the case in the Helleis *et al.*[7] study which used Cl_2O to generate ClO. Cl_2O fragments to give Cl and ClO peaks upon EI mass detection, thereby masking the actual ClO peak. Thus, to mitigate this effect, they used less Cl_2O, making it thereafter possible for excess Cl atoms to react with CH_3O_2 in the flow tube.

Wall losses also feature heavily in both the Helleis *et al.*[7] and Kukui *et al.*[10] work whereas the higher pressure regime of the Leather *et al.*[13] study operated under turbulent flow conditions which limited these effects. In the present work there are minimal heterogeneous effects to account for as the slow flowing high pressure photolysis mixture is probed along the central longitudinal axis of the reactor.

There is considerable spread in the reported values of $k_{(5.1)}$ in this work compared to the previous temperature dependence studies. However, this study did not use steady-state conditions to measure $[ClO]_t$ and the preclusion of $[CH_3O_2]_t$ measurements makes the results sensitive to the inevitable perturbations in experimental conditions which have been extensively studied. However, there are 8 different temperatures at which $k_{(5.1)}$ was studied in this work over a 50 K range (compared to 4 over T = 225 – 335 K, 4 over T = 233 – 300 K and 5 over T = 223 – 298 K in previous studies) combining hundreds of individual photolysis experiments which gives some confidence to the parameterisation in equation (5.3 xiii). Thus, whilst the spread in data introduces large uncertainty limits in the Arrhenius parameterisation, the majority of these data points lie well within limits of the reported uncertainty from Leather *et al.*[13] hence the good agreement in the temperature dependence of $k_{(5.1)}$. The potential of secondary chemistry from the reaction of both reactants with HO_2 has been addressed which would be expected to lead to a weaker positive temperature dependence if unaccounted for (as demonstrated above). This is due to the relatively strong negative temperature of these reactions, an underestimation of which may account for the difference between the reported E/R of Leather *et al.*[13] and this work. Thus, in light of two fundamentally different approaches in studying the kinetics of reaction (5.1) showing good agreement, this work supports the reduced effectiveness of the catalytic ozone loss involving ClO + CH_3O_2 at polar stratospheric temperatures as was also found by Leather *et al.*[13]

5.4.3 Atmospheric Implications

In comparison with previous work, the atmospheric implications of this work support those made by Leather *et al.*,[13] a summary of which is provided here. The smaller rate constants reported here and in Leather *et al.*[13] imply that the importance of reaction (5.1) in both Spring Polar vortices is considerably less than previously estimated by the earlier temperature dependence studies. Leather *et al.*[13] estimate that the effectiveness of reaction (5.1) in converting CH_3O_2 to CH_3O is reduced by a factor of 1.5 contributing to only 10 % of this conversion. Furthermore, the effectiveness in the partitioning of active chlorine into the reservoir CH_3OCl species by reaction (5.1), which is believed to be the minor product channel of this reaction, becomes less significant at stratospheric temperatures. The strong positive temperature dependence reported here implies that the importance of reaction (5.1) in the troposphere is restricted to the low altitude and latitude regions such as the Southern Ocean where ambient temperatures are found along with conditions of very low NO_x, BrO and IO (which all react more efficiently with ClO than CH_3O_2) and ClO levels can be expected to be relatively high for the troposphere. However, under these conditions HO_2 levels dominate which reacts with ClO more efficiently than CH_3O_2 at ambient temperatures (Chapter 4) but also with CH_3O_2 itself. Thus the implications of the results presented here and in Leather *et al.*[13] suggest a modest effect of reaction (5.1) in the chemistry of the atmosphere.

5.5 Conclusions

The kinetics of the total reaction of ClO + CH_3O_2 has been investigated as a function of temperature (T = 298 – 250 K) by the laser flash photolysis technique, using broadband UV absorption spectroscopy coupled to CCD detection at p = 760 Torr. This is the first study of reaction (5.1) using the flash photolysis technique both at room temperature and as function of temperature.

This work has found a significant positive activation energy for the ClO + CH_3O_2 reaction under investigation by measuring the decay of ClO through reaction with CH_3O_2 relative to the well defined kinetics of the reversible ClO self-reaction and the formation of its dimer Cl_2O_2. Secondary chemistry has been found to potentially underestimate the positive temperature dependence of this reaction if unaccounted for. The results of this work are supported by those of Leather *et al.*[13] which to date is the most sensitive discharge-flow study operated over pressures of the same order of magnitude as this work.

5.6 References

1. Crutzen, P.J., R. Muller, C. Bruhl, and T. Peter, On the Potential Importance of the Gas-Phase Reaction CH_3O_2 + ClO → ClOO + CH_3O and the Heterogeneous Reaction HOCl + HCl → H_2O + Cl_2 in Ozone Hole Chemistry. *Geophysical Research Letters*, 1992. **19**(11): 1113-1116.
2. Muller, R., T. Peter, P.J. Crutzen, H. Oelhaf, G.P. Adrian, T. Vonclarmann, A. Wegner, U. Schmidt, and D. Lary, Chlorine Chemistry and the Potential for Ozone Depletion in the Arctic Stratosphere in the Winter of 1991/92. *Geophysical Research Letters*, 1994. **21**(13): 1427-1430.
3. Strahan, S.E., A.R. Douglass, and P.A. Newman, The Contributions of Chemistry and Transport to Low Arctic Ozone in March 2011 Derived from Aura MLS Observations. *Journal of Geophysical Research-Atmospheres*, 2013. **118**(3): 1563-1576.
4. Farman, J.C., B.G. Gardiner, and J.D. Shanklin, Large Losses of Total Ozone in Antarctica Reveal ClO_x/NO_x Interaction. *Nature*, 1985. **315**(6016): 207-210.

5. Molina, L.T. and M.J. Molina, Production of Cl_2O_2 from the Self-reaction of the ClO Radical. *Journal of physical chemistry*, 1987. **91**(2): 433-436.
6. Simon, F.G., J.P. Burrows, W. Schneider, G.K. Moortgat, and P.J. Crutzen, Study of the Reaction ClO + CH_3O_2 → Products at 300 K. *Journal of physical chemistry*, 1989. **93**(23): 7807-7813.
7. Helleis, F., J.N. Crowley, and G.K. Moortgat, Temperature Dependent Rate Constants and Product Branching Ratios for the Gas-Phase Reaction Between CH_3O_2 and ClO. *Journal of physical chemistry*, 1993. **97**(44): 11464-11473.
8. Helleis, F., J. Crowley, and G. Moortgat, Temperature Dependent CH_3OCl Formation in the Reaction Between CH_3O_2 and ClO. *Geophysical Research Letters*, 1994. **21**(17): 1795-1798.
9. Kenner, R.D., K.R. Ryan, and I.C. Plumb, Kinetics of the Reaction of CH_3O_2 with ClO 293 K. *Geophysical Research Letters*, 1993. **20**(15): 1571-1574.
10. Kukui, A.S., T.P.W. Jungkamp, and R.N. Schindler, Determination of the Rate-Constant and of Product Branching Ratios in the Reaction of CH_3O_2 with OCl Between 233 K and 300 K. *Berichte Der Bunsen-Gesellschaft-Physical Chemistry Chemical Physics*, 1994. **98**(10): 1298-1302.
11. Biggs, P., C.E. Canosamas, J.M. Fracheboud, D.E. Shallcross, and R.P. Wayne, Efficiency of Formation of CH_3O in the Reaction of CH_3O_2 with ClO. *Geophysical Research Letters*, 1995. **22**(10): 1221-1224.
12. Daele, V. and G. Poulet, Kinetics and Products of the Reactions of CH_3O_2 with Cl and ClO. *Journal De Chimie Physique Et De Physico-Chimie Biologique*, 1996. **93**(6): 1081-1099.
13. Leather, K.E., A. Bacak, R. Wamsley, A.T. Archibald, A. Husk, D.E. Shallcross, and C.J. Percival, Temperature and Pressure Dependence of the Rate Coefficient for the Reaction Between ClO and CH_3O_2 in the Gas-Phase. *Physical Chemistry Chemical Physics*, 2012. **14**(10): 3425-3434.
14. Sander, S.P., J. Abbatt, J. R. Barker, J. B. Burkholder, R. R. Friedl, D. M. Golden, R. E. Huie, C. E. Kolb, M. J. Kurylo, G. and V.L.O. K. Moortgat, P. H. Wine, "Chemical Kinetics and Photochemical Data for Use in Atmospheric Studies, Evaluation No. 17," JPL Publication 10-6, Jet Propulsion Laboratory, Pasadena, 2011 http://jpldataeval.jpl.nasa.gov.
15. Atkinson, R., D.L. Baulch, R.A. Cox, J.N. Crowley, R.F. Hampson, R.G. Hynes, M.E. Jenkin, M.J. Rossi, J. Troe, and T.J. Wallington, Evaluated Kinetic and

Photochemical Data for Atmospheric Chemistry: Volume IV - Gas Phase Reactions of Organic Halogen Species. *Atmospheric Chemistry and Physics*, 2008. **8**(15): 4141-4496.

16. Kosmas, A.M. and E. Drougas, A Computational Investigation of the Atmospheric Reaction CH_3O_2 + ClO. *Chemical Physics*, 2009. **358**(3): 230-234.
17. Rowley, D.M., M.H. Harwood, R.A. Freshwater, and R.L. Jones, Novel Flash Photolysis UV Absorption System Employing Charge-Coupled Device (CCD) Detection: A Study of the BrO + BrO Reaction at 298 K. *Journal of physical chemistry*, 1996. **100**(8): 3020-3029.
18. Hinshelwood, C.N. and C.R. Prichard, A Homogeneous Gas Reaction – The Thermal Decomposition of Chlorine Monoxide Part I. *Journal of the Chemical Society*, 1923. **123**: 2730-2738.
19. Ferracci, V. and D.M. Rowley, Kinetic and Thermochemical Studies of the ClO + ClO + M $\rightleftharpoons$ Cl_2O_2 + M Reaction. *Physical Chemistry Chemical Physics*, 2010. **12**(37): 11596-11608.
20. Atkinson, R., D.L. Baulch, R.A. Cox, J.N. Crowley, R.F. Hampson, R.G. Hynes, M.E. Jenkin, M.J. Rossi, and J. Troe, Evaluated Kinetic and Photochemical Data for Atmospheric Chemistry: Volume II - Gas Phase Reactions of Organic Species. *Atmospheric Chemistry and Physics*, 2006. **6**: 3625-4055.
21. Boakes, G., W.H.H. Mok, and D.M. Rowley, Kinetic Studies of the ClO + ClO Association Reaction as a Function of Temperature and Pressure. *Physical Chemistry Chemical Physics*, 2005. **7**(24): 4102-4113.

Chapter 6: The Kinetics of the BrO + HO_2 Reaction

6.1 Introduction

The importance of the chemistry involving halogen containing species has implications throughout the troposphere and stratosphere (as discussed in preceding chapters). In particular, the catalytic nature of atmospheric atomic halogens with ozone has a profound impact on global ozone budgets. The coupling of halogen oxide and odd hydrogen reaction cycles also modifies odd oxygen chemistry *via* the formation of photolabile species whose photolysis products are potentially ozone destroying. An example involving bromine is the HOBr catalytic cycle first proposed as a particularly significant ozone destroying cycle by Yung *et al.*:[1]

$$\mathrm{BrO + HO_2 \rightarrow HOBr + O_2} \qquad (6.1a)$$

$$\mathrm{\rightarrow HBr + O_3} \qquad (6.1b)$$

$$\mathrm{HOBr} + h\nu \rightarrow \mathrm{OH + Br} \qquad (6.2)$$

$$\mathrm{OH + O_3 \rightarrow HO_2 + O_2} \qquad (6.3)$$

$$\mathrm{Br + O_3 \rightarrow BrO + O_2} \qquad (6.4)$$

$$\mathit{net}\text{: } \mathrm{2O_3 \rightarrow 3O_2}$$

Under sunlit conditions, the formation of HOBr is the rate determining step for this cycle in the lower stratosphere.

Sources of bromine to the troposphere and the lower stratosphere are believed to arise from a significant biogenic source, contrary to earlier assumptions that atmospheric bromine originates from the anthropogenic halons and methyl bromide alone.[2] This previously unrecognised bromine inventory meant that early atmospheric models predicted BrO levels around two to three times lower than what was typically observed in the atmosphere. Yang *et al.*[3] show that the inclusion of this additional biogenic source of bromine in their model results in BrO levels ranging from 1 – 8 pptv in the troposphere; more consistent with those subsequently measured by the Global Ozone Monitoring Experiment. Due to the short lived nature of bromocarbons, the formation of BrO is ubiquitous to the troposphere and the lower stratosphere in addition, to the upper stratosphere arising from the longer lived brominated species. This is corroborated by recent measurements which have shown that most tropospheric BrO in the tropics is found in the free troposphere.[4] In the polar troposphere, measurements concerning the sources of observed BrO show significant BrO activation in the planetary boundary layer supporting the notion of bromine activation by high winds over snow, as discussed in Chapter 1.[5]

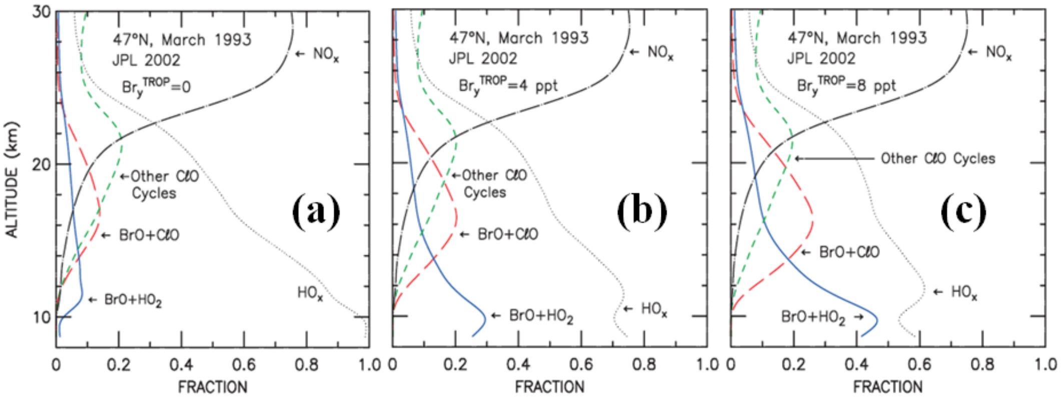

Figure 6.1 *Fraction of odd oxygen loss by various catalytic cycles modelled at 47°N, March 1993, for model runs with* Br_y^{TROP} *mixing ratios of: (a) = 0; (b) = 4; and (c) = 8 ppt. From Salawitch et al.*[6]

The effect of more BrO in the atmosphere results in increased rates of ozone loss, as it does with ClO, however, the dominant reaction pathways for this loss involving BrO and other species changes with altitude. Figure 6.1 shows the simulated fraction of odd oxygen loss by various catalytic cycles as a function of tropospheric inorganic bromine, denoted Br_y^{TROP}. It can be seen that while HO_x dominates the photochemical loss of ozone below 14 km, the contribution of the BrO + HO_2 reaction becomes considerable in the higher Br_y^{TROP} scenarios. Thus, the atmospheric weight of reaction (6.1) is apparent and an understanding of the kinetics and products of this reaction under tropospheric/lower stratospheric conditions is consequently of particular interest.

6.1.1 Previous Studies of BrO + HO_2

There have been a number of previous studies on the kinetics of the BrO + HO_2 reaction using a variety of techniques, including both the flash photolysis and discharge-flow tube methods. The first study came from Cox and Sheppard,[7] who applied the molecular-modulation UV absorption spectroscopy technique to a photolysed $O_3/Br_2/H_2/O_2$ system at T = 303 K and p = 1 atm. Poulet *et al.*[8] used a discharge-flow reactor coupled to a mass spectrometric technique to measure the rate constant under conditions of excess HO_2 at T = 298 K and p = 1 Torr. BrO and HO_2 were formed in the Poulet *et al.*[8] work *via* the $O(^3P)$ + Br_2 and Cl + CH_3OH/O_2 reactions respectively. Bridier *et al.*[9] employed the photolysis of $Br_2/O_3/Cl_2/CH_3OH/O_2$/He mixtures at T = 300 K in which HO_2 and BrO radical concentrations were monitored *via* UV absorption spectroscopy. Conditions were such that the concentrations of the reactant radicals were of a similar magnitude in all experiments. Larichev *et al.*[10] studied reaction (6.1) *via* the discharge-flow mass spectrometric method over the temperature range T = 233 – 344 K with an excess of HO_2 over BrO. Radicals were prepared *via* the $O(^3P)$ + Br_2 (BrO formation) and Cl + CH_3OH/O_2 (HO_2 formation) reactions. Elrod *et al.*[11] were the next to study the temperature dependence of BrO + HO_2. They used a turbulent flow system at a total pressure of p = 130 mbar at T = 298 – 210 K and the reactant/product species were monitored by chemical ionisation mass spectrometry. Again, $k_{(6.1)}$ was determined by monitoring the BrO radical concentrations in an excess of HO_2 radicals. BrO was produced by the $O(^3P)$ + Br_2 reaction and HO_2 by the H + O_2 + M reaction. The subsequent study was reported by Li *et al.*[12] where a discharge-flow reactor coupled with molecular beam mass spectrometry was used to study the reaction (6.1) over the temperature range T = 233 – 348 K. BrO radicals were produced by the Br + O_3 or $O(^3P)$ + Br_2 reactions and HO_2 radicals were generated by the F + H_2O_2 or Cl + CH_3OH (and subsequent O_2) reactions. Experiments were carried out under conditions of both [BrO] << [HO_2] and [HO_2] << [BrO]. Cronkhite *et al.*[13] used laser flash photolysis of $Cl_2/CH_3OH/O_2/Br_2/O_3/N_2$ mixtures at λ = 308 nm, coupled with simultaneous time-resolved detection of both species *via* separate probes: HO_2 by infrared tuneable diode laser absorption spectroscopy; and BrO by ultraviolet absorption spectroscopy, to investigate the kinetics of reaction (6.1) at $T = (296 \pm 3)$ K. The most recent laboratory determination of the temperature dependence of $k_{(6.1)}$ was by Bedjanian *et al.*,[14] employing the mass spectrometric discharge-flow method at temperatures between $T = 230 – 360$ K and at a total pressure of $p = 1$ Torr of helium. In these experiments BrO radicals were produced by either the Br + O_3 or $O(^3P)$ + Br_2 reactions and the HO_2 radicals by the F + H_2O_2 reaction. Experiments were carried out under conditions of both [BrO] << [HO_2] and [HO_2] << [BrO]. Finally, Bloss *et al.*[15] studied reaction (6.1) using the technique of flash photolysis/ time resolved UV absorption spectroscopy. BrO and HO_2 radicals were generated *via* the Br + O_3 and Cl + CH_3OH/O_2 methods respectively at $T = 298$ K and $p = 760$ Torr of O_2. The kinetic data from the above studies discussed above are summarised in Table 6.1 below.

All reported values of the room temperature rate constant for reaction (6.1) agree that the reaction is fast (*i.e.* close to the collisional limit). However, there is a significant spread in the data by up to a factor of 2 but when considering the relatively large uncertainty reported in each study there is general agreement, aside from the work of Cox and Sheppard,[7] who reported a much lower value for $k_{(6.1)}$ by nearly a factor of 10. The room temperature values of $k_{(6.1)}$ appear to cluster in two general groups: Poulet *et al.*,[8] Bridier *et al.*,[9] Larichev *et al.*[10] and Bedjanian *et al.*[14] are in agreement with values at over 3×10^{-11} cm^3 molecule^{-1} s^{-1} and the work of Li *et al.*,[12] Cronkhite *et al.*[13] and Bloss *et al.*[15] who purport values of around 2×10^{-11} cm^3 molecule^{-1} s^{-1} with Elrod *et al.*[11] even lower. However, there is no apparent explanation for this, as reported by Bedjanian *et al.*,[14] which is the most extensive study of reaction (6.1) to date. Further, there is no strong discretion between different techniques although the ambient pressure flash photolysis studies seem largely in the latter group. Also, there is no obvious pressure trend for $k_{(6.1)}$ neither among the discharge-flow investigations nor the flash photolysis. Differences in $k_{(6.1)}$ arising from which species was monitored by investigations using pseudo first order conditions could have implications as identified by Li *et al.*[12] However, Bedjanian *et al.*[14] investigated reaction (6.1) under both excess HO_2 and BrO, finding no discrepancies even when applying a third method of measuring relative rates. The scope of the observed discrepancies in the room temperature literature values is acknowledged by the IUPAC[16] recommendation for $k_{(6.1)}$ which is the mean of the work of Bridier *et al.*,[9] Larichev *et al.*,[10] Elrod *et al.*,[11] Li *et al.*,[12] Cronkhite *et al.*,[13] Bedjanian *et al.*[14] and Bloss *et al.*,[15] hence the significant uncertainty. The JPL NASA[17] recommendation is somewhat more selective (as reflected in the reported uncertainty) and is the mean of the values reported by Elrod *et al.*,[11] Li *et al.*,[12] Cronkhite *et al.*,[13] Bedjanian *et al.*[14] and Bloss *et al.*[15] only. The exclusion of Larichev *et al.*[10] appears to avoid double counting in deriving the mean in this case since this study and the study of Bedjanian *et al.*[14] were conducted in the same laboratory using the same technique and it is therefore assumed the latter supersedes the former. It appears that the Bridier *et al.*[9] study was omitted due to the non-pseudo-first order conditions employed, although being similar to the Bloss *et al.*[15] investigation.

Knowledge of the temperature dependence of the BrO + HO_2 reaction is consequently somewhat limited. While there have been four studies measuring $k_{(6.1)}$ as a function of temperature, two are from the same laboratory and all were conducted using the discharge-flow technique. However, all studies agree that reaction (6.1) has a negative temperature dependence. Furthermore, there is good agreement in the magnitude of ($-E/R$) apart from the most recent study which reports a substantially lower temperature dependence. Again, if the work of Bedjanian *et al.*[14] supersedes Larichev *et al.*,[10] then more uncertainty is placed on the temperature dependence of this reaction. This uncertainty is reflected in the large uncertainty placed on the recommended ($-E/R$) in the IUPAC[16] evaluation and the difference between the JPL NASA[17] recommendation which again omits Larichev *et al.*[10] thus raising the average value of $k_{(6.1)}$.

To date, reaction (6.1a) is the sole observed product channel for the BrO + HO_2 reaction as determined from mass spectrometric studies. Larichev *et al.*[10] and Bedjanian *et al.*[14] were unable to find any evidence of O_3 formation and reported upper limits for the branching ratio for channel (6.1b) as < 0.015 and < 0.004 respectively, based on their detection limits. Aside from the flow tube studies there have been no product studies of reaction (6.1). Furthermore, $k_{(6.1)}$ appears to be independent of pressure over the range covered by the previous studies ranging from $p = 1$ mbar to $p = 1$ bar and there is no evidence for adduct formation. This is supported theoretically by computational studies carried out by Guha and Francisco[18] and

Kaltsoyannis and Rowley.[19] Kaltsoyannis and Rowley[19] predict that analogous to ClO + HO_2, the BrO + HO_2 reaction proceeds along the triplet potential energy surface, forming a hydrogen-bond interaction before the hydrogen is thereafter transferred to the halogen moiety. Their work also shows most agreement with Bedjanian *et al.*,[14] suggesting a weak, near-zero temperature dependence.

Study	T / K	$k_{(6.1)}$/ cm^3 molecule^{-1} s^{-1}
Cox and Sheppard[7]	303	$(0.5\,^{+0.5}_{-0.3}) \times 10^{-11}$
Poulet *et al.*[8]	298	$(3.3 \pm 0.5) \times 10^{-11a}$
Bridier *et al.*[9]	300	$(3.4 \pm 1.0) \times 10^{-11}$
Larichev *et al.*[10]	303	$(3.4 \pm 0.6) \times 10^{-11a}$
	233 – 344	$4.77 \times 10^{-12} \exp[(580 \pm 100)/T]$
Elrod *et al.*[11]	298	$(1.4 \pm 0.3) \times 10^{-11a}$
	210 – 298	$2.5 \times 10^{-12} \exp[(520 \pm 80)/T]$
Li *et al.*[12]	298	$(1.73 \pm 0.61) \times 10^{-11a}$
	298	$(2.05 \pm 0.64) \times 10^{-11b}$
	233 – 348	$3.13 \times 10^{-12} \exp[(536 \pm 206)/T]$
Cronkhite *et al.*[13]	296	$(2.0 \pm 0.6) \times 10^{-11a}$
Bedjanian *et al.*[14]	298	$(3.1 \pm 0.8) \times 10^{-11}$
	230 – 360	$9.4 \times 10^{-12} \exp[(345 \pm 60)/T]$
Bloss *et al.*[15]	298	$(2.35 \pm 0.82) \times 10^{-11}$
IUPAC[16]	298	$(2.4 \pm 0.8) \times 10^{-11}$
	210 – 360	$4.5 \times 10^{-12} \exp[(500 \pm 200)/T]$
JPL NASA[17]	298	$(2.1 \pm 0.3) \times 10^{-11}$
		$4.5 \times 10^{-12} \exp(460/T)$

[a] *Under excess HO_2* [b] *Under excess BrO*

Table 6.1 *Summary of the previous kinetic studies of the BrO + HO_2 reaction.*

6.2 Experimental

The aims of these experiments were to measure the kinetics of the BrO + HO_2 reaction as a function of temperature, employing the laser flash photolysis of $Br_2/Cl_2/O_3/CH_3OH/O_2/N_2$ mixtures. The reactive species generated were monitored *via* UV absorption spectroscopy coupled to a charge coupled device (CCD) detection system as described in detail in Chapter 3. Application of a CCD detector meant that BrO could be monitored unequivocally using broadband differential spectroscopy which also allowed the accurate measurement of [BrO] as a function of time. As reported in chapters 4 and 5, the measurement of the peroxy (HO_2) radical abundance was not possible and had to be inferred *via* numerical modelling of the reaction system, ensuring that experimental conditions were such that the temporal behaviour of BrO had the greatest sensitivity to the principal reaction (which was independently checked). Parameterisation of the chemistry in experiments carried out in the presence or absence of the peroxy radical precursor, methanol, was applied from work previously carried out in this laboratory. The ensuing changes in the temporal behaviour of BrO and the kinetics obtained in the presence of methanol were attributed to the reaction of BrO with HO_2 and were quantified.

6.2.1 Radical Generation

Precursor gases were delivered through Teflon tubing linked to a Pyrex mixing line where they were mixed and diluted in the O_2 (BOC, > 99.98 %) carrier flow. The flow rates of the non-corrosive N_2 and O_2 gases were set using calibrated mass flow controllers (MKS), whereas the Cl_2 (BOC, 5 % by volume in nitrogen, > 99 % purity) was controlled by a Teflon needle valve with the flow measured by a calibrated glass ball meter. Both bromine and methanol vapour were supplied to the mixing line by passing nitrogen through different lines to two separate Pyrex bubblers containing either bromine liquid (Acros, 99.8 %) or methanol liquid (Sigma Aldrich, 99.9 %) held at T = 0 °C *via* an ice bath in a Dewar flask. Bromine concentrations were determined spectroscopically *via* non-photolysed experiments with Br_2 absent or present in the reactor. Br_2 absorbances were fit to JPL NASA[17] recommended absorption cross sections (Appendix III) using the Beer-Lambert law and good agreement was found between measured concentrations and those calculated from the corresponding vapour pressure of the bromine gas flows and temperature. Methanol concentrations were verified *via* gravimetric analysis as in Stone and Rowley[20] and again there was good agreement with the calculated [CH_3OH] from flow rates except at the faster flows of methanol in which methanol saturation of the carrier gas was presumably lower than 100 %. Ozone was generated *in situ* by flowing oxygen through a chamber containing a "pen-ray" mercury lamp, the emitted UV radiation of which (λ = 254 nm) photolysed a small fraction of the O_2. This method of producing O_3 was calibrated at different flows of oxygen, spectroscopically as with bromine. The reaction vessel was controlled thermally by recycling perfluoroether fluid (Galden HT180) supplied from a thermostat unit (Huber CC180) as described in Chapter 3. Concentrations of the precursor gases in the photolysis mixtures were typically: $Br_2 = (0.95 - 2.0) \times 10^{16}$ molecules cm^{-3}; $Cl_2 = (1.5 - 3.1) \times 10^{16}$ molecules cm^{-3}; $O_3 = 2.5 \times 10^{15}$ molecules cm^{-3}; $CH_3OH = (1.3 - 6.6) \times 10^{17}$ molecules cm^{-3} and the carrier flow of synthetic air varied accordingly for a total flow of *ca.* 2.5×10^{19} molecules cm^{-3} or a total carrier flow of *ca.* 810 SCCM.

The reactive radical species BrO and HO_2 were generated using laser flash photolysis. Mixtures of $Br_2/Cl_2/O_3/CH_3OH/N_2$ in an O_2 carrier flow were photolysed by a pulsed laser (Lamda Physik) at λ = 351 nm, generating the precursor radicals Br and Cl:

$$Br_2 + hv \rightarrow 2Br \qquad (6.5)$$

$$Cl_2 + hv \rightarrow 2Cl \qquad (6.6)$$

these atoms thereafter reacted with ozone or methanol (and then the product with oxygen) to form BrO or HO_2 respectively:

$$Br + O_3 \rightarrow BrO + O_2 \qquad (6.7)$$

$$Cl + CH_3OH \rightarrow HCl + CH_2OH \qquad (6.8)$$

$$CH_2OH + O_2 \rightarrow HO_2 + HCHO \qquad (6.9)$$

Care in designing suitable experimental conditions meant that the potential of both unavoidable pre-photolysis equilibrium effects and subsequent competing chemistry effects, post-photolysis, were taken into consideration. Optimal gas concentrations were employed to ensure the maximum conversion of Br to BrO and Cl to HO_2 where both reactants of the principal reaction were thereafter formed in a stoichiometric, rapid fashion.

Experiments carried out in the absence of methanol effectively removed reactions (6.8) and (6.9) from the chemical scheme. However, Cl_2 was still flowed into the reactor and therefore Cl atoms were still generated upon illumination by the laser. Under these conditions, Cl atoms were most likely to react with Br_2 or O_3 respectively owing to their relative abundances in the photolysis mixture and their rate coefficients:

$$Cl + Br_2 \rightarrow BrCl + Br \tag{6.10}$$

$$Cl + O_3 \rightarrow ClO + O_2 \tag{6.11}$$

The potential formation of ClO and additional BrO arising from the photolysis of Cl_2 in the absence of methanol, gives the potential to determine the total radical concentration immediately formed post-photolysis. It is well known that BrO and ClO self-react and efficiently react with one another, the reactions of which have been extensively studied in this laboratory previously:[21-24]

$$BrO + BrO \rightarrow Products \tag{6.12}$$

$$ClO + ClO\ [+ M] \rightarrow Products \tag{6.13}$$

$$BrO + ClO \rightarrow Products \tag{6.14}$$

Indeed, the application of the previous parameterisations of the above reactions provides a tool in which the chemistry of BrO and ClO can be exploited in order to carry out an actinic calibration of the initial concentrations of atomic chlorine and atomic bromine, $[Cl]_0$ and $[Br]_0$, formed upon photolysis.

6.2.2 Monitoring of Species

As discussed in Chapters 3, 4 and 5, UV absorption spectroscopy coupled to CCD detection was employed to probe the reactive species within the reaction cell. Light from a xenon arc lamp was passed counter to the propagation of the laser beam and imaged on to the CCD detector *via* the spectrograph. In the present work, the spectrograph was set to a diffraction grating of 300 grooves/mm with the entrance slit width at 75 μm. This gave a spectral resolution of 1.1 nm and a dispersion of typically between 0.220 – 0.221 nm/pixel and a spectral coverage of around 66 nm on the CCD detector.

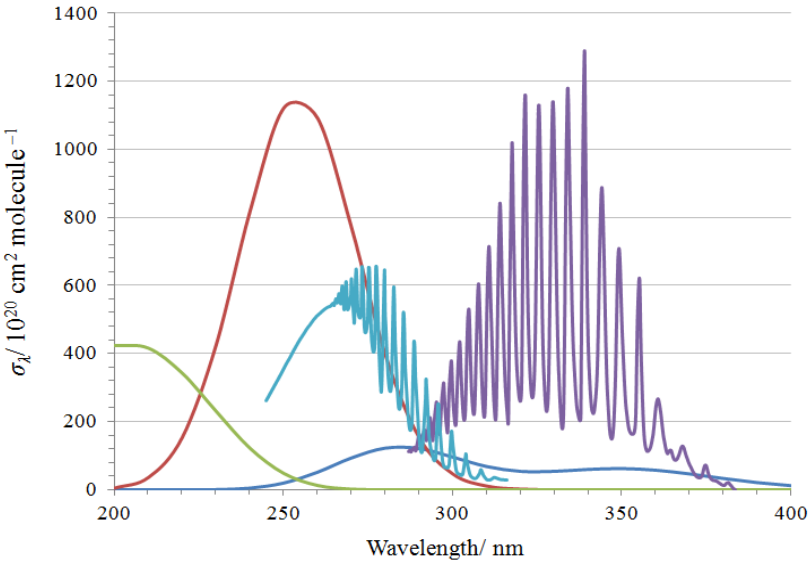

Figure 6.2 *The absorption cross sections, σ_x, of: BrO (purple); ClO (turquoise); HO_2 (green); O_3 (red); and HOBr (dark blue).*

As with the work described in the previous chapters, there are a number of potential absorbers present in the reaction mixture in the form of the two precursor halogen gases, photochemical intermediates and products, shown in Figures 6.2 and 6.3. Figure 6.2 shows the absorption cross sections of the radical species ClO, BrO and HO_2 along with the dominant product of reaction (6.1), HOBr, and ozone. Figure 6.3 illustrates the absorption cross sections of the halogen atom precursors Br_2 and Cl_2 along with BrCl, the potential formation of which was unavoidable owing to the equilibration reaction of Br_2 and Cl_2 in the precursor mixture as discussed in detail later below. Figure 6.3 also highlights the difficulty in accurately measuring the concentrations of the halogen mixtures owing to the overlapping cross sections of these species. Figure 6.2 shows that the spectral window of interest lay between 270 – 340 nm, where there is particular overlap of ClO, BrO and ozone absorptions. As discussed in Chapter 3, the application of differential spectroscopy allows the deconvolution of multiple overlapping absorbers provided they are spectrally structured, thus allowing unequivocal monitoring of ClO and BrO discussed in the following section.

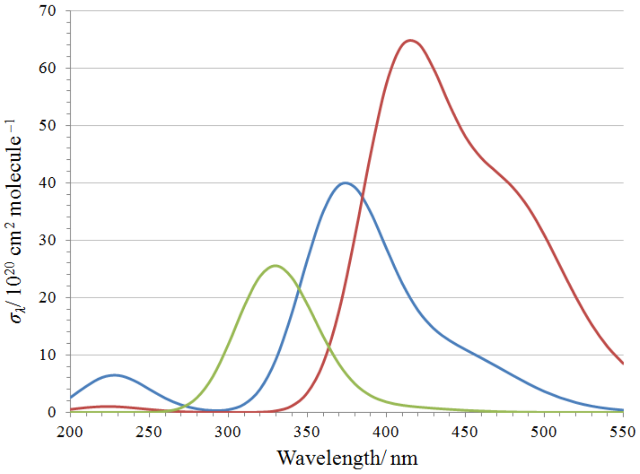

Figure 6.3 *The absorption cross sections of: Br_2 (red); BrCl (blue); and Cl_2 (green).*

Photolysis experiments were undertaken on several gas mixtures, differing in composition, and examples of the time averaged post-photolysis absorption spectra of these experiments are shown in Figures 6.4 (a) – (d). These separate mixtures comprised of (a) Cl_2/O_3/(synthetic) air (b) Br_2/O_3/air, then (c) $Br_2/Cl_2/O_3$/air and finally a mixture of $Br_2/Cl_2/O_3$/air/CH_3OH (d). These absorption spectra are representative of the changes in the total absorption of the gas mixture resulting from photolysis. Therefore, depending on the absorbing species formed or removed, there are both positive and negative contributions to the change in absorption relative to the total absorption of the gas mixture pre-photolysis. Each spectrum shows a positive structured contribution to the total absorbance characteristic to the formation of a halogen oxide although the structure and extent of these vibronic features depends on what gas mixture is photolysed. In Figures 6.4 (a) and (b), the absorbance is clearly characteristic of the ClO and BrO species respectively. Thereby comparing these with Figures 6.4 (c) and (d) it is evident that upon photolysis of the mixed halogen mixtures negligible ClO is formed, as evidenced by the loss of the characteristic ClO absorption signal.

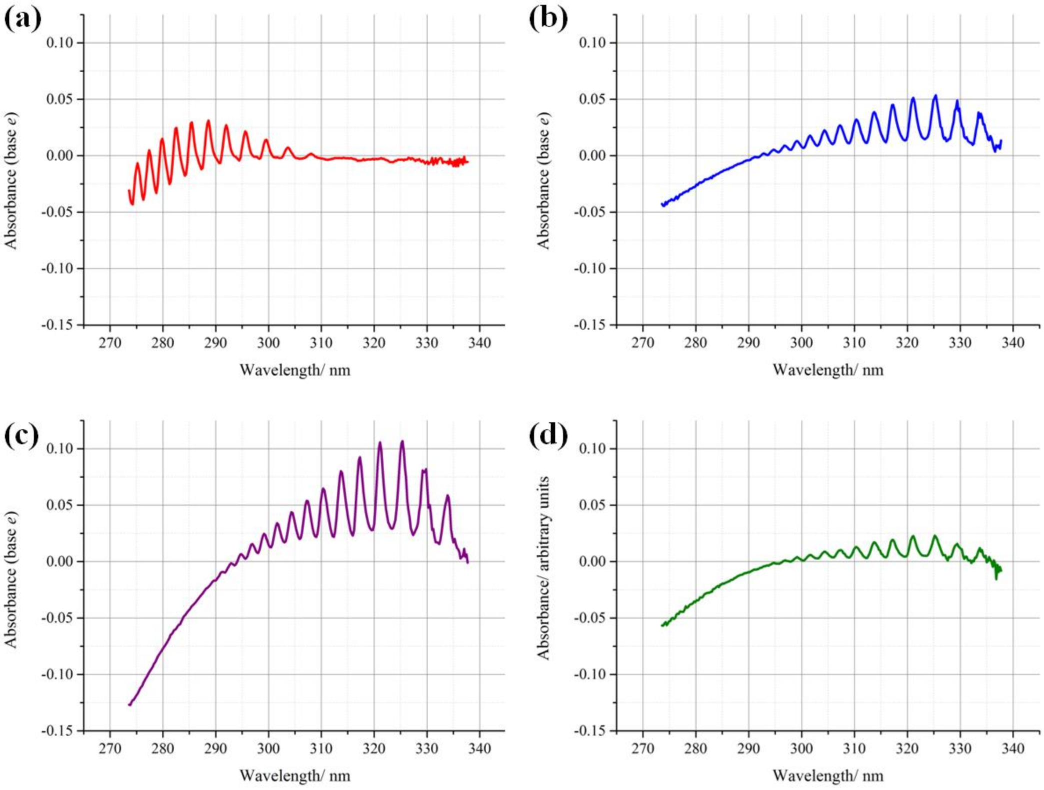

Figure 6.4 *Time averaged absorption spectra (over 250 μs), taken from t = 150 μs post-photolysis of the precursor mixtures: (a)* Cl_2/O_3*/air; (b)* Br_2/O_3*/air; (c)* $Br_2/Cl_2/O_3$*/air; and (d)* $Br_2/Cl_2/O_3/CH_3OH$*/air.*

Furthermore, in the $Br_2/Cl_2/O_3$/air mixture absent of methanol, there is an apparent enhancement in the BrO signal whereas in the photolysis of the same mixture but with the presence of methanol, there is a clear decrease in BrO. Similarly, by looking at the negative contributions in absorbance, there is an enhanced negative contribution between 270 – 290 nm is evident in Figure 6.4 (c) implying that there is an enhanced loss of an absorbing species in the mixture. These negative contributions to the total absorbance are attributed and consistent with the consumption of ozone. Due to the relatively large absorption cross sections and abundance of ozone in the gas mixtures employed in this work, the significant changes in absorbance predominantly result from ozone photo-initiated chemistry, meaning that changes in ozone concentration can also be monitored.

While the time averaged spectra can elucidate what species are formed or destroyed upon photolysis, taking sequences of these spectra at different times post-photolysis shows how these changes in absorbance evolve over time. Figures 6.5 (a) and (b) are time sequenced spectra of the same photolysis mixtures in Figures 6.4 (c) and (d) respectively. There are clear differences in the temporal behaviour in the absorbance of two otherwise identical mixtures in the absence/presence of methanol. In Figure 6.5 (a), there is an initial strong BrO absorbance post-photolysis that decays gradually with an initial negative O_3 absorption which becomes increasingly significant. By comparison, the changes in the absorbance of the mixture post-photolysis in Figure 6.5 (b) are much less pronounced; the initial BrO signal is weaker and decays more rapidly whereas the O_3 signal shows an initial negative absorption which subsequently remains almost constant.

The differences between the changes in the total absorption of the different photolysed reaction mixtures are attributed to changes in the reaction pathway of the initial chlorine atoms formed upon photolysis of Cl_2. The complete loss of the ClO signal and the corresponding enhancement of that of the BrO in the mixed halogen precursor mixture compared to the single halogen mixtures is indicative of the atomic chlorine reacting solely with Br_2. Therefore, the dominance of reaction (6.10) over (6.11) results in the liberation of additional bromine atoms which subsequently react with O_3 to give an increased yield in the initial BrO formed immediately post-photolysis. Accordingly, the significant *decrease* in the BrO signal of the mixed halogen mixture in the presence of methanol is attributed to the competition between reactions (6.10) and (6.8), which therefore inhibits additional BrO formation. The quantification of these processes and the accompanying changes in the temporal behaviour of BrO provided the means in which to evaluate the kinetics of the BrO + HO_2 reaction. However, this was only achieved by determining the changing concentrations of these species with time, as discussed below.

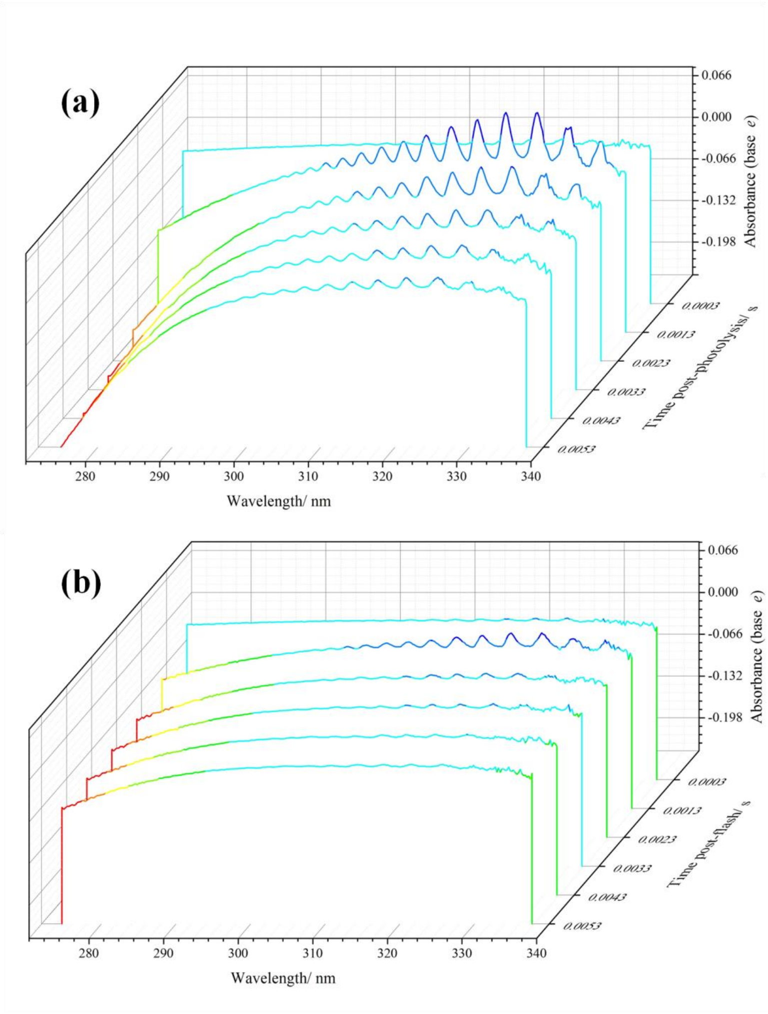

Figure 6.5 *Sequential post-photolysis absorption spectra of photolysis gas mixtures: (a) $Br_2/Cl_2/O_3$/air; and (b) $Br_2/Cl_2/O_3/CH_3OH$/air.*

6.2.3 Determination of BrO and Changes in O_3 Concentrations

The concentration of BrO was obtained *via* the application of differential spectroscopy described in detail in Chapter 3. By fitting the BrO differential absorption cross sections of the vibronic bands of BrO to the recorded experimental absorbance using the Beer-Lambert law, the unequivocal measurement of [BrO] was possible. Each sequential experimental absorbance spectrum recorded on the CCD was individually fit resulting in the determination of $[BrO]_t$ over the entire experimental time range.

The accurate determination of [BrO] relied heavily on the availability of precise BrO absorption cross section data. Previous work from Wilmouth *et al.*[25] provided the reference spectrum in the fitting procedure. These authors recorded the cross sections of the structured region of the BrO absorption spectrum at a resolution of 0.4 nm full-width half-maximum (FWHM). The instrument resolution used in this work was lower at 1.1 nm FWHM thus the higher resolution data were suitably degraded by applying in this case a 93-point Gaussian averaging kernel, the procedure of which is discussed in detail in Appendix II. The outcome of this averaging procedure is shown below in Figure 6.6 which compares the high resolution data of Wilmouth *et al.*[25] to the resultant resolution degraded spectrum.

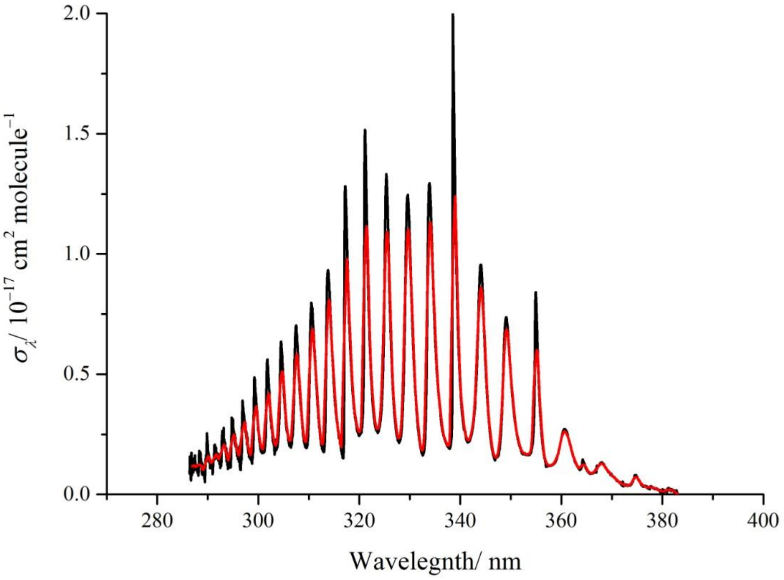

Figure 6.6 *The high resolution (0.4 nm FWHM) spectrum of BrO (black) and the corresponding smoothed low resolution (1.1 nm FWHM) spectrum (red). Original data were taken from Wilmouth et al.*[25]

As demonstrated in the previous section, BrO was the only discernible structured absorber observed in the photolysed gas mixtures over the experimental wavelength range. Unstructured absorbers were also present, although the observed changes in absorbance at the lower wavelengths of the spectral window used arose predominantly from changes in [O_3]. Comparing the experimental absorbance after subtracting the BrO contribution with the corresponding O_3 cross sections in Figure 6.7 (a), it can be seen that there is an anti-correlation between them as a function of wavelength. This similarity is illustrated further in the adjacent plot of the experimental absorbance against the O_3 cross section from JPL NASA[17] in Figure 6.7 (b). The observed linear correlation shows that the changes in the absorbance of the gas mixtures brought about upon photolysis in this spectral range are principally through changes to the concentration of ozone. Hence, the absolute *change* in ozone concentration, $\Delta[O_3]$, could therefore be determined and measured as a function of time. Consequently, the kinetic behaviour of O_3 in addition to BrO could be analysed simultaneously to obtain branching information, as discussed below in the results section.

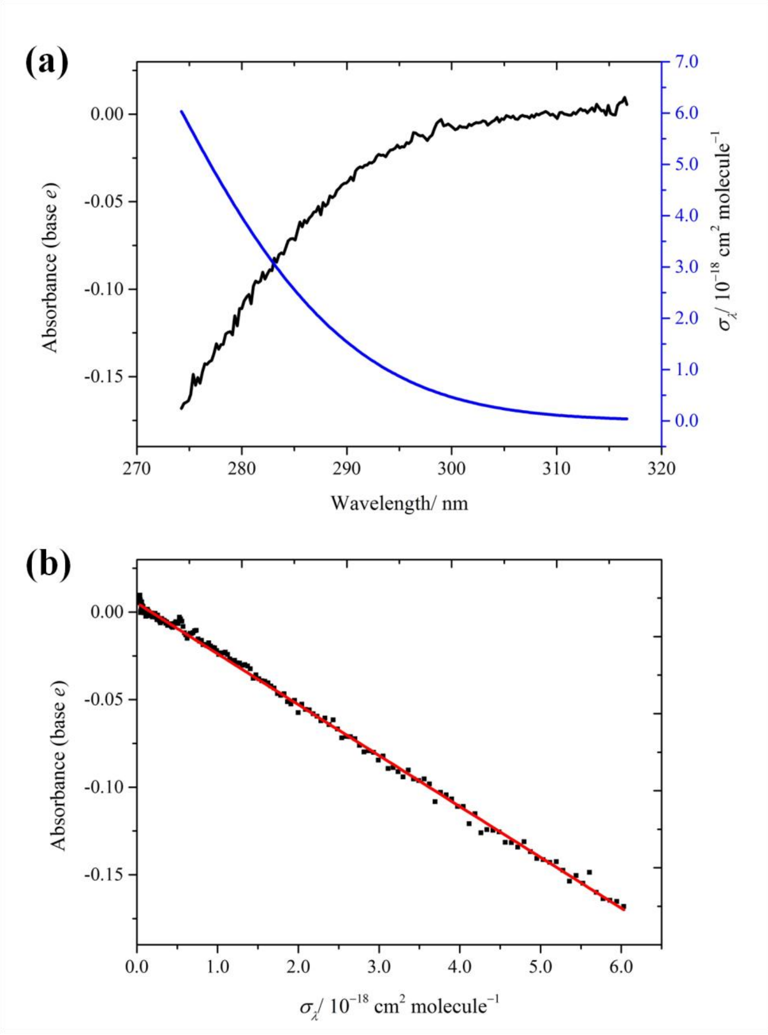

Figure 6.7 *Comparison of the experimental absorbance and O_3 cross section : (a) absorbance (black) and O_3 cross section (blue) as a function of wavelength; (b) absorbance versus O_3 cross section (black squares) and the corresponding fit using linear regression analysis (red).*

6.3 Results and Kinetic Analysis

6.3.1 Temporal Profiles of [BrO] and Δ[O_3] Recorded in the Absence or Presence of CH_3OH

Temporal traces of [BrO] and Δ[O_3] were obtained by applying the procedure outlined above and shown below in Figure 6.8 is a typical example of the observed behaviour of the two variables formed in Br_2/Cl_2/O_3/air mixtures photolysed either in the absence (shown as green traces) or presence (shown as blue and red traces) of methanol. These experiments were conducted under identical conditions aside from the amount of methanol present. The differences between the traces obtained from conditions of no methanol and those with increasing amounts of methanol are evident.

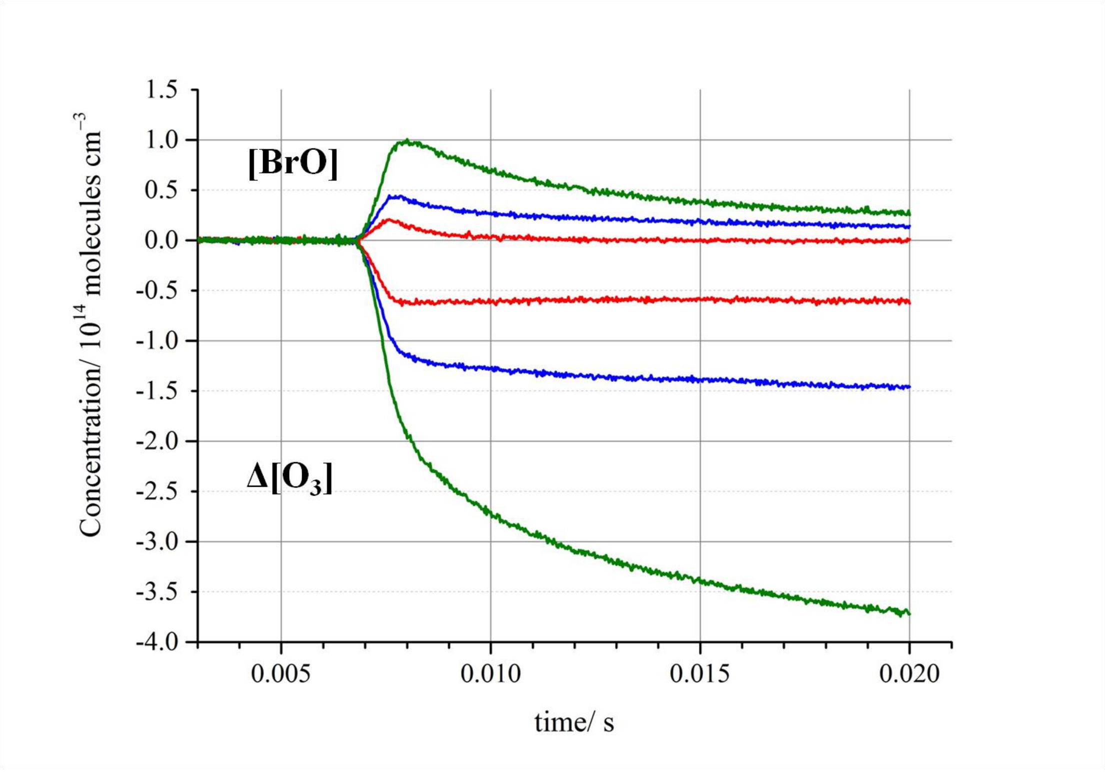

Figure 6.8 *Temporal traces of [BrO] and Δ[O_3] derived from photolysed mixtures of Br_2/Cl_2/O_3/air with: [CH_3OH] = 0 molecules cm^{-3} (green); [CH_3OH] = 6.9×10^{16} molecules cm^{-3} (blue); and [CH_3OH] = 1.4×10^{17} molecules cm^{-3}.*

Considering the BrO traces alone, there is a decrease in the maximum [BrO], $[BrO]_{max}$, between methanol free conditions compared to those with increasing methanol. What is more, doubling the amount of methanol present in the system serves to decrease $[BrO]_{max}$ further whereas the rate of BrO loss, even at these lower concentrations, appears to actually increase. The extent of BrO decay also becomes much more significant under the conditions with the largest levels of methanol where the total loss of BrO is observed. Similarly, there are comparable differences in the changes in ozone in each system: the extent of the sharp initial ozone loss and the more gradual decay that follows as the reaction proceeds further, both decrease with increasing methanol. The traces shown in Figure 6.8 in green, obtained under methanol free conditions, in which the loss of ozone continues throughout the reaction and the observed decay in BrO is slow, is characteristic of the regeneration of bromine atoms after the laser flash which react with more O_3 to generate additional BrO. This specific trace pair exhibits the kinetics of the well known BrO self-reaction, having two principal outcomes, which are either radical propagating or terminating:

$$BrO + BrO \rightarrow Br + Br + O_2 \tag{6.12a}$$

$$\rightarrow Br_2 + O_2 \tag{6.12b}$$

Hence, the increasing loss of ozone in this case is the result of catalytic chain chemistry. The subsequent decrease in the catalytic ozone loss with increasing $[CH_3OH]$ is therefore attributed to other chemistry occurring that competes with the BrO self-reaction. The trace pair shown in red, obtained from the experiments performed under the highest $[CH_3OH]$, appears to show completely different kinetic behaviour from those shown in green. The constant $\Delta[O_3]$, after the initial ozone decay, indicates that there is no halogen atom regeneration and the fast complete decay of BrO corroborates this.

The implication from these findings is that the BrO self-reaction is completely inhibited under high $[CH_3OH]$ and the observed loss of BrO is characteristic of a separate reaction. These conditions are such that BrO reacts predominantly with HO_2, the formation of which is initiated *via* reaction (6.8) which outcompetes reaction (6.10) under low $[Br_2]/[CH_3OH]$ ratios. However, in order to quantify this and analyse the kinetic behaviour of these two different photochemical regimes, the specific processes that govern radical formation must be well defined in addition to the radical decay.

6.3.2 Analysis of Radical Production Routes

Breaking down the reaction systems used in this study into key components and using numerical integration software (FACSIMILE), a model of the BrO + BrO reaction was developed. In an analogous fashion to chapters 4 and 5, this model was subsequently incorporated into a more comprehensive model of the BrO + HO_2 reaction, discussed below. Simulations enabled the key features of the chemistry carried out in these experiments to be categorised as follows: (i) the mixing of precursor gases; (ii) the partitioning of [Br] and [Cl] upon photolysis; (iii) and the reactive fate of the radicals *i.e.* the rapid formation and decay of BrO + HO_2. This breakdown and characterisation of the experiment from pre- to post-photolysis, discussed below, is vital to the kinetic analysis of the experimental data due to the complexity and nature of this reaction system and the consequent experimental setup.

To determine the rate coefficient for a bimolecular reaction such as BrO + HO_2, the absolute concentration of both species must be known. However in this study only BrO was monitored under the experimental conditions used. Further complications arose from the need to use two different precursor radicals owing to the insufficient reactivity of Br to abstract a hydrogen atom from CH_3OH, hence the inclusion of Cl_2 in the photolysis mixture. While Cl reacts with CH_3OH efficiently to eventually form HO_2, its reactivity is also a potential hindrance in determining the initial concentrations of the principal radical reactants, as is addressed below. As already discussed, upon illumination of the precursor mixture *via* the laser, both Br and Cl atoms are formed simultaneously through the photolysis of Br_2 and Cl_2 in the precursor mixture (reactions (6.5) and (6.6)). It then follows that the initial concentrations of atomic bromine and chlorine, $[Br]_0$ and $[Cl]_0$ respectively, are dependent on the fraction of Br_2 and Cl_2 present, defined as f_{Br_2} and f_{Cl_2} respectively, that are photolysed at $\lambda = 351$ nm:

$$[Br]_0 = 2f_{Br_2}[Br_2] \tag{6.3 i}$$

$$[\mathrm{Cl}]_0 = 2f_{\mathrm{Cl_2}}[\mathrm{Cl_2}] \qquad (6.3\ \mathrm{ii})$$

And so the ratio of $[\mathrm{Cl}]_0$ over $[\mathrm{Br}]_0$ may be expressed as:

$$\frac{[\mathrm{Cl}]_0}{[\mathrm{Br}]_0} = \frac{f_{\mathrm{Cl_2}}[\mathrm{Cl_2}]}{f_{\mathrm{Br_2}}[\mathrm{Br_2}]} = a\frac{[\mathrm{Cl_2}]}{[\mathrm{Br_2}]} \qquad (6.3\ \mathrm{iii})$$

where $a = \frac{f_{\mathrm{Cl_2}}}{f_{\mathrm{Br_2}}}$ *i.e.* the ratio of the fraction of Cl_2 photolysed over the fraction of Br_2 photolysed. This is also equal to the ratio of the absorption cross sections of the same species at λ = 351 nm, $\frac{\sigma_{\mathrm{Cl_2}}}{\sigma_{\mathrm{Br_2}}}$. Since the quantum yields for both photolysis are unity at this wavelength,[17] the relative amount of Cl and Br atoms is therefore directly proportional to the relative amounts of Br_2 and Cl_2 in the precursor mixture immediately after the laser flash. Hence the partitioning of the total number of atoms formed between Cl and Br is therefore described by a. Experimentally, this enables a relatively simple actinometric calibration of $[\mathrm{Br}]_0$ and $[\mathrm{Cl}]_0$ by measuring the amount of radicals formed in separate experiments of the self-reactions BrO + BrO and ClO + ClO. Only pure Br and Cl are required in generating BrO and ClO respectively and these reaction schemes therefore allow total conversion of the atomic halogen species to their corresponding monoxide radical species. However, this simple model is based on the assumption that the only photolabile species present in the precursor mixture are Br_2 and Cl_2. Previous studies have shown that concentrations of Br_2 and Cl_2 do not remain constant upon mixing, with the disproportionation of Br from Br_2 by Cl_2 *via* the equilibration reaction:[15,26]

$$\mathrm{Br_2 + Cl_2 \rightleftharpoons 2BrCl} \qquad (6.15)\ (–6.15)$$

The potential for BrCl formation is thereby unavoidable under the experimental conditions used in this study. Therefore the equilibrium mixture formed prior to photolysis must also be taken into account when calculating $[\mathrm{Br}]_0$ and $[\mathrm{Cl}]_0$ as the presence of BrCl can significantly alter $\frac{[\mathrm{Cl}]_0}{[\mathrm{Br}]_0}$ which is brought about by the overall change in the *absorbance* of the mixture. This is described below.

6.3.3 Mixing of Precursor Gases: Equilibrium of Br$_2$, Cl$_2$ and BrCl

Upon mixing, a given amount of bromine and chlorine disproportionate to react described by reactions (6.15) & (–6.15) and the rate equation for this reaction is expressed as:

$$-\frac{d[\mathrm{Br_2}]}{dt} = -\frac{d[\mathrm{Cl_2}]}{dt} = \frac{d[\mathrm{BrCl}]}{2dt} = \frac{k_f}{2}[\mathrm{Br_2}][\mathrm{Cl_2}] - k_r[\mathrm{BrCl}] \qquad (6.3\ \mathrm{iv})$$

Thereafter the concentrations of Br$_2$, Cl$_2$ and BrCl may be rewritten as:

$$[\mathrm{Br_2}] = [\mathrm{Br_2}]_{\mathrm{eq}} + x \qquad (6.3\ \mathrm{v})$$

$$[\mathrm{Cl_2}] = [\mathrm{Cl_2}]_{\mathrm{eq}} + x \qquad (6.3\ \mathrm{vi})$$

$$[\mathrm{BrCl}] = [\mathrm{BrCl}]_{\mathrm{eq}} - 2x \qquad (6.3\ \mathrm{vii})$$

where *x* is the amount of substance in excess of the initial reactants and *vice versa* for the product. Substituting the above into equation (6.3 iv) gives:

$$-\frac{dx}{dt} = \frac{k_f}{2}\left([\mathrm{Br_2}]_{\mathrm{eq}} + x\right)\left([\mathrm{Cl_2}]_{\mathrm{eq}} + x\right) - k_r\left([\mathrm{BrCl}]_{\mathrm{eq}} - 2x\right) \qquad (6.3\ \mathrm{viii})$$

Expanding the above then yields:

$$-\frac{dx}{dt} = \frac{k_f}{2}x^2 + \frac{k_f}{2}x\left([\mathrm{Br_2}]_{\mathrm{eq}} + [\mathrm{Cl_2}]_{\mathrm{eq}}\right) + \frac{k_f}{2}[\mathrm{Br_2}]_{\mathrm{eq}}[\mathrm{Cl_2}]_{\mathrm{eq}} - k_r[\mathrm{BrCl}]_{\mathrm{eq}} + 2k_r x \qquad (6.3\ \mathrm{ix})$$

At equilibrium, when the net rate of change in reactants and products is equal to zero equation (6.3 iv) can be rearranged to:

$$\frac{k_f}{2}[\mathrm{Br_2}][\mathrm{Cl_2}] = k_r[\mathrm{BrCl}] \qquad (6.3\ \mathrm{x})$$

Hence, equation (6.3 ix) simplifies to:

$$-\frac{dx}{dt} = \frac{k_f}{2}x^2 + \frac{k_f}{2}x\left([\mathrm{Br_2}]_{\mathrm{eq}} + [\mathrm{Cl_2}]_{\mathrm{eq}}\right) + 2k_r x \qquad (6.3\ \mathrm{xi})$$

Therefore:

$$\frac{dx}{x\left(\frac{k_f}{2}x + \frac{k_f}{2}\left([\mathrm{Br_2}]_{\mathrm{eq}} + [\mathrm{Cl_2}]_{\mathrm{eq}}\right) + 2k_r\right)} = -dt \qquad (6.3\ \mathrm{xii})$$

which is a differential equation of the form:

$$\frac{dx}{x(a+bx)} = -dt \qquad (6.3\ \mathrm{xiii})$$

where $a = \frac{k_f}{2}\left([\mathrm{Br_2}]_{\mathrm{eq}} + [\mathrm{Cl_2}]_{\mathrm{eq}}\right) + 2k_r$ and $b = \frac{k_f}{2}$

Integrating the above gives:

$$\int_{x_0}^{x_t} \frac{dx}{x(a+bx)} = -\int_0^t dt \qquad (6.3\ \mathrm{xiv})$$

Therefore:

$$-t = -\frac{1}{a}\ln\left(\frac{a+bx_t}{x_t}\right) + \frac{1}{a}\ln\left(\frac{a+bx_0}{x_0}\right) \qquad (6.3\ \mathrm{xv})$$

$$\ln\left(\frac{a+bx_0}{x_0}.\frac{x_t}{a+bx_t}\right) = -at \qquad (6.3\ \mathrm{xvi})$$

Thus:

$$x_t = \frac{ax_0\exp(-at)}{a+bx_0-bx_0\exp(-at)} \qquad (6.3\ \mathrm{xvii})$$

Experimentally at $t = 0$, before any reaction commences *i.e.* prior to the mixing of Br_2 and Cl_2 in the gas line, the concentration of BrCl must be zero, hence:

$$x_0 = \tfrac{1}{2}[\mathrm{BrCl}]_{\mathrm{eq}} \qquad (6.3\ \mathrm{xviii})$$

So the initial pre-photolysis (post mixing) concentrations of Br_2 and Cl_2 are given by:

$$[\mathrm{Br_2}]_0 = [\mathrm{Br_2}]_{\mathrm{eq}} + \tfrac{1}{2}[\mathrm{BrCl}]_{\mathrm{eq}} \qquad (6.3\ \mathrm{xix})$$

$$[\mathrm{Cl_2}]_0 = [\mathrm{Cl_2}]_{\mathrm{eq}} + \tfrac{1}{2}[\mathrm{BrCl}]_{\mathrm{eq}} \qquad (6.3\ \mathrm{xx})$$

By definition, the equilibrium constant of reactions (6.15) & (–6.15) is:

$$K_c = \frac{[\mathrm{BrCl}]_{\mathrm{eq}}^2}{[\mathrm{Br_2}]_{\mathrm{eq}}[\mathrm{Cl_2}]_{\mathrm{eq}}} \qquad (6.3\ \mathrm{xxi})$$

Rearranging equations (6.3 xix) and (6.3 xx) and substituting into the above yields:

$$K_c = \frac{[\mathrm{BrCl}]_{\mathrm{eq}}^2}{\left([\mathrm{Br_2}]_0 - \tfrac{1}{2}[\mathrm{BrCl}]_{\mathrm{eq}}\right)\left([\mathrm{Cl_2}]_0 - \tfrac{1}{2}[\mathrm{BrCl}]_{\mathrm{eq}}\right)} \qquad (6.3\ \mathrm{xxii})$$

Upon expansion:

$$K_c = \frac{[\mathrm{BrCl}]_{\mathrm{eq}}^2}{\tfrac{1}{4}[\mathrm{BrCl}]_{\mathrm{eq}}^2 - \tfrac{1}{2}[\mathrm{BrCl}]_{\mathrm{eq}}\left([\mathrm{Br_2}]_0 + [\mathrm{Cl_2}]_0\right) + [\mathrm{Br_2}]_0[\mathrm{Cl_2}]_0} \qquad (6.3\ \mathrm{xxiii})$$

This expression can then be arranged to give:

$$\left(\frac{K_c}{4} - 1\right)[\mathrm{BrCl}]_{\mathrm{eq}}^2 - \frac{K_c}{2}[\mathrm{BrCl}]_{\mathrm{eq}}\left([\mathrm{Br_2}]_0 + [\mathrm{Cl_2}]_0\right) + K_c[\mathrm{Br_2}]_0[\mathrm{Cl_2}]_0 = 0 \qquad (6.3\ \mathrm{xxiv})$$

which is an equation of the form:

$$ax^2 + bx + c = 0 \qquad (6.3\ \text{xxv})$$

and can be solved by:

$$x = \frac{-b \pm \sqrt{b^2 - 4ac}}{2a} \qquad (6.3\ \text{xxvi})$$

where $x = [\mathrm{BrCl}]_{\mathrm{eq}}$, $a = \frac{K_c}{4} - 1$, $b = \frac{K_c}{2}\left([\mathrm{Br_2}]_0 + [\mathrm{Cl_2}]_0\right)$ and $c = K_c[\mathrm{Br_2}]_0[\mathrm{Cl_2}]_0$

Hence the equilibrium concentrations of Br_2, Cl_2 and BrCl can be calculated from the above expression using $[Br_2]_0$ and $[Cl_2]_0$, which are known as the flow controlled concentrations of bromine and chlorine that are used experimentally, and by applying the well determined experimental value of $K_c = 10.1 \pm 1.1$ at $T = 298$ K taken from Maric *et al.*[26] Figure 6.9 below shows the effect that reactions (6.15) and (–6.15) have on the expected halogen precursor ratio at equilibrium compared to the initial flows of molecular chlorine and bromine used experimentally. It can be seen that the expense of forming BrCl is a loss in the proportion of Br_2.

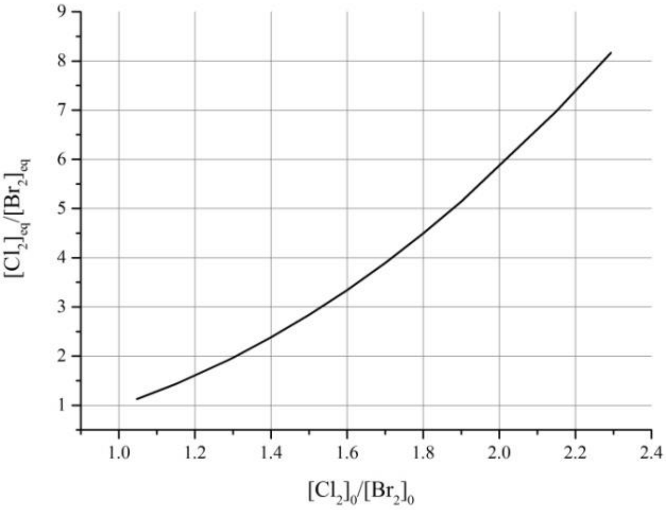

Figure 6.9 *A plot of the initial ratio of halogen precursors against the predicted ratio at equilibrium.*

The effects of this equilibrium mixture upon the initial levels of Br and Cl atoms formed upon photolysis are discussed in the following section.

6.3.4 Photolysis of the Precursor Gas Mixture: Radical Generation

The formation of atomic bromine and chlorine after the photolysis of Br_2 and Cl_2 and indeed BrCl, when considering an equilibrium mixture, gives a total initial atom number density post-photolysis, denoted $[TA]_0$, from the sum of the Br and Cl atom number density:

$$[TA]_0 = [Br]_0 + [Cl]_0 \qquad (6.3\ xxvii)$$

Therefore $[Cl]_0$ can be expressed as a fraction, δ, of $[TA]_0$ which defines the portioning of $[Br]_0$ and $[Cl]_0$ immediately post-photolysis:

$$[Cl]_0 = \delta[TA]_0 \qquad (6.3\ xxviii)$$

which implies:

$$[Br]_0 = (1 - \delta)[TA]_0 \qquad (6.3\ xxix)$$

Therefore, the ratio of $[Cl]_0$ over $[Br]_0$ may be simply expressed as:

$$\frac{[Cl]_0}{[Br]_0} = \frac{\delta}{(1 - \delta)} \qquad (6.3\ xxx)$$

Giving:

$$\delta = \frac{\frac{[Cl]_0}{[Br]_0}}{\left(1 + \frac{[Cl]_0}{[Br]_0}\right)} \qquad (6.3\ xxxi)$$

As discussed above, the ratio of the initial concentrations of atomic bromine and chlorine formed from the photolysis of a non-BrCl equilibrium mixture were found to be dependent on the ratio of the chlorine and bromine concentrations multiplied by the ratio of their corresponding absorption cross sections (equation (6.3 iii)). However the presence of BrCl in the photolysis mixture means that this no longer necessarily holds.

As alluded above, the photolysis of BrCl provides another source of Br and Cl atoms from the precursor gas mixture:

$$\mathrm{BrCl} + h\nu \rightarrow \mathrm{Br} + \mathrm{Cl} \qquad (6.16)$$

While the conversion of Br_2 and Cl_2 to 2BrCl and its subsequent photolysis gives the same stoichiometric conversion of Br and Cl atoms as the direct photolysis of Br_2 and Cl_2 does, differences in the absorption cross sections of these species at 351 nm means that the relative concentration of each species at equilibrium will have a significant impact on $\frac{[\mathrm{Cl}]_0}{[\mathrm{Br}]_0}$. This is brought about by the relative changes in the optical density of the photolysis mixture compared to a notional mixture without formation of BrCl. With an additional radical source in the reaction scheme, a mixture of Br_2 and Cl_2 in equilibrium with BrCl therefore gives the following initial radical concentrations:

$$[\mathrm{Br}]_0 = 2f_{\mathrm{Br_2}}[\mathrm{Br_2}]_{\mathrm{eq}} + f_{\mathrm{BrCl}}[\mathrm{BrCl}]_{\mathrm{eq}} \qquad (6.3\ \mathrm{xxxii})$$

$$[\mathrm{Cl}]_0 = 2f_{\mathrm{Cl_2}}[\mathrm{Cl_2}]_{\mathrm{eq}} + f_{\mathrm{BrCl}}[\mathrm{BrCl}]_{\mathrm{eq}} \qquad (6.3\ \mathrm{xxxiii})$$

where $f_{\mathrm{Br_2}}, f_{\mathrm{Cl_2}}$ and f_{BrCl} represent the fractional photolysis of these three molecules. Therefore the expression of the ratio of $[\mathrm{Cl}]_0$ over $[\mathrm{Br}]_0$ is modified to:

$$\frac{[\mathrm{Cl}]_0}{[\mathrm{Br}]_0} = \frac{2f_{\mathrm{Cl_2}}[\mathrm{Cl_2}]_{\mathrm{eq}} + f_{\mathrm{BrCl}}[\mathrm{BrCl}]_{\mathrm{eq}}}{2f_{\mathrm{Br_2}}[\mathrm{Br_2}]_{\mathrm{eq}} + f_{\mathrm{BrCl}}[\mathrm{BrCl}]_{\mathrm{eq}}} \qquad (6.3\ \mathrm{xxxiv})$$

Rearranging results in:

$$\begin{aligned}\frac{[\mathrm{Cl}]_0}{[\mathrm{Br}]_0}\left(2f_{\mathrm{Br_2}}[\mathrm{Br_2}]_{\mathrm{eq}} + f_{\mathrm{BrCl}}[\mathrm{BrCl}]_{\mathrm{eq}}\right)&\\ = 2f_{\mathrm{Cl_2}}[\mathrm{Cl_2}]_{\mathrm{eq}} + f_{\mathrm{BrCl}}[\mathrm{BrCl}]_{\mathrm{eq}}&\end{aligned} \tag{6.3 xxxv}$$

Expanding, then separating $f_{\mathrm{BrCl}}[\mathrm{BrCl}]_{\mathrm{eq}}$ and simplifying gives:

$$\frac{[\mathrm{Cl}]_0}{[\mathrm{Br}]_0}2f_{\mathrm{Br_2}}[\mathrm{Br_2}]_{\mathrm{eq}} - 2f_{\mathrm{Cl_2}}[\mathrm{Cl_2}]_{\mathrm{eq}} = f_{\mathrm{BrCl}}[\mathrm{BrCl}]_{\mathrm{eq}}\left(1 - \frac{[\mathrm{Cl}]_0}{[\mathrm{Br}]_0}\right) \tag{6.3 xxxvi}$$

which dividing by $f_{\mathrm{BrCl}}[\mathrm{BrCl}]_{\mathrm{eq}}$ throughout yields:

$$\frac{[\mathrm{Cl}]_0}{[\mathrm{Br}]_0}2\frac{f_{\mathrm{Br_2}}}{f_{\mathrm{BrCl}}}\frac{[\mathrm{Br_2}]_{\mathrm{eq}}}{[\mathrm{BrCl}]_{\mathrm{eq}}} - 2\frac{f_{\mathrm{Cl_2}}}{f_{\mathrm{BrCl}}}\frac{[\mathrm{Cl_2}]_{\mathrm{eq}}}{[\mathrm{BrCl}]_{\mathrm{eq}}} = 1 - \frac{[\mathrm{Cl}]_0}{[\mathrm{Br}]_0} \tag{6.3 xxxvii}$$

As was previously defined, the ratio of the photolysis fractions of two different species are expressed as:

$$\frac{f_{\mathrm{Br_2}}}{f_{\mathrm{BrCl}}} = \frac{\sigma_{\mathrm{Br_2}}}{\sigma_{\mathrm{BrCl}}} = b \tag{6.3 xxxviii}$$

$$\frac{f_{\mathrm{Cl_2}}}{f_{\mathrm{BrCl}}} = \frac{\sigma_{\mathrm{Cl_2}}}{\sigma_{\mathrm{BrCl}}} = c \tag{6.3 xxxix}$$

Therefore by making the above substitutions and then rearranging the result is:

$$\frac{[\mathrm{Cl}]_0}{[\mathrm{Br}]_0} = \left(2c\frac{[\mathrm{Cl_2}]_{\mathrm{eq}}}{[\mathrm{BrCl}]_{\mathrm{eq}}} + 1\right)\left(2b\frac{[\mathrm{Br_2}]_{\mathrm{eq}}}{[\mathrm{BrCl}]_{\mathrm{eq}}} + 1\right)^{-1} \tag{6.3 xl}$$

Consequently δ can now be calculated as a function of $[\mathrm{Br_2}]_0$ and $[\mathrm{Cl_2}]_0$ given the absorption cross sections of Br_2, Cl_2 and BrCl and the equilibrium constant from previous work.[26] However, there has been no experimental determination of neither $k_{(6.15)}$ nor $k_{(-6.15)}$ for reactions (6.15) and (–6.15) and so it is not possible to establish whether the pre-flash mixture will have reached equilibrium before photolysis. Therefore, the two extreme scenarios of a “non-equilibrium” system (*i.e.* only Br_2 and Cl_2) and the *fully* equilibrated system represent a lower and upper limit respectively on the value of δ as shown below in Figure 6.10. Under the experimental conditions employed, the result of equilibrium between Br_2, Cl_2 and BrCl would result in a reduction in the *proportion* of photolytically formed chlorine atoms. Intuitively the value of δ should lie between these two limits.

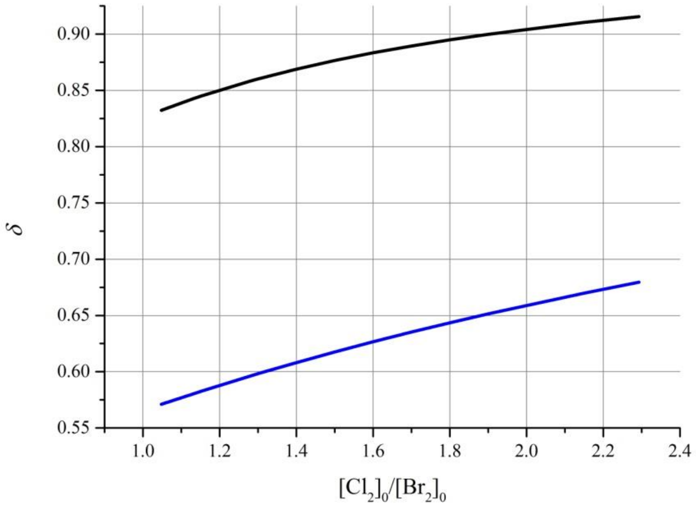

Figure 6.10 *The proportion of chlorine atoms formed upon photolysis: Under halogen precursor non-equilibrium conditions (black); under equilibrium conditions (blue).*

6.3.5 Analysis of the Temporal Traces Recorded in the Absence of CH_3OH: Actinic Calibration of the Photolysis Mixture

Once liberated upon photolysis, Br and Cl react under experimental conditions to ultimately form BrO:

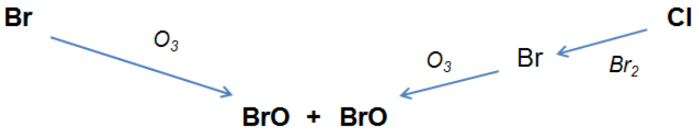

Thus, if all the atomic chlorine is effectively converted to bromine rapidly, at a much faster rate than the bromine atoms formed directly by photolysis react with ozone, it should follow that the formation of BrO should be rapid and the maximum [BrO] clearly defined. Figure 6.11 below shows a typical BrO trace recorded under methanol free conditions showing the temporal behaviour of [BrO]. There *is* rapid BrO formation with a clearly defined maximum implying that Cl does indeed react sufficiently rapid enough under experimental conditions as to not convolute the subsequent BrO decay kinetics.

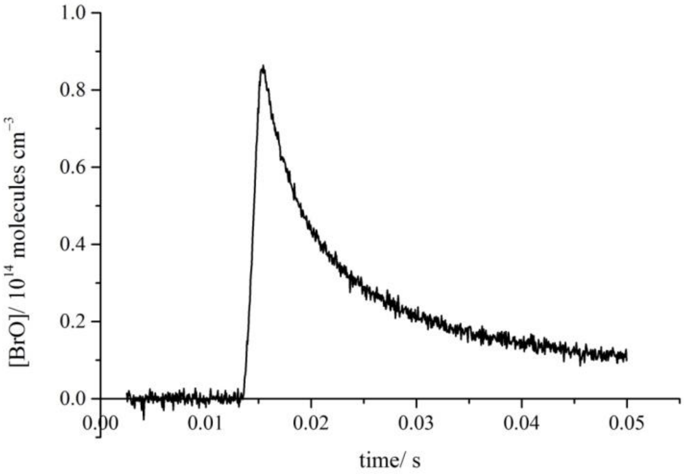

Figure 6.11 *A typical temporal trace of [BrO] under methanol free conditions recorded at T = 298 K.*

As was discussed above, $\Delta[O_3]$ traces were also obtained, showing the changes in ozone concentration simultaneously to [BrO]. Thus, the kinetics of both channels of the BrO self-reaction, which has two reaction routes, could be established. The $\Delta[O_3]$ trace enabled the kinetics of the additional loss of O_3 brought about by reaction (6.12a) to be measured. Therefore, simultaneously fitting the rate constants $k_{(6.12a)}$ and $k_{(6.12b)}$ to these trace pairs allowed the parameterisation of the BrO self-reaction which provided information on the total radical number density formed post-photolysis. Assuming that the conversion of Cl to Br is rapid, which is expected due to the rate of the Cl + Br_2 reaction and has been demonstrated *via* the absence of ClO formation thus implying that the competition of ozone for Cl is insignificant, equation (6.3 xxvii) becomes:

$$[\mathrm{TA}]_0 = [\mathrm{Br}]_0 + [\mathrm{Br}]_{0,\mathrm{Cl}} \qquad (6.3\ \mathrm{xli})$$

where $[\mathrm{Br}]_{0,\mathrm{Cl}}$ is defined as the bromine atom number density formed *via* Cl which is approximately equal to $[\mathrm{Cl}]_0$. These bromine atoms are indiscernible, thus under these circumstances:

$$[\mathrm{TA}]_0 \approx [\mathrm{Br}]_{0,\mathrm{total}} \qquad (6.3\ \mathrm{xlii})$$

Therefore, the parameterisation of the BrO self-reaction could be used for the actinic calibration of the total number density of radicals initially formed upon the photolysis of a given mixture of $Br_2/Cl_2/O_3$/synthetic air. In addition, the conversion of Cl to Br also supersedes the requirement of knowing the initial partitioning between these atoms in determining $[\mathrm{TA}]_0$.

A numerical model of the BrO self-reaction was built, encompassing the same chemistry as reported in Ferracci *et al.*,[21] who comprehensively studied the temperature dependence of both reactions (6.12a) and (6.12b) in this laboratory, the details of which are included in Table 6.2. The parameters $k_{(6.12a)}$, $k_{(6.12b)}$ and $[\mathrm{TA}]_0$ were optimised using the fitting procedure in the numerical integration software package, FACSIMILE, which uses least squares optimisation. The advantage of using this software rather than a classical solution is that the numerical model encompasses *both* the initial formation chemistry and the subsequent decay chemistry of Br, Cl, BrO and O_3 and can easily be expanded to accommodate the additional chemistry of HO_2 for the experiments in which methanol was present. All trace pairs of $[\mathrm{BrO}]_t$ and $\Delta[O_3]_t$ were analysed in this way as a function of temperature. Figure 6.12 shows an example of an experimental BrO and $\Delta[O_3]$ trace pair plotted with a corresponding simulated trace pair from an optimised fit. In general, the data were fit well by the optimising procedure of FACSIMILE although there was a small deviation between the experimental and simulated data for peak [BrO]. Possible causes of this discrepancy are considered below in the sensitivity analysis. Similarly, the $\Delta[O_3]_t$ traces, optimised alongside the $[\mathrm{BrO}]_t$ traces, were also fit extremely well by the model given in Table 6.2.

Reaction Label & Reaction		Rate coefficient[a] ($k(T)$ at 760 Torr,)
k_{1f}	$Br + O_3 \rightarrow BrO + O_2$	$1.60 \times 10^{-11} \exp(-780/T)$
k_{2f}	$Cl + O_3 \rightarrow ClO + O_2$	$2.30 \times 10^{-11} \exp(-200/T)$
k_{3f}	$Cl + Cl (+ M) \rightarrow Cl_2 (+ M)$	$6.15 \times 10^{-34} \exp(906/T)$
k_{4f}	$Br + Br \rightarrow Br_2$	$4.80 \times 10^{-15} \exp(1136/T)$
k_{5f}	$Cl + Br_2 \rightarrow BrCl + Br$	$2.30 \times 10^{-10} \exp(-135/T)$[b]
k_{6f}	$Br + Cl_2 \rightarrow BrCl + Cl$	1.70×10^{-15}[c]
k_{6r}	$Cl + BrCl \rightarrow Cl_2 + Br$	1.45×10^{-11}[d]
k_{7f}	$Br + BrCl \rightarrow Cl + Br_2$	3.30×10^{-15}
k_{8f}	$Br + BrO \rightarrow Br_2O$	$1.90 \times 10^{-14} \exp(1370/T)$[e]
k_{9f}	$Br_2O + Br \rightarrow BrO + Br_2$	4.00×10^{-11}[f]
k_{10fa}	$BrO + BrO \rightarrow Br + Br + O_2$	$1.92 \times 10^{-12} \exp(126/T)$[g]
k_{10fb}	$BrO + BrO \rightarrow Br_2 + O_2$	$3.40 \times 10^{-13} \exp(181/T)$[g]
		$2.50 \times 10^{-12} \exp(630/T)$[g]
k_{11fa}	$BrO + ClO \rightarrow Br + OClO$	$9.50 \times 10^{-13} \exp(550/T)$
k_{11fb}	$BrO + ClO \rightarrow Br + ClOO$	$2.30 \times 10^{-12} \exp(260/T)$
k_{11fc}	$BrO + ClO \rightarrow BrCl + O_2$	$4.50 \times 10^{-12} \exp(280/T)$[h]
k_{12f}	$ClO + ClO (+ M) \rightarrow Cl_2O_2 (+ M)$	$k_0 = 1.60 \times 10^{-32} \times (T/300)^{-4.5}$[i]
k_{12r}	$Cl_2O_2 \rightarrow ClO + ClO \rightarrow$	$k_\infty = 3.00 \times 10^{-12} \times (T/300)^{-2}$
		$K_{eq} = 1.72 \times 10^{-27} \exp(8649/T)$[j]
k_{13f}	$Cl + O_2 \rightarrow ClOO$	$k_0 = 2.20 \times 10^{-33} \times (T/300)^{-3.1}$[i]
k_{13r}	$ClOO \rightarrow Cl + O_2$	$k_\infty = 1.80 \times 10^{-10} \times (T/300)^0$
		$K_{eq} = 6.60 \times 10^{-25} \exp(2502/T)$[j]

[a]Units are cm^3 molecule^{-1} s^{-1} unless otherwise stated, [b]taken from Bedjanian et al.,[27] [c]taken from Dolson et al.,[28] [d]taken from Baulch et al.,[29] [e]taken from Harwood et al.,[30] [f]taken from Rowley et al.,[31] [g]taken from Ferracci et al.,[21] [h]taken from Ferracci et al.,[24] [i]units of cm^6 molecule^{-2} s^{-1} and [j]units of cm^3 molecule^{-1}

Table 6.2 *A description of the chemical mechanism used to simulate and optimise the BrO self-reaction.*

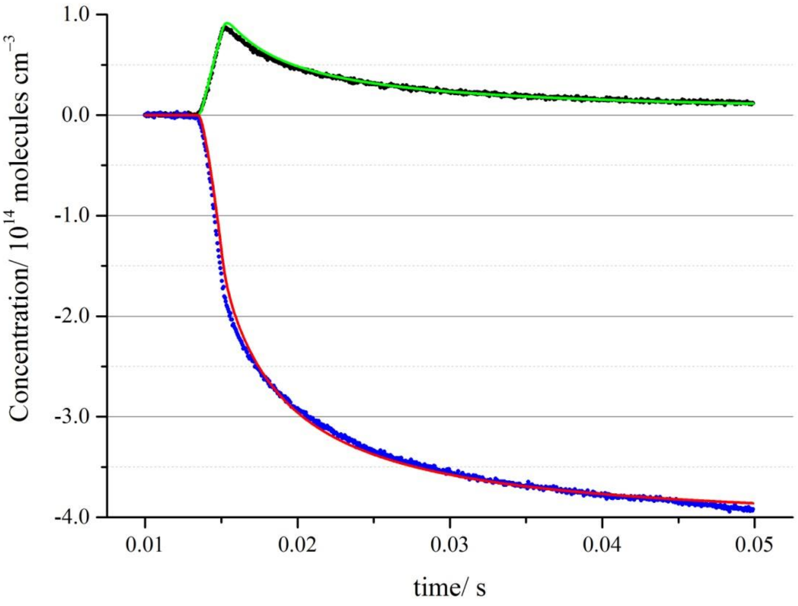

Figure 6.12 *Optimised fits of [BrO]$_t$ and Δ[O$_3$]$_t$: Black circles = experimental [BrO]$_t$; Green line = Optimised [BrO]$_t$; Blue circles = experimental Δ[O$_3$]$_t$; Red line = optimised Δ[O$_3$]$_t$.*

The optimised values of [TA]$_0$, $k_{(6.12a)}$ and $k_{(6.12b)}$ at each temperature investigated are tabulated below in Table 6.3, along with the ratio of the initial pre-mixing concentrations of Cl$_2$ and Br$_2$. The temperature dependence of these results are displayed in Figure 6.19 in the discussion and compared primarily to the work of Ferracci *et al.*[21] These results, which exhibit Arrhenius behaviour, were optimised by a linear regression analysis, giving the following temperature dependence for $k_{(6.12a)}$, $k_{(6.12b)}$ and $k_{(6.12)}$ respectively:

$$k_{(6.12a)}\left(T/\mathrm{K}\right) = 2.47\,^{+1.71}_{-1.01} \times 10^{-12}\, e^{\left(\frac{(51 \pm 144)}{T}\right)}\mathrm{cm^3\ molecule^{-1}\ s^{-1}} \qquad (6.3\ \mathrm{xliii})$$

$$k_{(6.12b)}\left(T/\mathrm{K}\right) = 1.48\,^{+0.55}_{-0.40} \times 10^{-13}\, e^{\left(\frac{(624 \pm 87)}{T}\right)}\mathrm{cm^3\ molecule^{-1}\ s^{-1}} \qquad (6.3\ \mathrm{xliv})$$

$$k_{(6.12)}\left(T/\mathrm{K}\right) = 1.81\,^{+0.68}_{-0.50} \times 10^{-12}\, e^{\left(\frac{(247 \pm 88)}{T}\right)}\mathrm{cm^3\ molecule^{-1}\ s^{-1}} \qquad (6.3\ \mathrm{xlv})$$

T / K	$[Cl_2]_0/[Br_2]_0$	$[TA]_0{}^a$/ 10^{14}	$k_{(6.12a)}$/ 10^{-12b}	$k_{(6.12b)}$/ 10^{-12b}	$k_{(6.12)}$/ 10^{-12b}
314.1	1.45 − 1.62	1.2 − 1.4	(2.78 ± 0.48)	(1.06 ± 0.12)	(3.84 ± 0.80)
298.15	1.05 − 2.29	1.5 − 1.9	(2.86 ± 0.10)	(1.32 ± 0.17)	(4.18 ± 0.56)
283	1.44 − 1.72	1.3 − 1.4	(3.12 ± 0.02)	(1.26 ± 0.06)	(4.38 ± 0.20)
268.15	1.32	(1.33 ± 0.07)	(3.02 ± 0.05)	(1.45 ± 0.21)	(4.47 ± 0.64)
257.15	1.85	(1.63 ± 0.04)	(2.65 ± 0.40)	(1.71 ± 0.04)	(5.20 ± 0.18)
246.15	1.44	(1.65 ± 0.04)	(3.49 ± 0.10)	(1.91 ± 0.33)	(4.56 ± 1.05)

[a]*Units in molecules* cm^{-3} [b]*Units in* cm^3 *molecule*$^{-1}$ s^{-1}

Table 6.3 *The results of the optimised values* $k_{(6.12a)}$, $k_{(6.12b)}$, $k_{(6.12)}$ *and* $[TA]_0$.

These data were used in the analysis of the temporal traces of [BrO] and $\Delta[O_3]$ recorded in the presence of methanol discussed below. However, first an analysis of the formation of the HO_2 reactant is given which is the principal consequence of the addition of methanol to the photolysis mixtures.

6.3.6 Introduction of CH_3OH: Analysis of HO_2 Formation

The introduction of methanol to the photolysis mixture opens a new reaction pathway for atomic chlorine resulting in two principal potential reaction paths for Cl:

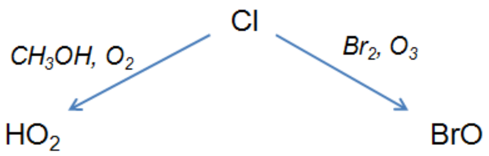

Thus, there is now a branching of the reactive fate of Cl between BrO and HO_2 formation, the ratio of which is dependent on the relative amounts of bromine and methanol present and their reactivity with Cl. The extent of the total fraction of Cl reacting with methanol is determined by the branching ratio, α:

$$\alpha = \frac{k_{(6.9)}[CH_3OH]}{k_{(6.9)}[CH_3OH] + k_{(6.11)}[Br_2]} \qquad (6.3\ xlvi)$$

With methanol present in the photolysis mixture there is a consequent decrease in the effective available atomic chlorine formed upon photolysis that can react with bromine. As was discussed in section 6.3.1, if sufficient HO_2 is formed, then the BrO reactivity is dominated by HO_2 and the BrO self-reaction is inhibited, limiting additional ozone loss post-reactant formation. Therefore the effect on the behaviour of $\Delta[O_3]_t$ is similar to a step function in which $\Delta[O_3]_t$ is constant after initial ozone loss post-photolysis as demonstrated below in Figure 6.13 which shows simulated $\Delta[O_3]_t$ traces as a function of $[CH_3OH]$ similar to the experimental $[CH_3OH]$ at $T = 298$ K.

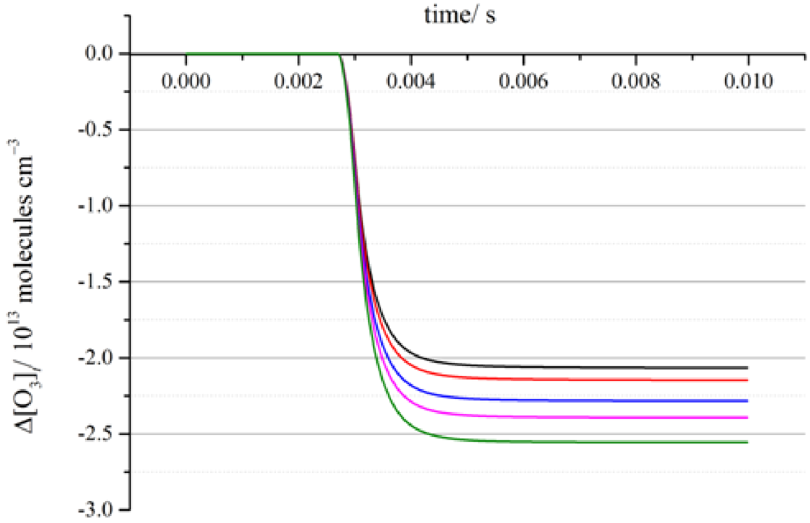

Figure 6.13 *Simulated* $\Delta[O_3]_t$ *with showing near zero catalytic loss of ozone after initial consumption via BrO formation post-photolysis.* $[CH_3OH]$/ *molecules* cm^{-3}: *Black* = 4.61×10^{17}; *Red* =3.69×10^{17}; *Blue* = 2.77×10^{17}; *Pink* = 2.31 *Green* = 1.84×10^{17}. $[TA]_0 = 1.50 \times 10^{14}$ *molecules* cm^{-3} *and* $\delta = 0.88$ $T = 298$ *K.*

The change in ozone concentration brought about by photolysis, $\Delta[O_3]$, is therefore dependent on the fraction of atomic chlorine that reacts with Br_2 as well as the amount of atomic bromine formed immediately post-laser flash:

$$\Delta[O_3] = (1-\alpha)[Cl]_0 + [Br]_0 \qquad (6.3\ xlvii)$$

Substituting equation (6.3 xlvi) results in:

$$\Delta[O_3] = \left(1 - \frac{k_{(6.9)}[CH_3OH]}{k_{(6.9)}[CH_3OH] + k_{(6.11)}[Br_2]}\right)[Cl]_0 + [Br]_0 \qquad (6.3\ xlviii)$$

giving

$$\frac{1}{\Delta[O_3]} = -\frac{k_{(6.11)}[Br_2]}{k_{(6.9)}[Cl]_0[CH_3OH]} + \frac{1}{[Br]_0} \qquad (6.3\ xlix)$$

which is of the form: $y = mx + c$, where $y = \frac{1}{\Delta[O_3]}$ and $x = \frac{1}{[CH_3OH]}$. Therefore a plot of $\Delta[O_3]^{-1}$ against $[CH_3OH\ ]^{-1}$ should yield a straight line, under the experimental conditions applied in this work where large concentrations of methanol were used to inhibit reaction (6.12). Figure 6.14 shows a plot of experimentally determined $\Delta[O_3]^{-1}$, calculated from such $\Delta[O_3]_t$ traces. The difference was taken between the pre-flash O$_3$ signal, averaged over a short period before the laser flash, and the O$_3$ signal averaged over a short period after the plateau had been reached.

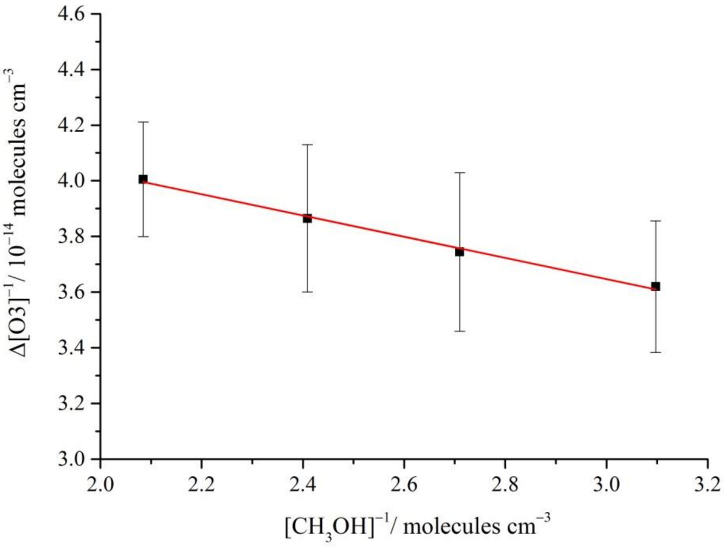

Figure 6.14 *A plot of $\Delta[O_3]^{-1}$ against $[CH_3OH]^{-1}$ at T = 298 K: The black squares are experimental data; The red line is the optimised fit by linear regression. Error bars are associated with the signal to noise ratio which was < 10 %.*

In this example $[CH_3OH] = 4.6 - 1.4 \times 10^{17}$ molecules cm^{-3} was used with $[TA]_0 = 1.6 \times 10^{14}$ molecules cm^{-3}. Fitting equation (6.3 xlix) to data such as these enabled the determination of the partitioning of $[Cl]_0$ and $[Br]_0$ by finding the intercept, which is equal to $[Br]_0^{-1}$ and then substituting into equation (6.3 xxix). This was performed over a wide range of both different methanol concentrations and ratios of $[Cl_2]_0/[Br_2]_0$ at T = 298 K and a more limited range at other temperatures. These results are summarised in Table 6.4 and the T = 298 K values of δ are plotted in Figure 6.15 with the calculated values of δ both under conditions where there is an assumption of no reaction between Br_2 and Cl_2 and one where there is full equilibrium. The experimental results show that there is in fact no significant pre-photolysis reaction between Br_2 and Cl_2 upon mixing under the lower halogen concentrations employed in this study. This implies that the time to reach equilibrium with BrCl is much longer than the mixing and residence time of the photolysis mixture in the reactor and that $k_{(6.7)}$ is therefore small albeit still unquantified at T = 298 K.

T / K	$[Cl_2]_0/[Br_2]_0$	δ
314.1	1.45	(0.78 ± 0.06)
	1.16	(0.72 ± 0.12)
298.15	1.28	(0.88 ± 0.09)
	1.05	(0.87 ± 0.03)
	1.15	(0.88 ± 0.03)
	1.13	(0.89 ± 0.03)
	2.29	(0.9 ± 0.16)
283.15	1.44	(0.83 ± 0.11)
	1.71	(0.78 ± 0.06)
268.15	1.44	(0.83 ± 0.08)
257.15	1.85	(0.88 ± 0.04)
246.15	1.44	(0.87 ± 0.13)

Table 6.4 *Experimentally determined δ as a function of temperature and as a function of the initial ratio of molecular chlorine over bromine.*

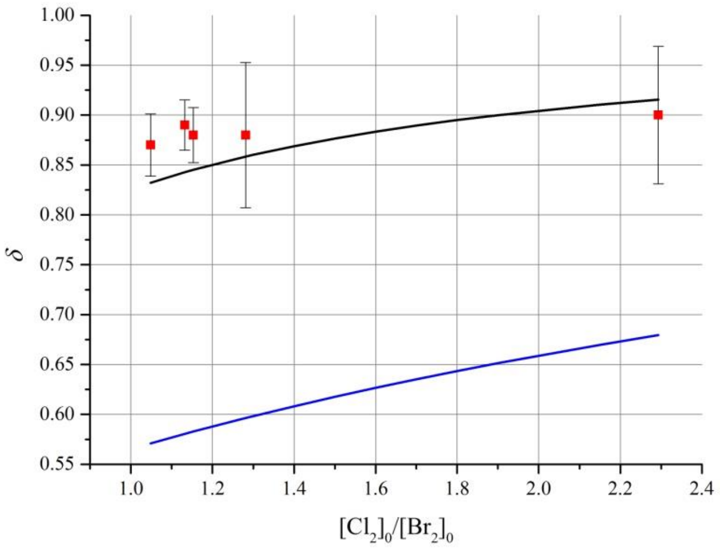

Figure 6.15 *Plot of δ against the ratio of initial halogen concentration: Red squares = experimental data; Black line = no reaction between* Cl_2 *and* Br_2*; Blue line = equilibrium* $[Cl_2]$ *and* $[Br_2]$*.*

6.3.7 Analysis of BrO Temporal Traces Recorded in the Presence of CH_3OH

As discussed above, traces of $[BrO]_t$ and $\Delta[O_3]_t$ were obtained in both the absence and presence of methanol and directly compared. The differences between these trace pairs was attributed to HO_2 chemistry initiated by the reaction of Cl + CH_3OH. The temporal behaviour of the concentration of HO_2 could not be monitored directly under the current experimental setup. However, by studying the BrO self-reaction and the changes in the amount of ozone consumed upon the addition of methanol to the photolysed mixtures, the total radical number density and the partitioning between them could be inferred. Typical conditions were such that peak $[HO_2]_t$ was calculated to be several times larger than peak $[BrO]_t$. Consequently, the quantification of the kinetics of reaction (6.1) relied on accurate modelling of $[HO_2]_t$. The chemistry of HO_2 has fortuitously been widely studied,[17] in particular the HO_2 self-reaction owing to its atmospheric importance, discussed in Chapter 1. The reaction:

$$HO_2 + HO_2 (+ M) \rightarrow H_2O_2 (+ M) \qquad (6.17)$$

has a negative temperature dependence and a pressure dependent contribution to the total rate of reaction. Importantly, HO_2 also reacts with CH_3OH reversibly, forming clusters that react efficiently with HO_2 and other $HO_2.CH_3OH$ complexes:[15,20,32,33]

$$HO_2 + CH_3OH + M \rightleftharpoons HO_2.CH_3OH + M \qquad (6.18)\ (-6.18)$$

$$HO_2 + HO_2.CH_3OH \rightarrow \text{Products} \qquad (6.19)$$

$$HO_2.CH_3OH + HO_2.CH_3OH \rightarrow \text{Products} \qquad (6.20)$$

These reactions result in an enhancement of the observed $k_{(6.17)}$ as a function of methanol concentration which must be taken into consideration, especially under high [CH_3OH] which are necessarily used in this work. There have been a number of studies aimed at quantifying the above reactions and the effect of [CH_3OH] on the observed $k_{(6.17)}$,[15,20,32,33] especially as methanol is frequently used as a precursor for HO_2 as in this work. Christensen *et al.*[33] have provided values for the rate coefficients of reactions (6.18) and (6.19) but at over a much more limited temperature range (T = 231 − 261 K) and at lower pressures (p = 50 − 100 Torr) used in this study and are therefore not adopted here. However, Stone and Rowley[20] provided a more comprehensive study of the HO_2 + HO_2 and the observed enhancement of $k_{(6.17)}$ over a similar temperature range and levels of [CH_3OH] to those employed in the current work. Thus, the numerical integration model was expanded to include reaction (6.17) using the JPL NASA[17] recommendation for both the pressure dependent and independent self-reactions and reactions (6.18), (6.19) and (6.20) were accounted for using a parameterised linear methanol enhancement as reported by Stone and Rowley.[20] Other additional reactions occurring due to the addition of methanol were considered. Simulations were carried out in which these reactions were systematically removed from the model and the subsequent effect on the simulated $[BrO]_t$ and $\Delta[O_3]_t$ traces noted. The reactions that were found to have a significant effect are given in Table 6.5 below but all reactions considered were kept in the mechanism for completeness.

	Reaction Label and Reaction	Rate coefficient[a] ($k(T)$ at760 Torr)
	Principal Reaction	
k_f	$BrO + HO_2 \rightarrow HOBr + O_2$	$4.50 \times 10^{-12} \exp(460/T)$
	HO$_2$ Chemistry	
k_{14f}	$Cl + CH_3OH \rightarrow CH_2OH + HCl$	5.50×10^{-11}
k_{15f}	$CH_2OH + O_2 \rightarrow HCHO + HO_2$	9.10×10^{-11}
k_{16f}	$Br + HO_2 \rightarrow HBr + O_2$	2.00×10^{-12}
k_{17f}	$HO_2 + HO_2 \rightarrow H_2O_2 + O_2$	$3.00 \times 10^{-13} \exp(460/T) + 5.17 \times 10^{-14} \exp(920/T)$ CH$_3$OH Enhancement: $k_{17f} \times (1 + (5.6 \times 10^{-22}) \times [CH_3OH] \times \exp((2550/T)))$
k_{18f}	$ClO + HO_2 \rightarrow HOCl + O_2$	$2.60 \times 10^{-12} \exp(290/T)$

[a]Units are cm^3 molecule^{-1} s^{-1} unless otherwise stated [b]units of cm^6 molecule^{-2} s^{-1} and [c]units of cm^3 molecule^{-1}

***Table 6.5** The significant reactions included in the expanded chemical mechanism used in the fitting procedure of reaction (6.1).*

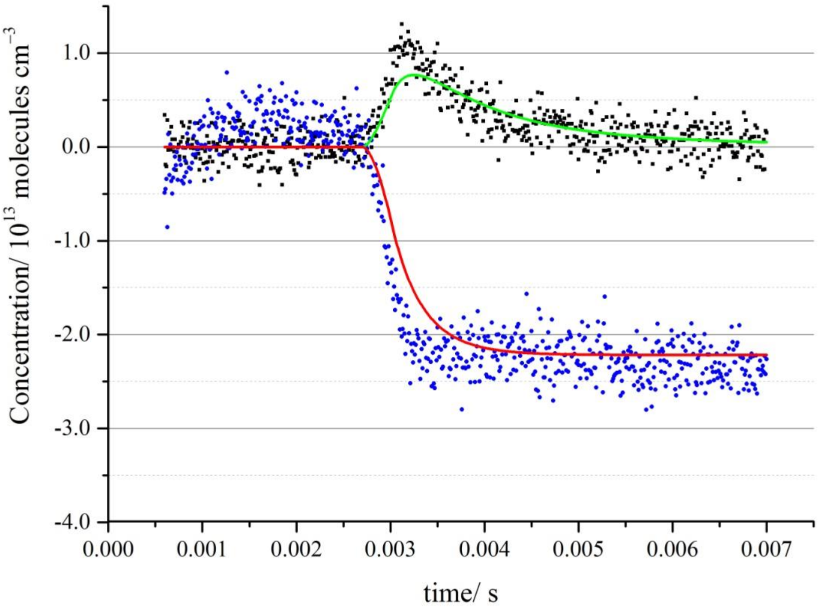

***Figure 6.16** A typical example of an optimised fit of [BrO]$_t$ and Δ[O$_3$]$_t$ to experimental data, recorded at T = 298 K.*

Optimisation of the experimental traces of $[BrO]_t$ and $\Delta[O_3]_t$ recorded in the presence of methanol was performed in an analogous fashion to that of the BrO self-reaction traces. However, only $k_{(6.1)}$ was now varied during each procedure as the other variables ($[TA]_0$ and δ) had already been determined as discussed earlier, thus constraining the model. Figure 6.16 shows the quality of the results of a typical experimental and optimised simulation of a $[BrO]_t$ and $\Delta[O_3]_t$ trace pair. The agreement between the experimental and optimised $[BrO]_t$ is on the whole very good as is that with $\Delta[O_3]_t$. However as with the optimised traces for the BrO self-reaction, the quality of the fit during the BrO formation/O_3 decay is not as strong and reasons for this are addressed and analysed in the sensitivity analysis. Optimised values of $k_{(6.1)}$ were obtained for each temperature studied. Table 6.6 summarises these results and an Arrhenius plot for BrO + HO_2 is given in Figure 6.17 showing the averaged values of $k_{(6.1)}$ and their associated uncertainty as a function of temperature.

T / K	$k_{(6.1)}{}^{a}$/ 10^{-11}	$[Cl_2]_0/[Br_2]_0$	$[CH_3OH]_0{}^{b}$/ 10^{17}
314.1	(2.55 ± 0.33)	1.45 − 1.62	1.75 − 4.38
298.15	(2.89 ± 0.31)	1.05 − 2.29	1.81 − 4.78
283.0	(3.08 ± 0.79)	1.44 − 1.72	0.97 − 3.86
268.15	(2.77 ± 0.52)	1.32	2.04 − 4.07
257.15	(2.73 ± 0.69)	1.85	1.06 − 1.60
246.15	(3.7 ± 1.5)	1.44	1.10

^{a}*Units in* cm^3 *molecule*$^{-1}$ s^{-1} ^{b}*Units in molecules* cm^{-3}

Table 6.6 *Final results of the temperature dependence of* $k_{(6.1)}$ *and experimental conditions.*

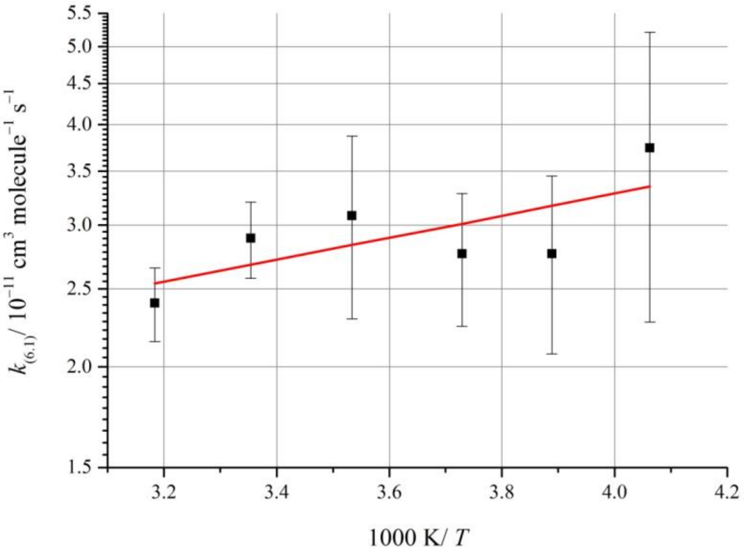

Figure 6.17 *Arrhenius plot of the temperature dependence of the rate coefficient for reaction (6.1) (black squares) and the corresponding parameterisation (red line). Errors are 1σ, statistical only, from multiple experiments.*

The temperature dependence of reaction (6.1) was parameterised by linear regression and the data were found to be well described by the following expression:

$$k_{(6.1)}\,(T/K) = 9.28\,^{+7.17}_{-4.04} \times 10^{-12} e^{\left(\frac{(316 \pm 157)}{T}\right)} \text{cm}^3 \text{ molecule}^{-1} \text{ s}^{-1} \qquad (6.3\text{ l})$$

which is compared to the recommendation from IUPAC[16] and JPL NASA[17] respectively:

$$k_{(6.1)}(T/K) = 4.5 \times 10^{-12}\, e^{\left(\frac{(500 \pm 200)}{T}\right)} \text{cm}^3 \text{ molecule}^{-1} \text{s}^{-1} \qquad (6.3\text{ li})$$

$$k_{(6.1)}(T/K) = 4.5 \times 10^{-12}\, e^{\left(\frac{(460)}{T}\right)} \text{cm}^3 \text{ molecule}^{-1} \text{s}^{-1} \qquad (6.3\text{ lii})$$

6.4 Discussion

6.4.1 Sensitivity Analysis

6.4.1.1 The BrO Self-Reaction

The sensitivity of the rate coefficients derived for reaction (6.12) with respect to the uncertainty in secondary chemistry were found to be minimal, owing to the constraint provided in the fitting procedure *via* the simultaneous optimisation of both $[BrO]_t$ and $\Delta[O_3]_t$ traces. However, a sensitivity analysis was made by taking a simulated trace pair of $[BrO]_t$ and $\Delta[O_3]_t$ traces generated using the FACSIMILE model given in Table 6.2 at T = 298 K and T = 246 K, then optimising the parameters $[TA]_0$, $k_{(6.12a)}$ and $k_{(6.12b)}$ using the same model at the relevant temperature and noting the results. This process was then repeated, subsequently halving or doubling each individual reaction rate coefficient in an iterative manner and the percentage difference between the input and output parameters was calculated. The results showed that the model was most sensitive to $k_{(6.12a)}$ and $k_{(6.12b)}$, as expected from in a doubling and halving of the output total rate constant of reaction (6.12) to the same corresponding perturbation of the input parameter. The effect of perturbing the BrO forming Br + O_3 reaction was small; changing extracted $k_{(6.12a)}$ and $k_{(6.12b)}$ by no more than 8 % each. However, the effect of perturbing the Cl + Br_2 reaction (reaction (6.10)) was greatest on the two rate coefficients apart from the principal reaction, which changed $k_{(6.12a)}$ and $k_{(6.12b)}$ by ~ 20 % on doubling and $k_{(6.12b)}$ by ~ minus 37 % on halving. These effects increase at T = 246 K, affecting $k_{(6.12b)}$ most. The parameter $[TA]_0$ also displayed the greatest sensitivity to the Br + O_3 reaction followed by the Cl + Br_2 reaction only, again becoming more significant at the lower temperature, showing a maximum change of around 48 % at T = 246 K with a doubling of the BrO forming reaction (reaction (6.7)). However the uncertainty in reaction (6.7) from JPL NASA[17] is actually much smaller than multiplying/dividing by a factor of 2, given as a factor of 1.15 at T = 298 K meaning the potential systematic inaccuracies in the experimentally obtained $[TA]_0$ are in fact much smaller.

6.4.1.2 The BrO + HO_2 Reaction

A similar sensitivity analysis was carried out on a corresponding $[BrO]_t$ and $\Delta[O_3]_t$ trace pair with the expanded BrO + HO_2 model at T = 298 K and T = 246 K: the results are given below in Figures 6.18 (a) and (b) respectively. The results are displayed as the percentage difference between the input/output values of reaction (6.1) with the reaction label used in the FACSIMILE model in Tables 6.2 and 6.5 for each perturbation. At T = 298 K the model displays the greatest sensitivity to the principal reaction although there is significant sensitivity regarding the HO_2 self-reaction (and thus the methanol enhancement of reaction (6.17) as well). Sensitivity to reaction (6.8) is high but the uncertainty in this rate constant is however small (a factor of 1.2 as is the case for reaction (6.17) at T = 298 K). The next greatest source of sensitivity is in the formation chemistry as predicted and again, as with the BrO self-reaction model, the Cl + Br_2 reaction (reaction (6.10)) is potentially a significant source of uncertainty. The sensitivity towards these reactions becomes even greater at lower temperatures, where the principal reaction is faster. It is clear that the model is most sensitive to HO_2 chemistry and the radical formation chemistry which is unsurprising when considering the experimental conditions employed *i.e.* large $[HO_2]_0$ and the short timescales of the experiments.

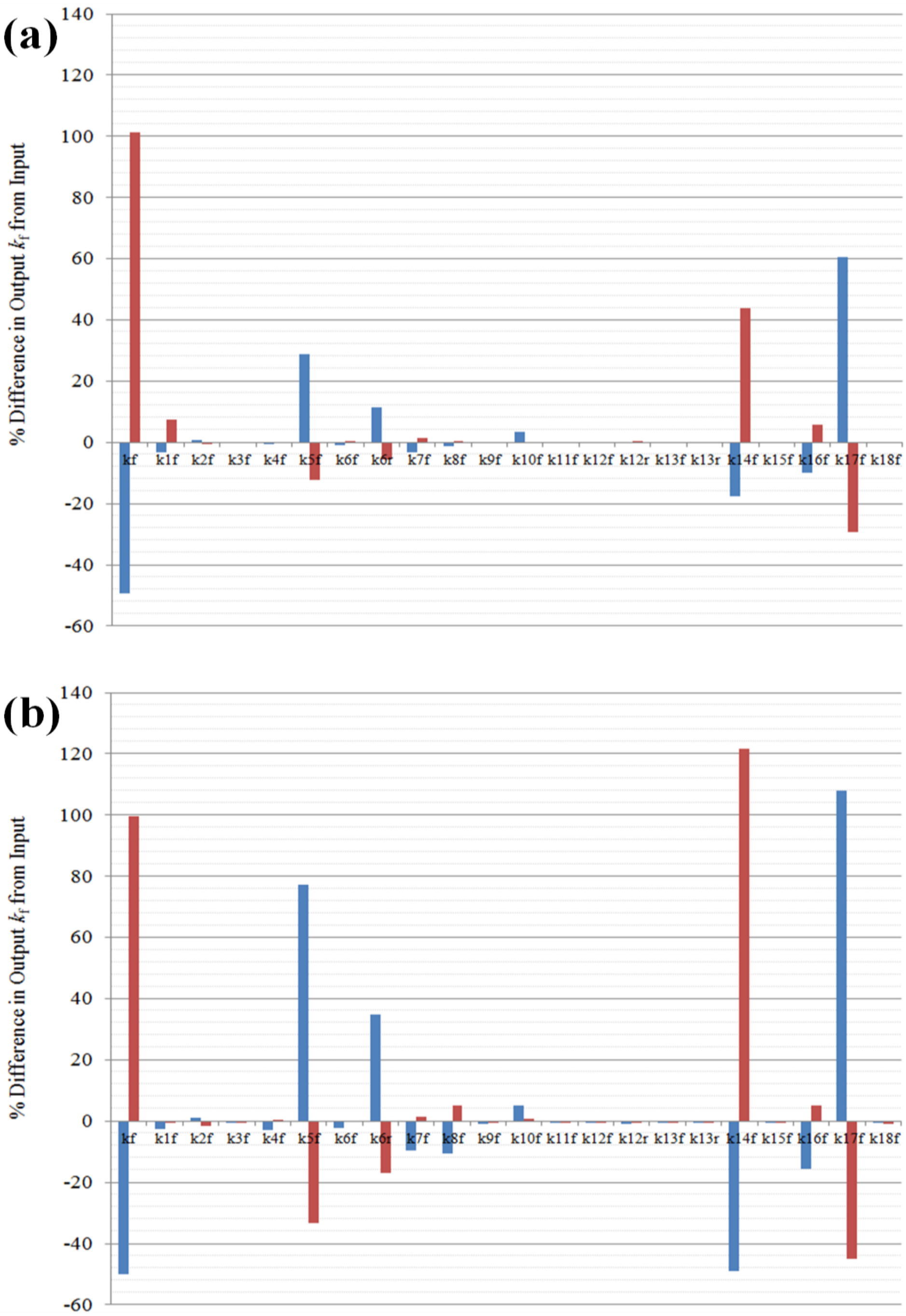

***Figure 6.18** The percentage change in the output value of $k_{(6.1)}$ (k_f), from the input after optimisation with perturbed input parameters: (a) T = 298 K; and (b) T = 246 K. The blue bars are results from halving the literature value for a given rate constant and the red are from doubling.*

The sensitivity of the model to the parameters that were constrained in the optimisation of $k_{(6.1)}$ was also analysed in a similar fashion. The parameters: $[TA]_0$; δ; $[O_3]_0$ (the initial ozone concentration); and $[CH_3OH]_0$ (the initial methanol concentration), were altered by ± 20 %, ± 10 %, ± 50 % and ± 50 % respectively in an iterative manner. These limits represent the values equal to or larger than the approximate errors observed for such parameters. The greatest uncertainty arose from δ, increasing the output value of $k_{(6.1)}$ by a factor of 3 for an underestimation of 10 % in δ. The calculated uncertainty of δ was typically around 7 − 8 %, however, the main source of this uncertainty was from the uncertainty in $\Delta[O_3]$ principally due to the signal to noise ratio exhibited by those traces. Perturbations in $[TA]_0$ were also significant but much less so, introducing an uncertainty of a maximum of ~ 25 % for a 20 % change in $[TA]_0$. The deviation in the experimental $[TA]_0$ was much smaller; typically 3 − 7 % between experiments run in the absence of methanol at the beginning and end of a series. However, the change $[TA]_0$ of *ca.* 20 % is accurate when considering the additional systematic error associated with the uncertainty in the BrO differential cross section used. Wilmouth *et al.*[25] reported an uncertainty of ± 11 % in the (7,0) band (λ = 338.5 nm) at T = 298 K, which gives a combined error in the [BrO] when this uncertainty is scaled into the temporal profiles of BrO of *ca.* 20 % and therefore $[TA]_0$ (under methanol free conditions). The difference in input/output $k_{(6.1)}$ resulting from the changes in initial $[CH_3OH]$ introduced a 25 % overestimation from a 50 % underestimation of methanol concentration but a similar overestimation was insignificant by comparison. Changes in $[O_3]_0$ perturbed $k_{(6.1)}$ by a maximum of 7 %.

Due to the nature of these experiments *i.e.* obtaining kinetic information from a mixed bimolecular reaction in which only one reactant is directly measured, the model used to optimise the rate coefficient of interest is obviously inevitably sensitive to the input parameters. However, the parameters in this work were well constrained experimentally and while the reported uncertainty in the final kinetic parameters is relatively large, they appear accurate, especially when compared to the results of the complementary discharge-flow tube studies carried out in other groups, discussed in the following section.

6.4.2 Comparison with Previous Studies

6.4.2.1 The BrO Self-Reaction

Both channels of the BrO self-reaction have recently been studied extensively in this laboratory as a function of temperature.[21] Unsurprisingly, the optimised experimental conditions employed in this study were therefore chosen to be very similar, the only difference being the use of Cl_2 in the present work as an extra source of Br atoms *via* the reaction of Cl with Br_2. Therefore the results of the current work are compared to that of Ferracci *et al.*[21] only, since that study was more comprehensive and extensive than from what the current parameterisations of this work were derived from. Principally used as a tool in deriving $[TA]_0$, the kinetics of the BrO self-reaction had a greater indirect effect on the optimised $k_{(6.1)}$ under the experimental conditions employed than $k_{(6.12)}$ itself.

In Figures 6.19 (a) and (b), Arrhenius plots are given showing the temperature dependence of the experimentally derived values of $k_{(6.12a)}$, $k_{(6.12b)}$ and $k_{(6.12)}$ from the data of the present study alongside the corresponding parameterisations as derived by Ferracci *et al.*[21] There is excellent agreement between the two studies for $k_{(6.12a)}$ and the total rate constant $k_{(6.12)}$. However, there is some disagreement regarding $k_{(6.12b)}$, which is consistently larger in this work than that reported by Ferracci *et al.*[21]

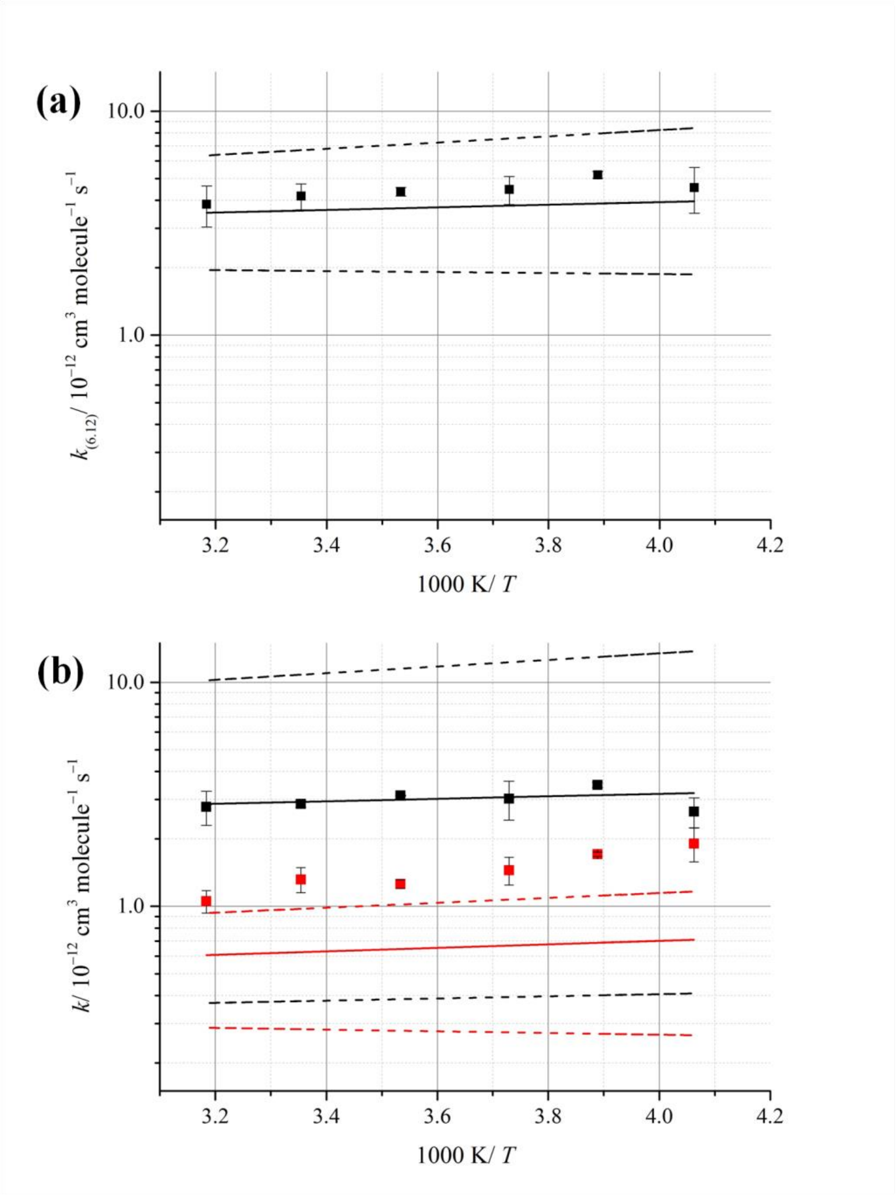

Figure 6.19 *Arrhenius plot of the temperature dependence of: (a)* $k_{(6.12a)}$ *(black) and* $k_{(6.12b)}$ *(red); (b) the total rate constant of reaction (6.12). The squares are data from this study and the lines are the parameterisation of Ferracci et al.*[21]

6.4.2.2 The BrO + HO$_2$ Reaction

The room temperature values of $k_{(6.1)}$ derived in this work and all other kinetic studies of reaction (6.1) are shown in Figure 6.20, excepting the work of Cox and Sheppard.[7] There is a clear divide between studies that agree on a value of $k_{(6.1)}$ around 2×10^{-11}

cm^3 molecule^{-1} s^{-1} and those closer to 3 × 10^{-11} cm^3 molecule^{-1} s^{-1} at T = 298 K. This work lies somewhat in between the two but is closest in agreement with values reported by Bedjanian *et al.*[14] However, when considering the reported uncertainties of the literature data above, this work also agrees with Bloss *et al.*,[15] Bridier *et al.*[9] and Larichev *et al.*[10] The work of Bridier *et al.*[9] and Bloss *et al.*[15] used the flash photolysis technique and similar reaction schemes at the same pressure as employed in this work. As in this study, Bloss *et al.*[15] used broadband UV spectroscopy and monitored BrO only whereas Bridier *et al.*[9] used single wavelength spectroscopy to measure both HO_2 and BrO at 210/220 nm and 313/329 nm respectively. As discussed in the experimental section of this chapter, there is significant overlap of HO_2 absorption by other precursor absorbers (mainly O_3), therefore the potential for significant uncertainty in the derived [HO_2] in the Bridier *et al.*[9] work is high, potentially explaining the large error in the Bridier *et al.*[9] value. The main difference between the Bloss *et al.*[15] study and the current one is in the determination of the initial radical number density post-photolysis *i.e.* the actinic calibration and the subsequent treatment of $[Cl]_0/[Br]_0$ resulting from the possible formation of BrCl in the photolysis mixture. Changes in $[TA]_0$ by mixing chlorine and bromine compared to single halogen mixtures do not apply in the present work as near identical halogen mixtures were used in the presence/absence of the HO_2 precursor. Also, using the vibronic structure of BrO and measuring the kinetics of the BrO self-reaction, the unequivocal determination of [BrO] allowed the accurate determination of $[TA]_0$ in the present work. The measurement of the changes in ozone concentration throughout the entire duration of each photolysis experiment was also uniquely made in this work which enabled the determination of the partitioning of $[Cl]_0/[Br]_0$ and any perturbations resulting from reactions (6.15) and (–6.15). This work implies that there is no significant BrCl formation during the transit of the halogen precursors through the mixing line and reactor. This differs from that of Bloss *et al*.[15] who considered the changes in the optical density resulting from the possible formation of BrCl but only as far as to allow their kinetic model to optimise $[Cl]_0$ to account for the discrepancies in the actinic calibration of $[Cl]_0$. What is more, the effect of methanol on the HO_2 self-reaction and how this is accounted for will also have a potential impact on the experimentally retrieved rate constants for reaction (6.1). While the parameterisation of the methanol enhancement on this reaction from Bloss *et al*.[15] would have been suitable in this study, it was only suitable for T = 298 K which is why the Stone and

Rowley[20] parameterisation of the methanol enhancement was applied in the present work. However, the overall affect on the values of $k_{(6.1)}$ (T = 298 K) arising from these differences in approach appear to be small as indicated by their general agreement.

All the other studies of BrO + HO_2 were carried out at low pressures and, apart from Cronkite *et al.*,[13] used the discharge-flow-tube method. Cronkhite *et al.*[13] used a similar chemical mechanism as used here but photolysed Cl_2 and O_3 at 308 nm to generate radicals. BrO was monitored by UV spectroscopy whereas HO_2 was monitored using a tuneable diode laser in the infrared region thus eliminating the problem of overlapping absorbers in the UV as, for example, in the Bridier *et al.*[9] work. The principal uncertainty arose in the Cronkhite *et al.*[13] study from the infrared line strengths to determine [HO_2] which was in excess of [BrO].

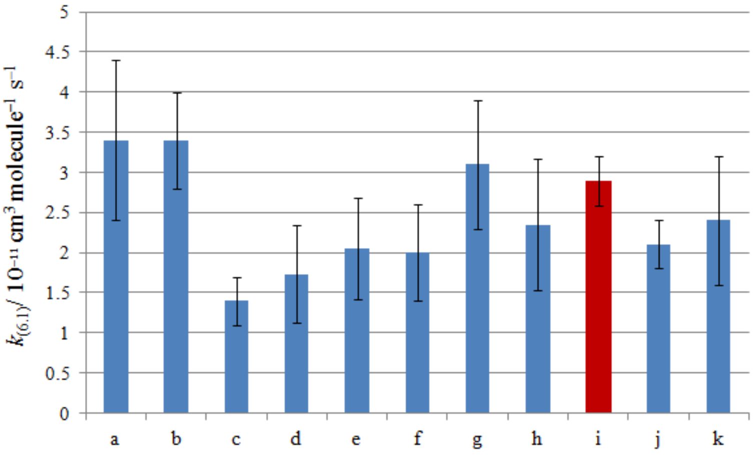

Figure 6.20 *A histogram plot of room temperature values of $k_{(6.1)}$ as found in the literature in addition to this study: (a) Bridier et al.;[9] (b) Larichev et al.;[10] (c) Elrod et al.;[11] Li et al.[12] (d) HO_2 excess, (e) BrO excess; (f) Cronkhite et al.;[13] (g) Bedjanian et al.;[14] (h) Bloss et al.;[15] (i) this work; (j) IUPAC;[16] and (k) JPL NASA.[17]*

The remaining studies discussed below all measured the temperature dependence of reaction (6.1). The parameterisations of the kinetics of previous studies and the experimental data from this work are shown in Figure 6.21, confirming the negative temperature dependence of the BrO + HO_2 reaction. In particular, the apparent discrepancies in the reported absolute values of $k_{(6.1)}$ as a function of temperature appear to arise from the differences in the room temperature values rather than the reported E/R (as shown in Table 6.1), aside from the work of Bedjanian *et al.*[14] The determination of $k_{(6.1)}$ as a function of temperature was first carried out by Larichev *et al.*[10] However the work of Larichev *et al.*[10] is superseded by the study of Bedjanian *et al.*[14] whose studies were conducted in the same laboratory using the same apparatus. Problems concerning the Larichev *et al.*[10] study arose through heterogeneous secondary chemistry effects which at the lowest temperature studied led to an apparent spurious measurement of $k_{(6.1)}$. Wall loses are a problematic feature of all the flow-tube studies, especially at low temperatures. However, the work of Bedjanian *et al.*[14] employed a different experimental configuration to Larichev *et al.,*[10] aimed at minimising the first order wall losses by changing the HO_2 radical source and moving it onto an inner movable injector. Aside from Bedjanian *et al.*[14] who utilised the F + H_2O_2 precursor reaction for HO_2 only, the other temperature dependence studies used the Cl + CH_3OH method of forming HO_2 which also has significant complications arising at low temperatures. However, Elrod *et al.*[11] used a heated coil to keep the inner movable injector at room temperature and Li *et al.*[12] used both methods with both [BrO] >> [HO_2] and *vice versa*. Therefore the differences between the low ambient temperature values of $k_{(6.1)}$ and the high are difficult to reconcile. However, Bedjanian *et al.*[14] also utilised a relative rates method to determine $k_{(6.1)}$ which produced data in excellent agreement with their absolute determinations. The present work reports values in good agreement with the work of Bedjanian *et al.*[14] as shown in Figure 6.21. Therefore, the experiments in the present work, operated under entirely different conditions to all previous temperature dependence studies barring temperature, lends support to a larger room temperature value of $k_{(6.1)}$ and a weaker temperature dependence than previously reported. This is in accordance with results implied from computational studies in addition to, when comparing this work to the previous low pressure studies, the apparent lack of a pressure dependence for reaction (6.1). Further, the branching ratios determined, imply that reaction (6.1) proceeds principally through channel (6.1a) at all atmospheric temperatures, supporting the assumption of no secondary chemistry arising from the BrO + HO_2 reaction, as made in this work.

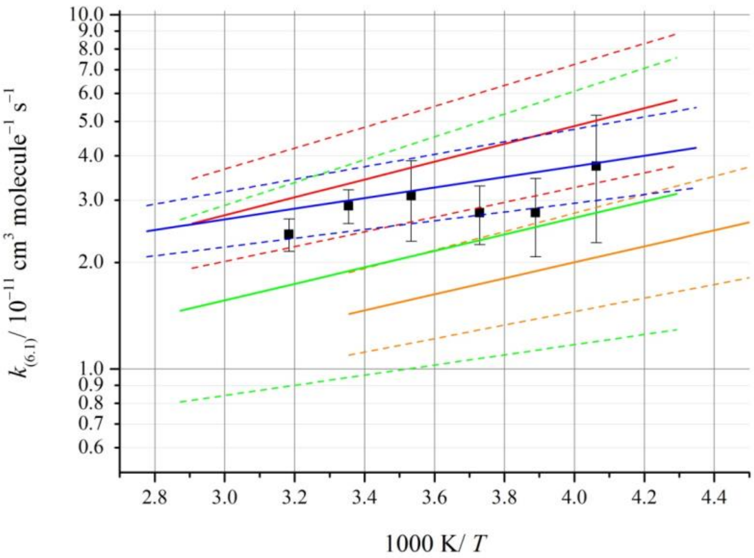

***Figure 6.21** An Arrhenius plot of the temperature dependence of $k_{(6.1)}$: This work (black squares); Larichev et al.[10] (red); Elrod et al.[11] (orange); Li et al.[12] (Green); and Bedjanian et al.[14] (blue).*

6.4.3 Atmospheric Implications

As was discussed at the beginning of this chapter, reaction (6.1) is believed to be the most important in the bromine inititated destruction of ozone at low altitudes at mid-latitudes. In addition, the formation of HOBr in the stratosphere is believed to be the rate limiting step in the catalytic destruction of ozone by bromine atoms. Thus in light of this work compared to previous studies of reaction (6.1), the atmospheric implications are that the reaction of BrO + HOBr is more significant at the ambient temperatures found in the atmosphere at lower altitudes and latitudes where the BrO + HO_2 catalytic destruction is already believed to be important (see Figure 6.1). Thus the present work suggests that this reaction cycle is more important than implied by the current recommendations. However, the weaker negative temperature dependence reported here implies stratospheric importance of reaction is also important. The implications of smaller rate constants for reaction (6.1) at these temperatures are that the formation of HOBr is *more* rate limiting in the destruction of ozone. This suggests that the BrO + HO_2 catalytic cycle is less efficient in the stratosphere than currently thought.

6.5 Conclusions

The kinetics of the atmospherically relevant reaction of BrO + HO_2 have been studied using the laser flash photolysis technique with UV spectroscopy afforded by CCD detection. As a function of temperature at p = 760 ± 20 Torr, the BrO radical was the only reactant directly measured. However the experimental variable $\Delta[O_3]_t$ was used to measure the extent of ozone decay and to therefore help constrain the total initial halogen atom number density and partitioning. By measuring $[BrO]_t$ under conditions where HO_2 was initially in excess, $[BrO]_t$ decay was measured under different $[CH_3OH]$ and halogen precursor concentrations. This is the first flash photolysis study of the temperature dependence of reaction (6.1) and the first carried out at high pressure.

The room temperature results reported here for $k_{(6.1)}$ are larger than those currently recommended by IUPAC[16] and JPL NASA[17] although this work does not report the largest room temperature $k_{(6.1)}$ and is in good agreement with Bloss *et al.*[15] who used a similar experimental setup. The results of this work in fact report the weakest temperature dependence of reaction (6.1) to date but they are generally in excellent agreement with the work of Bedjanian *et al.*[14] when considering the uncertainty, who measured $k_{(6.1)}$ over a wider temperature range using entirely different methods. Also, the agreement between this study with previous work despite the significant differences in pressure (the previous temperature dependence studies were performed at pressures significantly lower than in the current work) lends some credence to the absence of a pressure dependence for this reaction.

6.6 References

1. Yung, Y.L., J.P. Pinto, R.T. Watson, and S.P. Sander, Atmospheric Bromine and Ozone Perturbations in the Lower Stratosphere. *Journal of the Atmospheric Sciences*, 1980. **37**(2): 339-353.

2. Salawitch, R.J., Atmospheric Chemistry – Biogenic Bromine. *Nature*, 2006. **439**(7074): 275-277.
3. Yang, X., R.A. Cox, N.J. Warwick, J.A. Pyle, G.D. Carver, F.M. O'Connor, and N.H. Savage, Tropospheric Bromine Chemistry and its Impacts on Ozone: A Model Study. *Journal of Geophysical Research-Atmospheres*, 2005. **110**(D23).
4. Theys, N., M. Van Roozendael, F. Hendrick, X. Yang, I. De Smedt, A. Richter, M. Begoin, Q. Errera, P.V. Johnston, K. Kreher, and M. De Maziere, Global Observations of Tropospheric BrO Columns Using GOME-2 Satellite Data. *Atmospheric Chemistry and Physics*, 2011. **11**(4): 1791-1811.
5. Choi, S., Y. Wang, R.J. Salawitch, T. Canty, J. Joiner, T. Zeng, T.P. Kurosu, K. Chance, A. Richter, L.G. Huey, J. Liao, J.A. Neuman, J.B. Nowak, J.E. Dibb, A.J. Weinheimer, G. Diskin, T.B. Ryerson, A. da Silva, J. Curry, D. Kinnison, S. Tilmes, and P.F. Levelt, Analysis of Satellite-Derived Arctic Tropospheric BrO Columns in Conjunction with Aircraft Measurements During ARCTAS and ARCPAC. *Atmospheric Chemistry and Physics*, 2012. **12**(3): 1255-1285.
6. Salawitch, R.J., D.K. Weisenstein, L.J. Kovalenko, C.E. Sioris, P.O. Wennberg, K. Chance, M.K.W. Ko, and C.A. McLinden, Sensitivity of Ozone to Bromine in the Lower Stratosphere. *Geophysical Research Letters*, 2005. **32**(5).
7. Cox, R.A. and D.W. Sheppard, Rate Coefficient for the Reaction of BrO with HO_2 at 303 K. *Journal of the Chemical Society-Faraday Transactions II*, 1982. **78**: 1383-1389.
8. Poulet, G., M. Pirre, F. Maguin, R. Ramaroson, and G. Lebras, Role of the BrO + HO_2 Reaction in the Stratospheric Chemistry of Bromine. *Geophysical Research Letters*, 1992. **19**(23): 2305-2308.
9. Bridier, I., B. Veyret, and R. Lesclaux, Flash Photolysis Kinetic-Study of Reactions of the BrO Radical with BrO and HO_2. *Chemical Physics Letters*, 1993. **201**(5-6): 563-568.
10. Larichev, M., F. Maguin, G. Lebras, and G. Poulet, Kinetics and Mechanism of the BrO + HO_2 Reaction. *Journal of physical chemistry*, 1995. **99**(43): 15911-15918.
11. Elrod, M.J., R.F. Meads, J.B. Lipson, J.V. Seeley, and M.J. Molina, Temperature Dependence of the Rate Constant for the HO_2 + BrO Reaction. *Journal of physical chemistry*, 1996. **100**(14): 5808-5812.

12. Li, Z.J., R.R. Friedl, and S.P. Sander, Kinetics of the HO_2 + BrO Reaction Over the Temperature Range 233-348 K. *Journal of the Chemical Society-Faraday Transactions*, 1997. **93**(16): 2683-2691.
13. Cronkhite, J.M., R.E. Stickel, J.M. Nicovich, and P.H. Wine, Laser Flash Photolysis Studies of Radical-Radical Reaction Kinetics: The HO_2 + BrO Reaction. *Journal of Physical Chemistry A*, 1998. **102**(33): 6651-6658.
14. Bedjanian, Y., V. Riffault, and G. Poulet, Kinetic Study of the Reactions of BrO Radicals with HO_2 and DO_2. *Journal of Physical Chemistry A*, 2001. **105**(13): 3167-3175.
15. Bloss, W.J., D.M. Rowley, R.A. Cox, and R.L. Jones, Rate Ccoefficient for the BrO + HO_2 Reaction at 298 K. *Physical Chemistry Chemical Physics*, 2002. **4**(15): 3639-3647.
16. Atkinson, R., D.L. Baulch, R.A. Cox, J.N. Crowley, R.F. Hampson, R.G. Hynes, M.E. Jenkin, M.J. Rossi, and J. Troe, Evaluated Kinetic and Photochemical Data for Atmospheric Chemistry: Volume III – Gas Phase Reactions of Inorganic Halogens. *Atmospheric Chemistry and Physics*, 2007. **7**: 981-1191.
17. Sander, S.P., J. Abbatt, J. R. Barker, J. B. Burkholder, R. R. Friedl, D. M. Golden, R. E. Huie, C. E. Kolb, M. J. Kurylo, G. and V.L.O.a.P.H.W. K. Moortgat, "Chemical Kinetics and Photochemical Data for Use in Atmospheric Studies, Evaluation No. 17," JPL Publication 10-6, Jet Propulsion Laboratory, Pasadena, 2011 http://jpldataeval.jpl.nasa.gov.
18. Guha, S. and J.S. Francisco, An Examination of the Reaction Pathways for the HOOOBr and HOOBrO Complexes Formed from the HO_2 + BrO Feaction. *Journal of Physical Chemistry A*, 1999. **103**(40): 8000-8007.
19. Kaltsoyannis, N. and D.M. Rowley, *Ab initio* Investigations of the Potential Energy Surfaces of the XO + HO_2 Reaction (X = Chlorine or Bromine). *Physical Chemistry Chemical Physics*, 2002. **4**(3): 419-427.
20. Stone, D. and D.M. Rowley, Kinetics of the Gas Phase HO_2 Self-Reaction: Effects of Temperature, Pressure, Water and Methanol Vapours. *Physical Chemistry Chemical Physics*, 2005. **7**(10).
21. Ferracci, V., K. Hino, and D.M. Rowley, Kinetic Studies on the Temperature Dependence of the BrO + BrO Reaction Using Laser Flash Photolysis. *Physical Chemistry Chemical Physics*, 2011. **13**(17): 7997-8007.

22. Ferracci, V. and D.M. Rowley, Kinetic and Thermochemical Studies of the ClO + ClO + M $\rightleftharpoons$ Cl_2O_2 + M Reaction. *Physical Chemistry Chemical Physics*, 2010. **12**(37): 11596-11608.
23. Boakes, G., W.H.H. Mok, and D.M. Rowley, Kinetic Studies of the ClO + ClO Association Reaction as a Function of Temperature and Pressure. *Physical Chemistry Chemical Physics*, 2005. **7**(24): 4102-4113.
24. Ferracci, V. and D.M. Rowley, Kinetic Studies of the BrO + ClO Cross-Reaction Over the Range T = 246−314 K. *Physical Chemistry Chemical Physics*, 2014. **16**(3): 1182-1196.
25. Wilmouth, D.M., T.F. Hanisco, N.M. Donahue, and J.G. Anderson, Fourier transform ultraviolet spectroscopy of the A (2)Pi(3/2) ← X (II3/2)-I-2 transition of BrO. *Journal of Physical Chemistry A*, 1999. **103**(45): 8935-8945.
26. Maric, D., J.P. Burrows, and G.K. Moortgat, A Study of the UV—visible Absorption Spectra of Br_2 and BrCl. *Journal of Photochemistry and Photobiology A: Chemistry*, 1994. **83**(3): 179-192.
27. Bedjanian, Y., G. Laverdet, and G. Le Bras, Low-Pressure Study of the Reaction of Cl atoms with Isoprene. *Journal of Physical Chemistry A*, 1998. **102**(6): 953-959.
28. Dolson, D.A. and S.R. Leone, A Reinvestigation of the Laser-Initiated Cl_2/HBr Chain-reaction: Absolute Rate Constants and the v =2/v = 1 ratio from Cl + HBr → HCl(v) + Br. *Journal of physical chemistry*, 1987. **91**(13): 3543-3550.
29. Baulch, D.L., J. Duxbury, S.J. Grant, and D.C. Montague, Evaluated Kinetic Data for High-Temperature Reactions, Vol. 4, Homogenous Gas-Phase Reactions of Halogen-Containing and Cyanide-Containing Species. *Journal of Physical and Chemical Reference Data*, 1981. **10**: 1-721.
30. Harwood, M.H., D.M. Rowley, R.A. Cox, and R.L. Jones, Kinetics and Mechanism of the BrO Self-Reaction: Temperature and Pressure-Dependent Studies. *Journal of Physical Chemistry A*, 1998. **102**(10): 1790-1802.
31. Rowley, D.M., M.H. Harwood, R.A. Freshwater, and R.L. Jones, Novel Flash Photolysis UV Absorption System Employing Charge-Coupled Device (CCD) Detection: A Study of the BrO + BrO Reaction at 298 K. *Journal of physical chemistry*, 1996. **100**(8): 3020-3029.

32. Tang, Y.X., G.S. Tyndall, and J.J. Orlando, Spectroscopic and Kinetic Properties of HO_2 Radicals and the Enhancement of the HO_2 Self-reaction by CH_3OH and H_2O. *Journal of Physical Chemistry A*, 2010. **114**(1): 369-378.
33. Christensen, L.E., M. Okumura, J.C. Hansen, and S.P. Sander, Experimental and *ab initio* Study of the $HO_2.CH_3OH$ complex: Thermodynamics and Kinetics of Formation. *Journal of Physical Chemistry A*, 2006. **110**(21): 6948-6959.

Chapter 7: Summary and Concluding Remarks

The results presented in this thesis represent extensive laboratory investigations of three halogen oxide radical and peroxy radical cross-reactions of atmospheric importance as a function of temperature from ambient temperatures down to those which are relevant in the upper troposphere/lower stratosphere. The reactions studied: $ClO + HO_2$; $ClO + CH_3O_2$; and $BrO + HO_2$, have therefore afforded the comparison of cross-reactions between different species of radical families as discussed in more detail below. Furthermore, all three studies are the first to investigate these reactions as a function of temperature using the flash photolysis technique incorporating broadband spectroscopy, the advantages of which are also expanded upon below.

The novel use of broadband UV spectroscopy *via* the unique incorporation of a CCD detection system in this work has demonstrated the potential of the experimentally recorded rapid-time resolved absorption *spectra* rather than single wavelength absorbance in determining reaction kinetics. These studies have demonstrated the ability of the experimental setup to unequivocally measure the absolute concentrations of ClO (Chapters 4 and 5) and BrO (Chapter 6) by exploiting the absorbances of the fingerprint vibronic structured region of each species and thereafter applying differential spectroscopy. Given differential monitoring, the quality of the signal is suitable for analysis to determine the pure halogen oxide chemistry. Measuring the temporal behaviour of the concentration of a particular halogen oxide radical both in the presence and absence of the co-reactant peroxy radical precursors has been successful in determining key experimental parameters. Specifically, the information gained from the self-reactions of ClO and BrO, which have previously been studied extensively in this laboratory, permitted subsequent actinic calibration of the initial radical number density for both species post-photolysis. The stability of the halogen oxide signal, recorded with and without the peroxy precursor lent further credence to the method adopted in these experiments. The subsequent results were also reinforced by the retrieval of kinetic parameters of the self-reactions that, in general, were in excellent agreement with previous work. The dependence of the perturbations in the temporal behaviour of each halogen oxide as a function of peroxy radical precursor concentration and the subsequent analysis of this temporal phenomenon gave considerable insight into peroxy radical concentrations. The inference of initial peroxy radical concentrations was crucial in the elucidation of the kinetic parameters of each reaction studied in this work, the accuracy of which depended on the stability of the experimental conditions employed between experiments with/without peroxy radicals which was, as discussed above, verified by alternate experiments. Complete numerical modelling of the reaction systems employed was of also key importance in determining the optimised kinetic parameters and, further, their implicit sensitivity to concurrent chemistry and initial conditions.

The reactions of ClO with HO_2 and ClO with CH_3O_2 were studied in a near identical method to each other: the kinetics of ClO dimerisation were first characterised in order to calibrate the pure ClO temporal behaviour and initial radical density at each temperature, prior to the addition of CH_3OH (Chapter 4) or CH_4 (Chapter 5) as precursors to the co-radical species. The changes in concentration of ClO both initially post-photolysis, and then temporally were attributed to additional peroxy radical chemistry, the formation of which is widely known to take place *via* the initial oxidation of CH_3OH or CH_4 (respectively) by Cl atoms and the subsequent reaction of the substituted alkyl or alkyl radical in the presence of excess oxygen to form HO_2 or CH_3O_2 respectively.[1,2] The initial concentrations of these peroxy radicals were determined by quantifying the partitioning of ClO and Cl concentrations formed upon photolysis and the subsequent competition for Cl between Cl_2O (the ClO precursor) and the peroxy radical precursor. Under the experimental conditions employed for each reaction under investigation, it was not possible to directly monitor HO_2 or CH_3O_2. However, the initial concentrations of the peroxy radicals could be inferred from back-to-back experiments and confirmed through the use of extensive numerical modelling and by careful constraint of key parameters including the total radical number density formed upon photolysis, the partitioning between initially generated ClO and Cl (δ) and the initial concentration of either CH_3OH or CH_4 precursors.

The total rate constants for the ClO + HO_2 reaction, $k_{(4.1)}$, and the ClO + CH_3O_2 reaction, $k_{(5.1)}$, were extracted from the experimental temporal traces of [ClO] using a fitting procedure in the numerical integration package, FACSIMILE. The results were found to be particularly sensitive to the initial parameters discussed above and the kinetics of, in particular, the competing chemistry of the reversible ClO dimer forming self-reaction which is fortuitously well-established. The most significant difference in the fitting procedures between the optimisation of $k_{(4.1)}$ and $k_{(5.1)}$ was the fixing or varying of the parameter δ discussed and defined above. It was found that varying δ in the fitting procedure alongside $k_{(4.1)}$ resulted in improved sensitivity of the retrieved value of $k_{(4.1)}$ at the expense of the retrieved value of δ. However, barring the highest temperatures studied, the model used for optimising $k_{(5.1)}$ did *not* produce the same results when δ was varied and, in fact, resulted in a greater spread of data for the obtained values of $k_{(5.1)}$ at each temperature compared to those obtained when it was fixed during the fitting procedure. This was attributed to unavoidable secondary chemistry effects, specifically the regeneration of Cl which primarily reacted to regenerate ClO or CH_3O_2. Thus the extent of ClO and CH_3O_2 regeneration was dependent on δ in addition to the branching ratio of the Cl forming pathway which could not be directly measured under the experimental setup used in this work. Furthermore, the self and cross-reactions of both CH_3O_2 and HO_2, present as a consequence of the radical carrier product channels of the ClO + CH_3O_2 reaction and the CH_3O_2 self-reaction introduced further uncertainty into the model. These effects became more pronounced with increasing [CH_4] and decreasing temperatures, owing to the negative temperature dependent behaviour of the peroxy radical reactions and of the ClO + HO_2 reaction. As a consequence, it was necessary to constrain δ at lower temperatures when optimising $k_{(5.1)}$. In comparison, the products of the ClO + HO_2 reaction as well as the competing HO_2 self-reaction are believed to be principally radical terminating and Cl atom regeneration was not in this case an issue.

The experimental work carried out on the reaction of BrO + HO_2 reported in Chapter 6 used an analogous approach to that described in Chapters 4 & 5. However the principal differences here arose from the need to use halogen mixtures of both Br_2 and Cl_2 in the photolysis mixtures for the BrO + HO_2 study and utilising the BrO self-reaction as a means to calibrate the total atom number density formed post-photolysis. Another key difference was the conditions employed under the photolysis experiments themselves (reported in Chapter 6) compared to those reported in Chapters 4 & 5: conditions of excess HO_2 were attempted to maximise the sensitivity of BrO decay to its reaction with HO_2 and to inhibit the BrO self-reaction which features a Br regenerating product channel. Although the Br forming reaction channel of the BrO self-reaction was measured in this work, uncertainty in these measurements may have led to an inaccurate characterisation of the BrO + HO_2 reaction if a significant BrO flux was not through reaction with HO_2. Furthermore, the BrO self-reaction needed to be inhibited as to determine the partitioning between the initial [Cl] and [Br] formed post-photolysis, knowledge of which was crucial to the fitting model employed on FACSIMILE.

The total rate constant of BrO + HO_2, $k_{(6.1)}$, measured in this work again relied heavily on extensive modelling of the photolysis system. The results found that the retrieved values of $k_{(6.1)}$ were significantly dependent on the partitioning of Cl and Br upon photolysis, again denoted δ and defined in Chapter 6 above. Calculation of δ prior to experiment was compromised in this case by the potential presence of BrCl arising from the unavoidable equilibration of Br_2 + Cl_2 to give 2BrCl, which would change the optical density of the photolysis mixture and therefore the atom yield at the photolysis laser wavelength. While the equilibrium constant of this reaction has been experimentally determined previously at ambient temperature,[3] no kinetic or temperature dependence information is available in the literature, thus the extent of reaction of the pre-photolysis mixture was unquantified at the point of its entering the reaction vessel in the current work. Consequently, δ was determined experimentally, the results of which actually implied that very little reaction, if any, had taken place between Cl_2 and Br_2 preceding the time of photolysis of the precursor mixture. In addition, the determined value of $k_{(6.1)}$ was also found to be dependent on the amount of CH_3OH present in the photolysis mixture. CH_3OH is the precursor used for the production of HO_2 but more importantly it also significantly enhances the HO_2 self-reaction due to the concentrations used in this work. The effects of methanol on the rate of the HO_2 self-reaction remain relatively poorly constrained in the literature, however this enhancement has been characterised previously in this laboratory under similar conditions as used in this work and another study has measured the effects of methanol enhancement on the HO_2 self-reaction at T = 298 K which therefore allowed the constraint of this effect in model used in this work.[4,5]

Comparing the results from different systems reported in this thesis, the absolute rate constants of the ClO + HO_2 and ClO + CH_3O_2 reactions are found to be comparable at ambient pressure and temperature. However, the temperature dependence of each reaction is significantly different: $ClO + HO_2$ has a significant negative temperature dependence whereas $ClO + CH_3O_2$ has a strong positive dependence, agreeing with previous work (discussed in Chapters 4 & 5). Reasons for this are hinted at in theoretical studies of these reactions which predict the energy barriers of the transition states to be relatively low compared to the potential energy levels of the initial reactants for $ClO + HO_2$ but high for $ClO + CH_3O_2$, perhaps implying steric effects.[6,7]

When comparing $ClO + HO_2$ with the analogous reaction of $BrO + HO_2$ the results show that these reactions are somewhat closer to one another in general than with $ClO + CH_3O_2$. The ambient pressure and temperature values of the overall rate constants of these reactions reported in this work show, in fact, striking similarity to one another. Both the $ClO + HO_2$ and $BrO + HO_2$ reaction exhibit negative temperature dependences in agreement with previous work. The weaker negative temperature dependence reported in the $BrO + HO_2$ is in near perfect accordance with theoretical predictions although the strong temperature dependence reported for $ClO + HO_2$ here is greater in magnitude than what has been reported both experimentally and theoretically. However, comparing the temperature dependences of all three reactions investigated in this work, it appears that for the general reaction:

$$XO + RO_2 \rightarrow \text{Products} \tag{7.1}$$

where XO is a halogen oxide radical and RO_2 is a peroxy radical, the nature of the species of RO_2 has a greater effect on the efficiency of the reaction than that of XO. Thus further work of halogen oxide radical and peroxy radical reactions should include kinetic studies of halogen oxide radical reaction with larger peroxy radicals than used in this work. While the significance of the atmospheric implications of such studies may be more limited than those of the present work, given the abundance of larger peroxy radical precursors, a greater fundamental understanding of this class of reaction may be achieved.

Future work on the reactions studied in this thesis on the experimental setup used specifically should involve modifications to the apparatus in order to reduce the uncertainty in the results reported here. There are a number of possibilities in modifying the experimental setup to make this technique even more powerful. The inclusion of a second spectroscopic probe, preferably in the infrared region, would be advantageous as this would potentially permit the monitoring of the RO_2 species in addition to the XO. Furthermore, RO_2 species have structured absorption spectra in the infrared region making this spectral region more adept at monitoring these species than in the UV region. The addition of a mass spectrometric detection system downstream of the reaction cell would give information on the final products of these reactions thus providing complimentary data to the kinetic analysis.

The atmospheric implications of the reactions studied in this work depend on the products formed. The ROX type product is a reservoir species of the active halogen and odd hydrogen species as it is not immediately photolysed upon its formation. Thus, the rate of formation of ROX is important in the partitioning of active/reservoir species of the atmospheric halogens and the odd hydrogen family. The partitioning of active/reservoir species will have a greater impact on atmospheric ozone budgets than the formation of products that lead to the direct recycling of active species that react with ozone. This is because both XO and RO_2 react with odd oxygen (although less efficiently than halogen atoms and OH in particular) thus they still deplete atmospheric ozone budgets. However ROX can be an important source of halogen atoms under conditions of low XO concentrations where the halogen oxide self-reactions become less prevalent.

In light of this, the results of this thesis show that the BrO + HO_2 reaction, which is assumed to effectively proceed through the HOBr channel only, is significant at tropospheric temperatures. The reaction possibly occurs at faster rates than already considered at low latitudes and altitudes, whereas it is slower under low temperatures experienced at high latitudes or at higher altitudes. Thus, the partitioning of active bromine and HO_x into reservoir species could therefore be predicted to be greatest at lower altitudes and latitudes, in particular in the non-coastal marine boundary layer, where mixing ratios of BrO are too low to be dominated by its self-reaction chemistry, thus providing a significant source of Br upon the photolysis of HOBr. Conversely, the ClO + HO_2 results, which again assume that the reaction proceeds through the HOCl channel only, imply that this reaction is faster at all temperatures throughout the atmosphere than currently predicted. Furthermore, the reaction becomes particularly efficient at temperatures approaching those that are found in the lower stratosphere. The implications of this in the atmosphere suggest that this reaction is most effective at the tropical upper troposphere/lower stratosphere region and could be a more significant source of active/reservoir chlorine partitioning than currently believed compared to the competing heterogeneous processes. This in fact disagrees with the very recent work of Kuribayashi *et al.*,[8] who have *estimated* a value of $k_{(4.1)}$ much lower at 245 K than what has been found in this work. However, this estimation is made from satellite observations of the mesosphere, where significantly lower pressures are found than what were applied in this work, which has implications if indeed there *is* a pressure dependence of the $ClO + HO_2$ reaction. Finally, the $ClO + CH_3O_2$ reaction rate constants measured in this work imply that its role in Polar stratospheric ozone destruction is predicted to be much less significant than currently believed. Not only does this reaction evidently proceed through product channels that go on to efficiently form Cl atoms and peroxy radicals but the strong positive temperature dependence implies that the importance of this reaction is limited to the late Winter and Spring time polar vortex in the stratosphere.

In conclusion, the work presented in this thesis presents detailed temperature dependence studies of three atmospherically relevant radical reactions. These reactions, which are mixed radical reactions, have been studied using the laser flash photolysis technique with UV spectroscopy coupled to CCD detection. As these reactions are mixed, the challenge in accurately generating both co-reacting radical species and subsequently measuring their concentrations is therefore considerable. However, the power that CCD detection offers has been crucial in elucidating key reactant species directly (*i.e.* XO) and afforded the inference of other specie concentrations through the quality of the temporal traces obtained from differential fitting and the reproducibility of the experiments. The results obtained for the $ClO + CH_3O_2$ and $BrO + HO_2$ reactions in particular, are in excellent agreement with previous laboratory studies and support the case for a change of their recommended values for atmospheric modelling as currently recommended by JPL NASA[1] and IUPAC,[2,9] which do not consider the most recent work. To conclude, this study has confirmed the (well-established) importance of the products generated by the photolysis of halogenated pollutants that can perturb the composition of the atmosphere. Furthermore, it highlights the need, perhaps, for understanding the efficiency and outcome of these free radical reactions that result, which is in many cases lacking. Atmospheric models rely upon accurate quantitative data to interpret field observations: such data can only, in this opinion, be provided by laboratory studies carried out under controlled conditions. Conversely, the inference of detailed kinetic and mechanistic parameters for specific reactions from field observations is devoid of control, which as a consequence precludes any meaningful sensitivity analysis.

The depletion of ozone through halogen chemistry is well known, if not especially well-characterised. Ozone is known to be a solar UV filter, but perhaps more importantly, a source of radicals that define the atmosphere's ability to oxidise and thus control the abundance of species including greenhouse gases, proving that it is crucial in the balance of Earth's energy budget. Not only does the halogen budget affect this, but the effects that halogens have on peroxy radical species are paramount.

The inherent complexity of the gas phase chemistry of the systems reported in this thesis poses significant limitations, which perhaps partly explains the lack of agreement of the previous studies of the systems investigated here. Making a single free radical in a controlled manner using laser flash photolysis is difficult. Making two, separately, in a single photolysis event and in known ratios requires some consideration (with much trial and error). Monitoring two such radicals in real time is extremely challenging. However, if one radical can be measured unequivocally and accurately using, as in this work, a broadband spectroscopic method, then the presence of the other may be inferred *via* observation of its affect on the monitored species. However, this inference has to be backed up by reproducibility of the results but above all by careful examination of any assumptions made through sensitivity analysis.

Finally, if we are to understand nature through the scientific method, we must recognise and appreciate that elucidating the mechanisms and components of what is in essence, the dissipation of energy throughout the Universe released on its formation, is not a simple task. The compartmentalisation of information is, as can be the application of metaphor, a useful tool in gaining meaning, but it is not without its limitations. As in the case of the atmosphere, the 'family' assumption for atmospheric gas phase free radicals is a convenient conceptual idea, but radical families are quite happy to cross-breed in reality and are also not restricted to just one phase. We need humility and care in our studies of atmospheric processes to expound such phenomena fully, in order to take our understanding of the chemistry of the atmosphere, as a whole, forward.

7.1 References

1. Sander, S.P., J. Abbatt, J. R. Barker, J. B. Burkholder, R. R. Friedl, D. M. Golden, R. E. Huie, C. E. Kolb, M. J. Kurylo, G. and V.L.Orkin K. Moortgat, P. H. Wine, "Chemical Kinetics and Photochemical Data for Use in Atmospheric Studies, Evaluation No. 17," JPL Publication 10-6, Jet Propulsion Laboratory, Pasadena, 2011 http://jpldataeval.jpl.nasa.gov.
2. Atkinson, R., D.L. Baulch, R.A. Cox, J.N. Crowley, R.F. Hampson, R.G. Hynes, M.E. Jenkin, M.J. Rossi, and J. Troe, Evaluated Kinetic and Photochemical Data for Atmospheric Chemistry: Volume II – Gas Phase Reactions of Organic Species. *Atmospheric Chemistry and Physics*, 2006. **6**: 3625-4055.
3. Maric, D., J.P. Burrows, and G.K. Moortgat, A Study of the UV—visible Absorption Spectra of Br_2 and BrCl. *Journal of Photochemistry and Photobiology A: Chemistry*, 1994. **83**(3): 179-192.
4. Stone, D. and D.M. Rowley, Kinetics of the Gas Phase HO_2 Self-Reaction: Effects of Temperature, Pressure, Water and Methanol Vapours. *Physical Chemistry Chemical Physics*, 2005. **7**(10): 2156-2163.
5. Bloss, W.J., D.M. Rowley, R.A. Cox, and R.L. Jones, Rate Coefficient for the BrO + HO_2 Reaction at 298 K. *Physical Chemistry Chemical Physics*, 2002. **4**(15): 3639-3647.
6. Kaltsoyannis, N. and D.M. Rowley, *Ab initio* Investigations of the Potential Energy Surfaces of the XO + HO_2 Reaction (X = Bhlorine or Bromine). *Physical Chemistry Chemical Physics*, 2002. **4**(3): 419-427.
7. Kosmas, A.M. and E. Drougas, A Computational Investigation of the Atmospheric Reaction CH_3O_2 + ClO. *Chemical Physics*, 2009. **358**(3): 230-234.
8. Kuribayashi, K., H. Sagawa, R. Lehmann, T.O. Sato, and Y. Kasai, Direct Estimation of the Rate Constant of the Reaction $ClO + HO_2 \rightarrow HOCl + O_2$ from

SMILES Atmospheric Observations. *Atmospheric Chemistry and Physics*, 2014. **14**(1): 255-266.

9. Atkinson, R., D.L. Baulch, R.A. Cox, J.N. Crowley, R.F. Hampson, R.G. Hynes, M.E. Jenkin, M.J. Rossi, and J. Troe, Evaluated Kinetic and Photochemical Data for Atmospheric Chemistry: Volume III – Gas Phase Reactions of Inorganic Halogens. *Atmospheric Chemistry and Physics*, 2007. **7**: 981-1191.

Appendix I: Calibration Procedures

Several calibration procedures were required for each reaction studied which were essential to the accuracy of the experiments performed. What follows is a description of these procedures.

AI.1 Gas Flow rates of Inert Gases: Mass Flow Controller Calibration

Mass flow controllers (MFCs) were used to deliver accurate flow rates of the largely inert carrier gases (N_2/O_2) and their flows through bubblers in which the concentrations of liquid precursors were controlled. Routine calibrations of the MFC units were performed by setting a specific voltage on the MFC controller unit and reading the MFC output. The output flow was passed through a burette in which a sidearm was attached upstream of it *via* a T-piece. Soapy water was injected into the gas flow causing it to bubble. These bubbles were monitored, observing the time the meniscus took to flow through a given volume. Various flow rates were set in a random order and their observed rates recorded and plotted as in Figure A1.1. These plots were fitted using linear regression to give a calibration line for each MFC unit used.

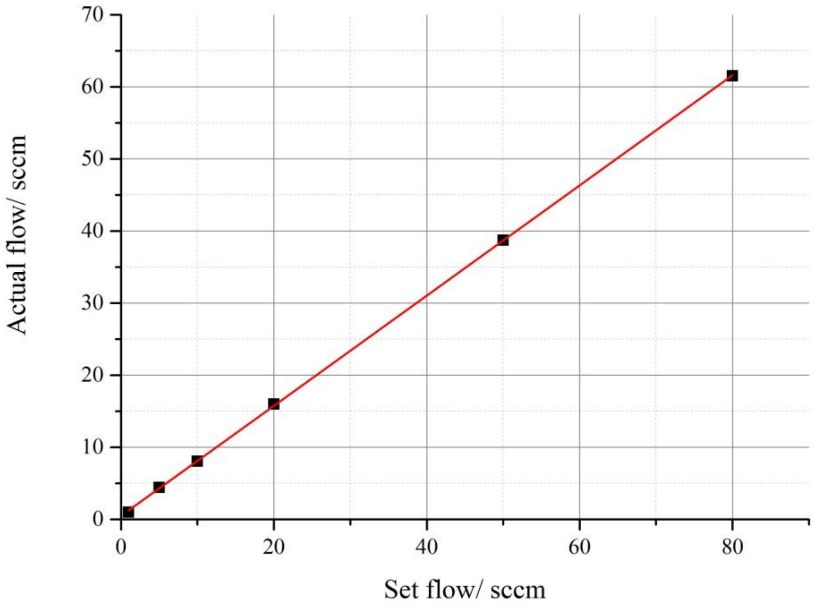

Figure AI.1 *A calibration plot for a mass flow controller.*

AI.2 Flow Rates of Corrosive Gases: Rotameter Calibration

A rotameter was used to measure the flow of the diluted chlorine gas rather than an MFC due to the corrosive nature of the gas. The rotameter was routinely calibrated by passing a known flow of nitrogen gas through the rotameter and recording the corresponding position of the ball within the rotameter. The figure below provides an example of a calibration plot for a rotameter, as used in experiments, with the corresponding optimised trend line based on a polynomial function.

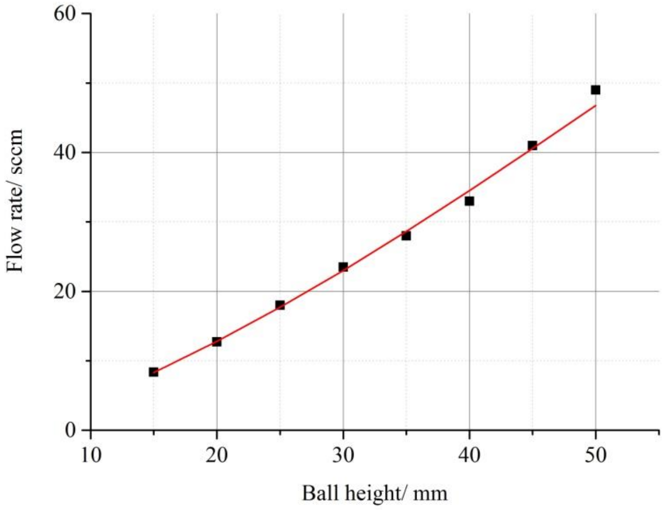

Figure AI.2 *An example of a calibration plot for a rotameter used in the experiments.*

AI.3 Wavelength Calibration

Wavelength calibration of the CCD detector was conducted for each day of experiments conducted. Calibration was undertaken by measuring the emission spectra of a low pressure mercury pen-ray lamp (Oriel) using the identical spectral settings that were applied to a particular set of experiments, changing only the position of the spectral window which was centred on the primary emission peak, shown in Figure AI.3.

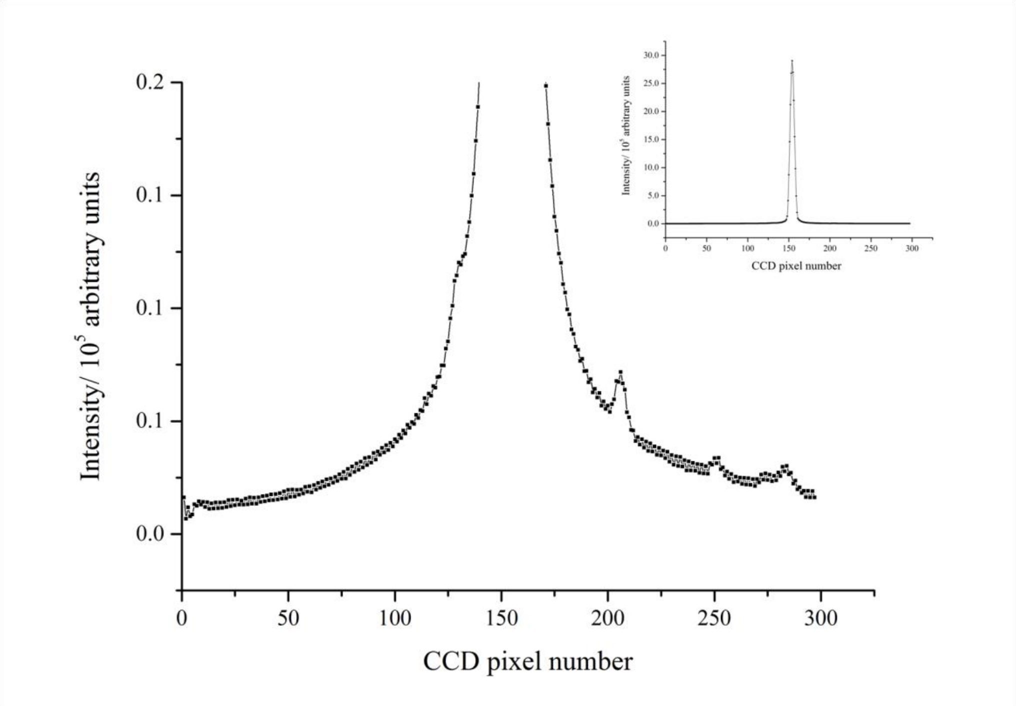

Figure AI.3 *The emission spectra of a low pressure Hg pen-ray lamp. The main figure is a zoomed in view of the inset spectrum, showing the principal Hg emission peak at 253.65 nm.*

By recording what pixel number corresponded to a particular well wavelength-defined emission peak in the recorded spectrum, a plot of pixel number *versus* wavelength gave a linear relationship upon selecting several peaks (typically the peaks occurring at 248.20, 253.65 and 265.20 nm), shown in Figure AI.4. Thus the gradient of this linear relationship was equal to the wavelength dispersion and the intercept was the lower limit of the spectral overage at a particular spectrograph setting.

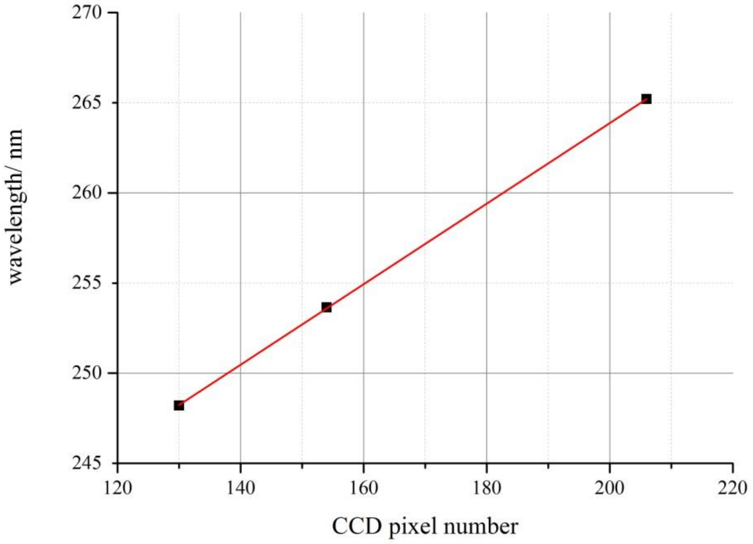

Figure AI.4 *A calibration plot for the wavelength axis (columns) of the CCD detector.*

Appendix II: Vibronic Spectra and the Effect of Instrument Function

Unlike smooth UV absorption spectra, structured vibronic spectra, as used extensively in this work, are strongly dependent on the resolution and, therefore, function of the instrument. Hence it is not appropriate to use literature cross sections direct, if the resolution they were recorded on does not match the experimental resolution at which they are to be used.

AII.1 Measuring the instrument function

Any given electronic transition, including vibronic transitions, has a natural line width associated with the observed radiation (absorptive or emissive), as governed by Heisenberg's uncertainty principle. When observed through a dispersive detection system, as is the case in the current work, the ability to detect monochromatic light is subject to the instrument function of the system, which influences the observed magnitude and width of the peak function. Even monochromatic light is spread over a range of apparent wavelengths when passed through a diffraction grating, governed by this instrument function which in turn is dependent on the spectral resolution. The spectrograph/CCD detection system employed in this work has a spectral resolution which is a function of the entrance slit width and dispersion of spectrograph (*i.e.* the applied diffraction grating).

Figure AII.1, below, shows a singlet emission peak of mercury (See Appendix I), recorded at a diffraction grating of 300 grooves/ mm and at a slit width of 75 µm and the function that best describes the shape of this peak is Gaussian. Thus, the resolution of the instrument function could be determined by measuring the *full-width half-maximum* (FWHM) of a Gaussian function, fitted to the recorded peak, defined as:

$$y = I_{\max} \exp \{-a(\lambda - \lambda_{\max})^2\} \qquad \text{(AII.i)}$$

where $I_{\max}$ is the maximum intensity of the Gaussian, a is the width parameter and $\lambda_{\max}$ is the wavelength of the maximum intensity. The condition of the FWHM is:

$$y = \frac{I_{\max}}{2} \tag{AII.ii}$$

From this definition, the resolution (*i.e.* FWHM) is given by the following expression:

$$\text{resolution (FWHM)} = 2\left\{\lambda_{\max}^{2} - \left(\lambda_{\max}^{2} + a^{-1}\ln\frac{1}{2}\right)\right\}^{0.5} \tag{AII.iii}$$

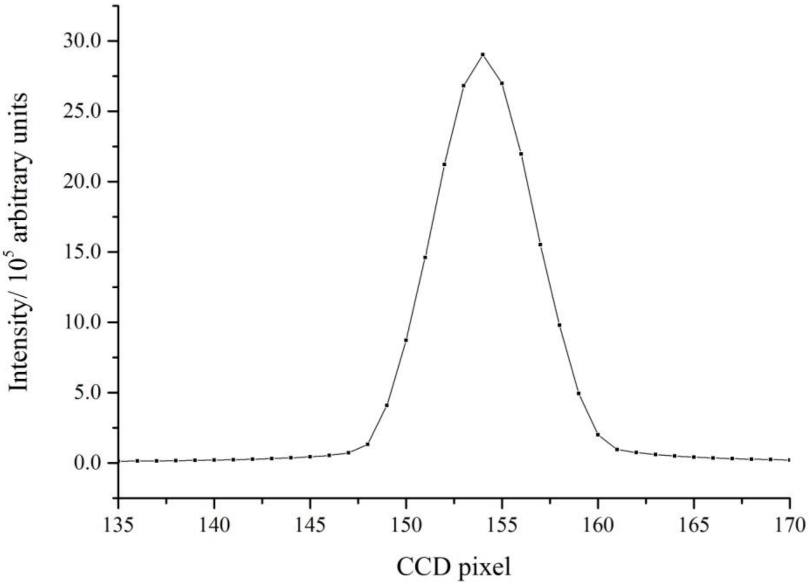

Figure AII.1 *A mercury singlet peak recorded on the CCD detector.*

AII.2 Spectral Convolution

As discussed in Chapter 2, certain species exhibit vibronic structure in their absorption spectra which is observed as a progression of individual peaks. The intensity and shape of these peaks are strongly dependent on the resolution of the apparatus used, with the consequence of reduced peak intensity and increased width with decreasing resolution, which results in the apparent smoothing of the observed spectra. Consequently, the absorption cross sections, which are crucial in accurately determining the concentrations of such species spectroscopically, of these spectral lines become convoluted with decreasing resolution function.

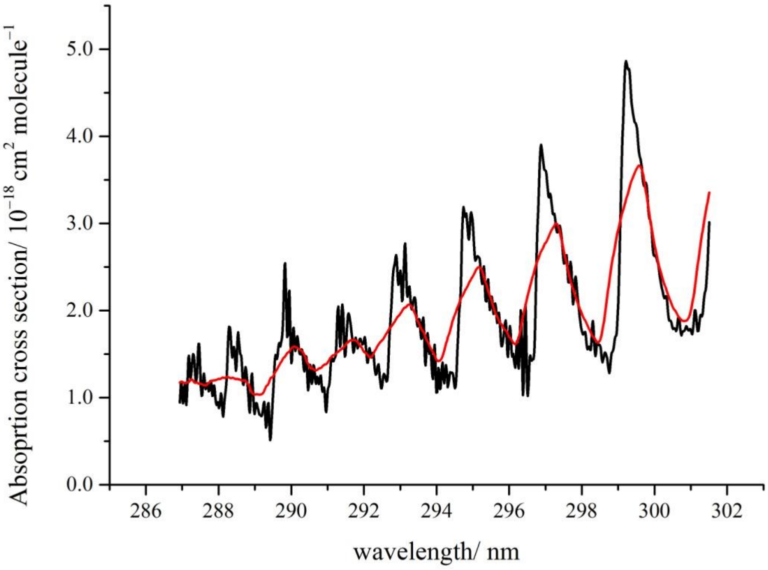

Figure AII.2 *A zoomed in view of the BrO absorption cross sections taken from Wilmouth et al.*[1] *resolution 0.4 nm (in black) and the corresponding cross sections after application of the averaging procedure (in red), resolution 1.1 nm.*

The use of absorption spectra which were differentially fit to literature cross sections was key in determining the halogen oxide radical specie concentrations in this work. For BrO in particular, the literature cross section used was measured at a much higher resolution than the experimental setup employed here.[1] Thus, it was necessary to effectively degrade the resolution of the absorption cross sections by smoothing them. Cross sections were smoothed to appropriate lower resolutions by applying sliding average routines that incorporated a Gaussian function (due to the resolution function of the apparatus). The smoothing kernel used in the averaging was comprised of a Gaussian function that was selected with the appropriate FWHM to match the resolution of the experimental apparatus. The resultant smoothed cross sections (as shown in Figure AII.2, in red) could therefore be used in the differential fitting routine once transposed onto a suitable wavelength grid.

AII.3 References

1. Wilmouth, D.M., T.F. Hanisco, N.M. Donahue, and J.G. Anderson, Fourier transform ultraviolet spectroscopy of the A (2)Pi(3/2) ← X (II3/2)-I-2 transition of BrO. *Journal of Physical Chemistry A,* 1999. **103**(45): 8935-8945.

Appendix III: Gaussian Fitting to Literature Absorption Cross Section Data

Certain reactant precursors absorb in the UV region which enabled the determination of their concentration by spectroscopic means. The spectra of these species exhibit smooth absorptions and were therefore resolution independent. Literature data of these species is available but often in intervals of integer wavelengths. The wavelength dispersion onto the CCD *via* the spectrograph was much smaller than these intervals, thus, cross section values were needed for the wavelength range over each experimental grid. The shape of these absorption cross sections can be well described by a single or the sum of multiple Gaussian functions:

$$y = \sigma_{\max} \exp\left(- a \left[\ln\left(\frac{\lambda_{\max}}{\lambda}\right)\right]\right) \qquad \text{(AIII.i)}$$

where $\sigma_{\max}$ is the peak absorption of the Gaussian, $\lambda_{\max}$ is wavelength (λ) at which the max occurs and a is the width parameter. The use of this function is justified as the wavefunction of the ground electronic state of a species is usually Gaussian in shape. As smooth UV absorption spectra arise from electronic transitions from the ground state to dissociative states, their shape resembles the ground state wavefunction. The parameters of the Gaussian function(s) used to describe the absorption cross sections of a particular species were optimised to fit the literature data by a least squares routine.